UNIVERSITÀ DELLA CALABRIA

UNIVERSITY OF CALABRIA
The Department of Biology, Ecology and Earth Sciences

Research doctorate in
Science and Engineering of the Environment, Construction and Energy
(XXXII cycle; 2016-2019)

TITLE

“Facies analysis and fluid inclusion studies of the Messinian evaporites, Calabria, Southern Italy”

Scientific disciplinary sector: GEO/02

Coordinator Prof. Salvatore Critelli

[redacted]

Firma oscurata in base alle linee
guida del Garante della privacy

Supervisor Dr Rocco Dominici

Firma oscurata in base alle linee
guida del Garante della privacy

Co-Supervisor Dr Alessandra Costanzo

Firma oscurata in base alle linee
guida del Garante della privacy

PhD Student Dr Mara Cipriani

Firma oscurata in base alle linee
guida del Garante della privacy

Index

La Natura compone alcune delle sue poesie più belle
davanti al microscopio e al telescopio.
(Theodore Roszak)

Abstract (English Version)

Messinian salinity crisis (MSC) is, from about 30 years, one of the most important and debated topic in the scientific community, both in environment and economic field.

In this context, Calabrian evaporite deposits, poorly investigated in the past, offer an interesting opportunity to expand the knowledge because they confirm and increase the models created for other Mediterranean basins, and add important information on the main halite and gypsum facies. In this regard, saline evaporitic facies outcropping in the Crotone, Catanzaro and Ionic Basins were investigated using a multidisciplinary approach from classical petrography, to the study of fluid inclusions (FIs) to isotopic geochemistry.

(A) The halite samples from the Crotone Basin have highlighted three primary facies; two known in the literature as *banded* and *white* while the third, never observed before, called in this work *transparent*. The transparent facies seems recrystallized but the analyses conducted show instead a primary origin. The three facies form in different environment and with a dissimilar deposition rate (fast or slow) due to pycnocline oscillation (daily or seasonal). Pycnocline oscillations can explain the different temperature of homogenization found within the FIs (from +20° to +33°C). The facies form in a hybrid brine (salinity av. ~26.2 eq. wt% NaCl) enriched in Ca-Mg-Na-K-Cl elements, regardless of their deposition rates. During their growth, crystals trap primary FIs and microalgae (blue, green and yellow). Primary FIs and organic matters, associated with secondary fluid inclusions testifying plastic and ductile deformations that don't remove primary features, demonstrating low recrystallization during burial process. Moreover, isotopic data attribute these facies at the second step of the MSC (5.6-5.5 Ma) during *Halite deposition stage* in the Mediterranean Basin.

(B) The selenite samples from the Catanzaro Trough belong to banded and giant facies. The crystals record *middle-frequency climatic oscillation* between the depositional cycles and *high-frequency climatic oscillation* (seasonal) between cloudy and clear microfacies observed within the crystals. These microfacies testify a different brine condition associated with seasonal variation: cloudy intervals form during continental water inflow in the humid phase (Mg and Ca as dominant elements and low salinity values - av.~3 eq. wt% NaCl), while, clear intervals form in marine water during the arid phase (Na, K and Cl as dominant elements and high salinity values - av.~21.5 eq. wt% NaCl). Isotopic data attribute these facies at the third step of the MSC (5.5-5.3 Ma) placing, for the first time, the formation of the giant facies at the *Upper Gypsum stage* in the Mediterranean Basin.

(C) The analyses conducted on the gypsum deposit from the Ionian Basin have shown that these crystals do not display primary features. This deposit is an olistostrome. The isotopic data confirm secondary origin attributing these facies at the second step of the MSC (5.5-5.3 Ma) during the *Resedimented Lower Gypsum deposition stage* in the Mediterranean Basin.

The data obtained from the study of the Calabrian Messinian deposits indicate a surprising variety and diversity of evaporitic facies. In this work, it emerges that the formation of the different facies is strongly conditioned by climate (wet/arid) and intrinsic

characteristics of the basin (depth, arrival of continental water flows etc.) which promote the development of one facies rather than of another.

Abstract (Italian Version)

La Crisi di Salinità del Messiniano (MSC) è, da oltre 30 anni, tra gli eventi che suscita maggiore interesse nel mondo accademico, sia per i suoi risvolti in ambito ambientale (ricostruzioni paleoclimatiche e paleobiologiche) che per le sue implicazioni in campo economico. In quest’ottica, i depositi evaporitici Calabresi, scarsamente investigati nel passato, offrono un’interessante opportunità di ampliamento delle conoscenze finora ottenute, poiché da una parte, confermano e implementano i modelli ricostruiti per altri bacini del Mediterraneo, e dall’altra, forniscono importanti informazioni sulle principali facies di halite e gesso. A tal proposito, sono state investigate le facies evaporitiche saline affioranti nei Bacini di Crotone, Catanzaro e Ionico mediante un approccio multidisciplinare che va dalla petrografia classica, allo studio delle inclusioni fluide (FIs) alla geochimica isotopica.

(A) I campioni di halite, provenienti dal Bacino di Crotone, appartengono a tre facies primarie, due delle quali precedentemente descritte in letteratura e denominate rispettivamente *banded* e *white* e una, mai osservata fino ad ora, definita in questo studio come *transparent*. Quest’ultima, in apparenza ricristallizzata, è risultata essere di origine primaria. Lo studio multidisciplinare ha messo in luce come la formazione delle tre facies sia influenzata dalle oscillazioni giornalieri e/o stagionali del picnoclino che di base determina diversi ambienti e tassi deposizionali. Le oscillazioni del picnoclino, correlate alle variazioni climatiche, spiegano le diverse temperature di omogeneizzazione (da +20° a +33°C) rinvenute all’interno delle FIs nei cristalli di halite. Indipendentemente dai tassi di deposizione, le facies si formano e si accrescono in un bacino ibrido, arricchito in Ca-Mg-Na-K-Cl, e con una salinità media di circa 26.2 eq. wt% NaCl. Durante la loro crescita intrappolano, al loro interno, inclusioni fluide e microalghe blu, verdi e gialle. La presenza di FIs primarie e di microorganismi, associate alle inclusioni fluide secondarie che testimoniano deformazioni fragili e duttili senza mascherare le strutture primarie, dimostrano che questi depositi hanno subito un basso grado di ricristallizzazione durante il seppellimento. Inoltre, i dati isotopi hanno permesso di ricondurre queste facies al secondo stage della MSC (5.6-5.5 Ma) durante la deposizione dell’*Halite* nel Mediterraneo.

(B) I campioni di selenite provenienti dalla Stretta di Catanzaro appartengono alla banded e alla giant facies. I cristalli hanno registrato oscillazioni climatiche sia a *media frequenza*, tra un ciclo deposizionale ed un altro che ad *altissima frequenza* tra le microfacies cloudy e clear osservate all’interno dei cristalli. Le microfacies testimoniano diverse condizioni della salamoia associate a variazioni stagionali: gli intervalli cloudy registrano afflussi di acqua continentale tipici di un clima umido (Mg e Ca come elementi dominanti e bassi valori di salinità ~3 eq. wt% NaCl), al contrario, gli intervalli clear sono associati ad una fase arida in cui vi erano scarsi o nulli input di acqua continentale (Na, K e Cl come elementi dominanti e alti valori di salinità ~ 21.5 eq. wt% NaCl). I dati isotopici attribuiscono queste facies al terzo stage della MSC (5.5-5.3 Ma), durante la deposizione delle *Upper Gypsum* nel Mediterraneo. I dati scaturiti da questo studio hanno permesso di associare, per la prima volta, la giant facies alla formazione delle *Upper Gypsum* e non alle *Lower Gypsum*.

(C) Le analisi condotte sul deposito di gessi prelevati dal Bacino Ionico hanno evidenziato cristalli totalmente ricristallizzati (senza strutture relitte primarie) al contrario di quanto era emerso dall'osservazione in situ. Queste evidenze sono state confermate dai dati isotopici che attribuiscono tali cristalli al secondo stage della MSC (5.5-5.3 Ma) durante la formazione delle *Resedimented Lower Gypsum* nel Mediterraneo riconducendo il deposito ad un olistostroma.

I dati, ottenuti dallo studio dei depositi Messiniani Calabresi, indicano una sorprendente varietà e diversità di facies evaporitiche. In questo lavoro emerge che, la formazione delle diverse facies è strettamente condizionata dal clima (umido/arido) e dalle caratteristiche intrinseche del bacino di formazione (profondità, arrivo di flussi di acqua continentale etc.) che favoriscono lo sviluppo di una facies rispetto ad un'altra.

Introduction

The Messinian salinity crisis (MSC), occurred around 6 Ma ago, is a complex geological event which transformed the Mediterranean Sea into a giant saline basin causing a catastrophic hydrological and biological crisis (CIESM, 2008). This event, represents from about 30 years, one of the most important and controversial topics in the scientific community. The peculiar geological event triggered the formation of extensive evaporite deposits which, in less than 640 ka, accumulated on the bottom of the Mediterranean basin (Roveri *et al*., 2008; Lugli *et al*., 2010; Manzi *et al*. 2009, 2012) known as Lower Evaporites, Halite and Upper Evaporites. Over the years, numerous scientific studies have been carried out on several deposits dislocated in the Mediterranean basin (e.g. Spain, Central-Northern Italy, Sicily, Turkey, Cyprus) contributing to better understanding of their formation mechanisms, however only stratigraphic and petrographic preliminary study (Lugli *et al*., 2007; Cianflone *et al*., 2011, 2012; Speranza *et al*., 2012; Costanzo *et al*., 2019) have been conducted on the evaporite deposits from the Calabria region (Southern Italy), leaving many unresolved questions. In the Calabria region there are different evaporite outcrops associated with the main deposition events of the MSC; a detail study of these deposits could increase the knowledges on the geological evolution of their basins during the Messinian age and to provide to answers to these questions. The main evaporite deposits are located in the Crotone basin (halite salt domes), in the Catanzaro Trough (selenite deposit) and in the Ionian Basin (selenite deposit).

The aims of this PhD project are:

1) Providing an overview of the MSC problems in the Mediterranean and in the Calabria region: problems solved and unsolved - Chapter 1.

2) Identification and description of (i) the different evaporite facies, (ii) the biological content and (ii) the deformation degree (plastic/ductile strain), using the Optical Microscopy, Ultra-Violet Microspectroscopy, Laser Raman Microspectroscopy (LRS) and Scanning Electron Microscope (SEM) - Chapter 2.

3) Interpreting of the evolution of paleoenvironment and paleoclimatic conditions (salinity, temperature of homogenization, chemical composition) under which the halite and the selenite were formed related to the climatic oscillations using the Optical Microscopy and Fluid Inclusion Microthermometry - Chapter 3 and 4.

4) Dating the crystals and to accurately place in the MSC scenario which is composed by three developmental phases (Stage 1: Lower Gypsum, stage 2: Resedimented Lower Gypsum and Halite and stage 3: Upper Gypsum) and to understand the reason for a simultaneous presence, in a restricted area, of facies belonging to the Lower and the Upper Gypsum, using $^{87}Sr/^{86}Sr$ ratio measurement - Chapter 5.

5) Interpretation of the sedimentological facies and their relationships with hydrological and geochemical factors characterizing the original depositional environments and creation of new depositional models for the halite and selenite outcrops - Chapter 6.

The overall objective of this research is therefore of insert the Calabrian evaporites into the interpretive framework of the MSC, confident that they can contribute improving the interpretation of the several uncertainties relating to one of the most complex and important geological events of the Cenozoic.

CHAPTER 1. The Messinian salinity crisis in the Mediterranean basin and geological setting of the Calabria region

1.1 Introduction

The Messinian Salinity Crisis (MSC), which affected the Mediterranean has been considered the most catastrophic examples of regional environment change in Neogene period (CIESM, 2008). This event caused the deposition of kilometric scale evaporite units (Figure 1.1). For more than 30 years the MSC has represented one of the most important and controversial topics of scientific debate, stimulating interdisciplinary research projects that aim to understand the multiple mechanisms involved in this event: its timing, the geographic upheavals, the relationships between external forcing and physical systems response, the implications for the biological activity.

The interest in Messinian events has shed new light on evaporite deposits which until recently were mostly considered as “geochemical events”, devoid of any sedimentological and biological significance. New extensive studies on commercial solar works have been the basis for understanding the sedimentology, petrology and geochemistry of evaporite facies and their relationships with biological activity (CIESM, 2008).

From that is deduced that innumerable studies have been made and continue to exist on the evaporites located in the Mediterranean area, with the exception of the Calabrian evaporites which are the deposits less investigate from paleoenvironment and paleoclimatic point of view.

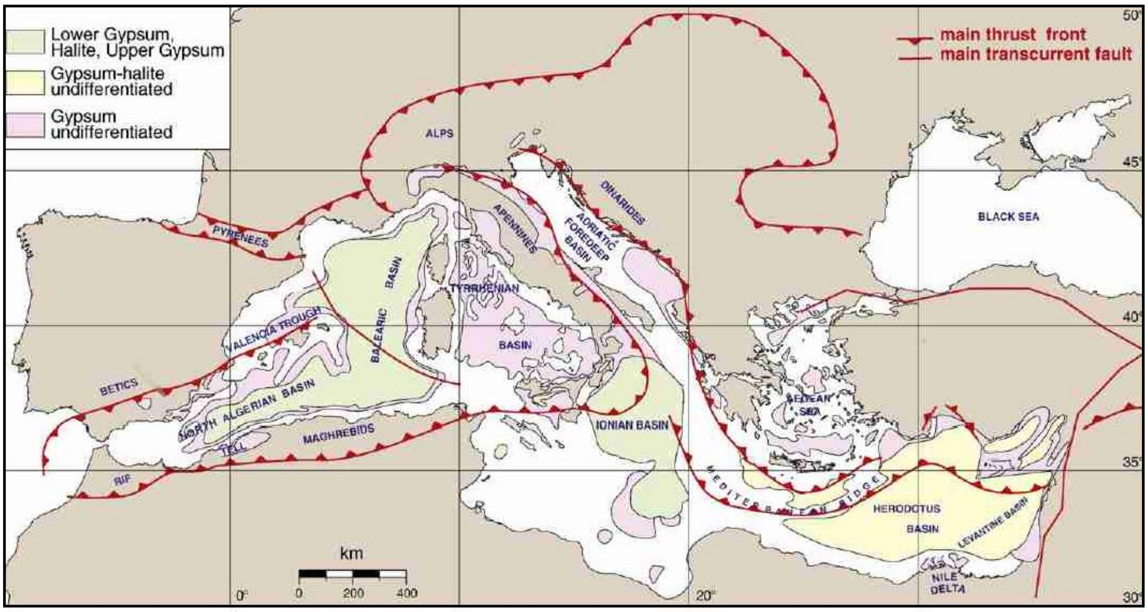

Figure 1.1. Distribution of the Messinian Evaporites in the Mediterranean area (modify after Rouchy & Caruso, 2006).

1.2 Old and new scenario of the Messinian Salinity Crisis

The Messinian Salinity Crisis (MSC) origins is linked to two contemporary factors: a slowly evolving paleogeography driven by plate tectonics (caused the temporary reduction of the marine connections between the Mediterranean and the Atlantic Ocean) and a eustatic fall in sea level linked with global cooling. Ohneiser *et al.*, (2015) have been demonstrate that desiccation and refilling were timed by the interplay between glacio-eustatic sea-level variations, glacial isostatic adjustment and mantle deformation in response to changing water and evaporite loads, using a $\delta^{18}O$ record to model relative sea-level changes.

The MSC actual magnitude was not realized, nor could it be predicted, from the relatively small and scattered outcrops of Upper Miocene gypsum and halite deposits of perimediterranean areas.

This became fully appreciated only at the beginning of the ‘70s, when Deep Sea Drilling Project (DSDP) cores recovered evaporite rocks from the M reflector (Hsü & Cita, 1973), a seismic feature recognized below the deep Mediterranean basin floors since the pioneering seismic surveys of the ‘50s. It soon became clear that a salt layer varying in thickness from 1.500 m to more than 3.000 m for a total estimated volume of 1 million km^3 had been laid down throughout the whole Mediterranean basin at the end of the

Miocene. The DSDP drilling Leg 13 recovered gypsiferous strata in the upper few meters of the basinal sequences, but the full Messinian succession could not be drilled at that time. It is estimated that 95% of the total volume of the Messinian evaporites preserved in the deep basins. These evidences led to the suggestion that these basins were almost completely desiccated.

When the deep Mediterranean evaporites were first discovered, discussion about the most appropriate scenario for their formation begun. Three models were formulated:

- Deep desiccated basin (Hsü & Cita, 1973);
- Shallow water desiccated basin (Nesteroff, 1973);
- Deep non desiccated basin (Selli, 1973).

Discussing discrepancies between the various scenarios took up most of the following fifteen years while significant progresses were achieved on the biostratigraphic definition of the Messinian Stage (Colalongo *et al.*, 1979), the impact of fluvial erosion (Clauzon, 1973, 1978) and the origin of evaporites (Rouchy, 1982).

In the early nineties, a serious effort was made to provide a chronology of the events that occurred during the Messinian Stage, first in the Atlantic area (Benson *et a*l., 1991), then in the Mediterranean itself (Gautier *et al.*, 1994), leading to the long expected magnetostratigraphy of the Messinian Salinity Crisis. The first climate reconstruction of the Sicilian Tortonian to Zanclean series was also published at that time (Suc & Bessais, 1990). These advances favoured the development of new scenarios: most of them (Butler *et al.*, 1995; Clauzon *et al.*, 1996; Riding *et al.*, 1998; Krijgsman *et al.*, 1999; Rouchy & Caruso, 2006) aimed to reduce certain contradictions of the “deep desiccated basin” model (Hsü & Cita, 1973); others (Manzi *et al.*, 2005) continued to cast doubts about the total desiccation of the Mediterranean basin.

So, all the scenarios, before 1995, can be divided in two groups: large and deep basins occupying areas around the deeper basins of the Mediterranean and small and shallow located in a marginal position.

A comprehensive facies model for Messinian primary *gypsum deposits* has been proposed by Vai & Ricci Lucchi (1977) based on Apennine examples.

Salt deposits are essentially known from the Sicilian salt mines, showing a mainly halitic composition with minor K and Mg salts intercalations in the middle part.

The *Upper Evaporites* have been described from outcrops in Sicily (Schreiber, 1997) and are present also in the Ionian Islands and Cyprus. The corresponding time interval is recorded by mainly clastic deposits with highly variable thicknesses in the other basins (Apennines, Sorbas). The strong lateral differences in lithology, thicknesses and paleontologic assemblages of the uppermost Messinian deposits have consolidated the idea of a parallel development of several disconnected Mediterranean sub-basins with different base levels that were much lower than the global ocean. Before CIESM Workshop (Almeria, November 2007) the most accepted theory was that of Rouchy & Caruso (2006) who, studied evaporitic units in Sicily, said that the deposition occurred in two distinct phases: lower and upper evaporites.

- the *Lower Gypsum* (are represented of Gypsum of Cattolica), deposited in the deeper basins during the period of greatest decline in the level of the sea and the simultaneous erosion of margins, beginning slightly diachronous between marginal basins and deep, it corresponds to the *Lower Evaporites* on the Mediterranean Sea;

- *Messinian Erosion Surface* (MES) is a disconformity surface and corresponding the main drop in the level of the sea and it is of zone by the growth of salt, it corresponds to the *Salt* on the Mediterranean Sea;

- the *Upper Gypsum* (are represented of Gypsum of Pasquasia) demonstrating the increase of fresh water occurred in the Messinian Upper and corresponds to the event called the Lago-Mare, immediately previous the return of sea level (in the early Pliocene), it corresponds to the *Upper Evaporites* on the Mediterranean Sea.

These units are also important in the chronostratigraphic level because the *Lower Evaporites* marks the beginning of the MSC. The MES is the largest drop in the level of the sea and the *Upper Evaporites* is the end of the MSC. Different interpretations of the palaeogeographic position of the Messinian Sicilian basin and more generally of the synchronous versus diachronous onset of MSC in marginal and deep basins have led to a number of controversial MSC scenarios, summarized (Figure 1.2) by Rouchy and Caruso (2006).

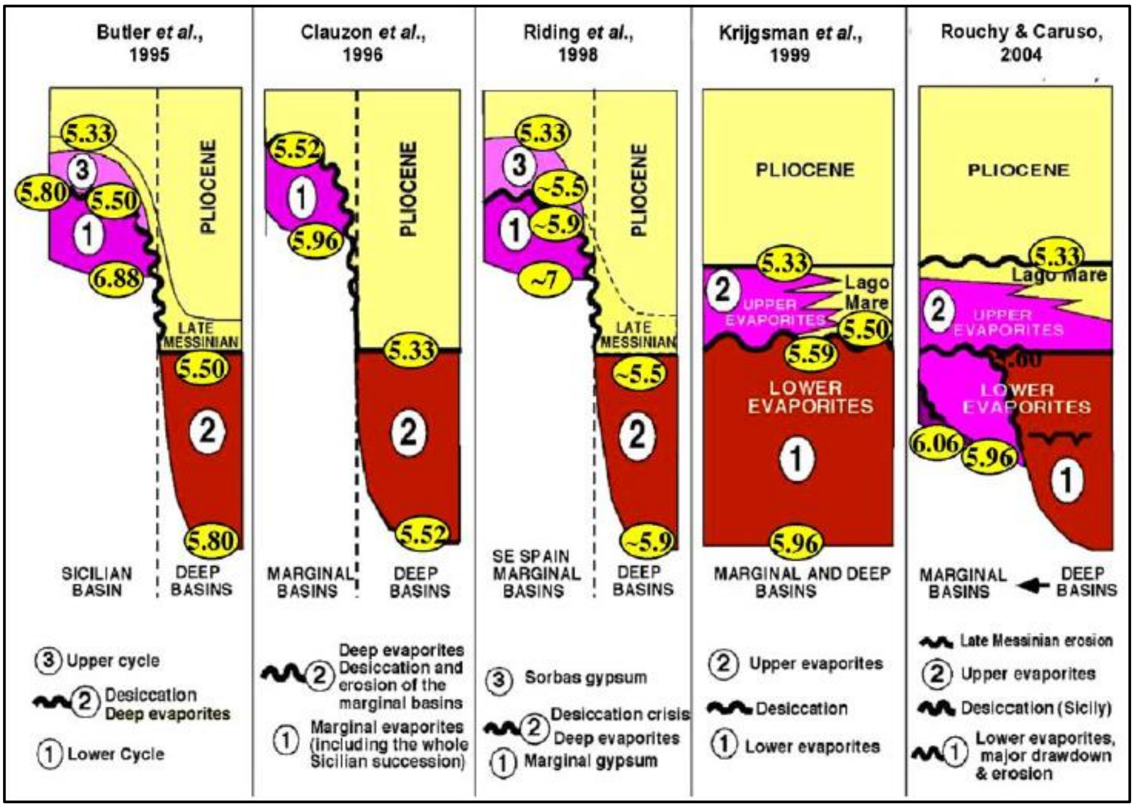

Figure 1.2. Different *MCS scenarios* (from Rouchy & Caruso, 2006).

Recently, during the CIESM Workshop (Almeria, 7-10 November 2007), it was proposed a new MSC scenario composed by three developmental phases (Roveri *et al.*, 2007). During each phase a particular association of evaporitic facies was deposited (Figure 1.3).

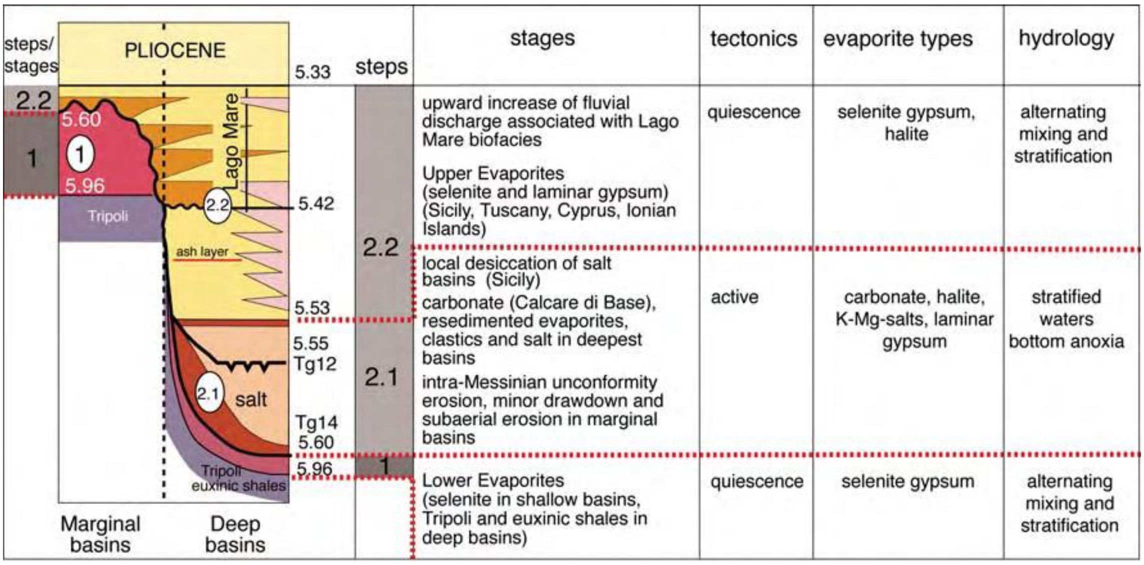

steps	stages	tectonics	evaporite types	hydrology
2.2	upward increase of fluvial discharge associated with Lago Mare biofacies Upper Evaporites (selenite and laminar gypsum) (Sicily, Tuscany, Cyprus, Ionian Islands)	quiescence	selenite gypsum, halite	alternating mixing and stratification
2.2 2.1	local desiccation of salt basins (Sicily) carbonate (Calcare di Base), resedimented evaporites, clastics and salt in deepest basins intra-Messinian unconformity erosion, minor drawdown and subaerial erosion in marginal basins	active	carbonate, halite, K-Mg-salts, laminar gypsum	stratified waters bottom anoxia
1	Lower Evaporites (selenite in shallow basins, Tripoli and euxinic shales in deep basins)	quiescence	selenite gypsum	alternating mixing and stratification

Figure 1.3. A New scenario of the MSC with the steps of evaporitic deposits in the time, role of tectonics, evaporites types and hydrology (from Roveri *et al*., 2007).

Evolutionary phases are:

- ***STEP 1** - 5.96 – 5.6 Ma – MSC onset and first evaporitic stage* – during the early Messinian the Mediterranean Basin underwent a progressive restriction of the deep-water circulation as evidenced by the generalized cyclical deposition of sediments of anoxic environments as sapropels (dark coloured, organic-rich shales indicating reduced oxygen conditions in the bottom waters). Data from both deep and shallow-water records suggest that salinity did not change significantly before 5.96 Ma. The hydrology and circulation pattern of the Mediterranean Basin rapidly changed at round 5.96 ± 0.02 Ma as recorded by the deposition of the first Messinian evaporites not associated with halite or massive carbonates and it is indicated in literature with the acronym PLG (*Primary Lower Gypsum*). The primary gypsum (selenite) accumulated during this stage is typical of environment with a maximum 200 m depth.

- ***STEP 2** - 5.6 – 5.55 Ma – MSC acme* – this stage is characterized by evidence for a substantial relative sea-level drop in the Mediterranean with subaerial exposure, erosion of evaporites basins, erosion for the PLG formed during the previous step, and deposition of primary evaporites (mainly halite and potash salts). The Mediterranean continental margins show the development of a high - relief erosion surface called with the acronym MES (*Messinian Erosion Surface*) with training, on the platform and slope, of the canyons by watercourses (Nile, Rhone – see Manzi *et al*., 2005) the onset of this erosion phase of the Mediterranean marginal areas is recorded in deep basin of the Apennines and Sicily by the abrupt activation of turbidite system comprising a complete suite of gravity-driven subaqueous deposits ranging from giant submarine slides, to chaotic bodies, debris flow, high to low-density turbidite flows. These deposits form a unit that has been generally overlooked in the MSC debate and/or considered a time equivalent of PLG. This unit called RLG (*Resedimented Lower Gypsum*) and consider these the best candidates for a possible equivalent of the deep Mediterranean Basin's *Lower Evaporites* unit (i.e. Lower Unit, LU). The RLG is associated with limestones (the *Calcare di base*- CdB called Calcare di base by Ogniben (1955), not present in all basins) and salt bodies (halite + K salt).

Salt unit – the salt founded exclusive within the clastic unit (carbonate and gypsum). The halite bodies show a shallowing-upward trend with cumulitic deposits at the base and very shallow-water deposits in the upper half; K and Mg salt are only found below a desiccation surface which has been recognized in the upper half of the unit (Lugli *et al.*, 1999). These characteristics of this surface suggest a very short exposure (possibly a few years) after which shallow-water halite started to be deposited again. This short temporally phases, but significant stratigraphically, is strongly linked to the combination tectonic (significant reorganization of the Eurasian plate and the African one) and climate events, in fact it is between two glaciations (TG14 and TG12), could have provoked a strong reduction in the Atlantic connections and in particular the short-lived blockage of the Mediterranean outflow thus triggering the evaporative sea-level drop of the Mediterranean Basin and halite precipitation.

- ***STEP 3*** - *5.55 – 5.33 Ma – Upper Evaporites and Lago Mare event(s)* – during this period, called *Upper Evaporites*, a generalized and rapid transition to environments characterized by periodic water salinity changes occurred throughout the Mediterranean Basin, as recorded by alternating evaporites and clastic deposits containing brackish to fresh water faunas (Orszag-Sperber, 2006). The Zanclean base marks the synchronous return at 5.33 Ma to fully marine conditions and thus the end of the MSC. A commonly observed allows subdivide the uppermost Messinian successions into two units (p-ev^1 and p-ev^2 of Roveri *et al*., 2001). The lower unit is characterized by the cyclical alternation of gypsum and shale beds and is more developed in the southern and eastern Mediterranean Sea. Gypsum facies differ from the PLG and suggest formation in very shallow waters. The Sr isotope values are lower than PLG indicating a substantial freshwater input as well as the intervening shale interval which contain rare and scattered brackish water assemblages (molluscs and ostracods, Flecker & Ellam, 2006). As for the PLG, the rhythmic alternation of gypsum and shale suggests cyclic salinity fluctuations likely driven by precession. The upper unit has an overall stronger freshwater signature, as testified by sedimentary facies (showing a generalized fluvial rejuvenation and/or change in the precipitation regime) and by fauna and flora typical brackish. This unit as a whole record the so-called Lago Mare event. Both units indicate a generalized increase of subsidence rate related to a phase of tectonic quiescence.

In the time, new models have been proposed based on the reinterpretation of some evaporitic facies both primary and re-sedimented. The model proposed by Roveri *et al.*, (2008) highlights the fact that the different evaporitic facies are distributed differently in different depozone system of Foreland basin of Maghrebian-Sicilian. The distribution lateral and vertical is so controlled of evolution morphostructural syn-sedimentary of the chain orogenic Maghrebian-Sicilian. The PLG maintain their original position stratigraphy above deposit of relatively low water and they were found only in the area of wedge top of shallow depth and in the area of the foreland ramp. At the top are cut of the MES and covered in angular unconformity of subsequent deposits Messinian or transgressive deposits of lower Pliocene. In the deepest basins of the wedge top the Lower Gypsum unit is represented by re-sedimented facies (RLG) of deep water that including turbidites, debris flow and olistoliths olistostromes. The presence of large slab of PLG embedded in a chaotic matrix formed from clay and chalk clastic suggests large mass processes for instability tectonics. The clastic deposits with deposits of halite occupy the structural depressions; they are as large lenses that pass vertically and laterally to gypsum re-sedimented. The CdB occupy the highs structural. RLG, halite and CdB make up a complex unity considered syntectonic for the rapid variations of facies and thickness. The Upper Evaporite characterized by alternating facies primary and marl occupy the deepest areas and are stratigraphically overlapping unit. They consist of RLG, halite and CdB. The stratigraphic model of the system of foreland basins of the Northern Apennines is very similar to that Sicilian Maghrebide. The PLG occupy only wedge top basins of shallow water and they are truncated to the roof from MES, on the latter in the deepest rest the RLG from this level stratigraphic on the Miocene succession is completely different from that of Sicily, in fact there aren’t other evaporites facies (halite and Upper gypsum) but only one clastic unit characterized by a complex vertical organization.

Over the years, new information has been added to Lower and Upper Gypsum, specifically, for on “ideal cycle” for the Vena del Gesso (Emilia Romagna), defined by Vai and Ricci Lucchi in 1977.

For the Primary Lower Gypsum (PLG), according to Lugli *et al.*, (2010) the facies association (Figure 1.4), which characterizes the “ideal cycle”, is a complete small scale sedimentary sub-water cycle. This is produced by the amount of increasing and decreasing of water saturation and by the sea level changes in the basin (Figure 1.5).

The cycle is divided into four phases enclosed from bottom to top by Facies F1 – bituminous shale – and facies F5 – nodular and lenticular selenite (deposits of sabka):

1. Formation of the EF3 facies (*massive and giant selenite*) at the beginning of evaporitic precipitation in low saturation conditions and in an environment relatively deep, with crystals that are always covered by frost during growth.

2. Development of conditions of higher and variable super-saturation due to continuous evaporation with crystal growth controlled by the oscillating level of frost of the pycnocline (Figure 9). These conditions favour the formation of EF4 facies (*banded selenite*).

3. The gradual rise in the level of frost with strong frost flow produces the formation of EF5 facies (*branching selenite*).

4. The inflow of undersaturated water ends abruptly the precipitation of gypsum with deposition of the EF6 facies (*limestone and dolostone*).

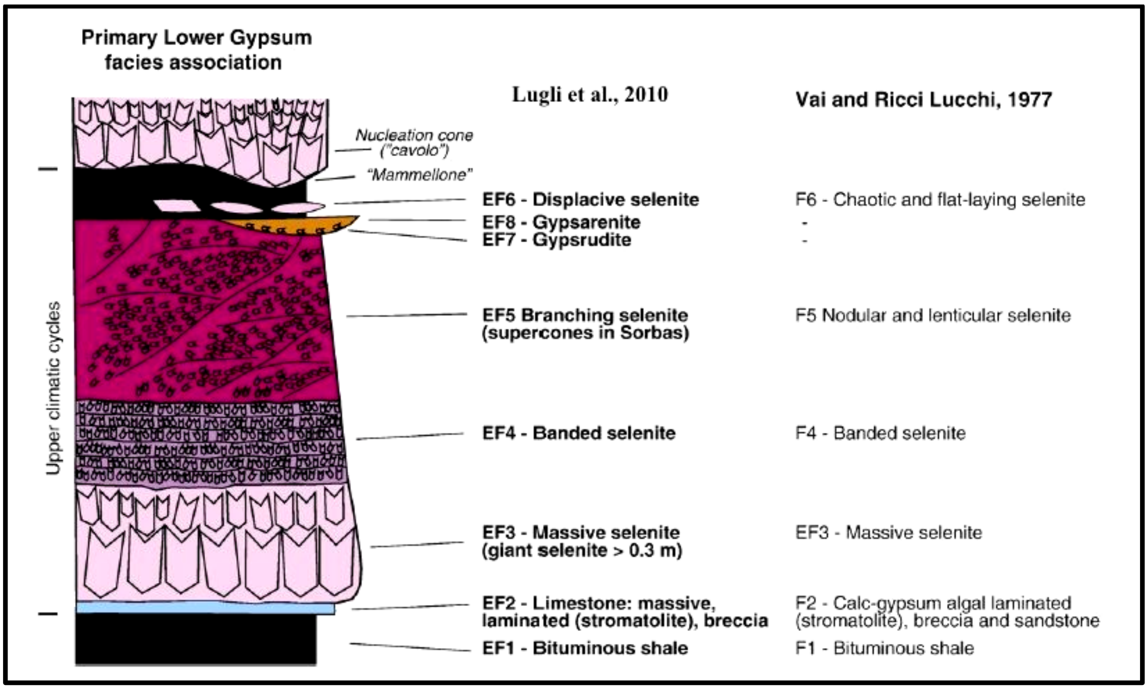

Figure 1.4. Ideal Cycle for the Vena del Gesso with the Messinian Evaporite facies (left; from Lugli *et al*., 2010) and the older classification (right; from Vai & Lucchi, 1977).

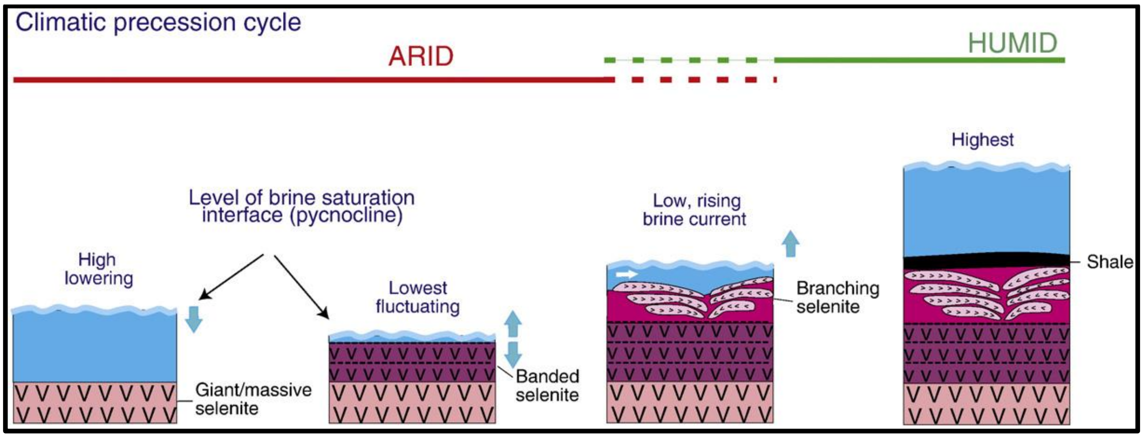

Figure 1.5. Growth stages for the different selenite types as a function of brine saturation level and precession climatic cycles. Note that branching selenite and supercones grow in the presence of currents and rising pycnocline levels (from Lugli *et al.*, 2010).

For the Primary Upper Gypsum (PUG), Manzi *et al.*, (2009) propose a new facies model and identify "Ideal Cycle" characterized by the overlapping of three associations of facies (A, B, C) (Figure 1.6). The association of facies A consists of sand bodies (UGF2) of a fluvial deltaic system advancing that resting on deposits of silty-pelitic prodelta (and UGF1 and UGF1b) with local intercalation levels of centimetre diatomic and an association typical of fauna and flora of brackish or moderately hypersaline. The association of facies B includes gypsarenite and gypsorudite (UGF3) from gravitational streams with different density followed by levels of few centimetres of laminar gypsum (UGF4), originated following the accumulation on the bottom of tiny crystals that were formed on the interface of pycnocline or at water-air interface. The association of facies C is composed by the alternating *selenite crusts* (UGF5a) and UGF4. Following decimetric intervals *of massive selenite* (UGF5b) separated by marl levels and characterized upward from an increase in size of the crystals; in the apical portion of the cycle may be present locally structures dome (UGF5c) to the top where you can spot levels of centimetre reworked gypsum selenite (UGF5d).

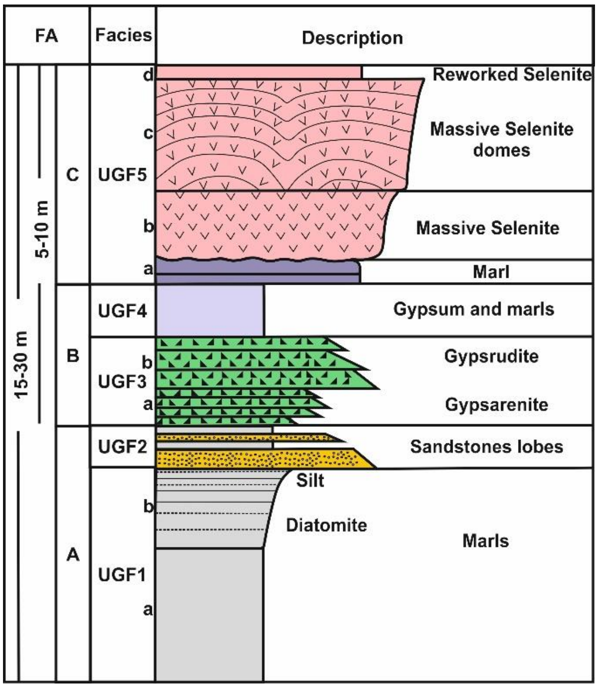

Figure 1.6. Ideal cycle of the Upper Evaporites with acronyms and their interpretation (from Manzi *et al.*, 2009).

1.3 Astrochronology for the Messinian Salinity Crisis

Progress in understanding of the Messinian Salinity Crisis has long been hampered by the absence of an accurate time frame. Magnetostratigraphic and biostratigraphic results on the pre-evaporitic marls provided the first reliable dating of the onset of evaporite deposition in the marginal basins (Gautier *et al.*, 1994; Sierro *et al.*, 1999; Krijgsman *et al.*, 1999). However, these techniques are not useful for dating intra-MSC sequences, because these successions are confined to a single (reversed) magnetic chron (C3r; Gautier *et al.*, 1994) and lack age diagnostic planktic foraminifera (CIESM, 2008). The construction of an astronomical time scale for the Messinian (Hilgen *et al.*, 1995; Krijgsman *et al.*, 1999, 2001) was a major step forward in the understanding of the depositional and paleoenvironment processes leading to the crisis and solved many of the ongoing chronological controversies. Cyclostratigraphic correlations between Messinian pre-evaporite sections are rather straightforward and were confirmed by high-resolution planktonic foraminiferal biostratigraphy (Krijgsman *et al.*, 1999). Astronomical tuning generally shows a good to excellent fit between the characteristic sedimentary cycle patterns and the astronomical target curve (Hilgen & Krijgsman, 1999; Sierro *et al.*, 2001), establishing that no sedimentary cycles are missing and that alternative correlations can be excluded. The tuning of the complete pre-evaporite Messinian resulted in an age of 7.25 Ma for the base of the Messinian and of 5.96 Ma for the onset of evaporite formation and, hence, the Messinian Salinity Crisis (Krijgsman *et al.*, 1999); these ages are now generally accepted.

The tuning of the evaporites themselves proved more problematical, however, even though these evaporites are also arranged in a cyclic way. The pre-evaporitic marl-sapropel cycles are replaced by gypsum-marl cycles of the Lower Gypsum units, indicating that the evaporite cycles are also related to precession-controlled oscillations in (circum) Mediterranean climate. The total numbers of evaporite (gypsum) cycles in the Lower Gypsum of Spain (17 cycles) and Italy (16 cycles) are in good agreement (e.g. Krijgsman *et al.*, 2001) and imply a total duration of approximately 350-370 kyr for this unit. The Upper Evaporite units and lateral equivalents of the Mediterranean latest Messinian also display a marked cyclicity, comprising in general seven to eight sedimentary cycles (Decima & Wezel, 1971; Vai & Lucchi, 1997; Fortuin & Krijgsman, 2003). The total number of sedimentary cycles agrees well with the total number of precession peaks suggesting that the Upper Evaporites were deposited in approximately 175 kyr, but slight revision of these correlations may be foreseen .Tentatively calibrating the post-evaporite cycles to the insolation curve leaves only a small “Messinian gap” (between 5.59 and 5.50 Ma) during which the desiccation of the Mediterranean, deposition of halite, and the accompanying isostatic rebound processes (tectonic tilting and erosion) must have occurred.

1.4 Messinian salt evaporite in the Calabria region

The presence of extensive Messinian evaporites (evaporitic carbonates and evaporitic salt -subdivision by Warren, 1999) in the Calabria region, have been well documented over the years (Roda, 1964; Van Dijk *et al.*, 2000; Lugli *et al.*, 2007; Barone *et al.*, 2008; Costa *et al.*, 2010; Cianflone *et al.*, 2012; Zecchin *et al.*, 2013; Guido *et al.*, 2014; Brutto *et al.*, 2016; Chiarella *et al.*, 2016; Critelli *et al.*, 2016; VIDEPI project, 2016; Costanzo *et al*. 2019). In this work, we focus on evaporitic salt (halite and selenite deposits) that are present as:

(i) burial salt domes that in some areas form small diapirs piercing late Messinian and Pliocene sediments in the Crotone Basin;

(ii) selenite deposit in the Catanzaro Trough and the Ionian Basin;

(iii) gypsurudite and gypsarenite located throughout the Calabria region.

Previous study, mainly stratigraphic and petrographic conducted on these deposits led to the following results highlighting some gaps mainly of paleo-environment nature:

1) in the Crotone Basin, Lugli *et al.*, (2007) recognised two different facies as exposed outcrops: banded and white. Through stratigraphic and petrographic observations, they have established that:

- the banded facies were completely recrystallized and deformed (no primary fluid inclusions and primary features). These facies were the result of flow, disruption and complete recrystallization of pure halite (white facies);

- the white facies can represent deposition in a saline lake which underwent stage of desiccation to form a dry salt pan;

The white facies was studied also from Speranza *et al.*, (2013), investigating the fluid inclusions trapped in the crystals to obtain temperature of homogenization (T_H= av. 21°C) and comparing them with the other Mediterranean basin.

Missing information about: (i) paleoenvironment and paleoclimatic conditions under which halite facies were formed related to the climatic oscillations (brine composition, salinity values, biological content) and (ii) chronological dating.

2) In the Catanzaro Trough, Cianflone *et al.*, (2011, 2012) recognised several primary and secondary selenite deposits as exposed outcrops (banded, massive and branching facies) or blocks (giant facies) describing them from a petrographic and stratigraphic point of view; in details, banded facies was associated to the Upper Gypsum, while massive, giant and branching was related to the Resedimented facies (dismantling product of the Lower Gypsum due to the rapid lowering of the sea level which produced an instability of the margins and their subsequent re-deposition). Costanzo *et al.*, (2019) conducted preliminary microthermometric studies.

Missing information about: paleoenvironment and paleoclimatic conditions under which selenite facies were formed related to the climatic oscillations (brine composition and temperature, salinity values, biological content) and (ii) isotopic dating to confirm the origin of the facies (Lower or Upper Gypsum).

3) In the Ionian Basin, the Benestare area is reported by ISPRA geological map of Bovalino as a quarry made up selenite member, olistostrome and limestone (Calcare di Base).

Missing information about: (i) selenite member and (ii) chronological dating.

In light of these previously study, our aim is to be able to answer the following questions:

(i) What are the processes that formed different halite and selenite facies?

(ii) Are these deposits recrystallized or show still primary features? What is their deformation degree?

(iii) In what conditions of salinity and temperature they formed?

(iv) Can their deposition be associated with climatic variations?

(v) Can they be dated?

(vi) Can depositional models be created?

1.5 Geological setting of the Calabrian Basins investigated

1.5.1 The Crotone Basin (CB)

The Crotone Basin is located in the Ionian side of the Calabrian Arc and is generally interpreted as a forearc basin positioned on the internal part of the Calabrian accretionary wedge (Bonardi *et al.*, 2001; Zecchin *et al.*, 2004). The basin is laterally bounded by two NW-trending sinistral shear zones (Rossano-San Nicola in the north and Petilia-Sosti in the south), and its opening started between the Serravallian and the Tortonian (13.80 - 7.12 Ma) (Van Dijk, 1991).

The depositional history of the Crotone Basin was characterized by a dominant extensional tectonic regime that was periodically interrupted by short compressional or transpressional phases in mid-Messinian, earliest mid-Pliocene and mid-Pleistocene time (Zecchin *et al.*, 2006). They reflect a composite tectonic event comprising an uplift/regression pulse, followed by a rapid subsidence\onlap (Van Dijk, 1991).

Three main tectono-sedimentary cycles (upper Serravallian lower Messinian, upper Messinian- Zanclean, and Piacenzian-Pleistocene) form the basin fill. The stratigraphic sequence consists mainly of clay and marl deposited in different contexts (from platform to lagoons) and sands of delta and conglomerates (submerged beach).

Along the western edge of the Crotone Basin the following units can be identified from the bottom to the top (Roda, 1964; Barone *et al*., 2008):

1. Paleozoic crystalline acid rocks, mainly granites;

2. continental deposits, mostly conglomerates and sandstones of Miocene age (*San Nicola Formation*);

3. sequence of transgressive Middle Miocene, comprising polygenic conglomerates, sandstones in the centre part and clays saliferous then to the roof (*Ponda Clay*); these contain bituminous shale (*Tripoli Formation*);

4. The evaporitic complex Miocene - Pliocene consists of clays saliferous and gessifere, gypsum and lenses of halite (*Evaporite Formation*); During the Miocene, the basin was situated on a normal growing accretionary wedge. The development of depositional sequences was controlled by the local tectonic activity of the accretionary wedge system.

5. clays and sandstones depositional environment of marine and continental of ages ranging from Middle Pliocene to the Holocene (*Petilia Policastro Formation, Carvane Group and Cavalieri Mari*), (Figure 1.7).

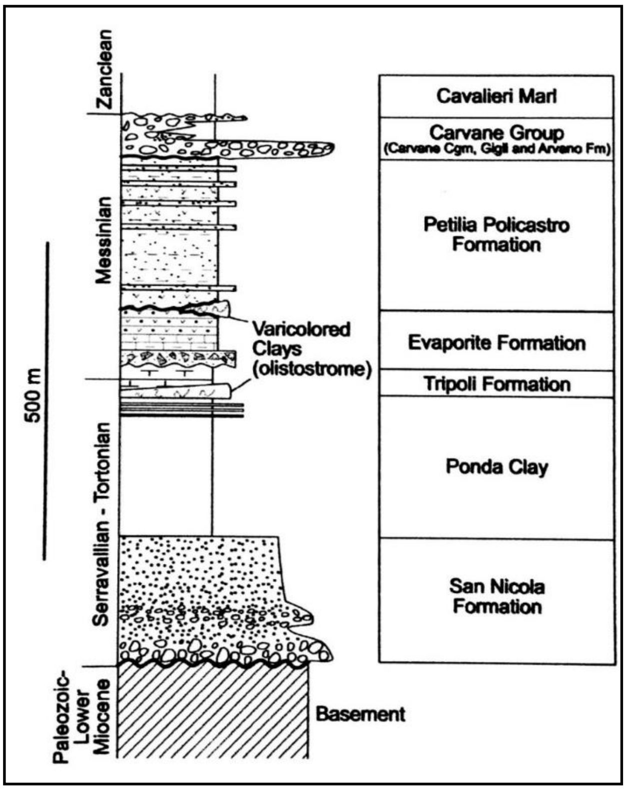

Figure 1.7. Succession of the Crotone Basin from the Palaeozoic to lower Zanclean and the formation names (modified after Barone *et al.*, 2008). Not in scale.

1.5.2 The Catanzaro Trough (CT)

The Catanzaro basin is a graben (called “*graben*” by Iovine & Tansi, 1998 and “*Catanzaro Trough*” by Gullà *et al*., 2005) and is a Neogene-Quaternary basin developed in the central Calabrian Arc, between the Serre and the Sila Massifs, and filled by up to 2000 m of continental to marine deposits. It extends from the Sant’Eufemia Basin (SE Tyrrhenian Sea), offshore, to the Catanzaro Basin (Brutto *et al*., 2016). The data show a complex tectonostratigraphic architecture of the basin, which is mainly controlled by the activity of NW–SE and NE–SW trending fault systems. The graben is surrounded by two horsts composed by Paleozoic crystalline-metamorphic Units belonging to Calabro Peloritano Arc (ACP) represented, respectively, by the Coastal Chain - Sila Plateau systems to the north and by the Serre Massif to the south (Amodio-Morelli *et al.,* 1976).

Along the northern edge of the "Catanzaro graben", the fault "Gizzeria-Nicastro-Pianopoli Marcellinara” is the most important tectonic element of regional scale as it juxtaposes the Paleozoic crystalline-metamorphic rocks of the Coastal Chain - Sila Plateau to Plio-Quaternary deposits (Gullà *et al*., 2005).

The metamorphic units are covered by a Miocene-Pliocene terrigenous sequences linked to two different sedimentary cycles: the Tortoniano-Messinian cycle made up conglomerate and bioclastic limestones and a Messinian-Pliocene cycle made up conglomerate (Riato conglomerate) with clasts of limestone, selenite blocks, resedimented evaporites (gypsrudites and gypsarenites) and sands (chaotic arrangement). (Di Nocera *et al*., 1974; Cianflone & Dominici, 2011). Evaporite rocks formed during the Messinian salinity event, but in contrast to other evaporitic basins of the Mediterranean, in the Catanzaro Trough, the first cycle evaporites (Lower Gypsum) are not recorded, instead the resedimented facies and the facies belonging to the second-cycle evaporites (Upper Gypsum) are found (Cianflone & Dominici, 2011).

The Catanzaro sedimentary infill (Figure 1.8) unconformably overlies Messinian evaporites and conglomerates and older metamorphic units over a combined erosional/transgressive surface of regional extent (Longhitano *et al.,* 2014).

The lowermost deposits of the Catanzaro Trough are represented by mudstones and marls, considered time correlative with the Zanclean Trubi Formation which is extensively exposed in many areas of southern Italy (Zecchin et al., 2013). The Trubi Formation is paraconformably overlain by succession composed of weakly cemented sandstones and mudstones deposited in a marine shelf environment; the age of this unit is upper Pliocene–Pleistocene. This sequence is bounded at the top by a widespread tectonically generated erosional surface.

The Lower Pleistocene consists of succession dominantly consisting of mixed siliciclastic/bioclastic sands and sandstones (Basile Unit) and subordinately of mudstones. The Middle-Upper Pleistocene stratigraphic interval consists of two laterally stacked and vertically stacked stratal units: the Vena di Maida (conglomerate and sandstone) and the Pianopoli (sandstone) units. The topmost boundary of the Basile Unit is a surface of subaerial exposure and incision (up to 4 m), which is overlain by coarse-grained fluvial and shallow-marine sediments (Longhitano *et al*., 2014).

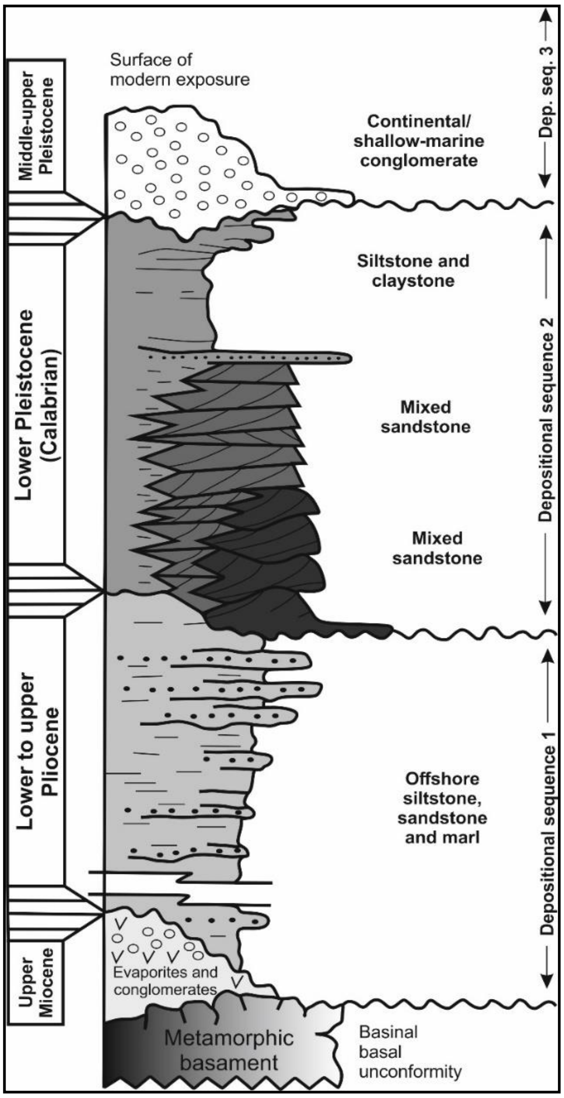

Figure 1.8. Succession of the Catanzaro Trough from the Upper Miocene to the Middle-upper Pleistocene and the deposits name (modified after Longhitano *et al.*, 2014). Not in scale.

1.5.3 The Ionian Basin (IB)

The area between the Aspromonte and Serre Massifs is made up of different crystalline and metamorphic tectonic units with relative Mesozoic sedimentary covers, and the onshore Ionian and Tyrrhenian basins. These basins are characterized by sedimentary successions, including from Cretaceous to Lower Miocene allochthonous terranes, covered by Oligocene to Quaternary deposits.

The basement is the result of the stacking of three tectonostratigraphic units involving Palaeozoic crustal rocks: The Africo-Madonna di Polsi Unit (phyllites, marbles, schists), Aspromonte Unit (gneiss, granitoids) and Stilo Unit (phyllites, marbles, schists, granitoids), (Cirrincione *et al.*, 2008; Pezzino *et al.*, 2008, Critelli *et al.*, 2016).

On top lies the (Amodio Morelli *et al.*, 1976; Colonna *et al.*, 1973) mostly constituted by a Palaeozoic metasedimentary section of Cambrian-to-Carboniferous phyllites, metarenites, metalimestones and metasiliceous rocks intruded by a late Variscan large plutonic body (Angì *et al.*, 2010; Bonardi *et al.*, 1984; Graessner & Schenk, 1999). This Unit is largely covered by Late Triassic-earliest Jurassic continental to marine deposits (Roda, 1965).

The Oligocene to Middle Miocene succession is represented by the Stilo-Capo d’Orlando Formation (Bonardi *et al.*, 1980; Bouillin *et al.*, 1985; Weltje, 1988, 1992; Dominici & Sonnino, 1999; Cavazza & DeCelles, 1993; Caruso *et al.*, 2013). This Formation has been interpreted as continental deposit passing to shelf and slope deposits by (Weltje, 1988, Boullin *et al.* 1985; Dominici & Sonnino, 1999; Caruso *et al.*, 2013) and as submarine-canyon deposits passing upward and laterally to overbank and slope deposits (Bonardi *et al.*, 1980; Cavazza & DeCelles, 1993).

The Variegated Clays rest on the Stilo-Capo d’Orlando Formation and are characterized by a predominant mélange type internal structure (Cavazza & Ingersoll, 2005; Cavazza & Barone, 2010; Critelli *et al.*, 2016).

The Serravallian to Messinian sequences rest unconformably on the oldest units and start with Serravallian-to-Tortonian marine strata (conglomerates, sandstones and pelites) and continue with the Messinian Gessoso-Solfifera Group (MGSG) of Cattolica Formation. Critielli *et al.* (2016) and Tripodi *et al.* (2013, 2018) describe the MGSG in the Benestare area made up of limestone (Calcare di Base Formation – GTL_1), massive or laminated, vacuolar, brecciated, microcrystalline limestone passing upward to selenite crystals (GTL$_2$) and gypsarenite and interbedded olistoliths of Variegated Clays (ob).

The Pliocene (Zanclean to Piacenzian) Trubi Formation (marls and marly-limestones), unconformably overlying Messinian deposits and older sedimentary units (Cita, 2001; Zecchin *et al*., 2012a,b, 2015; Critelli *et al*., 2016). To Piacenzian-Calabrian sandstone strata (the Monte Narbone Formation), which abruptly interrupted the typical pelagic sedimentation (Longhitano *et al*., 2012; Rossi *et al*., 2017). Pleistocene from continental to marine deposits is located on top of the stratigraphic succession (Miyauchi *et al.*, 1994; Catalano *et al*., 2008; Ferranti *et al*., 2008; Tripodi *et al*., 2018).

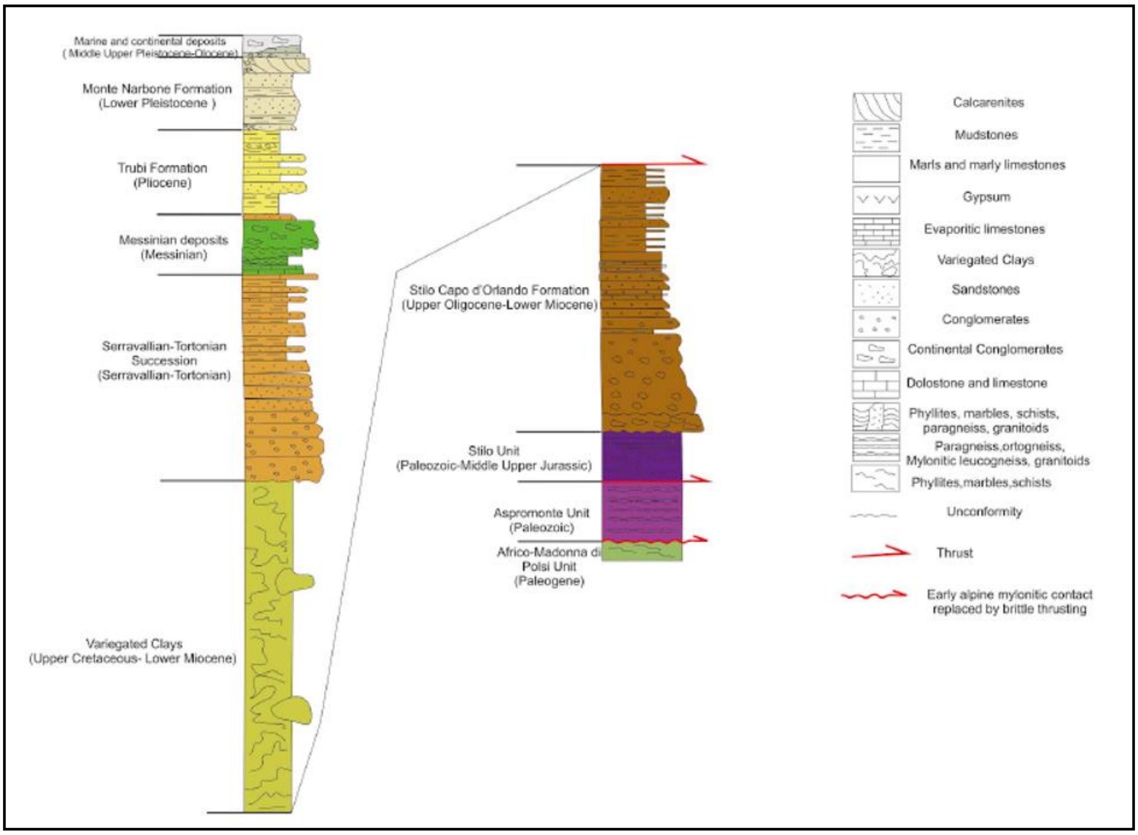

Figure 1.9. General column of the southern Calabria (modified after Tripodi *et al*., 2018). Not in scale.

CHAPTER 2. Sampling, rock petrography and organic matters investigation

2.1 Introduction

The evaporite samples investigated consist of halite (NaCl) and gypsum ($CaSO_4 * 2H_2O$). Halite (isotropic mineral) shows predominantly cubic habit (cubic crystal system). It is colourless or white (sometimes also blue, purple, red, pink, yellow, orange or grey due to impurities). The halite crystals can grow and float via solar concentration at the air-brine interface - called “raft” - when surface water salinities are suitable (Warren, 1999). On the surface, the crystals may take the form of pyramidal hopper (Figure 2.1a) and/or halite hopper (Figure 2.1b). When the crystals mass becomes heavy so much to exceed the holding ability of the forces of surface tension, they sink to the bottom, and continue to grow competitively as cumulate/massive crystals. If the rate growth along the corners is discontinuous, the crystals prefer the chevron fabric (Rouchy *et al.*, 1994). The chevron fabric indicates crystal growth pulses. Each pulse is characterised either by thin layers of less saline salts or by inclusions of brine that were poikilitically enclosed during crystal precipitation. These pulses reflect changes in crystal precipitation rate induced by short-term changes in salinity (daily to seasonal) on the subaqueous floor of the brine pan (Warren, 1982; Handford, 1991).

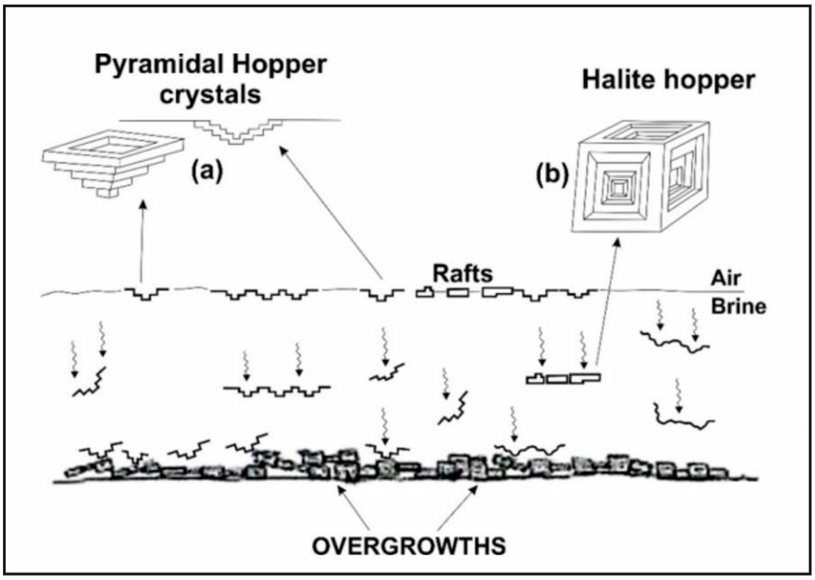

Figure 2.1. Main structure of halite and place of formation. a) Pyramidal hopper crystal and rafts (air-brine interface); b) halite hopper; (modified after Rouchy *et al.*, 1994).

Gypsum (anisotropic mineral) shows predominately massive habit (monoclinic crystal system). It is colourless to white (it can be yellow, tan, blue, pink, brown, reddish brown or grey due to impurities). In nature, three main gypsum varieties exist: fibrous or pinacoid (satin spar - Figure 2.2a), crystalline selenite (Figure 2.2b), and fine-grained (alabastrite). These varieties include several morphological and genetic types. In this study, we focus main on the crystalline selenite. Selenite crystals – swallowtail twinned gypsum – grow at the bottom of the basin where they weld together and form “twins” along (001) plane, in fact, the twin plane indicates the crystal growth direction. These crystals are characterized by: (1) competitive growth; (2) arrangement in beds with variable thicknesses and fabrics; (3) development of twins or intergrowths, which can be distinctive for each evaporite formation; and (4) zonation due to the presence of matrix inclusions (Ortì, 2011). Zonation is made up of thick turbid/cloudy intervals (enriched in organic and inorganic materials) and limpid/clear intervals (depleted in organic and inorganic materials) in the re-entrant angle of the twinned crystal.

Previous studies (*e.g.* Lugli *et al.* 2010; Ortì, 2011) highlighted the presence of different selenite layers with variable thicknesses, from a few centimetres to several metres, up to some tens of metres (giant facies). The most common stratiform facies are: bedded or banded selenite (beds between a few cm and 0.5m thick) and massive selenite (beds >0.5m thick), (Ortì, 2011). The difference between massive and banded facies changes according to the evaporite formations (Lo Cicero & Catalano, 1976; Vai & Ricci Lucchi, 1976, 1977; Lugli *et al*., 2010).

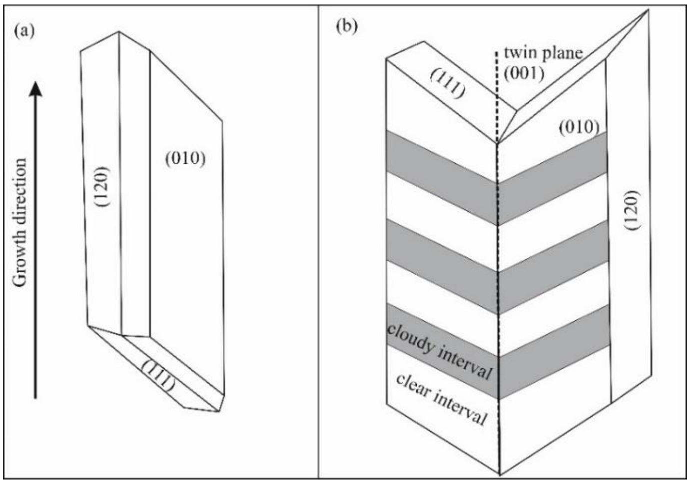

Figure 2.2. Schematic representation of (a) pinacoid gypsum and (b) selenite twinned crystal with main crystallographic directions. Selenite crystal shows the different intervals – cloudy and clear - and the twin plane on (001). (Modified after Rouchy *et al.*, 1994).

2.2 Crystals growth rate

Schreiber & Hsü (1980) estimated that in modern shallow water depositional rates were up to 10 m per 1000 years for halite and 1–2 m per 1000 years for $CaSO_4$. Recently, Komarov *et al*. (2000) studied the gypsum growth into a thermostated at 18°C and 30°C, estimating a growth rate respectively of~51 cm/y or~154 cm/y. For ancient, major deep-basin evaporites, can be only estimate their somewhat slower accumulation rates from biostratigraphic estimates because there is no modern working analogue to be taken as a model. (Schreiber *et al.*, 2007).

This chapter presents the results of the macroscopic and microscopic investigations on halite, selenite and gypsum rocks which are the fundamental steps for understanding the Messinian deposition events that have been recorded in the Calabria region.

2.3 Study areas and sampling

Research on the distribution of Messinian evaporitic deposits in the Calabria have been conducted using literature data, by consultation of geological maps and map's creation (using QGis software, Figure 2.3). This has revealed the presence of buried and exposed evaporites distributed throughout the Calabria region.

We focus on primary exposed deposits to investigate the deformation degree and to understand the origin of different facies. Deposits are located (Figure 2.3) in:

- the Crotone Basin (CB) with halite salt domes (Zecchin *et al.*, 2013; Lugli *et al.*, 2007; Costa *et al.*, 2010; Barone *et al.*, 2008; Roda 1964, CARTA ISPRA San Giovanni in fiore) and clastic deposits (Ferrini & Pasqua 1997). Deposits outcrop in the Coste del Sale, Zinga and Verzino areas;

- the Catanzaro Trough (CT) with a selenite and gypsum deposits (Costanzo *et al.*, 2019, Brutto *et al.*, 2016; Cianflone *et al.*, 2011, 2012), visible in and around the Marcellinara quarry;

- the Ionian Basin (IB) with selenite deposit (CARTA INSPRA, IB), observed in the Benestare quarry.

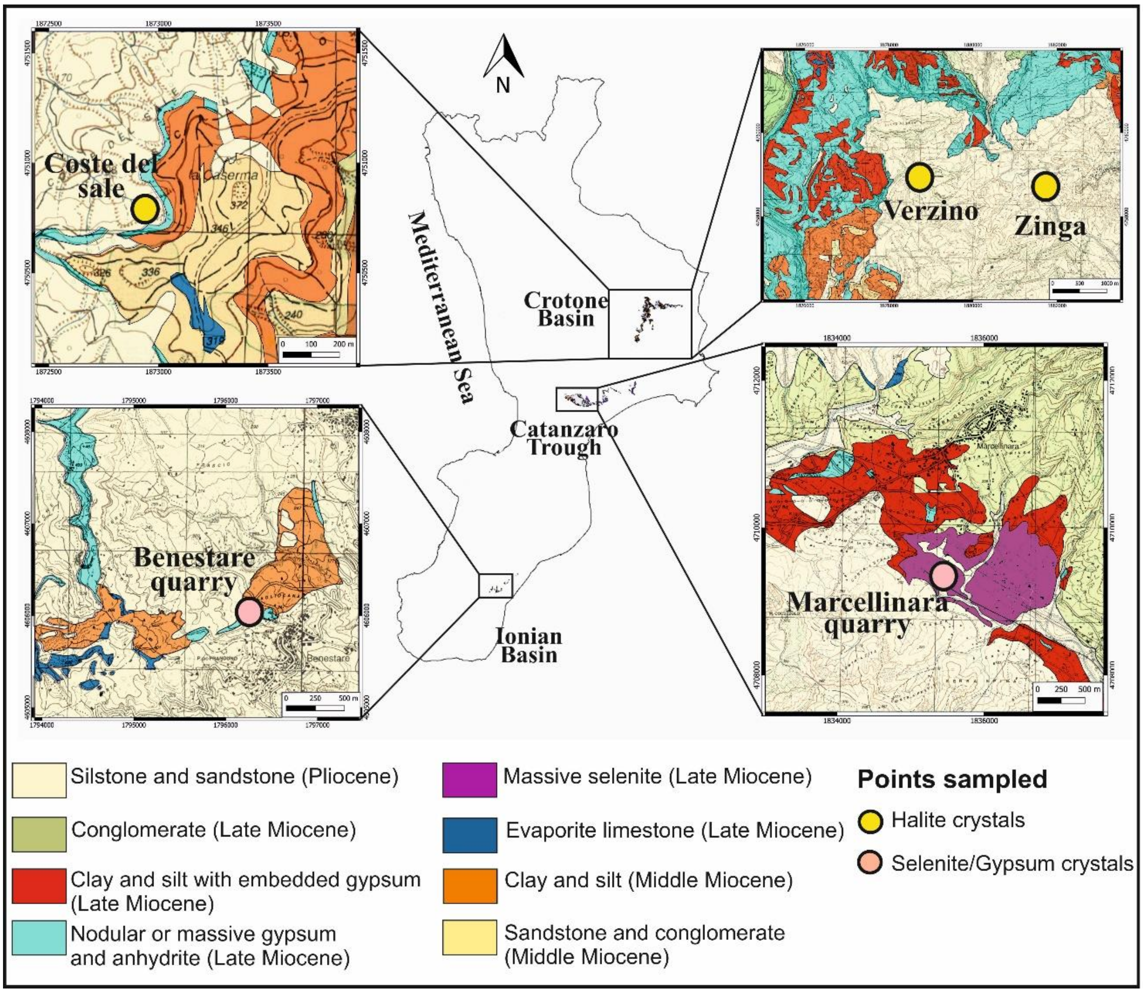

Figure 2.3. Lithological maps of miocenic and pliocenic sediments and points sampled in the Calabria region. Halite crystals sampled from salt domes located in the Coste del sale, Zinga and Verzino (Crotone Basin), selenite/gypsum crystals from the Marcellinara quarry (Catanzaro Trough) and selenite crystals from the Benestare quarry (Ionian Basin).

Twenty halite samples from exposed outcrops located in the Coste del Sale, Verzino and Zinga were taken; twenty-five selenite samples/gypsum were taken from the Marcellinara quarry; sixteen selenite samples were taken from the Benestare quarry.

The best samples were sent to the laboratory ALS Petrophysics (Normandy), to obtain halite wafer (~500 μm in thickness) and selenite/gypsum wafer (~200 μm in thickness) for a total of 22 wafers (see *Appendix A_1* for sampling procedure and wafer preparation). Subsequently, the samples were studied in the Geofluids Research Laboratory at NUI Galway, to investigate:

- habit and shape;

- colour;
- fractures;
- presence of microstructures in the crystals;
- presence of fluid inclusions;
- presence of inorganic and organic matters trapped fluid inclusions (inside and outside).

Organic matters dispersed throughout the crystals have been observed using *Ultra Violet microspectroscopy* (see *Appendix A_2* for organic matters investigation).

Further analyses on crystals and organic matters was carried out through *Laser Raman Spectroscopy* (LRS) and *Scanning Electron Microscope* (SEM), (see *Appendix A_3* and *A_4* for instruments description).

2.4 The halite samples from the Crotone Basin

In the Crotone Basin the sampling sites are located in areas of active tectonic deformation. Nowadays, three sites show exposed salt domes:

1) Coste del sale (39.20379° N, 16.82514° E) is located in the Caccuri village (geological map of Calabria, Caccuri, sheet 237 I, S.O, scale 1:25.000) This is the only area in the Crotone Basin where is possible to see the Ponda Clay Formation below the deposit.

2) Zinga (39.26134° N, 16.90229° E) is located in the Casabona village, (topographic map of Calabria, sheet 237 I, sector N-E, sector B, scale 1:10000);

3) Verzino village (39.25909° N, 16.87471° E, geological map of Calabria, sheet 237 I, N-E, sector D, scale 1:25000).

In these areas, three halite facies have been recognised:

- <u>Banded facies</u> (microcrystalline halite) consists in repetition of centimeter to decimeter thick dark and white layers made of halite with two different colours: white and grey. Both crystals show elongate and rounded halite up to 5 mm in length and competitive growth that determines mosaic texture. Clay minerals and halite cement are dispersed throughout the samples. Fluid inclusions are not visible to the naked eye. This facies in the Coste del Sale, Zinga and Verzino areas has been observed (Table 1).

-White facies (macrocrystalline halite) is made of massive clear halite crystals (>5 cm in size). Crystals show chevron habit with parallel grey bands rich in fluid inclusions (visible to the naked eye). This facies in the Zinga area has been recognised.

-Transparent facies (macrocrystalline halite), so called for its aspect, is made of massive and transparent halite, crystals (>5 cm in size). No preferential habits have been observed. Fluid inclusions throughout the sample are visible to the naked eye. This facies had never been observed.

The white and transparent facies have been identified in the same deposit (in continuity of deposition).

Locations name	**Samples name**	**Crystal types**	**Facies**
Coste del sale (Cs)	Cs 04-17	Microcrystalline	Banded
Zinga (Zi)	Zi-07	Microcrystalline	Banded
	Zi 11-17	Macrocrystalline	White
	Zi 12-17	Macrocrystalline	Transparent
Verzino (Ru)	Ru 17-17	Microcrystalline	Banded
	Ru 19-17	Microcrystalline	Banded

Table 1. Summary table and brief description of crystals observed.

2.4.1 Macroscopic and Microscopic Petrography

1) Coste del Sale shows an outcrop (~ 1.20 m in size) made of microcrystalline halite crystals belong to the banded facies (Figure 2.4a). Sample taken (called *Cs 04-17*) (Figure 2.4b) shows mosaic texture, white and grey halite crystals (Figure 2.4c) and chaotical arrangement. Crystals are approximately one millimetre in size. Clay matters dispersed throughout the sample have been observed.

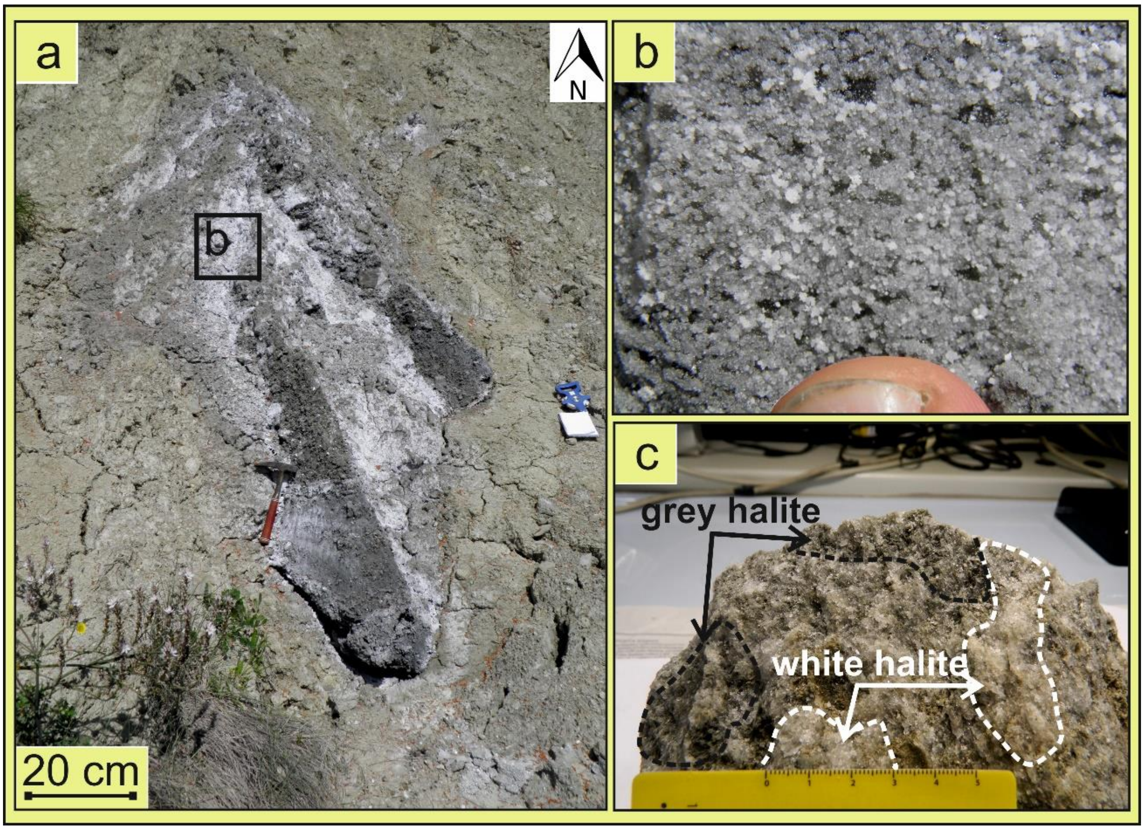

Figure 2.4. (a) Halite outcrop in the Coste del Sale; b) detail of microcrystalline halite; (c) sample *Cs 04-15* showing grey and white halite crystals.

Microscopically, the sample *Cs 04-17* is made of flattened elongated or rounded grey and white microcrystalline halite crystals (size from 2 to 5 mm) that show competitive crystal growth (syntaxial overgrowth). Crystals are oriented in the y axis direction (010). Thin brown film of clay matters separate and/or cover the crystals, conferring a darker appearance (cloudy halite), (Figure 2.5a). The main features observed are: **(i)** primary and secondary fluid inclusions (see chapter 3), **(ii)** corners crystals, **(iii)** dissolution following a pre-existing halite fabric along crystal rims (Figure 2.5b), **(iv)** diagenetic halite cement that growth in the empty space created of the dissolution; **(v)** Transparent and red matters throughout the sample**, (vi)** and pseudo-secondary or secondary fractures filling with clay matters, gypsum crystals or secondary fluid inclusions.

XPL observation and Raman spectroscopy analysis showed gypsum and anhydrite crystals (arrangement in cluster) dispersed around or inside the clay matters. have been observed.

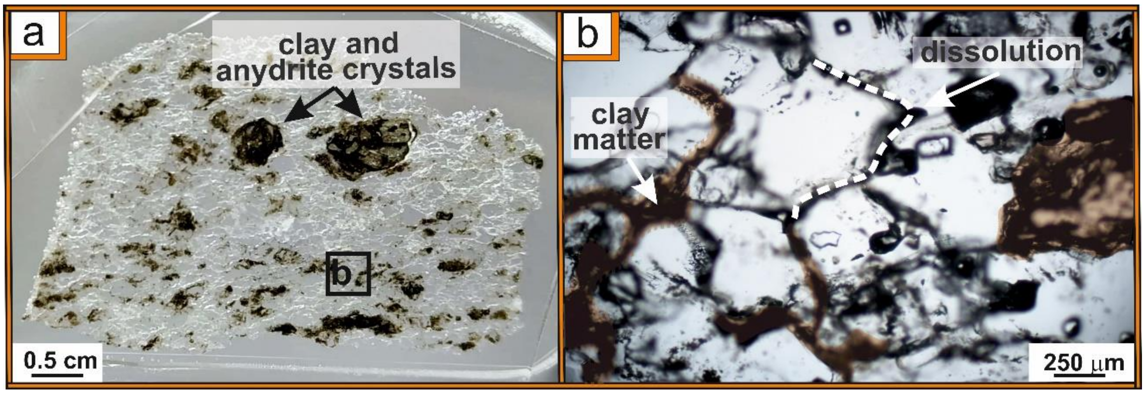

Figure 2.5. a) *Cs 04-17* showing rounded halite and anhydrite crystals immersed in clay matters; b) detail of the white halite crystals with dissolution phenomena on the rim (white dotted line) and thin films of clay matters (in brown colour).

2) In the Zinga area there are two outcrops made up of microcrystalline (first outcrop) and macrocrystalline (second outcrop) halite crystals.

The first outcrop (Figure 2.6a) shows repetition of white and grey layers of microcrystalline halite belong to banded facies (Figure 2.6b). White layers are less altered than grey. Sample *Zi 07-17* taken from the white layer,

shows mosaic texture and grey and white microcrystalline (millimetric in size) halite crystals (Figure 2.6c).

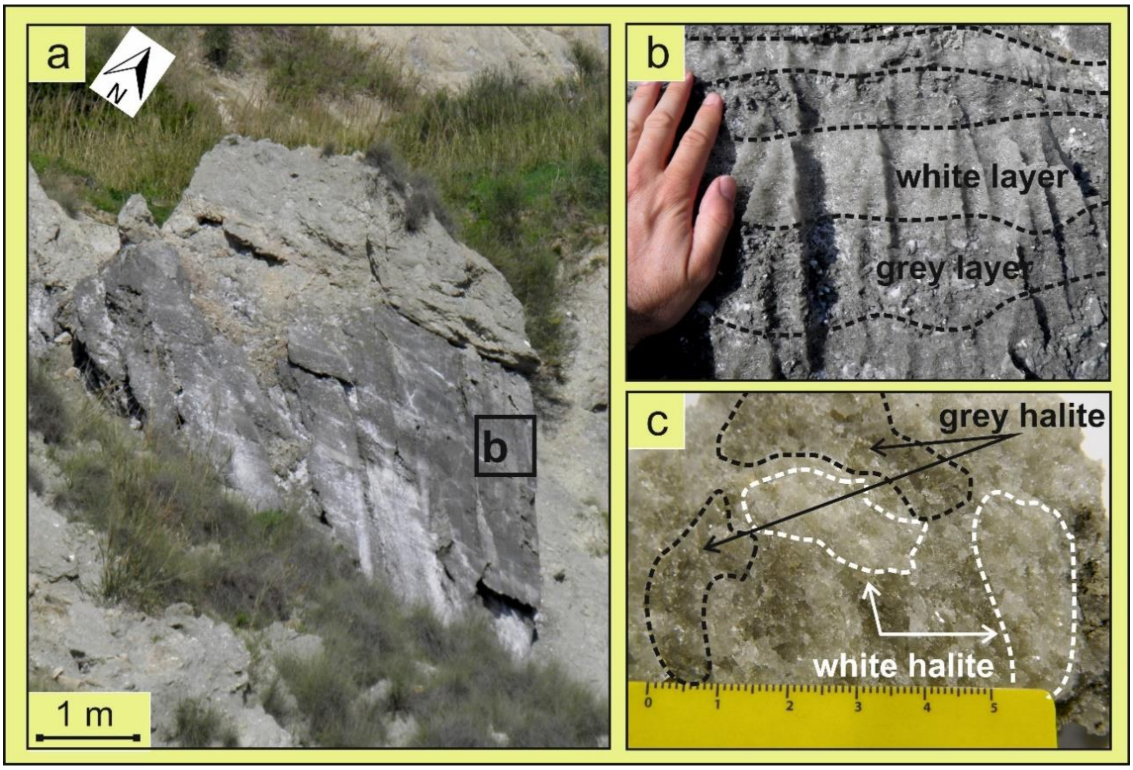

Figure 2.6. (a) Halite outcrop in Zinga; b) detail of outcrop: black dotted lines separate grey layers from white; (c) sample *Zi 07-17* (banded facies) shows microcrystalline grey and white halite crystal.

Microscopically, the sample *Zi 07-17* is made of elongated and flattened microcrystalline crystals (ranging in size from 2 to 7 mm), grey and white in colour (Figure 2.7a). The main characteristic recognised are: **(i)** competitive growth, **(ii)** faces oriented in (010) direction, **(iii)** corner crystals **(iv)** primary and secondary fluid inclusions (see chapter 3), **(v)** dissolution phenomena along the pre-existing halite fabric (Figure 2.7b), **(vi)** pseudo-secondary or secondary fractures filling by secondary fluid inclusions, **(vii)** thin films of clay matter separate crystals, fill the empty space created by dissolutions and sometimes cover the crystals (cloudy halite), **(viii)** clay matter is often associated with little and rounded birefringent crystals (unidentified), and **(ix)** isolated transparent and red matters throughout the sample.

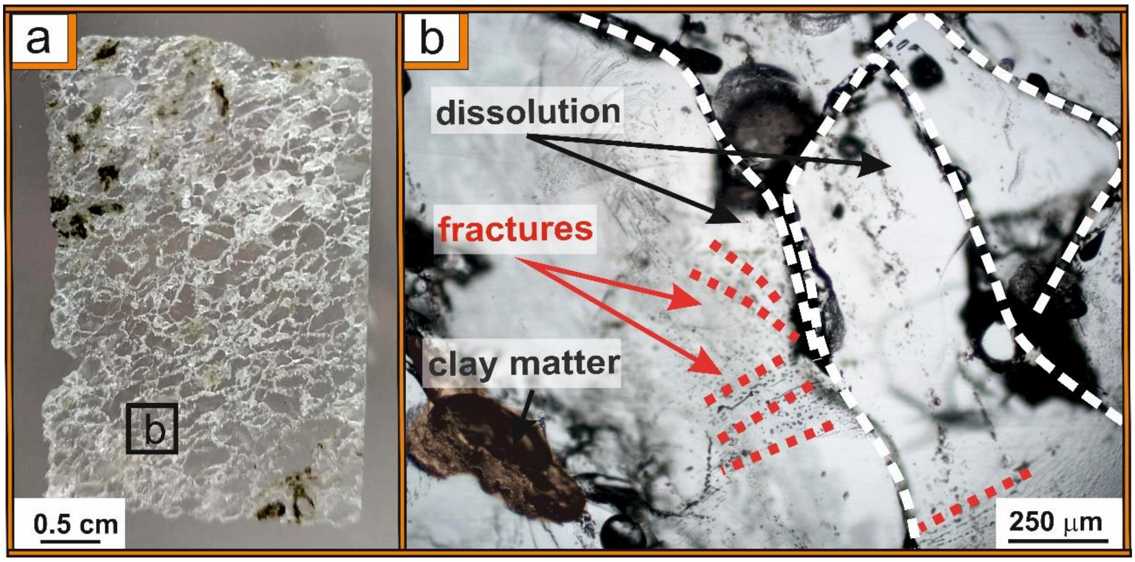

Figure 2.7. a) *Zi 07-17* showing elongated halite crystals; b) detail of halite crystals showing clay matter (in brown colour), fractures filled by secondary fluid inclusions (red dotted lines) and dissolution surface along the crystal's rim (white dotted line).

The *second outcrop* (Figure 2.8a) shows two different macrocrystalline halite facies in deposition continuity: white (at the bottom) and transparent (at the top).

The white facies shows massive crystals (>1 cm in size) made up of grey and white bands. Grey bands are rich in fluid inclusions (FIs – see chapter 3) visible to the naked eye (Figure 2.8b), in contrast white band are devoid of FIs. Thin films of clay matters are associated with little and rounded birefringent crystals (unidentified).

Transparent facies shows massive halite crystals (>1 cm in size) (Figure 2.8c), local clay matter and fluid inclusions visible to the naked eye.

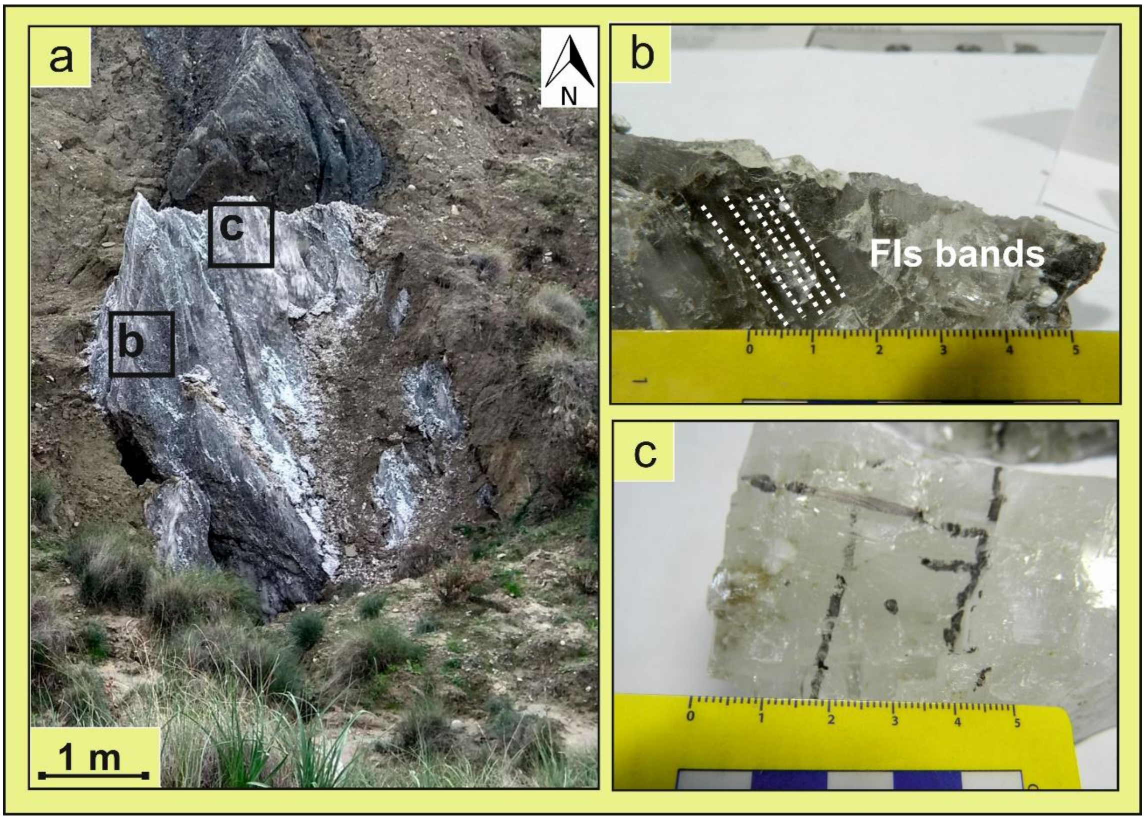

Figure 2.8. (a) Halite deposit in the Zinga area showing two macrocrystalline halite facies: white (b) and transparent (c); b) detail of massive halite crystal belong to the white facies (*Zi 11-17* sample) with FIs bands (white dotted lines) visible to the naked eye; (c) detail of massive transparent halite crystal (*Zi 12-17* sample) where the black lines indicate the direction to follow for subsequent cutting.

Microscopically, sample *Zi 11-17* is made up massive halite showing euhedral habit and rectangular shape. Two bands called milky and clear are visible to the naked eye (Figure 2.9a). The milky bands are made up fluid inclusion trails, in contrast, the clear are impoverished in fluid inclusions. In the milky zones, the alternation of fluid inclusions bands defines chevron shapes which are often interrupted by sharp and curved dissolution surfaces. (Figure 2.9b). 56 fluid inclusions trails in 2.5 cm of sample have been recognised. Rare fractures filled by secondary fluid inclusions and partial dissolution along the edges (Figure 2.9b) and transparent matters throughout the samples have been observed.

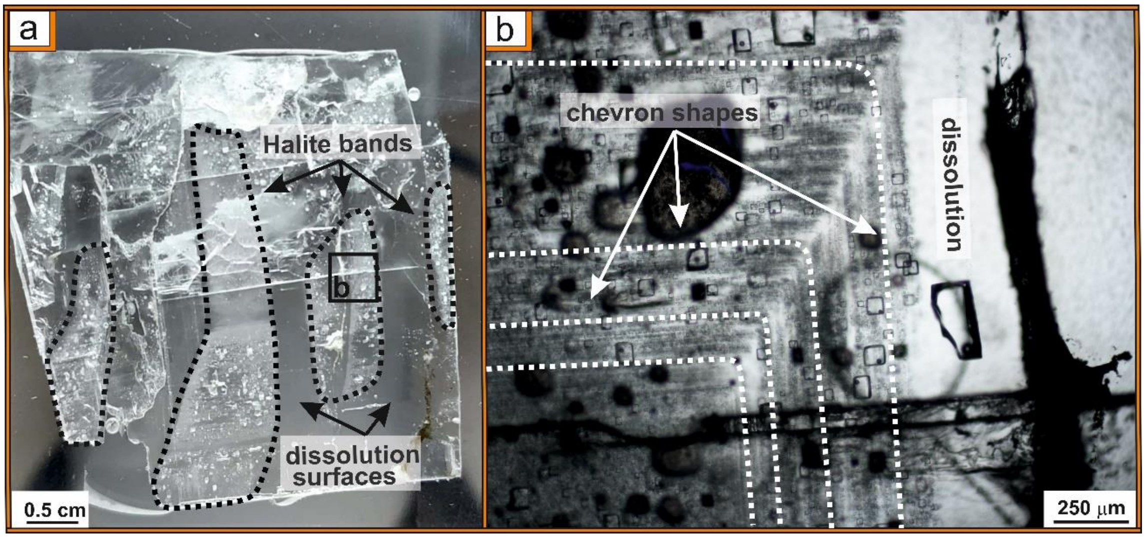

Figure 2.9. a) *Zi 11-17* showing milky bands (black dotted lines) interrupted by dissolution surfaces; b) detail of the clear and milky bands that define chevrons shape (white dotted lines) with local dissolution phenomena.

Sample *Zi 12-17* (Figure 2.10a) is made up transparent and opaque massive halite. In the transparent halite have been observed: **(i)** fluid inclusions, **(ii)** partial dissolution along the edges, **(iii)** pseudo-secondary or secondary fractures filled with secondary fluid inclusions or clay matters (Figure 2.10b), **(iv)** thin films of clay matter that cover the crystals (Figure 2.10c) associated with rounded birefringent crystals (unidentified) and, **(v)** isolated transparent matters.

Unlike, opaque halite (probably due to alteration/dissolution of the original halite) doesn’t show any structure neither primary nor secondary.

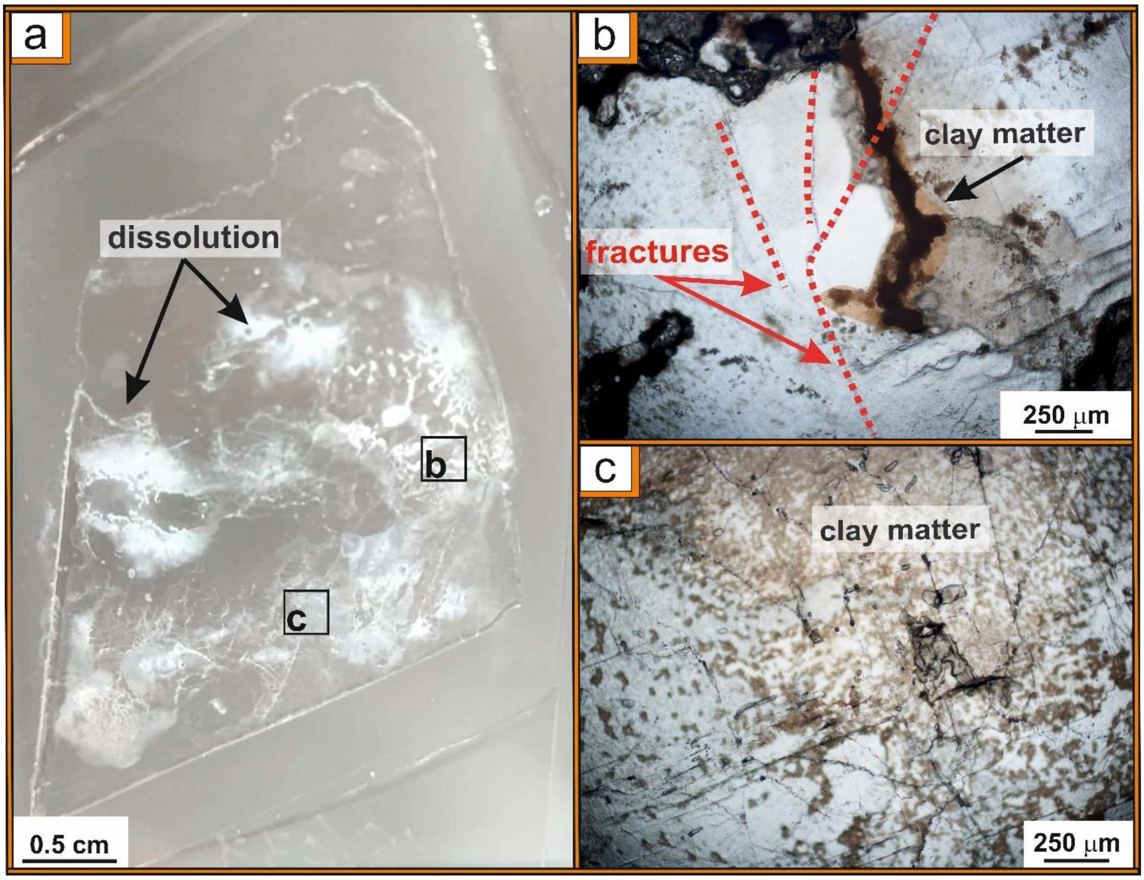

Figure 2.10. a) *Zi 12-17* showing transparent and opaque halite (dissolution); b) and c) detail of sample; b) the halite crystal with clay matter and fractures (red dotted lines) filled by secondary fluid inclusions; c) halite crystal covered by clay matters.

3) In the Verzino area five outcrops made of microcrystalline halite crystals belonging to the banded facies are identified. Two samples (*Ru 17-17* and *Ru 19-17)* from the main salt domes called "La Gola" and "La Gola Nord" (Figure 2.11a-c) were sampled.

Macroscopically, these deposits show repetition of white and grey layers composed of microcrystalline halite crystals. Crystals ranging in size from sub-millimetre to millimetre, seem squashed by deformation (Figure 2.11b-d). Samples *Ru 17-17* and *Ru 19-17* show mosaic texture and crystals stretch up to ~1-2 mm in length and up to ~0.5 mm in thickness. Clay have is dispersed throughout the samples.

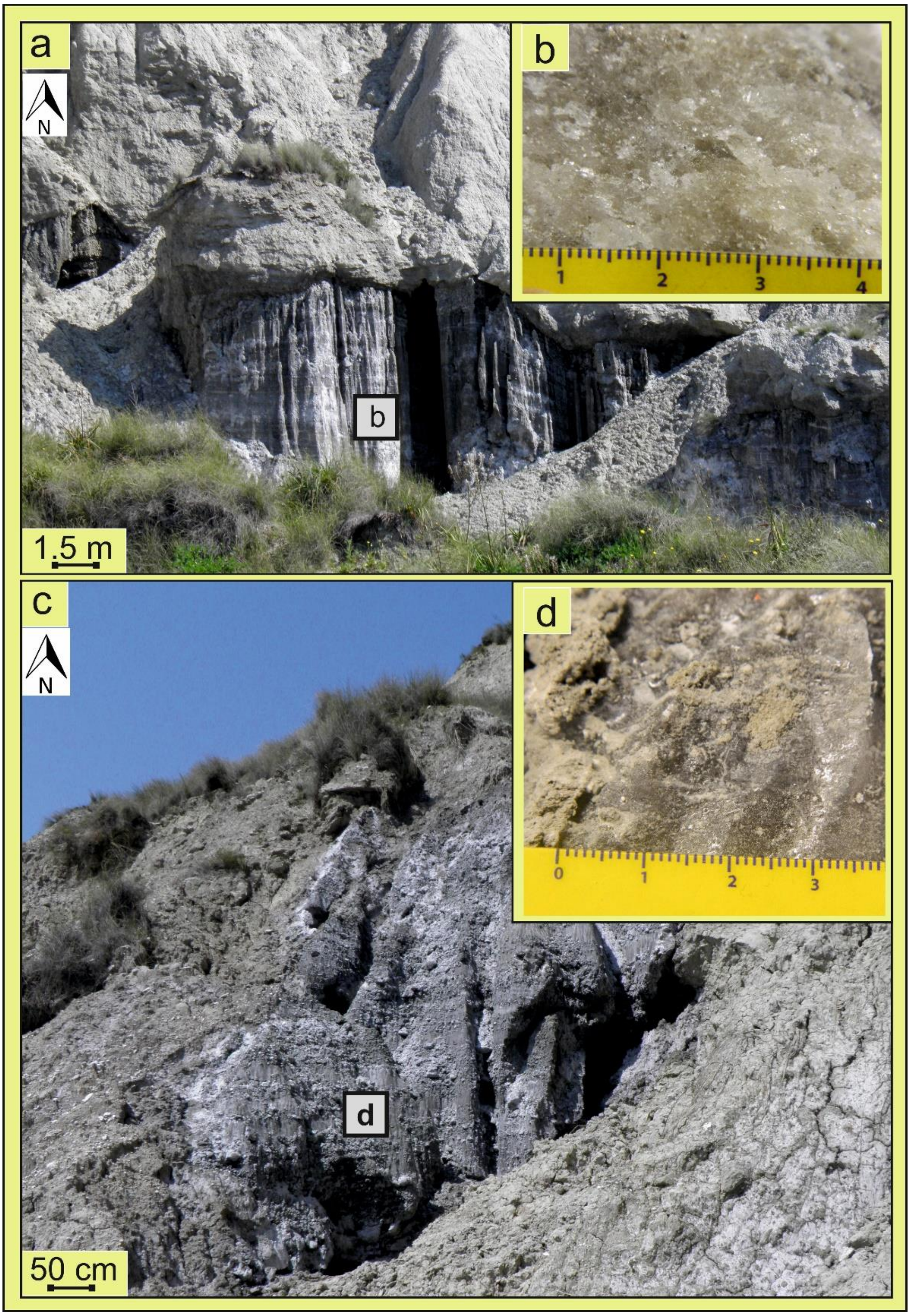

Figure 2.11. (a-c) Halite salt domes in the Verzino area showing microcrystalline halite crystals belong to the banded facies. (a) Salt dome called "La Gola" and (b) detail of *Ru 17-17* halite sample; (c) Salt dome called "La Gola Nord" and (d) detail of *Ru 19-17* halite sample.

Microscopically, sample *Ru 17-17* is made of elongated and flattened grey and white microcrystalline halite crystals (< 5 mm in size). Crystals show: **(i)** competitive growth, **(ii)** faces oriented in the y axis direction (Figure2.12a), **(iii)** rare relics primary structures (corner), **(iv)** pseudo-secondary or secondary fractures filled with secondary fluid inclusions or clay matter, **(v)** gypsum crystals dispersed throughout the sample, **(vi)** thin films of clay matter that fills the empty space created of the syndepositional dissolutions (Figure 2.12b), **(vii)** little and rounded birefringent crystals (unidentified) associated with clay matters, **(viii)** dissolution phenomena along the pre-existing halite fabric, **(ix)** and transparent matters disperse in the crystals.

Sample *Ru 19-17* is composed of elongated or rounded (Figure 2.12c) fractured grey and white microcrystalline halite crystals (< 0.5 cm in size). Crystals show competitive growth and chaotic orientation. Fluid inclusions and/or clay matter fill the pseudo-secondary or secondary fractures. Thin films of clay matter separate or cover the crystals (cloudy halite - Figure 2.12d) and fill the empty space created of the syndepositional dissolution. Little and rounded birefringent crystals (unidentified**)** and transparent matters dispersed throughout the samples have been observed.

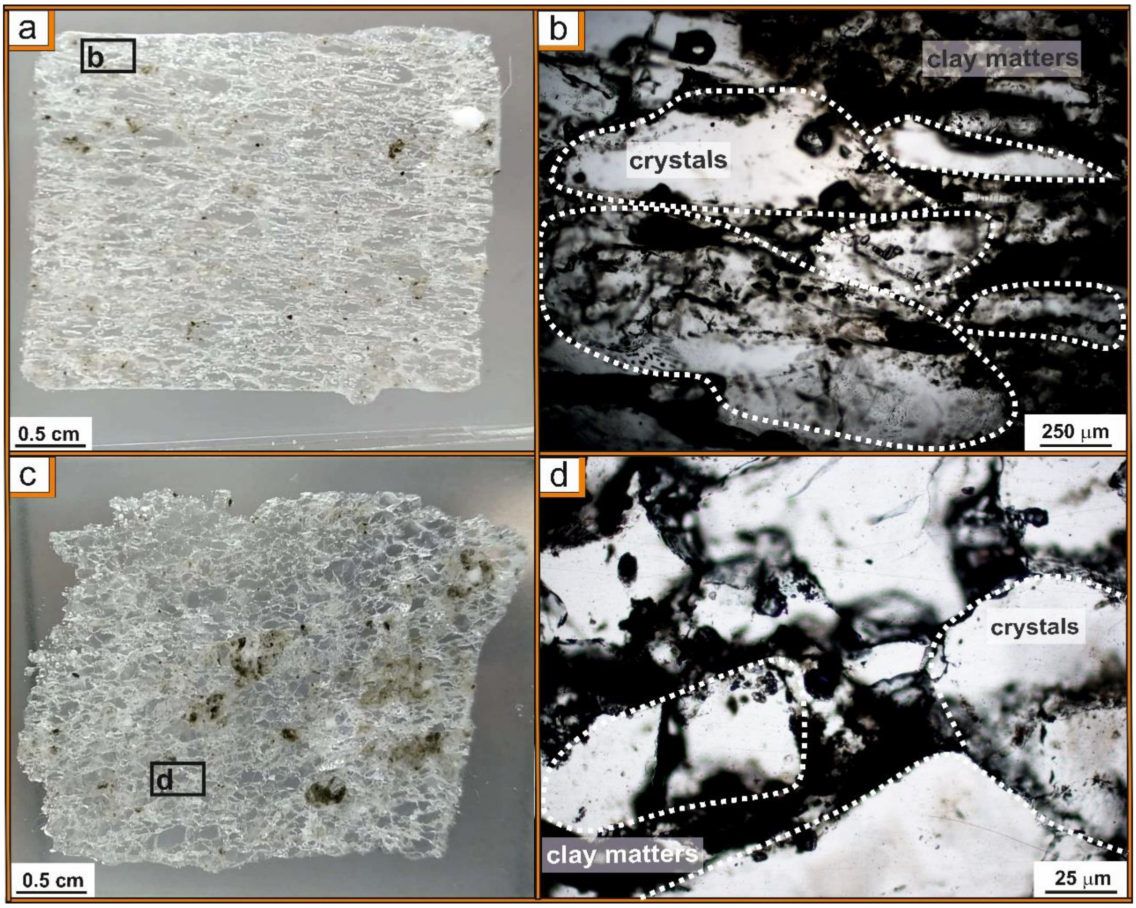

Figure 2.12. a) *Ru 17-17* and (c) *Ru 19-17* samples showing microcrystalline halite; b) and d) detail of elongated or rounded halite crystals (white dotted line) immersed in dark brown clay matters.

2.5 The selenite samples from the Catanzaro Trough

In the Catanzaro Trough the only area that shows selenite deposit is located in the Marcellinara quarry (38.91405° N, 16.48767° E - geological map of Calabria, Tiriolo, sheet 242 IV, N-O, scale 1:25000). This disuse quarry shows *chaotic* and *organised* selenite deposits. To facilitate sampling, the quarry was divided in 6 sectors (Figure 2.13):

- Sector 1 - chaotic deposit: with a low-angle direct fault (north-east immersion) and made up of reworked selenite (breccia) and giant selenite blocks.
- Sector 2 – chaotic deposit: made up reworked selenite crystals (on the top), collapsed blocks and local domes structures also known “Cavoli” (Schreiber, 1997) (on the bottom);
- Sector 3 – chaotic deposit: made up reworked and massive selenite facies;
- Sector 4 – organised deposit: consists of banded facies separated by dissolution surfaces and/or breccia layers;
- Sector 5 – organised deposit: made up nine cycles of banded selenite facies separated by dissolution surfaces and thin argillaceous/calcareous laminae;
- Sector 6 – chaotic deposit: contains reworked and massive selenite facies, just like the sector 3;

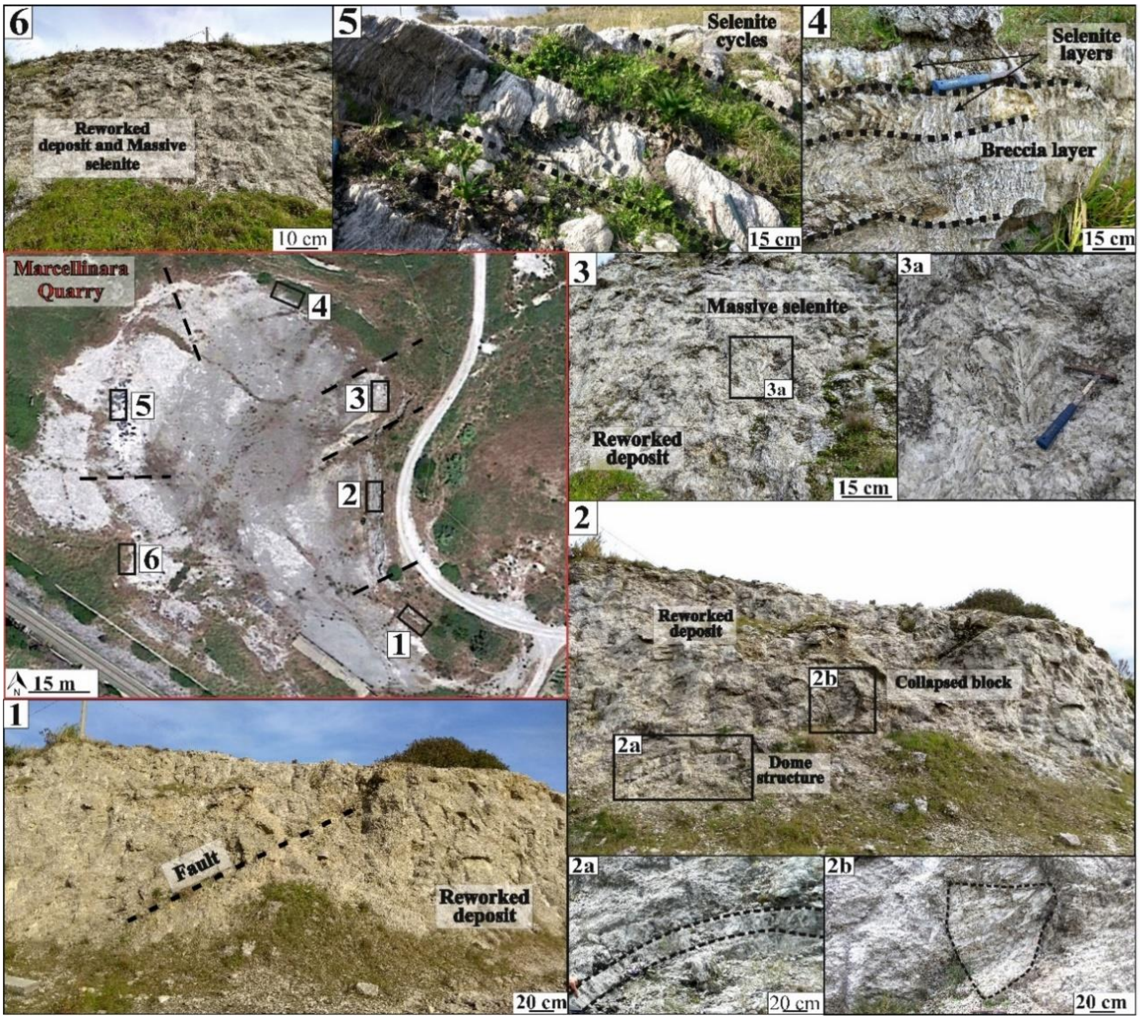

Figure 2.13. The Marcellinara quarry divides in 6 sectors. 1) Sector 1: chaotical deposit and normal fault; 2) sector 2: reworked deposit, dome structures (2a) and collapse block (2b); 3) sector 3: reworked deposit and massive selenite (3a); 4) sector 4: selenite layers interrupted by breccia layers; 5) sector 5: selenite layers; 6) sector 6: reworked deposit and massive selenite.

Stratigraphic observations and preliminary studies (Costanzo *et al*., 2019; Cianflone *et al.*, 2011, 2012) suggest that the sector 4 and 5 are made of selenite crystals belonging to the Upper Gypsum, while the Giant facies had been interpreted as resedimented blocks of the Lower Gypsum collapsed during the second step of the Messinian salinity crisis. This had been confirmed by the presence of **(i)** branching facies (Lower Gypsum) found as blocks within the Riato conglomerate (located near the quarry), **(ii)** collapse of selenite blocks and **(iii)** reworked selenite that indicated instability processes in the basin. This testified the presence of the Lower evaporites in the Catanzaro Trough subsequently dismantled and cannibalised (drastic lowering of the sea level).

Crystals from organised deposits (banded selenite in sector 4 and 5), chaotic or different deposits (giant facies in sector 1 and branching facies in Riato conglomerate) have been sampled to investigate the basin evolution and to understand the relationships between the three facies (Table 2).

Location name	Samples name	Crystal types	Facies and growth direction
Marcellinara (Ma)	Ma 19-17	Selenite	Banded - vertical growth
	Ma 24-17	Selenite	Banded – vertical growth
	Ma 27-17	Selenite	Banded – vertical growth
	Ma 01-17	Selenite	Banded – vertical growth
	Ma 02-17	Selenite	Banded – oblique growth
	Ma 03-17	Selenite	Banded – vertical growth
	Ma 04-17	Selenite	Banded – vertical growth
	Ma 05-17	Selenite	Banded – oblique growth
	Ma 06-17	Selenite	Banded – vertical growth
	Ma 07-17	Selenite	Banded – oblique growth
	Ma 08-17	Selenite	Banded – oblique growth
	Ma 09-17	Selenite	Banded – vertical growth
	Ma Br	Selenite	Branching – alignment growth
	Gi 01	Selenite	Giant – vertical growth

Table 2. Summary table of all samples from the Marcellinara quarry

2.5.1 Macroscopic facies description

Giant facies observed in the sector 1 (Figure 2.14) show metric crystals with [010] orientation and vertical crystal growth. The crystal sampled has been used for isotopic analysis (see chapter 5).

Figure 2.14. The giant selenite block. (Picture from Cianflone & Dominici, 2011).

Banded facies have been sampled in the sector 4 (Figure 2.15) and sector 5 (Figure 2.16).

In the sector 4 the deposit shows banded selenite layers interbedded by breccia layers and/or dissolution surfaces. From the top-down, crystals observed and sampled are:

1) crystals <10 cm in length and showing [010] orientation - sample *Ma 19-17*;

2) crystals ~ 20 cm in length with vertical growth and showing [010] orientation - sample *Ma 24-17;*

3) crystals ~ 10 cm in length with vertical growth and [120] orientation - sample *Ma 27-17*.

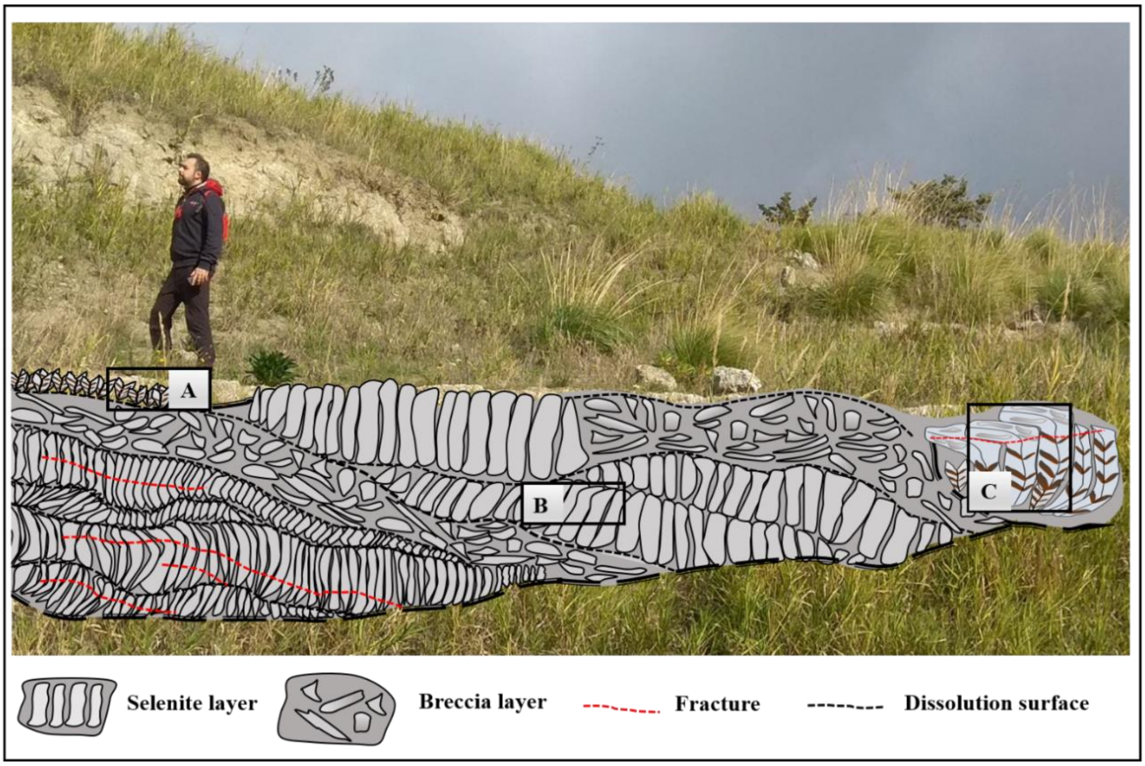

Figure 2.15. Deposit in the sector 4 showing reconstruction of the selenite layers separated by dissolution surfaces (black dotted lines) and breccia layer. A, B and C are points sampled.

In the sector 5 (Figure 2.16) there is the best outcrop composed of 9 cycles of banded selenite (south-east immersion) separated by dissolution surfaces and/or interbedded with thin argillaceous/calcareous laminae. From the top-down crystals observed and sampled are:

1) first cycle: crystals are ~ 40 cm in length with vertical growth and [010] orientation - sample *Ma 01-17*;

2) second cycle: crystals are ~ 57 cm in length with oblique growth and [010] orientation - sample *Ma 02-17*;

3) third cycle: crystal are ~12 cm in length with vertical growth and [010] orientation - sample *Ma 03-17*;

4) fourth cycle: crystals are ~6 cm in length with vertical growth and [120] orientation - sample *Ma 04-17*;

5) fifth cycle: crystals are ~6 cm in length with oblique growth and [120] orientation - sample *Ma 05-17*;

6) <u>sixth cycle</u>: crystals are ~6 cm in length with vertical growth and [120] orientation - sample *Ma 06-17*;

7) <u>seventh cycle</u>: crystals are ~26 cm in length with oblique growth and [120] orientation - sample *Ma 07-17*;

8) <u>eight cycle</u>: crystals are ~16 cm in length with oblique growth and [120] orientation - sample *Ma 08-17*;

9) <u>ninth cycle</u>: crystals are ~16 cm in length with vertical growth and [010] orientation - sample *Ma 09-17*.

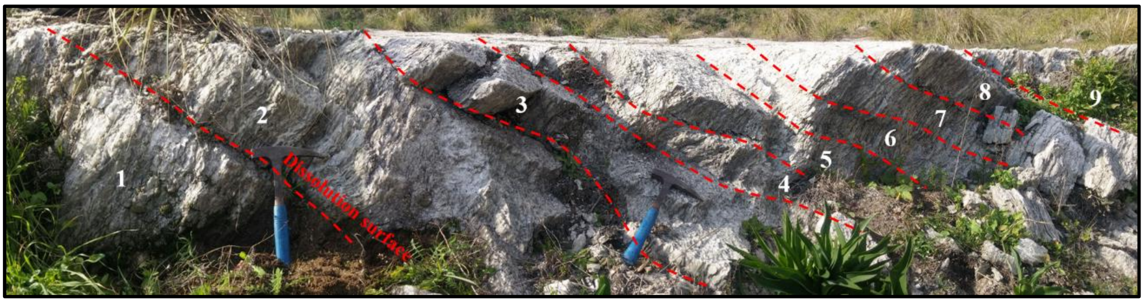

Figure 2.16. Deposit in sector 5 showing 9 cycles of selenite facies separated by dissolution surfaces and/or by thin argillaceous/calcareous laminae (red dotted lines).

Branching facies (arrangement in metric boulder) was been sampled (Figure 2.17) in the Riato conglomerate and shows millimetric gypsum crystals immersed in a calcareous matrix.

Figure 2.17. Alignment of rounded metric boulders of branching selenite. Magnification of the facies (red arrow). Picture from Cianflone & Dominici, (2011).

2.5.2 Microscopic petrography

The selenite crystals belong to the banded and giant facies show the alternation of turbid and limpid bands visible to the naked eye (microfacies). These microfacies called also cloudy and clear intervals are well recognised using transmitted light microscopy; cloudy intervals are enriched in organic and inorganic matters, in contrast, clear intervals are depleted in these matters.

Instead, the branching facies show microscopic chaotical gypsum crystals immersed in a brown matrix.

From 14 crystals sampled, 19 wafers cut parallel to the [010] face have been obtained. The crystals show white colours under PPL and from weak to high birefringence with oblique extinction (each 45° during a 360° rotation) under XPL.

Three samples from the sector 4 have been observed:

1) The sample *Ma 19-17* (~4 cm in size) is made of six cloudy intervals – 4 on the left and 2 on the right of the twin plane (Figure 2.18a-b). It shows the twin plan with zigzag pattern and oblique orientation (Figure 2.18c-d) filled by brown materials and little gypsum crystals (XPL). Long fractures parallel to the twin plane and small fractures perpendicular to the twin plane have been observed. These fractures don’t’ remove the primary features.

Brown (Figure 2.18e), orange and transparent organic matters (Figure 2.18f) organised in cluster are dispersed throughout the sample.

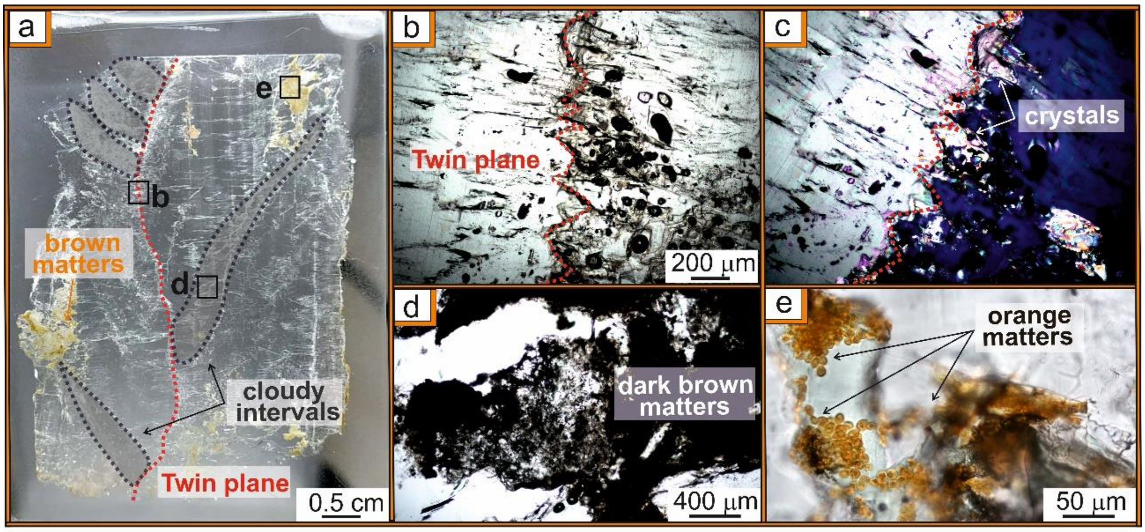

Figure 2.18. a) and b) Wafer showing the twin plane, cloudy intervals and brown matters; c) and d) the twin plane with zigzag patter and little gypsum crystals (under PPL and XPL); e) dark and clear brown matters; f) rounded orange matters.

2) The sample *Ma 24-17* (~10 cm in size) is made of thirteen cloudy intervals – 7 on the left and 6 on the right of the twin plane. Two wafers have been obtained (Figure 2.19a - d):

Ma 24-17a (top): is well preserved and shows brown matters and little gypsum crystals (XPL). The twin plane (Figure 2.19b), filled by brown matters and little gypsum crystals (Figure 2.19c), has vertical orientation and zig zag pattern. Rare fractures are parallel to the twin plane and don't' remove the primary features. Brown, orange and transparent organic matters, organised in cluster, are dispersed throughout the sample.

Ma 24-17b (bottom): is fractured with abundant brown, green (Figure 2.19e) and red (Figure 2.19f) matters dispersed throughout the sample. Twin plane is divided in two planes which creates narrower crystals than the others (Figure 2.19d).

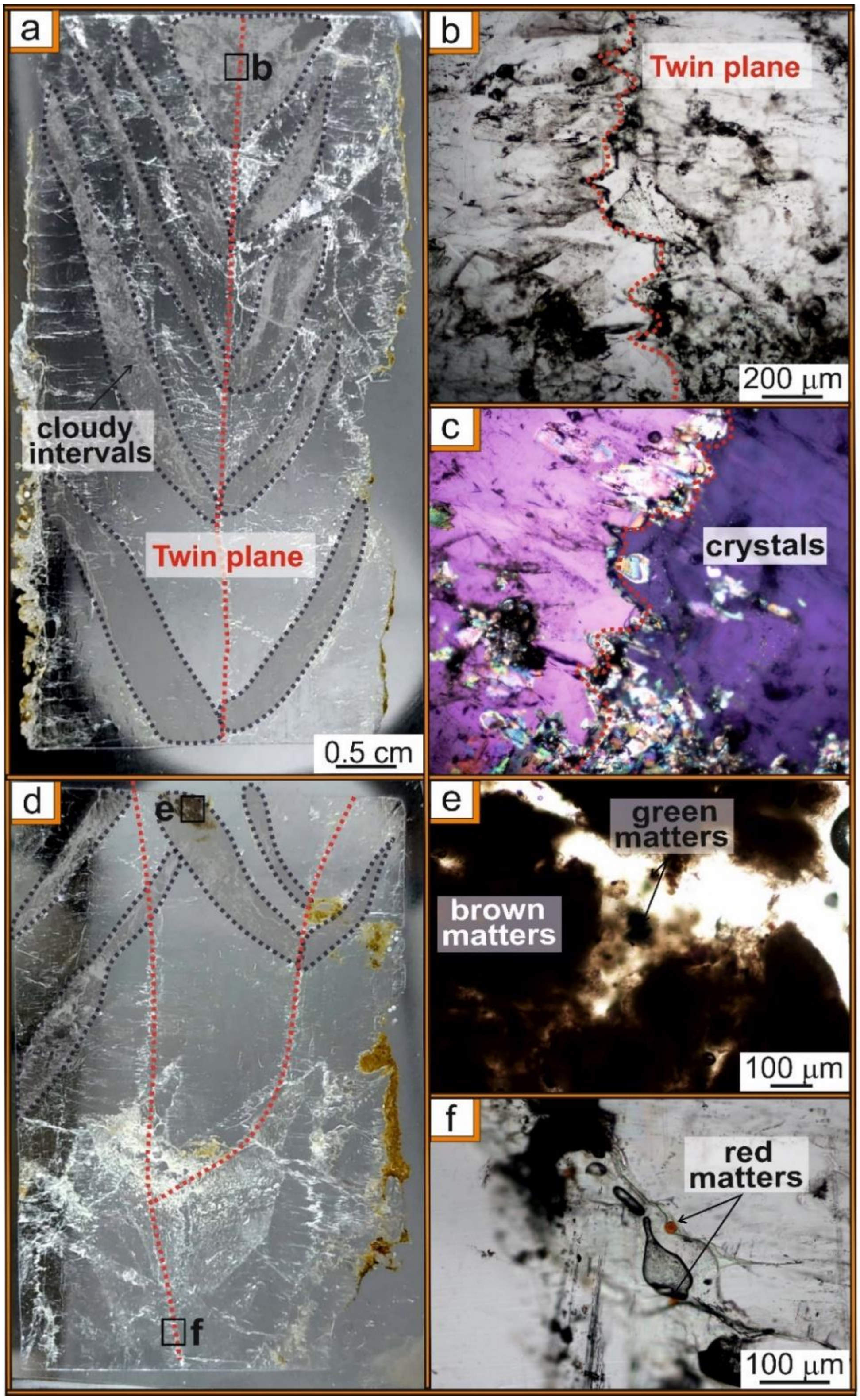

Figure 2.19. a) Wafer showing vertical twin plane and cloudy intervals; b) and c) twin plane with zigzag patter and little gypsum crystals (under PPL and XPL); d) the crystal shows splitting of the twin plane; e) brown and green matters in the cloudy interval; f) rounded red matters along the twin plane.

3) The sample *Ma 27-17* (~5 cm in size) is made of five cloudy intervals – 1 on the left and 4 on the right of the twin plane (Figure 2.20a). It shows the twin plane with zigzag pattern and vertical orientation (Figure 2.20b) filled by brown matters. Secondary fracture (Figure 2.20c) parallel to the twin plane, transparent and brown matters (Figure 2.20d) dispersed throughout the crystal have been observed. In cloudy interval isolated foraminifera (Figure 2.20e) has been recognised.

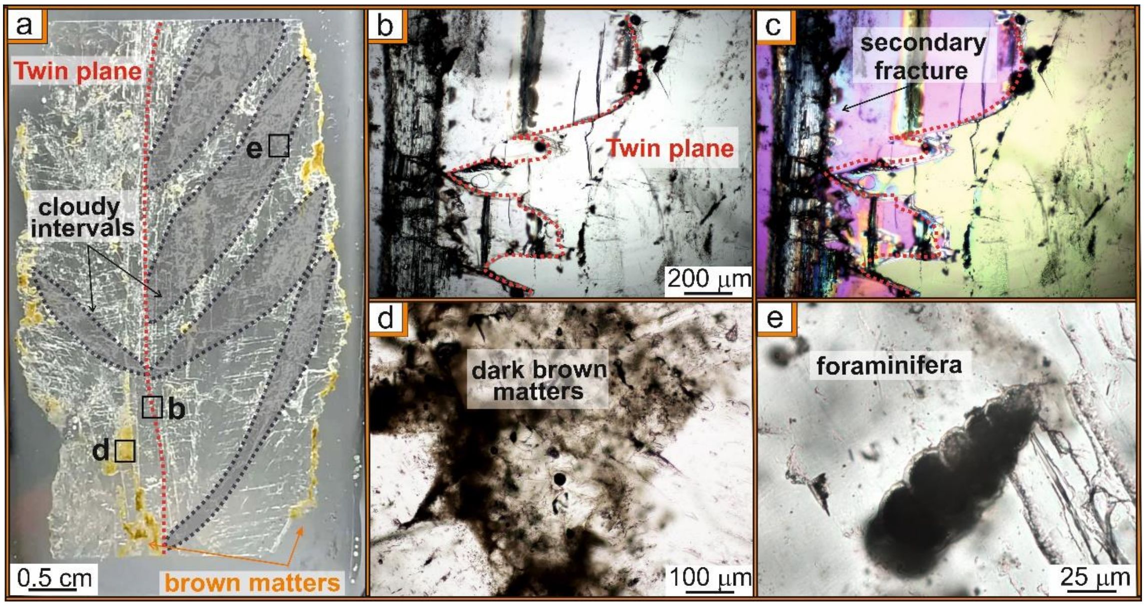

Figure 2.20. a) *Ma 27-17* showing the twin plane, cloudy intervals and brown matters; b) and c) detail of the twin plane with zigzag patter and secondary fracture (under PPL and XPL); d) dark brown matters dispersed throughout the crystal; f) isolated foraminifera in the cloudy interval.

Nine samples from the sector 5 have been investigated:

1) The sample *Ma 01-17* (~3 cm in size) does not show the twin plane but only 4 clear and 3 cloudy intervals located on the right side of the crystal (Figure 2.21a). The cloudy and clear intervals are well separated (Figure 2.21b). The cloudy intervals show parallel cleavage plans (Figure 2.21c), while the clear display only parallel and perpendicular secondary fractures filled with brown matters or fluid inclusions. Brown matters and rounded gypsum crystals fill pseudo and/or secondary fractures. Transparent and dark or clear brown matters have been observed mainly in the cloudy intervals.

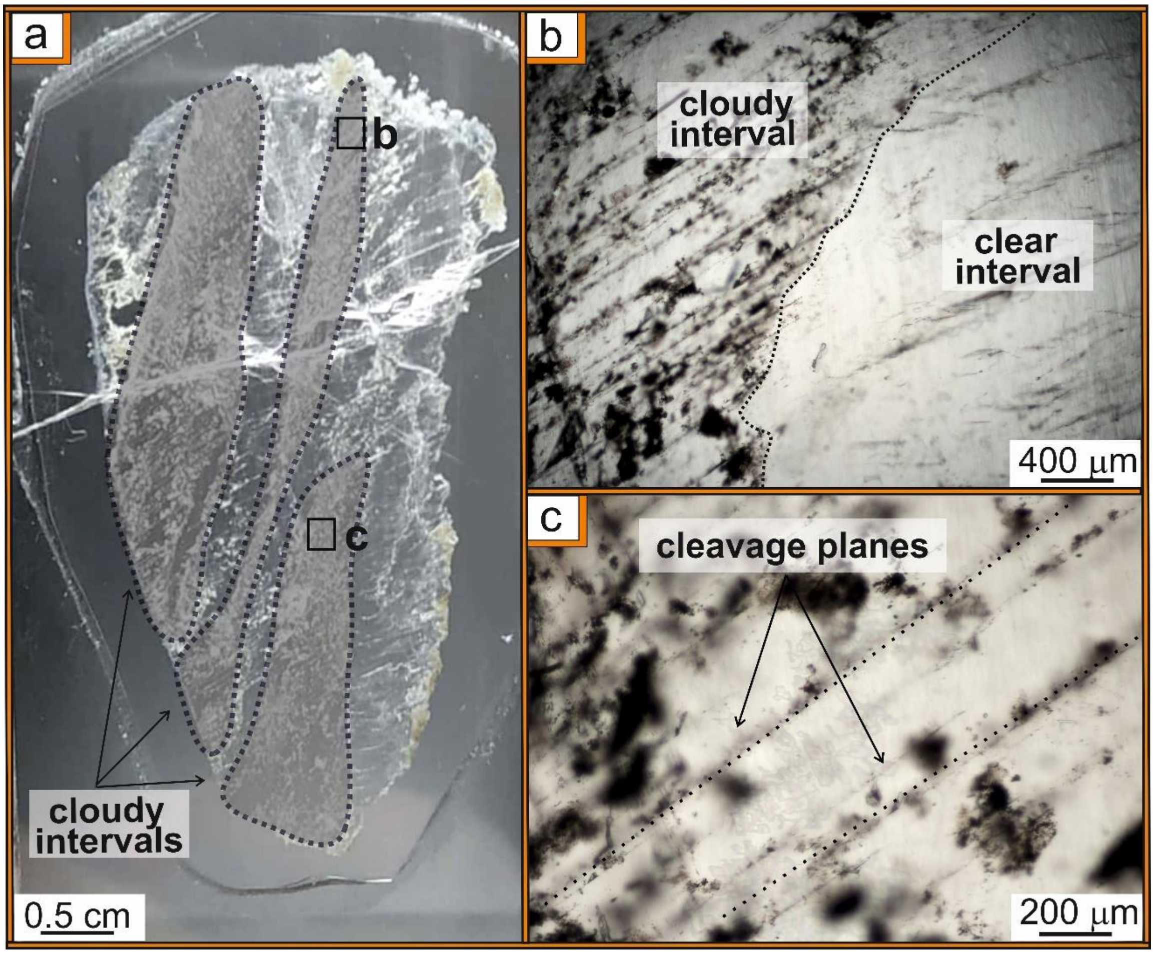

Figure 2.21. a) *Ma 01-17* crystal showing three cloudy intervals; b) black dotted line separates cloudy and clear intervals; c) detail of the cloudy interval with parallel cleavage plane (black dotted lines).

2) The sample *Ma 02-17* (~15 cm in size) is made of twenty cloudy intervals – 8 on the left and 12 on the right of the twin plane. Three wafers have been obtained (Figure 2.22a -c-e):

Ma 02-17a (top): shows two twin planes separate (Figure 2.22a) with linear pattern (Figure 2.22b), filled by brown matters. The twin planes generate two selenite crystals with cloudy intervals smaller. In the cloudy intervals, the cleavage plans are less marked than the bottom. Transparent and red matters have been observed.

Ma 02-17b (central): is fractured and displays splitting of the twin plane (Figure 2.22c-d). The twin plane, filled by brown matters, shows zigzag pattern and oblique orientation. Two twin planes create two narrower crystals. Transparent matters are dispersed throughout the sample.

Ma 02-17c (bottom): shows the twin plane with linear pattern (Figure 2.22e) and filled by brown matters. The cloudy intervals show cleavage plans and isolated foraminifera (Figure 2.22f). The clear intervals display only secondary fractures filled with brown matters or fluid inclusions. Abundant dark and clear brown matters organised in cluster are dispersed throughout the sample. The cloudy and clear intervals are not clearly separated (intermediate intervals).

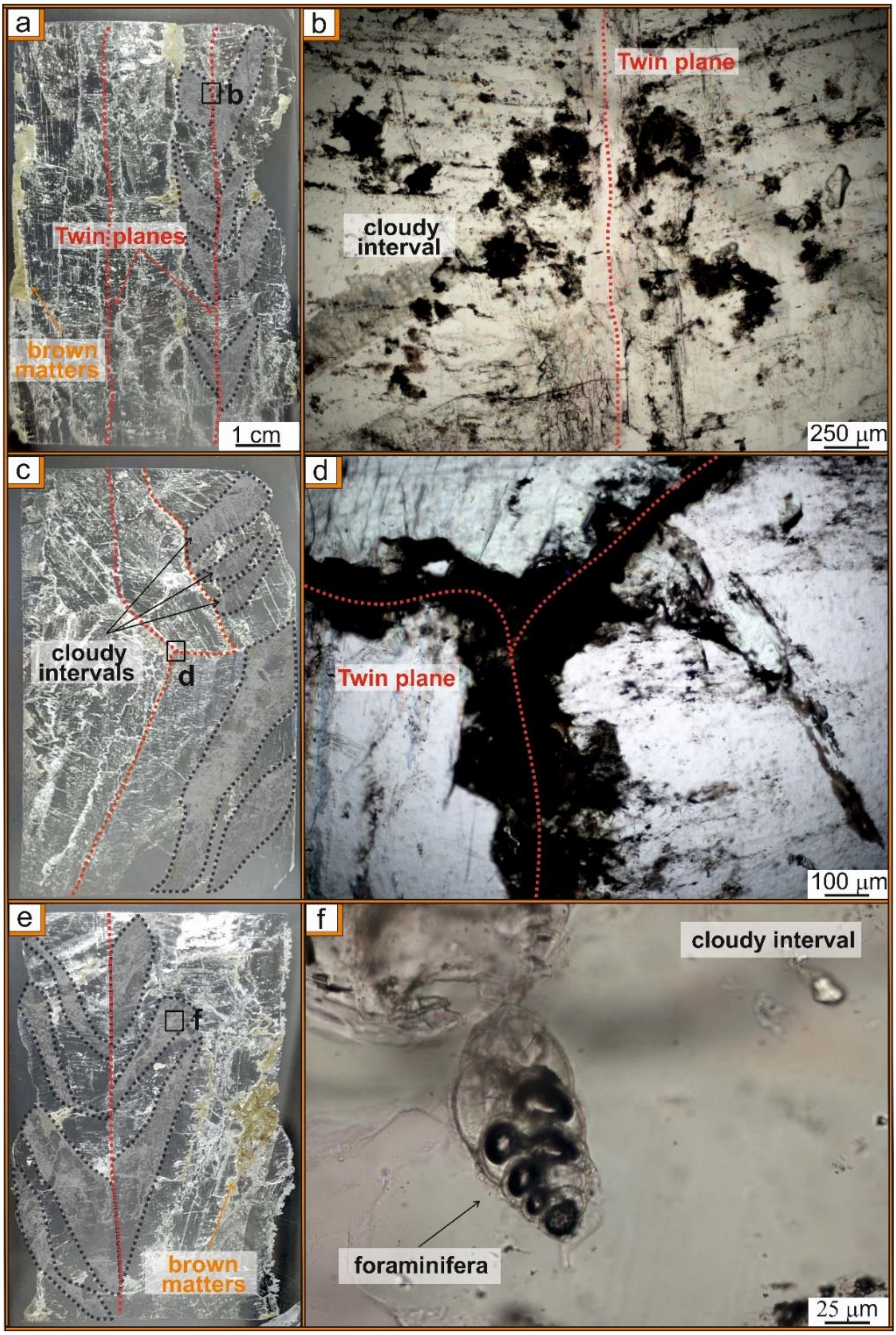

Figure 2.22. a) and b) *Ma 02-17a* displaying two twin planes with; (b) magnification of one linear twin plane; c) and d) *Ma 02-17b* shows splitting of the twin plane; e) *Ma 02-17c* showing vertical twin plane and brown matters; f) detail of foraminifer trapped in the cloudy interval.

3) The sample *Ma 03-17* (~4 cm in size) shows the twin plane and only the left side of the crystal made of three cloudy intervals (Figure 2.23a). The twin plane displays linear pattern and vertical orientation (Figure 2.23b). The cloudy intervals show cleavage plans, abundant dark and clear brown matters organised in cluster and individual foraminifera (Figure 2.23c). The clear intervals have only secondary fractures filled with brown matters or fluid inclusions. Transparent organic matter is dispersed in both intervals.

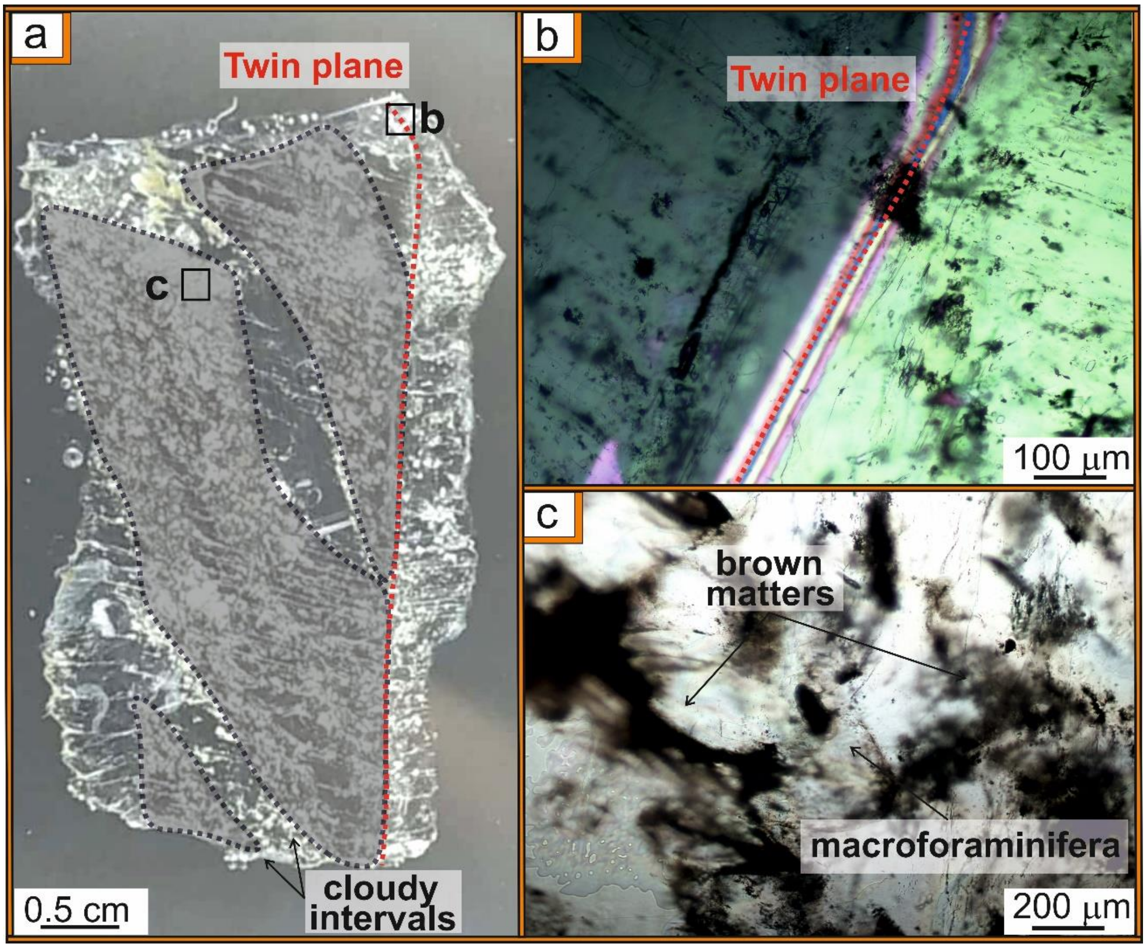

Figure. 2.23. a) *Ma 03-17* showing the win plane and cloudy intervals; b) magnification of the linear twin plane under XPL observation; c) brown matters and foraminifera in the cloudy interval.

4) The sample *Ma 04-17* (~3 cm in size) is made of nine cloudy intervals – 5 on the left and 4 on the right of the twin plane (Figure 2.24a). The twin plane shows zigzag pattern and vertical orientation (Figure 2.24b). The secondary and pseudo-secondary fractures are parallel or perpendicular to the twin plane. The cloudy intervals display cleavage planes and abundant dark brown, transparent and green matters (Figure 2.24c). The clear intervals show only secondary fractures filled with brown matters or fluid inclusions.

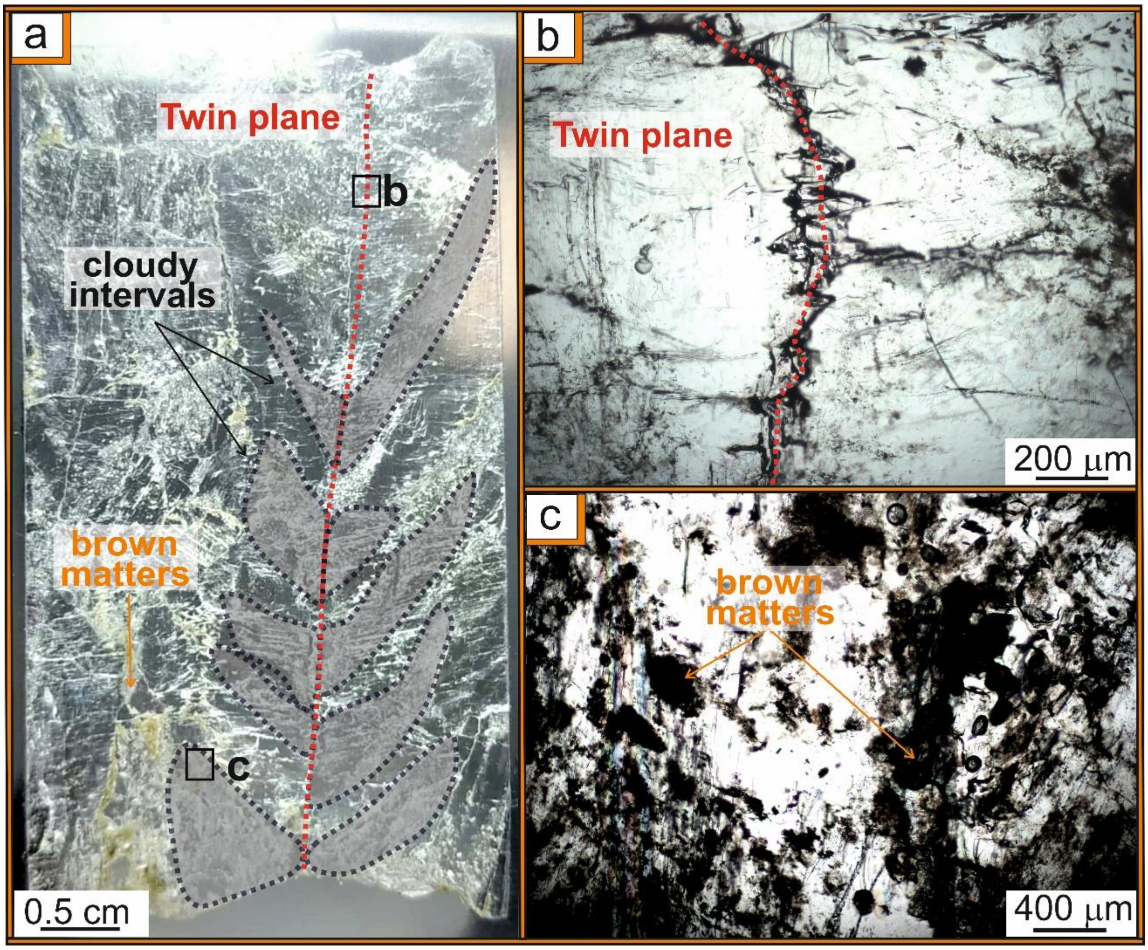

Figure 2.24. a) *Ma 04-17* showing the twin plane, cloudy intervals and brown matters; b) detail of the twin plane with zigzag pattern; c) detail of brown matters in the cloudy interval.

5) The sample *Ma 05-17* (~2cm in size) is made of seven cloudy intervals – 4 on the left and 3 on the right of the twin plane (Figure 2.25a). The twin plane shows zigzag pattern and oblique orientation (Figure2.25b). The cloudy intervals display cleavage plans and abundant transparent, dark/clear brown and green matters (Figure2.25c). The clear intervals show only secondary fractures filled with brown matters or fluid inclusions. Secondary fractures and brown matters have been observed throughout the sample.

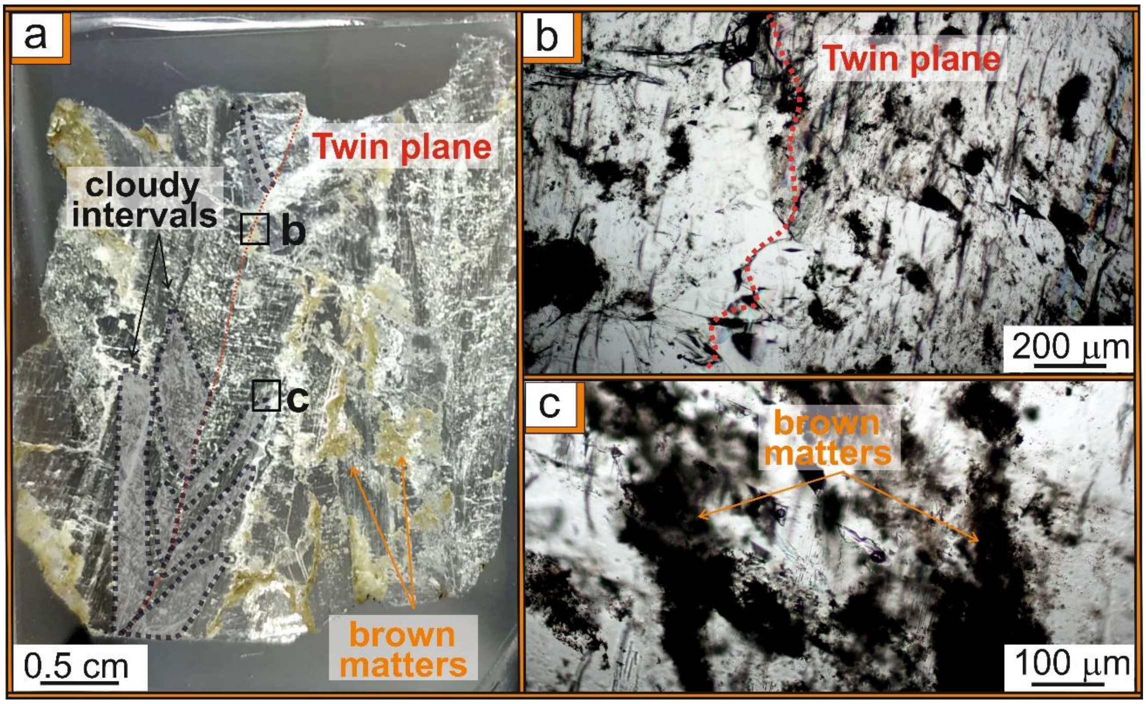

Figure 2.25. a) *Ma 05-17* showing oblique twin plane, cloudy intervals and brown matters; b) detail of the twin plane with zigzag pattern; c) detail of the brown matters in the cloudy interval.

6) The sample *Ma 06-17* (~4 cm in size) is made of seven cloudy intervals – 2 on the left and 5 on the right of the twin plane (Figure 2.26a). The twin plane shows linear pattern and vertical orientation (Figure2.26b). The cloudy intervals display parallel cleavage planes and abundant transparent, dark/clear brown matters. (Figure 2.26c). The clear intervals show secondary fractures filled with brown matters or fluid inclusions. Secondary fractures and brown matters have been observed throughout the sample.

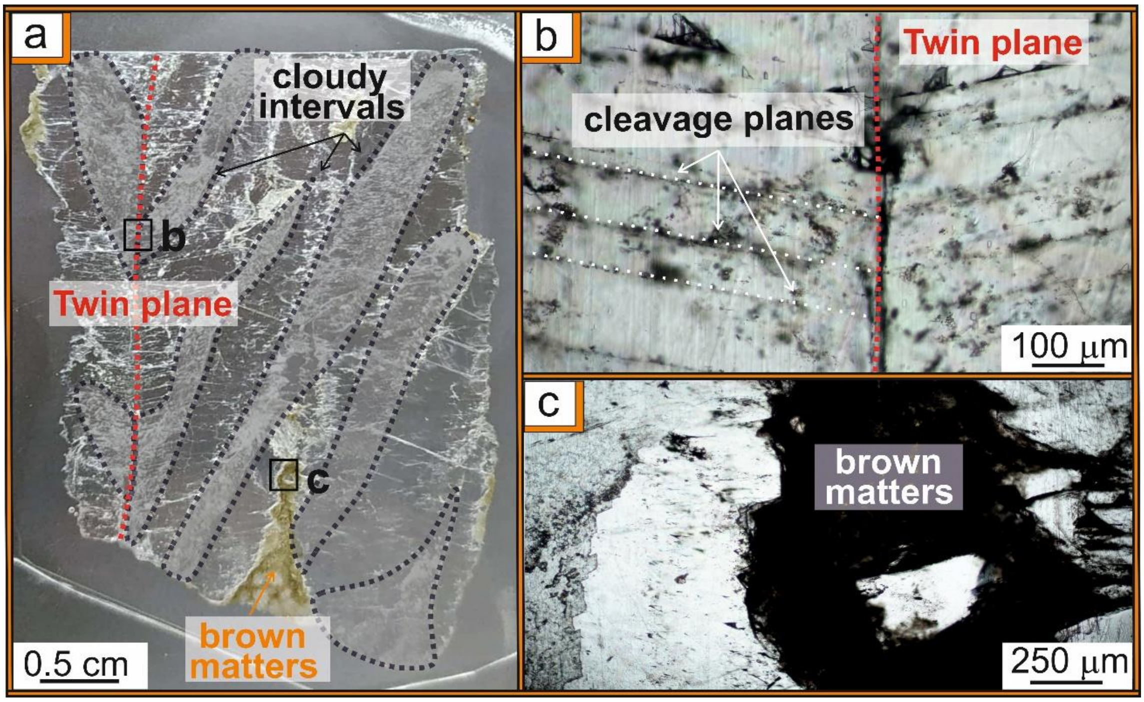

Figure 2.26. a) *Ma 06-17* showing vertical twin plane, cloudy intervals and brown matters; b) detail of the twin plane with regular pattern and cloudy interval with parallel cleavage planes; c) detail of the brown matters that fill the fracture in the clear interval.

7) The sample *Ma 07-17* (~4 cm in size) is made of nine cloudy intervals – 5 on the left and 4 on the right of the twin plane (Figure 2.27a). The twin plane shows zigzag pattern and vertical orientation. The cloudy intervals display parallel cleavage planes and anhydrite elongate crystals. Transparent, dark/clear brown (Figure 2.27b) and green matters and one foraminifer have been observed. The clear intervals show secondary fractures filled with brown matters or fluid inclusions (Figure 2.27c). Secondary fractures and brown matters have been observed throughout the sample.

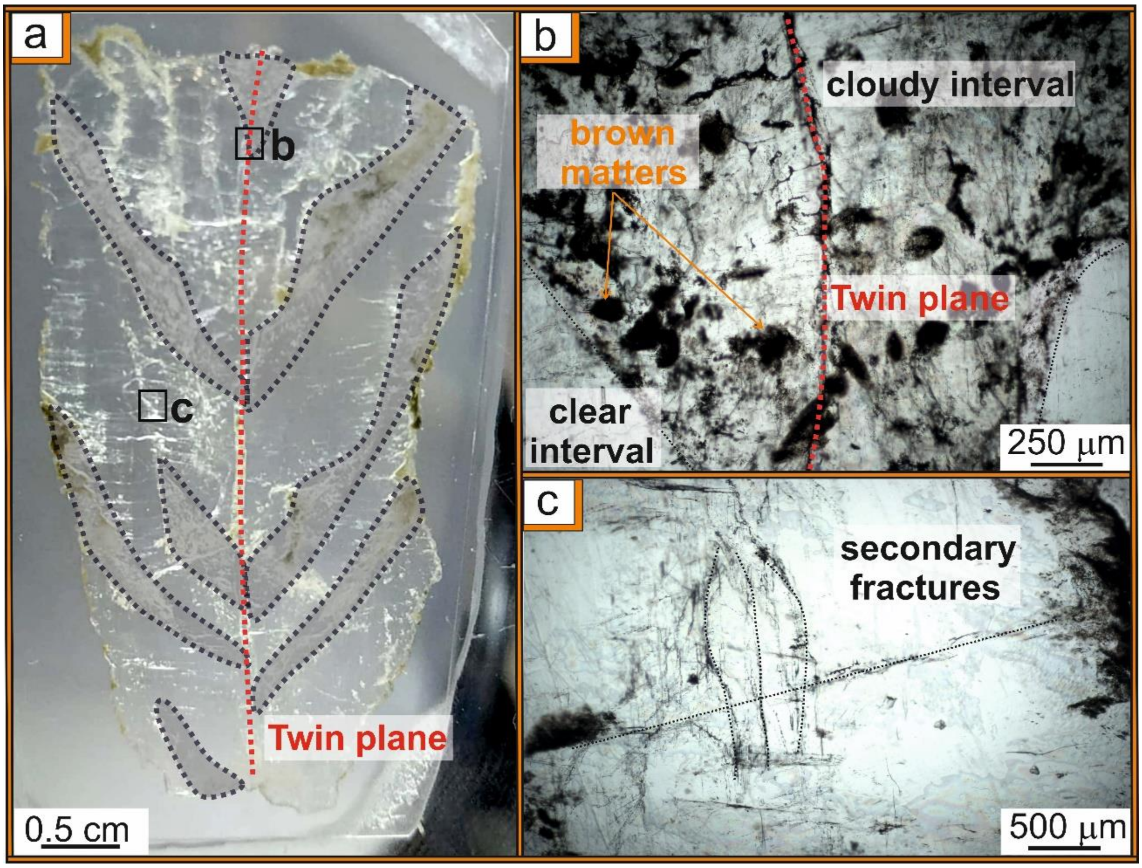

Figure .2.27. a) *Ma 07-17* showing vertical twin plane and cloudy intervals; b) detail of the twin plane with zigzag pattern and the brown matters. Black dotter lines separate cloudy and clear intervals; c) detail of the secondary fractures in the clear intervals (black dotter lines).

8) The sample *Ma 08-17* (~14 cm in size) is made of nine cloudy intervals – 7 on the left and 2 on the right of the twin plane. Two wafers have been obtained (Figure 2.28a -c):

Ma 08-17a (top): shows the twin plane (Figure 2.28a) with zigzag pattern and oblique orientation. The cloudy intervals display parallel cleavage planes, transparent and brown matters (Figure 2.28b).

Ma 08-17b (bottom): shows the twin plane with zigzag pattern and oblique orientation (Figure 2.28c-d) filled by brown matters and gypsum crystals. The cloudy intervals display parallel cleavage planes, transparent, dark/clear brown, green and violet matters.

In *Ma 08-17a* and *Ma 08-17b* clear intervals show only secondary fractures filled with brown matters or fluid inclusions.

Abundant dark and clear brown matters and secondary fractures have been observed throughout the sample.

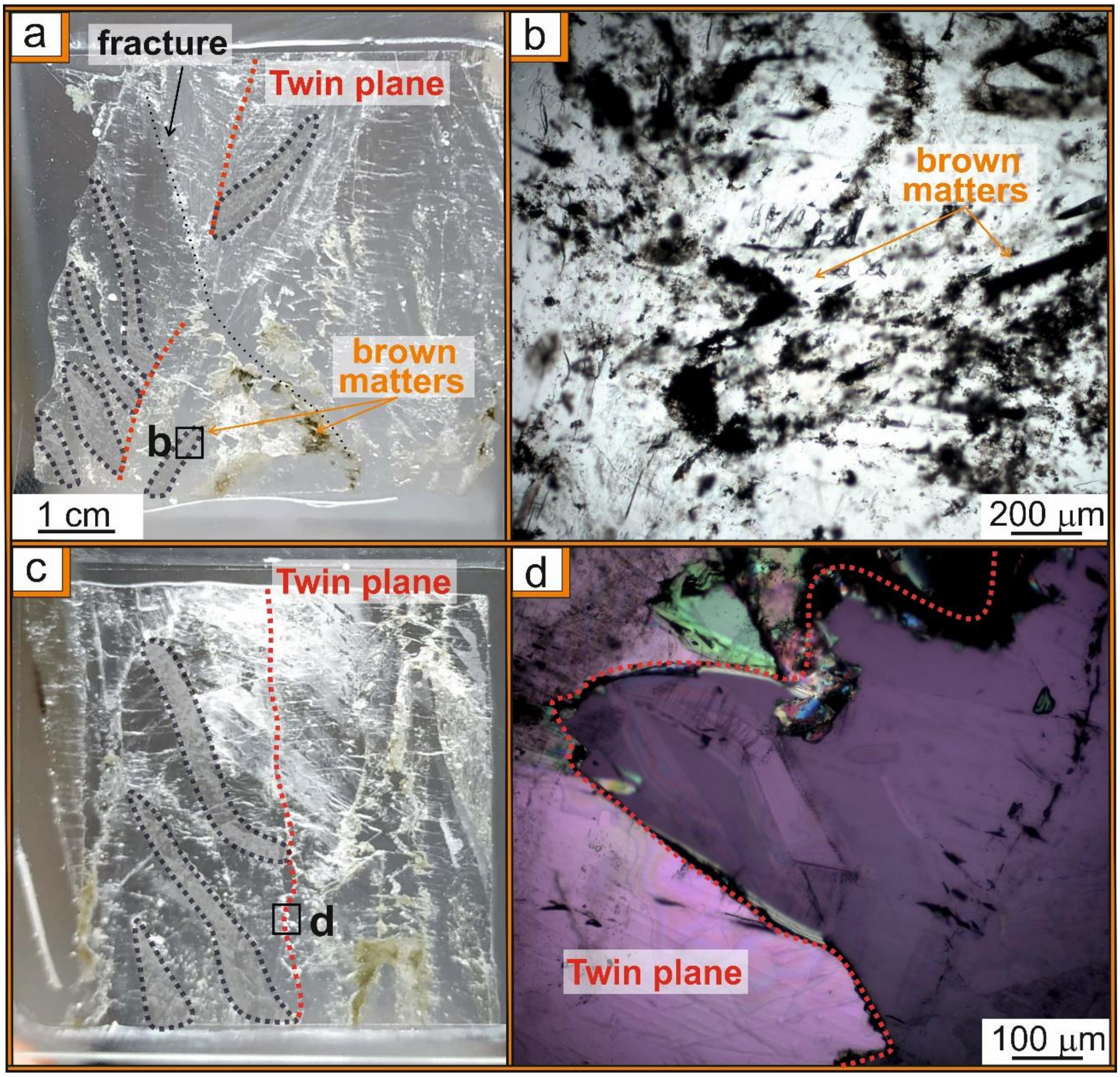

Figure 2.28. a) *Ma 08-17a* showing the twin planes, cloudy intervals with fracture and abundant brown matters; b) detail of the cloudy interval rich in brown matters; c) *Ma 08-17b* showing the twin plane with zigzag pattern; d) magnification of zigzag twin plane under XPL.

9) The sample *Ma 09-17* (~16 cm in size) doesn't show the twin plane but only the left side of the crystal that is made of five cloudy intervals. Two wafers have been obtained (Fig 2.29a-d):

Ma 09-17a (top) and Ma 09-17b (bottom): show the same features. The cloudy intervals display parallel cleavage planes, brown, transparent, red and green matters and little gypsum crystals organised in cluster (Figure 2.29b), while the clear have only secondary fractures filled with brown matters or fluid inclusions. Cloudy and clear intervals are well separated (Figure 2.29b).

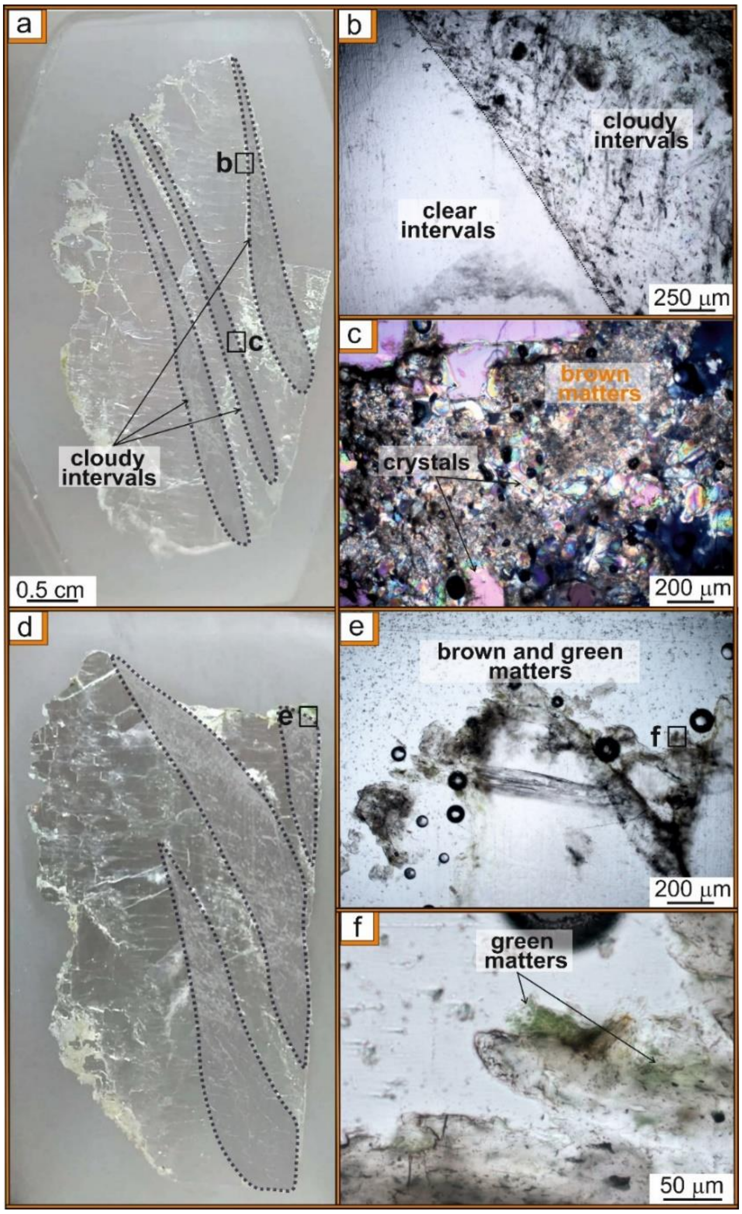

Figure 2.29. a) and b) *Ma 09-17a* showing the cloudy and clear intervals well separated; c) magnification of the brown matters and gypsum crystals dispersed in the cloudy intervals under XPL; d) *Ma 09-17b* showing cloudy and clear intervals well separated; e) and f) details of the green and brown matters in the cloudy intervals.

The branching sample (*Ma Br)* from the Riato conglomerate is made up a lot of small gypsum crystals (a few millimetres in size) immersed in a brown-yellow-orange matrix (Fig 2.30a). In details, it shows alternating oblique crystals bands [120] [$\bar{1}$11] and matrix (Fig 2.30b). The crystals splintered display the twin plane (Fig 2.30c), chaotic orientation and different shape - elongated, pentagonal or irregular. The matrix is made of calcium sulphate (investigated using Raman Spectroscopy). Red/orange agglomerates are dispersed throughout the sample.

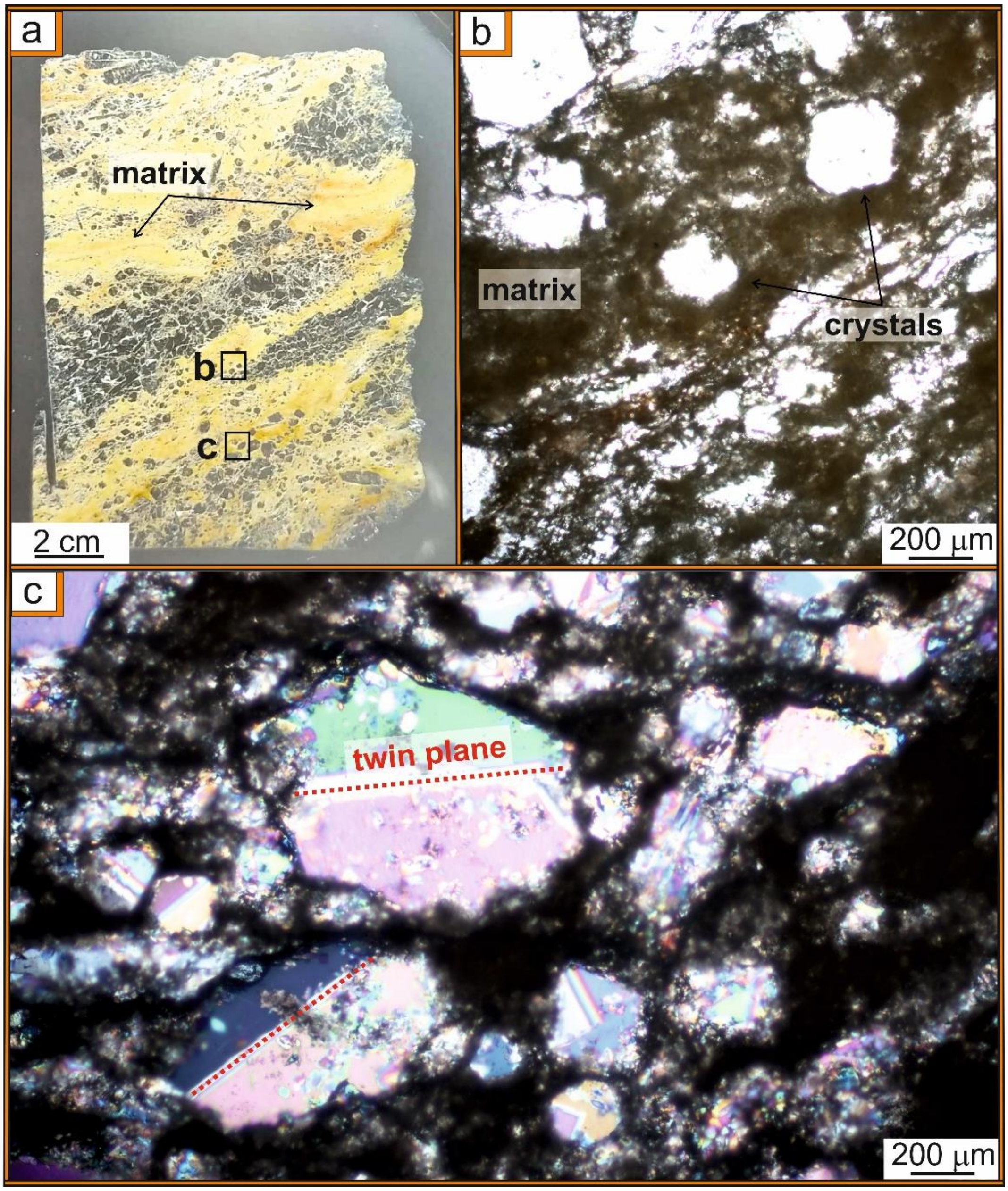

Figure 2.30. a) *Ma Br* shows alternating oblique bands (crystals and matrix); b) detail of the crystals immersed in the matrix c) crystal splintered with the twin plane visible under XPL.

From the giant selenite sample (*Gi 07*), four little crystal pieces have been sampled and observed. The pieces show abundant yellow and red organic matters organised in groups and rare fractures dispersed throughout the sample.

2.6 The selenite samples from the Ionian Basin

2.6.1 Macroscopic petrography

In the Ionian Basin, in Benestare area (38°11'17.65"N, 16° 8'15.93"E - geological map of Italy, Bovalino, project CARG, scale 1:50.000), there is a quarry made up of limestone deposit called GTL_1 (Calcare di Base) associated with local GTL_2 (selenite deposit).

The quarry appears to be seems made up of reworked selenite and selenite crystals (Figure 2.31) belonging to the banded (from centimetres to decimetres in size) and the branching facies. One sample from each facies have been collected (Table 3).

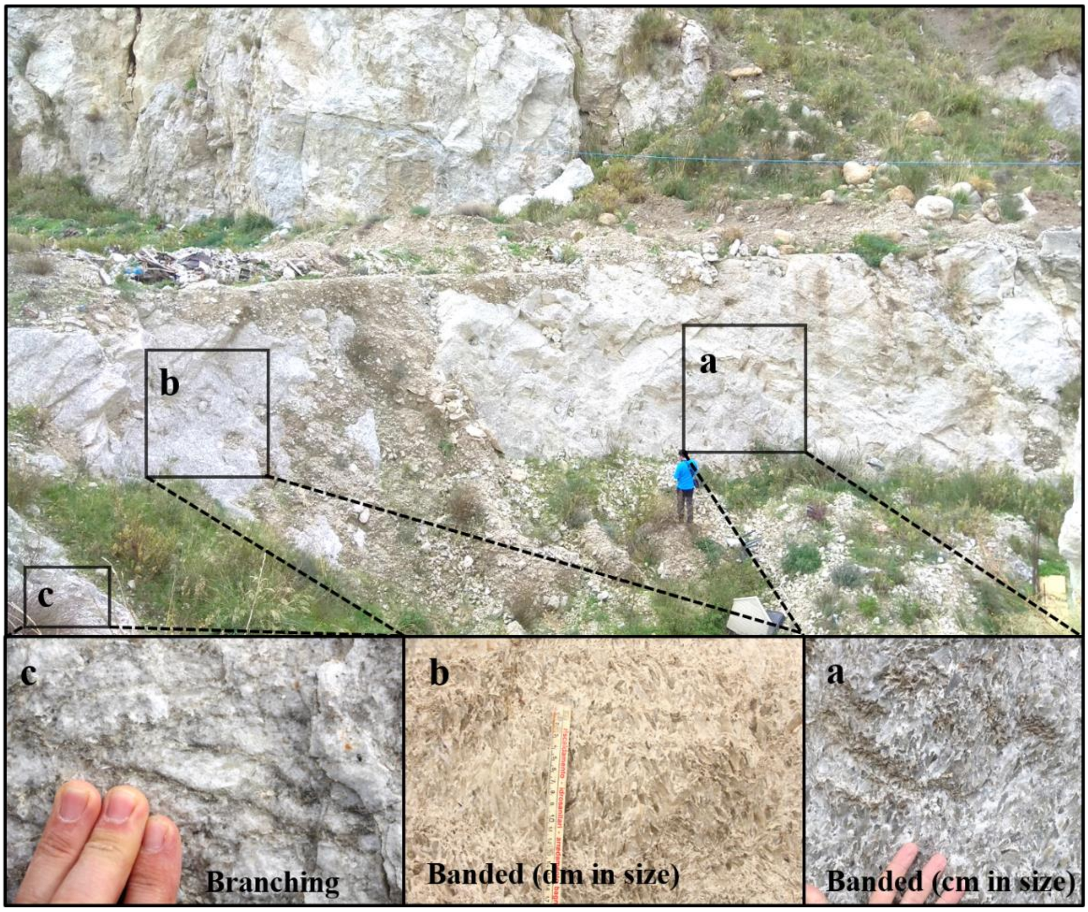

Figure 2.31. The Benestare quarry showing (a) banded facies (centimetres in size); b) banded facies (decimetres in size) and c) branching facies.

The banded facies is composed of selenite crystals (from 2 to 20 cm in length) with vertical growth and interbedded by thin argillaceous/calcareous laminae; two samples from centimetric (*Be 01-17)* and decimetric (*Be 03-17)* layer have been sampled.

The branching facies is made up of gypsum nodules immersed in a gypsum and carbonate matrix; sample *Be 05-17* has been collected;

Location name	**Samples name**	**Crystal types**	**Facies and growth direction**
Benestare (Be)	Be 01-17	Gypsum	Banded – vertical growth
	Be 03-17	Gypsum	Banded – vertical growth
	Be 05-17	Gypsum	Branching – alignment growth

Table 3. Summary table of the three samples from the Benestare quarry.

2.6.2 Microscopic petrography

1) The sample *Be 01-17* (Fig 2.32a) is made up of tabular crystals (< 1 cm in size) immersed in a clear brown-yellow matrix (Fig 2.32b). The crystals [120] are fractured and folded (Fig 2.32c) and show chaotic orientation. Transparent and red matters have been observed throughout the sample.

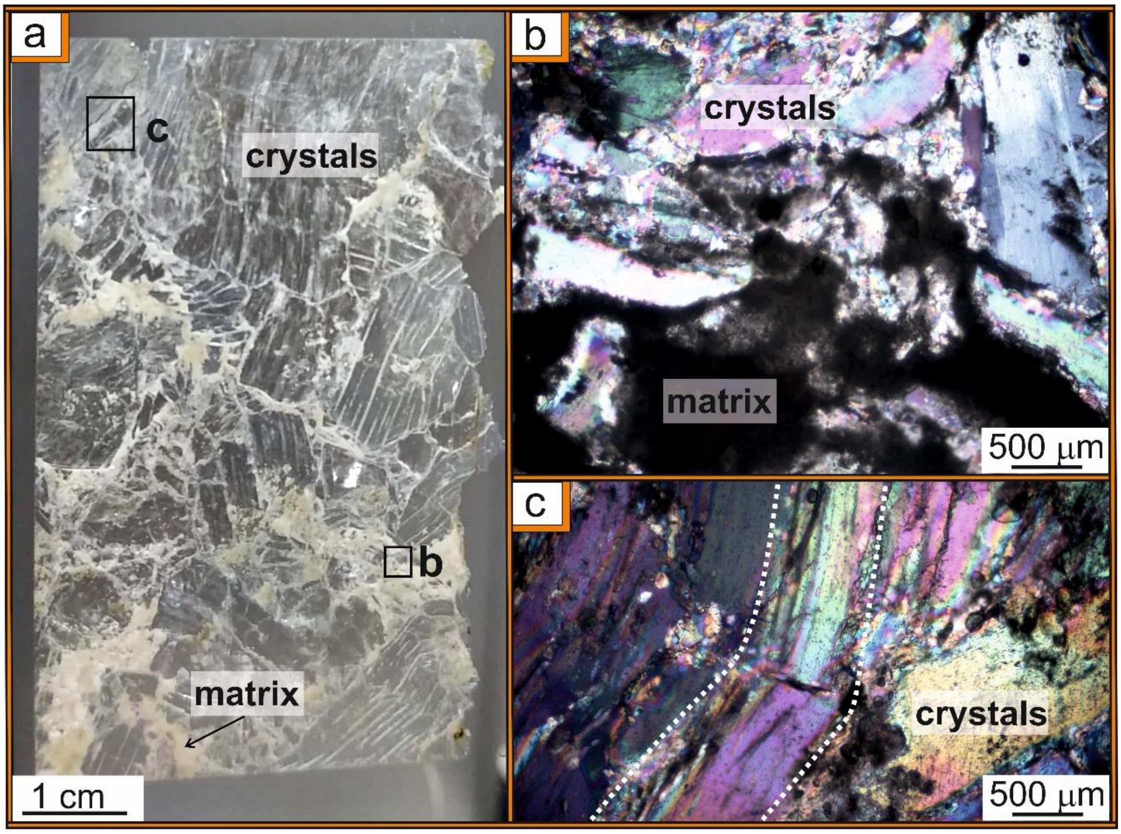

Figure 2.32. a) *Be 01-17* showing fractured crystals and brown matrix; b) and c) details of the crystals fractured and folded (c -white dotted lines) immersed in matrix.

2) The sample *Be 03-17* is made up of tabular and hexagonal crystals (< 1 cm in size), fractured and folded and immersed in a clear brown-red-orange matrix (Fig 2.33a-c). The crystals, show [120] and [$\bar{1}$11] face, chaotic orientation and the twin plane well visible (Fig 2.33b). Transparent and red matters have been observed throughout the sample.

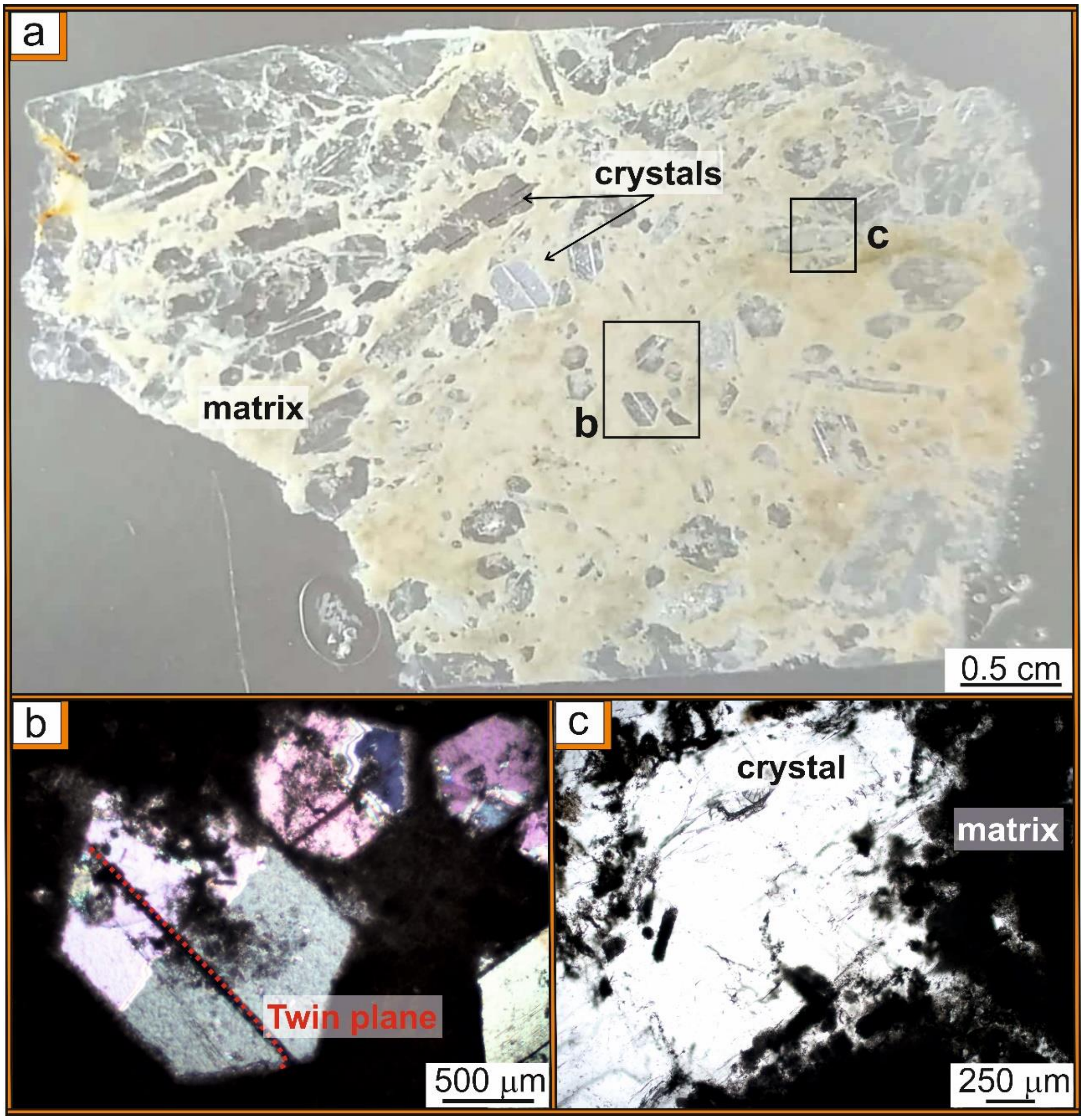

Figure 2.33. a) *Be 03-17* sample made up of crystal and matrix; b) showing hexagonal crystals [$\bar{1}$11] with the twin plane (red dotted line) immersed in brown matrix (c).

Petrographic observations of the samples *Be 01-17* and *Be 03-17* highlight some doubts about the crystals that appear fractured, folded and immersed in the matrix; therefore, it was considered necessary to carry out Raman analyses on the crystals and matrix.

3) The sample *Be 05-17* is made up of small crystals (a few millimetres in size) separated by horizontal thin layers of brown-red materials (Figure 2.34a-b). The crystals are fractured and show [120 and$\bar{1}11$] faces, chaotic orientation and different shapes - elongated, pentagonal and irregular. Transparent and red matters have been observed throughout the sample.

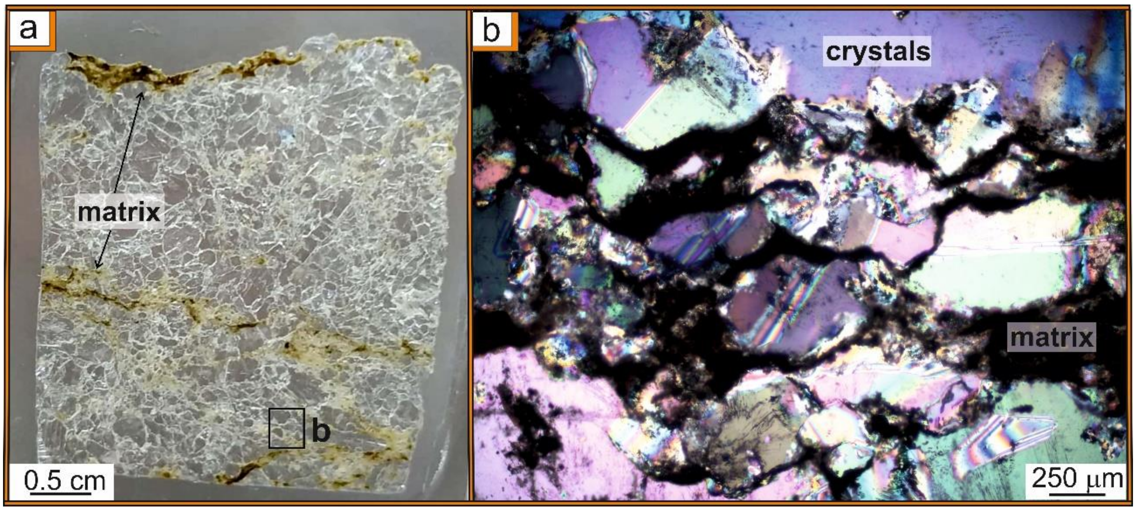

Figure 2.34. a) Be 05-17 showing crystals with chaotic orientation separated by thin layers of brown matter; b) detail of fractured crystals (XPL).

2.7 Organic matters investigation

In the halite and selenite crystals, trapped organic matters display a considerable range of colour, morphology, abundance and distribution. Under UV light, they can show from very strong to faint blue, red or green fluorescence.

Petrographic and SEM observation highlights nine different organic matters types. These materials have been compared with the literature data and reveal the presence of:

(1) transparent matters with filamentous morphology. When they are found immersed in clay aggregates are distributed individually or in groups. Show very strong blue fluorescence under UV light. They could be blue microalgae belonging to "***Oscillatoriales***". They are well visible through optical microscope (Figure 2.35a-a_1-b-b_1) and SEM (Figure 2.35$_n$); They are commonly found at most latitudes in shallow and turbid lakes, where they can tolerate continuous mixing of the water column (Reynolds *et al.*, 2002).

(2) transparent matters with rounded or irregular shape with individually arrangement. Display very strong green fluorescence under UV light. They could be green microalgae belonging to ***"Chlorophytas"*** (Figure 2.35c-c$_1$); They live mainly in fresh water (Waggoner, 1995);

(3) red matters with rounded or irregular shape with individually distribution. Display very strong red fluorescence under UV light; They could be red microalgae belong to "***Rhodophyta***" (Figure 2.35d-d$_1$). They contain a variety of pigments (Guiry, 1987; Waggoner, 1995). The most important pigment is phycoerythrin, which provides these algae with their red pigmentation by reflecting red light and absorbing blue light. Red algae are found around the world, from polar waters to the tropics, and are commonly found in tide pools and in coral reefs. They also can survive at greater depths in the ocean than some other algae, because the phycoerythrin's absorption of blue light waves, which penetrate deeper than other light waves do, allows red algae to carry out photosynthesis at a greater depth;

(4) red/orange matters with rounded morphology and distributed in colonies. Show very strong red fluorescence under UV light. They belong to "***Dunaliella cells***" (Figure 2.35e-e$_1$); this interpretation was confirmed by the Raman analysis, used because the dunaliella cells were very shallow, that revels presence of Carotene, typical pigment of these organisms (see *Appendix A_5* for spectrum of Carotene pigment). They are photosynthetic green algae, characteristic for their ability to outcompete other organisms and thrive in hypersaline environments. They can accumulate relatively large amounts of β-carotenoids and glycerol. Raman spectroscopy carried out of these cells has highlight carotenoids (Sankaranarayanan *et al.*, 2014);

(5) green or yellow matters with rounded morphology and distributed in colonies. Green matters show strong red fluorescence, while yellow matters do not emit fluorescence (Figure 2.35g). They could be green/yellow algae colonial belonging to "***Nannochloropsis*** or ***Chroococcidiopsis***" (Figure 2.35f-f$_1$-g). Some members of the genus are known for their ability to survive harsh environment conditions, including both high and low temperatures, ionizing radiation, and high salinity. Organisms capable of living in such harsh conditions are referred to as extremophiles (Cumbers & Rothscild, 2014);

(6) violet matters with rounded morphology and distributed in colonies. Don't display fluorescence; They could be "***Globus geosporum spores (conidium)"***. They are well visible through optical microscope (Figure 2.35h) and SEM (Figure 2.35o). They are widely distributed, with many species found in temperate regions. The conidia are dark brown to black when mature, paler at young, spherical to subspherical (David *et al*., 2005);

(7) Foraminifera emitting from strong to none fluorescence. They have multilocular shells (Figure 2.35i – 2.35i_1- 2.35l) and live in mixing zone between 0 and 60 m depth;

(8) brown/orange matters are clumped and create thin patinas. They do not fluorescence. They could be ***biofilm structures of cyanobacteria*** not well recognised (Figure 2.35m);

9) SEM observation revels the presence of: ***Emiliana huxleyi and Calcidiscus Leptoporus*** (coccoliths - Figure 2.35p-q), (Loeblich & Tappan, 1978) and ***Radiolarian*** (Figure 2.35r), they are marine plankton that prefer live above 100m;

In general, microalgae live in basin with temperature up to 35°C, while the presence of carotenoids and phycoerythrin pigments produced by photosynthesis processes could be designate a marine environment no deeper than 150 m.

In halite samples prevail blue, green, green/yellow and red microalgae; in the selenite samples from the Marcellinara quarry all organic matters types are present, while in the selenite sample from the Benestare quarry brown/orange matters are dominant while blue and green microalga are present in a minor amount.

In the Table the different organic matter types observed in the several facies are reported (Table 4).

.

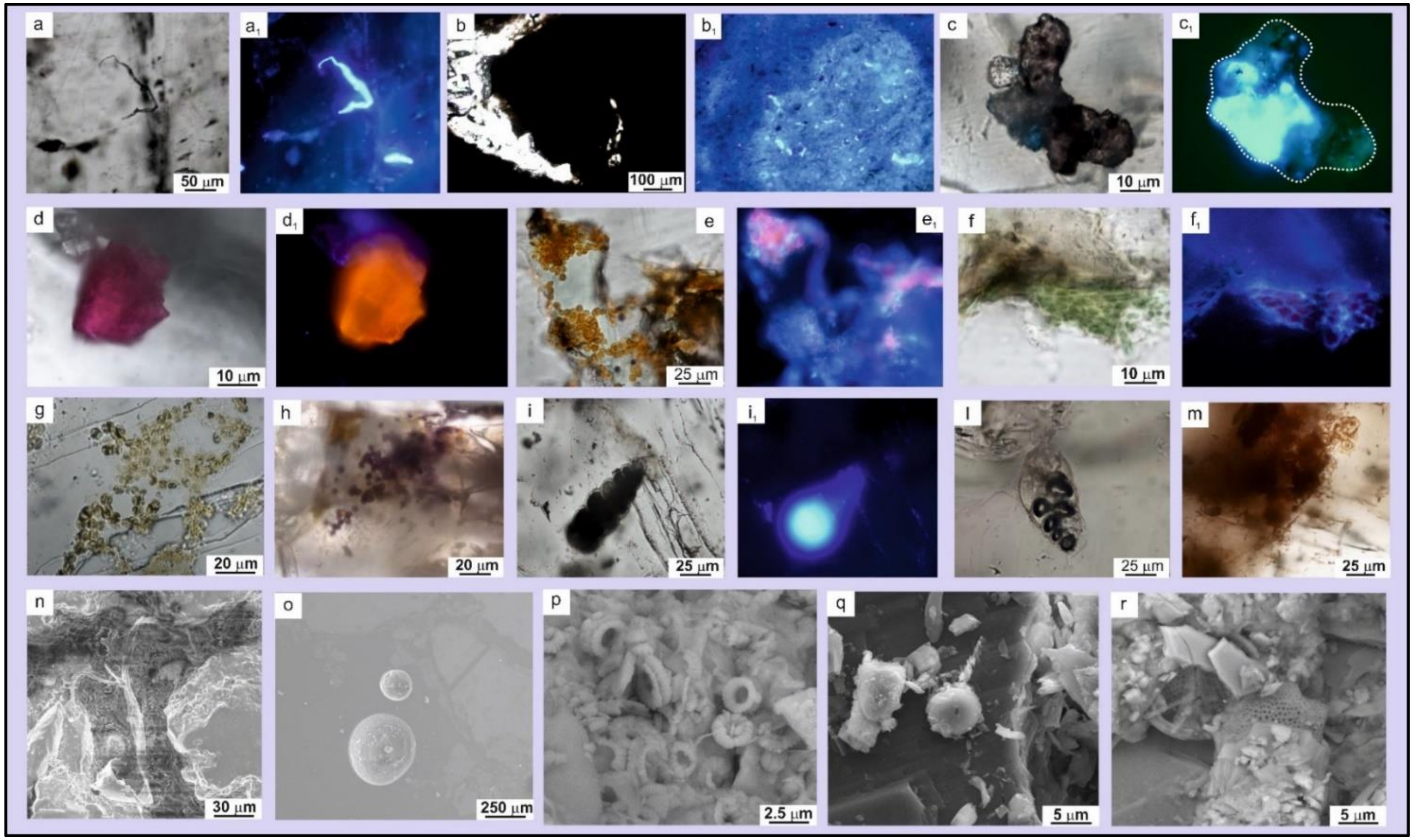

Figure 2.35. Organic matters observed through Ultra violet light and SEM (see text for description). (a) and (a_1) blue microalga (Oscillatoriales) emitting strong blue fluorescence, sometimes associated with clay aggregate (b) and (b_1); (c) and (c_1) green microalga showing green fluorescence (Chlorophytas); (d) and (d_1) red microalga displaying red fluorescence (Rhodophyta); (e) and (e_1) green microalga showing red fluorescence (Dunaliella cells); (f) and (f_1) green microalga emitting red fluorescence (Nannochloropsis or Chroococcidiopsis); (g) green/yellow microalgae (Nannochloropsis or Chroococcidiopsis); (h) Globus geosporum spores; (i), (i_2) and (l) foraminifera with blue fluorescence; (m) biofilm structures of cyanobacteria; (n) and (o) are respectively Oscillatoriales and Globus geosporum spores observed through SEM; (p) and (q) Emiliana huxleyi and Calcidiscus Leptoporus (coccoliths); (r) Radiolarian.

	Facies and Sampled Areas							
Organic matter types	**Halite crystals from the Crotone Basin**			**Selenite crystals from the Catanzaro Trough**			**Selenite crystals from the Ionian Basin**	
	Banded	***White***	***Transparent***	***Banded***	***Giant***	***Branching***	***Banded***	***Branching***
Oscillatoriales	Yes	Yes	Yes	Yes	Yes	Yes	Yes	Yes
Chlorophytas	Yes	No	No	Yes	Yes	Yes	χ	Yes
Rhodophyta	Yes	Yes	Yes	Yes	Yes	No	Yes	Yes
Nannochloropsis or Chroococcidiopsis	Yes	Yes	Yes	Yes	Yes	No	No	No
Dunaliella cells	Yes	Yes	Yes	Yes	Yes	No	No	No
Globus spores	No	No	No	Yes	Yes	No	No	No
Foraminifera	No	No	No	Yes	Yes	No	No	No
Biofilm	No	No	No	Yes	Yes	No	No	No
Coccoliths	No	No	No	Yes	Yes	No	No	No
Radiolarian	No	No	No	Yes	Yes	No	No	No

Table 4. Different organic matter types observed in the several facies from the Crotone Basin, the Catanzaro Trough and the Ionian Basin.

A good environment reconstruction depends on the quality of sampling and petrographic observation. Sampling must always be undertaken with a strong focus on crystals growth direction while the petrographic observation must be undertaken with detail and attention. The combination of a good sampling and petrographic observations can therefore provide important information about the crystal’s formation environment, their evolution during burial and exhumation and on aquatic biological life.

2.8 Summary and discussions

2.8.1 The halite facies

The Crotone Basin records three facies: *banded*, *white* and *transparent*. Five crystals have been sampled from different facies and areas.

A brief summary of all facies with their environment interpretation.
1) the <u>banded facies</u> sampled in the Coste del sale (*Cs 04-17*), Zinga (*Zi 07-17*), and Verzino (*Ru 17-17* and *Ru 19-17*) consists of microcrystalline halite (~5mm in length) showing competitive crystals growth, mosaic texture and relict primary structures. These four features provide us information on (i) origin, (ii) growth, and (iii) burial.

<u>Origin</u>*: Why microcrystalline appearance?*

According to the literature data, these crystals grow via solar concentration (called *rafts* and *pyramidal hopper* crystals) at the air-brine interface when surface water salinities are suitable (saturation condition) where trapping liquid and air bubbles in primary inclusions (see chapter 3 for fluid inclusions description), indeed, during the high exposure to sunlight, the temperature can be very hot and allow the precipitation and deposition of halite; the fast deposition of halite (short time) testify stable pycnocline.

<u>Growth</u>*: Why these deposits show competitive crystals growth?*

When the rafts become heavy fall down to the bottom of the basin (Warren 1999, 2006) and continue to grow competitively undisturbed by (no wind or waves action that could break them or transport them elsewhere – below wave base – relative deep zone). This process is favoured by clay matters that cover the crystals and drive them to competitive growth (sometimes with chaotic arrangement). At this time may occur syn-depositional diagenetic processes as the dissolution phenomena (initially along grain boundary and subsequently branched off to centre) and halite cement precipitation.

<u>Burial</u>: *Why crystals display mosaic texture?*

After burial, crystals ‘optimize’ their size, shape and orientation in order to minimize energy. Mosaic texture is a typical feature of pressures of burial (Stanton & Gorman, 1968). If dissolution and recrystallization are not too high, relict primary structures as corner and chevron habit can be preserve.

The four samples collected show similar features, with the difference that *Cs 04-17*, *Zi 07-17* and *Ru 17-17* display more relict primary structures and minor fracture and dissolution phenomena that *Ru 19-17*. This is confirmed by the fact that Coste del Sale is the only area where is possible to see the Ponda Clay Formation below the deposit which means poor recrystallization out by diapiric rise.

2) the <u>white facies</u> sampled in Zinga (*Zi 11-17*) consists of macrocrystalline halite showing milky (enriched in fluid inclusions) and white (impoverished in fluid inclusions) bands visible to the naked eye. Alternating bands define primary structures called as “chevrons shape” that indicates edges growth (Warren, 1999, 2006). Sometimes show sharp and curved dissolution surface along the edges. The chevron shapes are typical of crystals that are grew on the bottom basin, moreover testify growth pulses reflecting changes in crystal precipitation rate induced by short-term changes (daily) or seasonal in salinity (pycnocline oscillation –relatively shallow) on the subaqueous floor of the brine basin (Warren, 1999, 2006). Rare evidence of dissolution and recrystallization (fractures) processes which have not obliterated the primary structures, allow us to suppose that the deposit is not recrystallized. This deposit could be in almost totally in place or have undergone only a slight burial**.**

3) the <u>transparent facies</u> sampled in Zinga (*Zi 12-17*) consists of massive transparent macrocrystalline halite and is not discussed in previous literature. It shows mainly pure halite with local fluid inclusions trails, clay matters, opaque halite (by dissolution phenomena) and rare fractures filled by secondary fluid inclusions and/or clay matters. It

seemed recrystallized, but the presence of primary fluid inclusions (see chapter 3 for fluid inclusions description) confirm the primary origin. Pure halite is not the product of a complete recrystallization but is associated with a growth in a stable environment not subject to excessive pycnocline oscillations.

The banded, white and transparent facies trapped blue, green and red algae during their growth. Red (*Rhodophyta*) and green algae (*Dunaliella cells and Nannochloropsis or Chroococcidiopsis*) can respectively tolerate change of salinity and high salinity, blue algae (*Oscillatoriales*) can accept continuous mixing of the water column, while green algae (*Chlorophytas*) live mainly in fresh water. So probably, the blue and green algae were transported in the basin from currents or lived in the water during stage at minor salinity and then died for salinity increasing.

2.8.1.1 Growth rate

Schreiber & Hsü (1980) estimated a growth rate of approximately 10 m per 1000 years based on modern basins observations. This could be valid for the banded and the transparent facies (stable pycnocline) but, for the white facies that show chevron shapes (day or seasonal pycnocline oscillations), can be hypothesized different growth rates. In fact, in the white facies have been counted 56 pulses in 2.5 cm of crystal. Considering *day oscillations*, the growth rate could be approximately 7.3 m per 1000 years, while supposing *seasonal oscillations* the growth rate could be approximately 65 m per 1000 years testified a fast (daily) or low (seasonal) depositional rate in relation to climate temperature and pycnocline oscillation.

These results improve the results obtained by Lugli *et al.*, (2007), adding a new facies (transparent) and proving mainly that the banded facies is not completely recrystallised.

2.8.2 Selenite facies (Marcellinara quarry)

The Marcellinara quarry records three facies: *banded*, *giant* and *branching*. Fourteen crystals have been sampled to investigate the basin evolution and to understand depositional mechanisms.

A brief summary of all facies with their environment interpretation.

a) From petrographic observation *branching facies* (*Ma Br*) does not appear primary in origin. Branching facies observed in the Lower Gypsum (see Manzi *et al*., 2009; Lugli *et al*., 2010), show selenite crystals oriented in a preferential direction, organized in irregular nodules and separated by a fine carbonate sediment or a gypsum matrix, (the orientation of the crystals indicates that it grew laterally in an underwater environment subject to currents), contrariwise the branching facies record in Marcellinara appear reworked and subsequently immersed in a matrix made up of gypsum fragments and deteriorated blue and red algae.

b) *Giant facies* (sample *Gi 01*) has been identified in the sector 1 like as blocks. In other Mediterranean basin, this facies was recorded only in the Lower Gypsum (Manzi *et al*., 2009; Lugli *et al*., 2010). They formed during the maximum brine level (stable pycnocline) permanent covered of Ca sulphate-saturated brine (Babel, 2004) and vertical space and time for undisturbed syntaxial crystal growth. The high salinity is shown by *Chroococcidiopsis* (living in high salinity environment), observed in the crystal.

c) *Banded facies* has been recognised in the sector 4 and 5 like as selenite layers separated by dissolution surfaces, breccia layer and/or thin argillaceous/calcareous laminae.

> **(i)** The banded layers indicate supersaturation condition and minimum brine level; the crystals can show competitive growth and vertical or oblique twin plane (folded and fractured crystals). The folded crystals are associated with brine currents, while competitive growth is related with a faster growth rate.
>
> **(ii)** the dissolution surfaces testify pycnocline variations associated with unsaturated condition caused by a number of factors such as brine dilution (inflow of freshwater – winter dilution) or the deposition of sediment on the crystal apices (Ortì, 2011);

(iii) the breccia layers probably are derived from sub-aerial exposure (lowering of the brine level) and subsequent erosion of other selenite crystals which, due to gravitational flows, were deposited (like as chaotical deposit) on top of the selenite layer; the low corrosion rounding of the breccia layers suggests a minimal transport.

(iv) the thin argillaceous/calcareous laminae (1-2 mm in size) indicate unsaturated condition. They become poikilitically enclose within the selenite during the subsequent growth episode.

2.8.2.1 Depositional reconstruction of the two main deposits

(1) The Selenite deposit observed in the sector 4 may be so interpreted (from bottom to top - Figure 2.36):

(a) *Ma 27-17* (~10 cm in size – [120] face) was formed in a quiet environment without competitive crystal growth able to doing develop a vertical twin plane and microfacies well recognizable. (b) Subsequently, *Ma 27-17* has been covered by breccia layer. After its deposition the basin was return to its initial stability conditions, (c) forming a new selenite layer (*Ma 24-17* sample*). Ma 24-17* (~20 cm in size – [010] face) begins its growth in a competitive manner generating the splitting of the twin plane. Competitive growth is associated to a faster growth rate that generates fractures within the crystal and microfacies not well developed. Probably, the higher growth rate is associated with a brine richer in calcium sulphate due to the breccia below, as the broken and dispersed selenite crystals (immersed in the breccia) are more subject to dissolution. Vertical growth of the two twin planes does not indicate brine movement (flow phenomena). (d) Subsequently, crystal grew more slowly favouring well distinguishable microfacies returning to a condition of standard saturation. (e) Between *Ma 24-17* and *Ma 19-17* (<10 cm in size – [010] face) deposition, there is a moment of non-growth associated with the dissolution of the upper part of the crystals and deposition of the breccia layer. The sequence selenite/dissolution/breccia is repeated cyclically.

This deposit records an unstable formation environment with abrupt changes in just 70 cm.

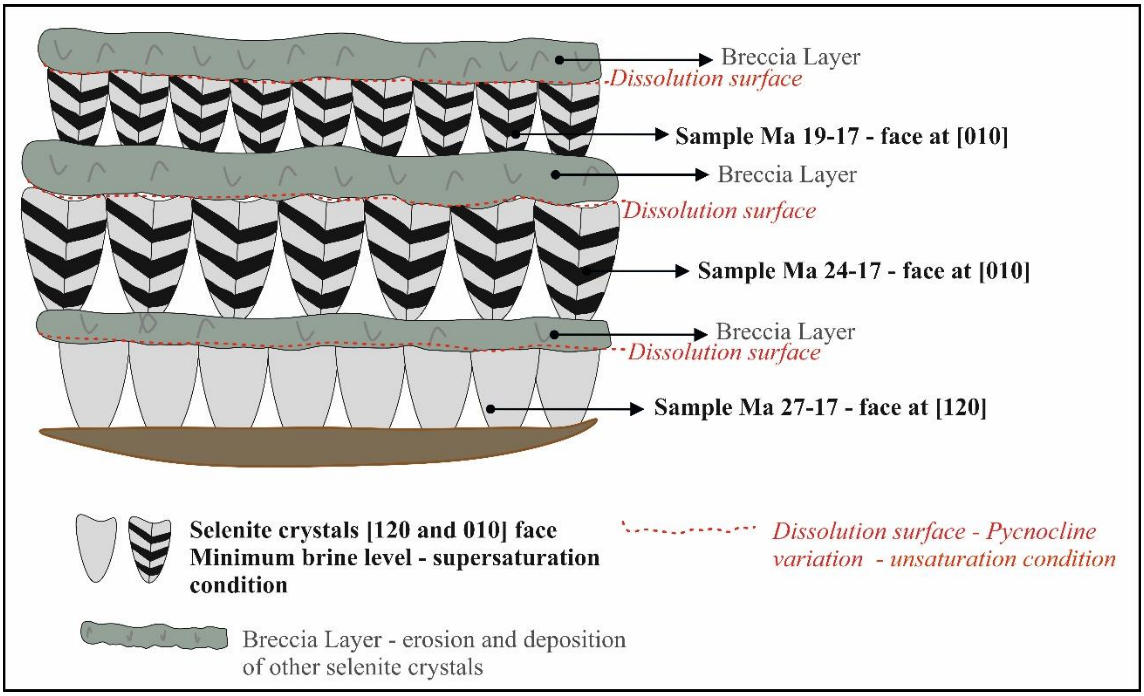

Figure 2.36. Schematic reconstruction of the deposit observed in the sector 4 showing the cyclic repetition between the banded facies – dissolution surfaces – and breccia layers (see the text for detail description).

<u>**(2)** The Selenite deposit observed in sector 5 </u>may be so interpreted (from bottom to top-Figure 2.37):

a) First selenite cycle (~40 cm in size) - *Ma 01-17* sample:

- [010] face
- formed in a quiet environment
- no competitive crystal growth
- vertical twin plane
- microfacies are well recognizable.

b) Second cycle (~56 cm in size) - *Ma 02-17* sample:

- [010] face
- formed in unstable environment
- shows two sub-cycles made of crystals 42 cm and 15 cm in size
- first sub-cycle shows no competitive crystal growth
- second sub-cycle displays competitive crystal growth that generate the splitting of the twin plane
- Microfacies are not well developed
- oblique twin plane.

(c) Third cycle (~12 cm in size) - *Ma 03-17* sample:

- [010] face
- formed in a quiet environment
- no competitive crystal growth
- vertical twin plane
- microfacies are well recognizable.

(d) Fourth cycle (~6 cm in size) - *Ma 04-17* sample:

- [120] face
- formed in a quiet environment
- competitive crystal growth
- vertical twin plane
- microfacies thin and very close together.

e) Fifth cycle (~6 cm in size) - *Ma 05-17* sample:

- [120] face
- formed in unstable environment
- show competitive crystal growth
- oblique twin plane
- abundant fractures
- oblique twin plane.

f) Sixth cycle (~9 cm in size) - *Ma 06-17* sample:

- [120] face
- formed in a quiet environment
- no competitive crystal growth
- vertical twin plane
- microfacies well recognizable.

g) Seventh cycle (~26 cm in size) - *Ma 07-17* sample:

- [120] face
- formed in in unstable environment
- no competitive crystal growth
- microfacies well recognizable
- oblique twin plane.

h) Eight cycle (~16 cm in size) - *Ma 08-17* sample:

- [120] face
- initially growth in a quiet environment – without competitive crystal growth
- progressively become competitive with curvature of the twin plane and abundant fractures.

i) Ninth cycle (~16 cm in size) - *Ma 09-17* sample:

- [010] face
- formed in a quiet environment
- no competitive crystal growth
- vertical twin plane
- microfacies are well recognizable.

This deposit (1.70 in length) does not records abrupt changes (breccia layers) which testifies a stable formation environment subject only to pycnocline oscillations. The sequence selenite/laminae are repeated cyclically.

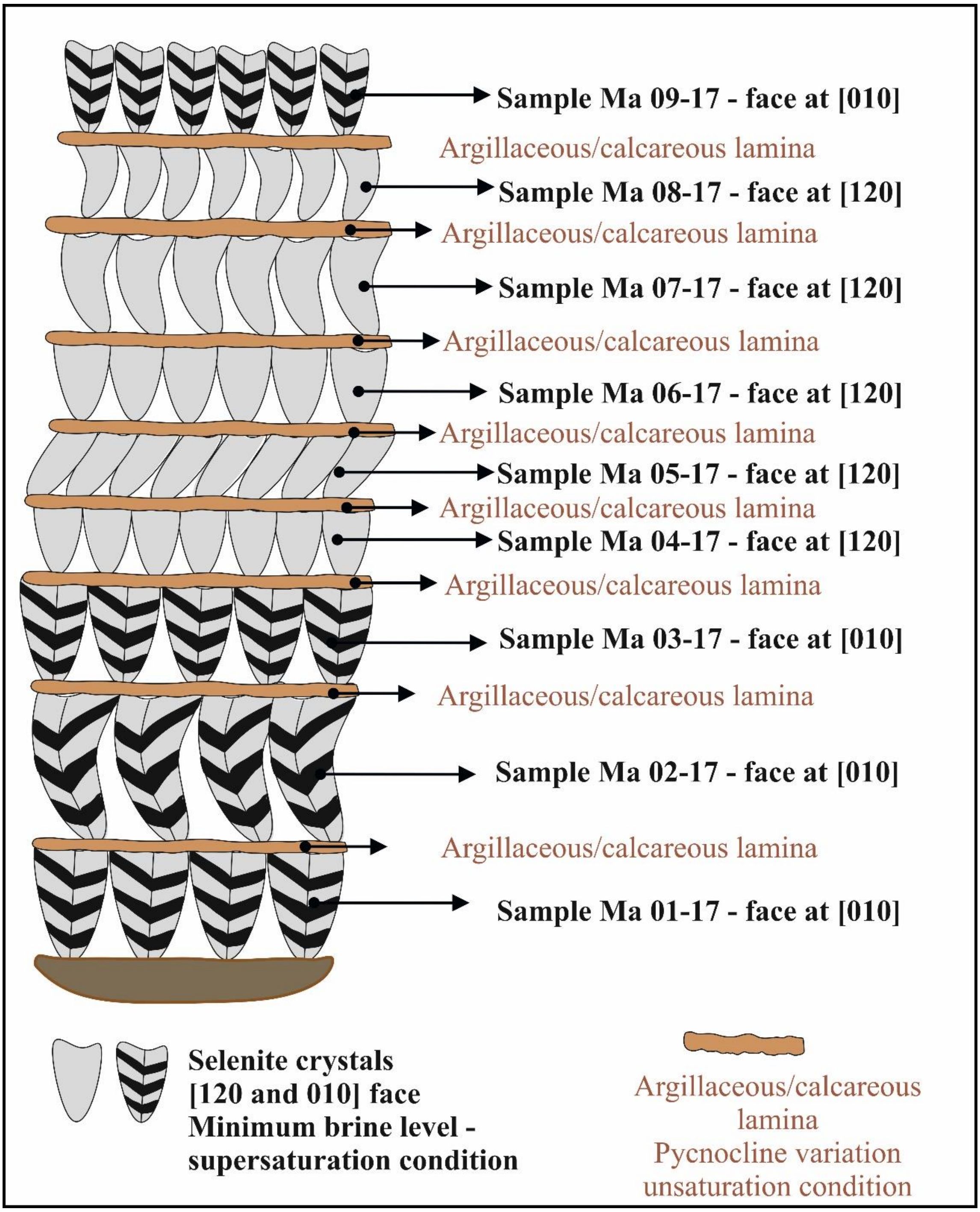

Figure 2.37. Schematic reconstruction of the deposit observed in the sector 5 showing the cyclic repetition between the banded facies and the thin argillaceous/calcareous laminae (see the text for detail description).

2.8.2.2 Middle and high frequency cyclicity

All sample from the banded and giant facies show cloudy and clear intervals (microfacies), and organic matters. The cloudy intervals (~2-4 mm in size) are enriched in organic and inorganic matters and show parallel cleavage plans; they growth in a disturbed system affected by fresh water inflow that generates crystallographic irregularities favouring the entrapment of the inclusions (see chapter 2 for Fluid inclusions evidences). In contrast, the clear intervals (between 2 and 5 mm in size) are impoverished in organic and inorganic matters and show fractures parallel and perpendicular to the twin plane (sin- and post-depositional). They growth in a stable environment.

The morphology of the twin selenite crystals is particularly appropriate for hosting the organic matters that live in the water column, which are trapped due to the rapid selenite growth rate. The abundance and diversity of organic matters found in the cloudy intervals can testify seasonal episode of ecological bloom. If cloudy and clear are associated with seasonal episodes means that cloudy intervals formed during wet phases (ecological bloom), while clear intervals formed during arid phases, indeed they trapped mainly blue (Oscillatoriales) and green microalgae (Chlorophytas) that did not tolerate high salinity. This hight-frequency cyclicity (dry and wet season) could be confirmed by the millimeter dimensions of the microfacies (av. 4 mm in size). Another data is provided by Schreiber & Hsü (1980), (data of modern saltine), which estimate a growth rate of approximately 1-2 m per 1000 year, so considering a crystal about 6 cm in size can hypothesize that it formed at least in 60 years; while the cloudy interval (av. 3 mm in size) formed in~ 3 years. This would provide year with different climate (more or less humid).

Instead, using the data provided by Komarov *et al.*, 2000 (they studied gypsum growth into a thermostated at 18°C and 30°C) and considering a basin with a temperature of about 18°C, a crystal of 6 cm in size formed in ~1.4 months (42 days), while cloudy interval in~ 2 days. Assuming 30°C temperature crystal (6 cm in size) formed in ~14 days months, while cloudy interval in~ 17 hours. This data would confirm a daily origin.

In both models, is difficult establish if the clear intervals formed slower or faster than cloudy intervals, because the presence few inclusions suggest a slower growth, in contrast the high salinity suggests a faster growth that cloudy intervals.

We consider the data of Schreiber & Hsü,1980 more reliable for the development times necessary for the ecological bloom.

If on one side, the microfacies testify high-frequency cyclicity the selenite layer interbedded by thin argillaceous/calcareous laminae could be associated with middle-frequency climatic oscillation (due to the small size of the laminae), however, this assumption is difficult to prove.

Summary of the hypothetical growth rates for the nine selenite cycles (sector 5) proposed by different authors (Table 5), not considering the two intervals.

Cycles	**Cycle thickness (cm)**	**Schreiber & Hsü, 1980 (years)**	**Komarov *et al.* 2000**			
			18°C		**30°C**	
			month	**day**	**month**	**day**
First	40	400	9.4	286	3.1	94.8
Second	55	550	12.9	394	4.3	130.4
Third	12	120	2.8	86	0.9	28.4
Fourth	6	60	1.4	43	0.5	14.2
Fifth	6	60	1.4	43	0.5	14.2
Sixth	9	90	2.1	64	0.7	21.3
Seventh	26	260	6.1	186	2.0	61.6
Eight	16	160	3.8	115	1.2	37.9
Ninth	16	160	3.8	115	1.2	37.9
Tot	**186 cm**	**1860 y**	**43.8**	**1331**	**14.5**	**441**

2.8.3 The selenite samples (Benestare quarry)

All selenite samples from the Benestare quarry display crystals fractured and folded with chaotic orientation. These crystals do not appear belonging to the banded and branching facies but they seem reworked and subsequently deposited and immersed in a brown matrix. The presence of the twin plane, especially in the sample *Be 03-17*, suggests that these are crystals of selenite (fractured) and not gypsum primary, as it should be per definition the branching facies.

The Raman spectroscopy conducted on crystals and matrix showed that crystals are made of gypsum, while the matrix is formed by dolomite; though, the gypsum spectrum covers the other peaks. In addition to the dolomite, the matrix is made up of blue and red microalga deteriorated and biofilm structures of cyanobacteria, which indicate an environment of formation similar to that found in the Branching facies from the Marcellinara quarry

CHAPTER 3. Fluid inclusion petrography

3.1 Introduction

In nature, there is no a ‘perfect’ crystal, as all crystals contain some imperfections that occur during crystal growth. These imperfections can occur in the form of occluded liquids, solid and vapour and they can provide a valuable key to understanding of the physical and chemical processes during their grow. During crystal growth the trapped fluid may be vapour, liquid or supercritical fluid, and the composition can range from essentially pure water to high salinity, brines of various salt composition. If a fluid phase is present during crystal growth, some of the fluid may be trapped as imperfections in the growing crystal, these are called fluid inclusions (FIs). Fluid inclusions are a common feature in minerals. Primary fabrics are often defined by concentrations of FIs along growth planes in the evaporitic rocks. In general, the FIs study is very important because provide information on origin (syn-depositional versus burial), temperature, pressure and composition of the fluid in which the crystal growth.

The pioneer of FIs work was Henry Clifton Sorby in the mid-1800s that elevated the status of fluid inclusions from simple scientific curiosity to objects of considerable scientific merit and importance. Unfortunately, the importance of this study was not realized until the early 1950s.

3.1.1 FIs classification and study

There are many ways to classify fluid inclusions (Goldstein, 2003) such as the classification based on the differing proportions of solids, liquids and vapour but the most useful classification schemes relate the timing of formation of the inclusion to that of the host mineral. Accordingly, FIs are classified as:

- *Primary fluid inclusions (P):* form when fluid is trapped on the active growing crystal surface; these FIs contain remnants of the surface brines from which crystal precipitated, and, therefore, hold potentially useful information about surface hydrochemistry in the past (Robert & Spencer, 1995).

- *Secondary fluid inclusions (S):* are easily identified if they occur parallel to fracture that crosscuts the entire crystal (fluids trapped enter the fracture). They are generally distinguishable from P inclusions on the basis of their distribution patterns, relationships to the host minerals and microfractures;

- *Pseudo-secondary fluid inclusions (PS):* are assumed to develop in a similar way to secondary inclusions, the only difference is that fracture and healing take place before crystal growth has terminated. They consist of an intermediate generation between P-and S-inclusions.

There are two important concepts in FIs studies: the *homogenization temperature* and the *fluid inclusion assemblage*:

- the *homogenization temperature* records of the water temperature at which the crystal grew and it is used for paleoclimate studies because there is a direct relationship between water temperature, air temperatures and climate. Homogenization temperatures can also guide the design of conditions used for culturing ancient microorganisms trapped inside halite (Lowenstein, 1998, 2012).
- *Fluid inclusion Assemblage* (FIA) was introduced by Goldstein & Reynolds (1994) to help to determine the temporal classification of FIs. The FIA describes a group of fluid inclusions all trapped at the same time, at approximately the same temperature and pressure and in a fluid of roughly the same composition in according with the environment of formation. The FIA, therefore, represents a “fluid event” in the history of the system. Utilizing appropriate petrographic analyses, it can be determined if all inclusions were trapped at the same time (Goldstein & Reynolds, 1994).

In general the trapped phases can be classified in: monophase liquid (L), monophase vapour (V), two-phase liquid rich (L+V), two-phase vapour rich (V+L), multiphase solid (S+L±V with S<50%), multi-solid (S+L±V with S>50%), immiscible liquid ($L_1+L_2\pm V$) and glass (GL±V±S), (Shepherd, 1985). Another important measurement for two-phase FIs is the degree of fill (F) defined as the volumetric proportion of liquid (V_L) relative to the total volume of the inclusion (V_{TOT}): $F=V_L/V_{TOT}$. FIs shapes are highly variable and are partly controlled by the crystallography of the host mineral (Figure 3.1), moreover

Roedder (1984) noted that the number of inclusions trapped in a crystal increases with decreasing inclusion size.

If the inclusion volume changes after trapping or have lost or gained components, or both (Bodnar, 2003), the inclusion is Re-equilibrated. The type of reequilibration that occurs is a function of many factors, among which:

- structure and composition of the host phase;
- inclusion size;
- fluid composition.

The reequilibration phenomena include: stretching, leakage or partial decrepitation and decrepitation.

<u>Streacking</u> is a term that is generally used to describe fluid inclusions whose volume has changed with poor or no discernible loss of fluid from the inclusion. Stretching usually results when an inclusion reequilibrates in a low strain rate environment in which the host phase deforms plastically, and is more common in softer minerals than in harder minerals. *Leakage or partial decrepitation* occur when, due to increase of the strain rate, crystal generates fractures adjacent to inclusions, with partial loss of fluid by advection along the microfractures.

Decrepitation occurs when the extent of fracture is so intense that all fluid is lost, leaving an empty, dark cavity in the host phase.

Another process is the *Necking down* that involves dissolution and re-precipitation of the host phase to reduce the surface area and produce many smaller inclusions from the original larger inclusion. This process is often referred to as maturation in the fluid inclusion literature (cf. Bodnar *et al*., 1985) because the inclusion shape tends to become more regular over time.

This chapter presents the results of fluid inclusions investigation in the halite and selenite deposits from the Calabria region, especially on:

-primary FIs (morphology, distribution and type) to understand environment of formation (*e.g* climate);

-secondary FIs (distribution) to understand the history evolution post and sin-depositional;

-organic matters trapped in inclusions to reconstruction the environment in which the crystals grew.

3.2 Fluid inclusion petrography

Fluid inclusion petrography focus on: types, size, shape, abundance, distribution, relationship to the crystal faces, presence of organic matters trapped in inclusions and reequilibration and necking-down processes. Primary, secondary and pseudo-secondary FIs are observed in all samples and show a several range of shape and Type.

In fact, optical examination indicates three Type of primary inclusions (P-Type 1, 2 and 3), one type of secondary inclusions (S-Type 4) and one type of pseudo-secondary inclusions (PS-Type 5), (see *Appendix B_1* to analytical methods).

In this work, FIs Types observed are:

Type 1 (P) – monophase liquid (L) showing elongated, tabular, dome, hexagonal, triangular, irregular and negative crystal shape (cubic and trapezoidal). These inclusions occur within parallel trails to the crystal growth, in clusters or are dispersed throughout the crystal. Their range in size is from 5 to 150 μm in halite crystals and from 5 to 120 μm in selenite.

Type 2 (P) – two-phase liquid rich (L+V). The degree of fill (F) has range between 0.50 and 0.99. Inclusions show elongated, tabular, dome, hexagonal, triangular, irregular and negative crystal shape (cubic and trapezoidal). Type 2 inclusions occur within parallel trails to the crystal growth, in cluster or as individual inclusions. Their range in size is from 5 to 400 μm in halite crystals and from 5 to 136 μm in selenite.

Type 3 (P) – multiphase solid (L±V±S±OM). They are subdivided into three different sub-types:

(1) ***Type 3a*** contain organic matters (L±V+OM);

(2) ***Type 3b*** have trapped solid phases (L±V+S);

(3) ***Type 3c*** contain solid crystals and organic matters (L±V+S+OM).

These inclusions show tabular, elongated or irregular shape and occur in trails or in isolated individuals. Their range in size is from 5 to 200 μm in halite crystals and from 5 to 80 μm in selenite.

(1) Type 3a inclusions contain brown, dark brown, red, orange and yellow matters and show rounded, spotted, elongated or irregular shapes. These inclusions have been observed under Ultra Violet light and show blue, green or red fluorescence. Fluorescence intensity is - between faint and very strong. The fluorescence intensity and colours depend on the type of organic material, on the maturity, quantity and on depth of the FIs within the sample.

(2) Type 3b inclusions contain transparent or light grey solids that show several shapes (tabular, hexagonal, rounded or cubic). Solids have been observed using transmitted light polarizing microscope (XPL). Under XPL show first and second order birefringence colours. These solids can be daughter minerals or captured minerals (see chapter 4). Daughter minerals in FIs are solid phases crystallised from the enclosed fluid after trapping. They indicate saturation of fluid inclusion of the fluid with respect to these phases at the conditions of observation (Roedder, 1984). Captured minerals, instead, are solid phases trapped together with a portion of the fluid. This means that they do not give a constant liquid/solid volume ratio and they are often anomalously large compared to their host inclusion (Shepherd *et al.*, 1985).

Type 4 (S) – monophase liquid (L), monophase vapour (V) or two-phase liquid rich or vapour rich (L±V/V±L) and show various shapes (negative crystal, elongated or irregular). The inclusion occurs within parallel trails to cleavage or along fractures, sometimes cut trails of Type 1, Type 2 and Type 3 inclusions. Their size ranging is from 2 to 20 μm. These inclusions show diffuse stretching, leakage, decrepitation and necking down phenomena.

Type 5 (PS) – monophase liquid rich (L) and monophase vapour (V). These inclusions show mainly negative crystal shape. Their size is generally <10 μm and they occur in parallel trails or clusters.

Secondary and pseudo-secondary FIs provide information on degree of fracture. If FIs are abundant, the crystals show high degree of fracture, if they are less abundant the crystals have medium or poor degree of fracture.

Regarding reequilibration phenomena, two processes are observed: *stretching* (plastic strain) and *leakage* (ductile strain). Reequilibration and necking down process are recognised main in the crystals's core or along their rims. In this work, the terms *faint*, *moderate* and *widespread* are used to quantify the necking down frequency, while *weak* and *strong* to establish his degree of evolution in the time (maturity).

In the following schematic classification (Figure 3.1) detailed characteristics for primary fluid inclusions hosted in halite and selenite crystals are reported.

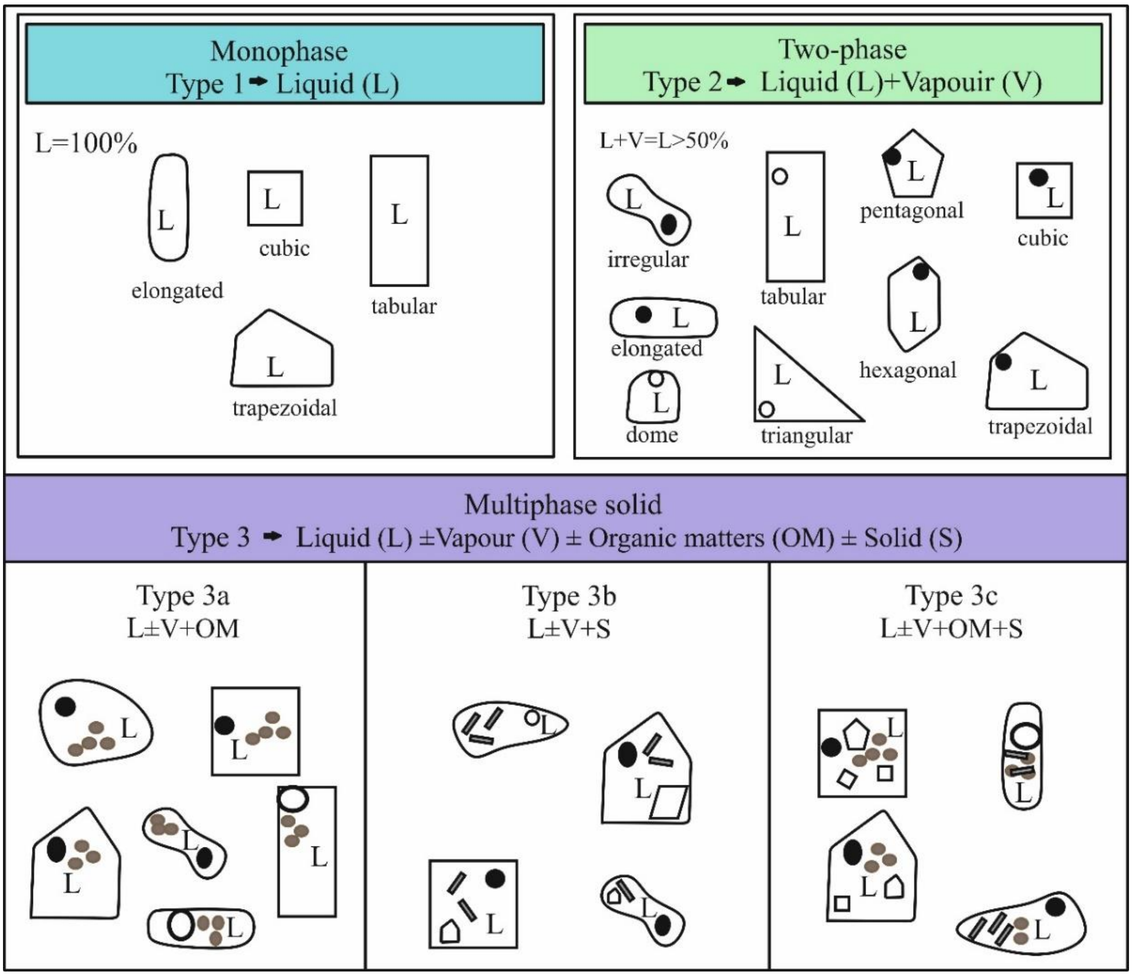

Figure 3.1 Schematic classification showing the FIs phases of the primary FIs recognized in this study. Phases present at room temperature and various morphologies observed are arranged with reference to the amount of liquid (L) and/or vapour (V), solid (S) and organic matters (OM) trapped in the inclusions.

3.2.1 FIs in the halite crystals (Coste del sale, Zinga and Verzino)

In halite samples primary, secondary and pseudo-secondary FIs are observed (Figure 3.1). Primary FIs (Type 1, 2 and 3) run parallel to the faster growth faces (100) and show mainly tabular and negative crystal shapes. Inclusions are distributed in linear trails, in groups or as individual inclusion.

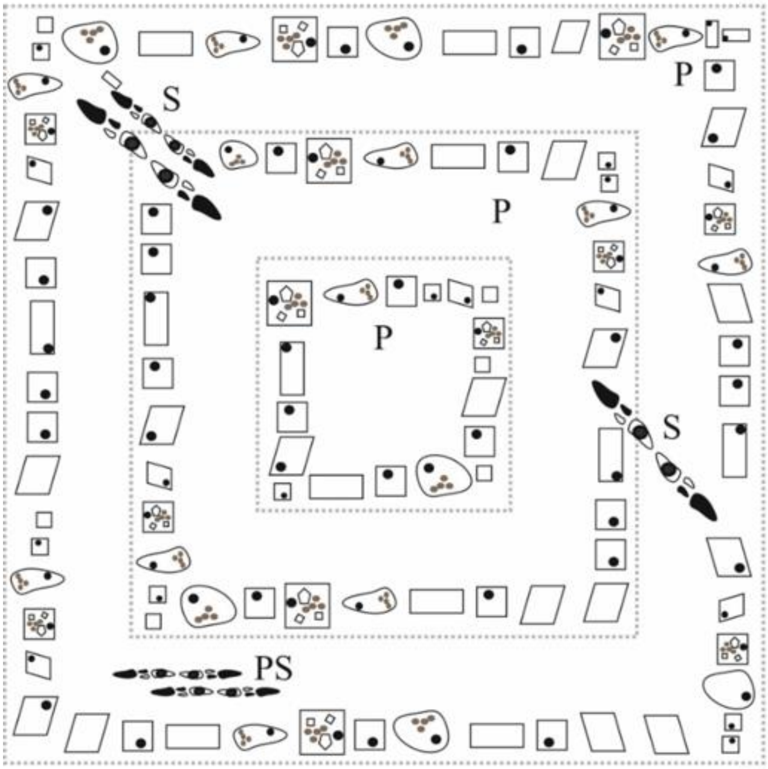

Figure 3.2. Idealized distribution of primary (P), secondary (S) and pseudo-secondary (PS) fluid inclusions showing different type and shape in halite crystal (right).

Secondary FIs (Type 4) are distributed in groups or in trails parallel or perpendicular to the crystal growth. Reequilibration phenomena and Necking down processes is recognised in all samples.

Pseudo-secondary FIs (Type 5) occur in linear trails and show similar features in all samples. The degree of fracture (fractures filled by FIs) is classified in poor, medium, high.

Detailed FIs observations in halite samples from the Coste del Sale, Zinga and Verzino are reported.

(a) Coste del sale:

In the sample *Cs 04-17*, forty-four primary FIs (Figure 3.3) throughout the wafer (8 cm^2 of area investigated on 12 cm^2 off the total surface) are observed: twenty-six Type 1, fifteen Type 2 and three Type 3a inclusions; Moreover, secondary inclusion trails throughout the sample have been observed. Pseudo-secondary FIs are less abundant than primary and secondary FIs. FIs Types observed are:

- **Type 1 – (L)** show elongated, tabular or negative crystal shapes and range in size from 5 to 20 μm (av.~8μm). These inclusions occur within trails parallel to the crystal growth zones or as individual inclusions (Figure 3.4a);

- **Type 2 – (L+V)** show irregular (Figure 3.4b), tabular or negative crystal shapes and range in size between 10 and 100 μm (av.~27 μm), ($F \geq 0.70$). They occur as individual inclusions or in groups associated with FIs Type 1;

- **Type 3a – (L+OM)** show tabular or negative crystal shapes and range in size between 10 μm and 95 μm (av.~50 μm). They occur as individual inclusions. Organic matters trapped within inclusions appear with irregular or rounded shapes and show orange or yellow colours (Figure 3.4c). These materials are distributed along crystal's rims or in the inclusion core. Under UV light show faint blue fluorescence;

- **Type 4 – (V/L and V/L)** display from irregular to negative crystal shapes (size <10 μm) and $F \leq 0.20$. These inclusions are distributed in cluster or in linear trends (Figure 3.4d).

- **Type 5 (rare) – (L/V)** show tabular or negative crystal shapes and have size <5 μm. Their arrangement occurs mainly in clusters.

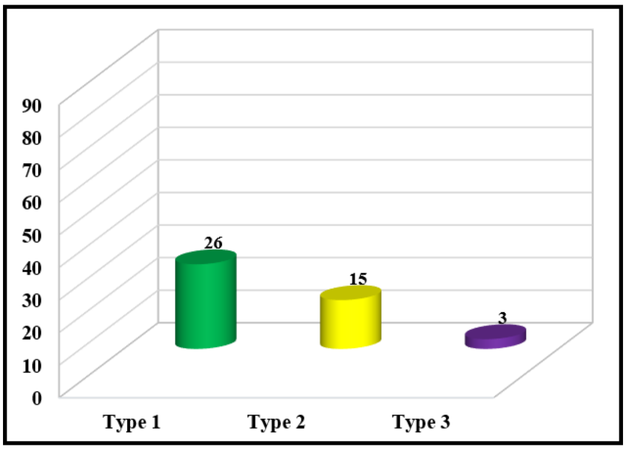

Figure 3.3. Distribution histogram showing FIs Types and their frequency in the sample *Cs 04-17*.

Faint necking down (weak maturity) and reequilibration (stretching) processes are observed around crystals' rims. Sample shows medium degree of fracture.

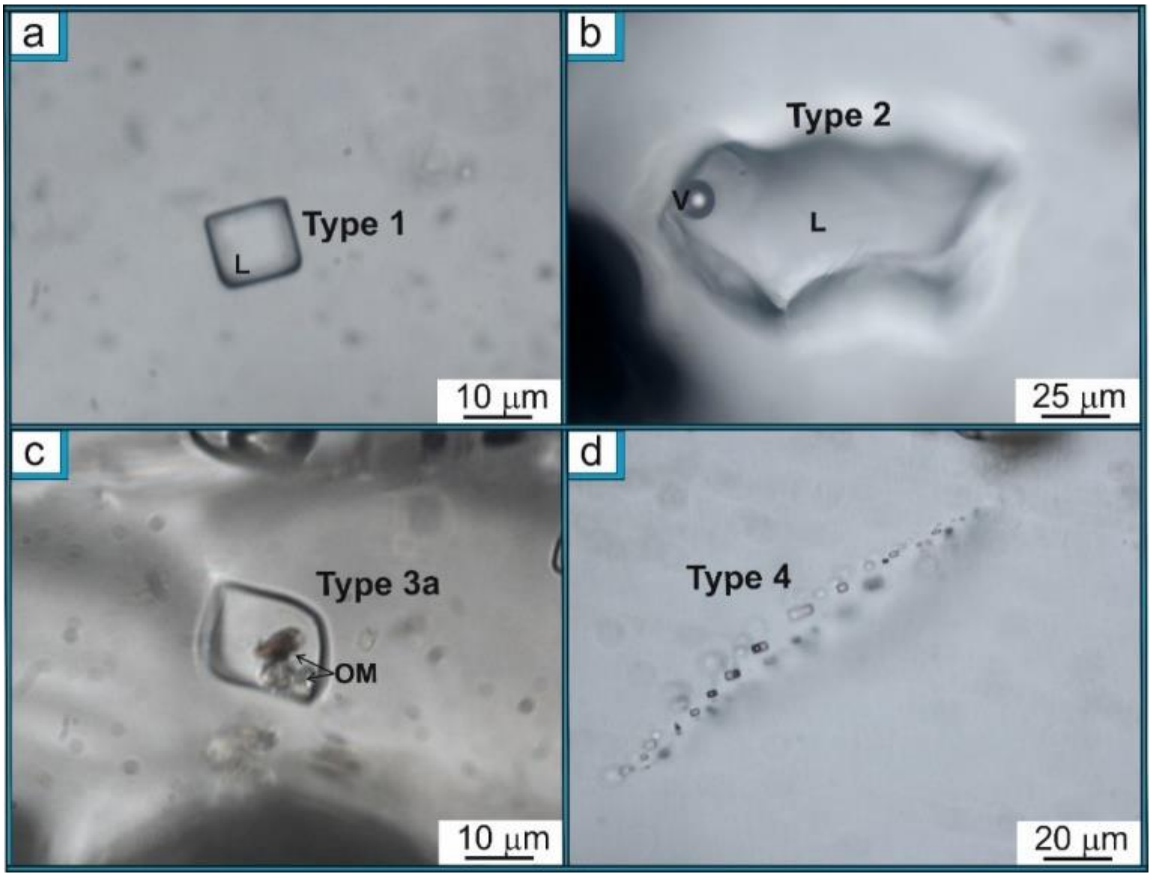

Figure 3.4. a) Isolated individual Type 1 inclusion showing negative crystal shape; b) individual Type 2 inclusion showing irregular shape; (c) Individual Type 3a inclusion showing negative crystal shape and organic matters (OM) with irregular shape. OMs are distributed in group in the core and along the inclusion's rims; (d) Type 4 inclusions occur in linear trail along crystal's rim and show tabular and negative crystal shapes.

(b) Zinga:

In the sample *Zi 07-17*, one hundred-eight primary FIs (Figure 3.5) throughout the wafer (4 cm^2 of area investigated on $10cm^2$ off the total surface) are observed: thirty-one Type 1, seventy-two Type 2 and five Type 3a-b inclusions. Secondary inclusion trails throughout the sample have been observed. Pseudo-secondary FIs are less abundant than primary and secondary FIs. FIs Types observed are:

- **Type 1 – (L)** show tabular or negative crystal shapes and range in size from 18 to 54 μm (av.~17 μm). These inclusions occur within trails parallel (Figure 3.6a) to the crystal growth zones or are organized in cluster;

- **Type 2 – (L+V)** show irregular or negative crystal shapes and range in size between 8 and 160 μm (av.~21 μm). They occur as individual inclusions or distributed in cluster ($0.50 \geq F \geq 0.90$);

- **Type 3a and 3b (rare) – (L±V±OM±S)** show irregular or negative crystal shapes, range in size between 48 and 150 μm (av.~20 μm) and are distributed in clusters. Organic matters show transparent colours and rounded shape and are located along inclusion's rims (Figure 3.6b). These materials, under UV light show faint blue fluorescence. Solid crystals show rounded and elongated shape and have chaotic arrangement; OM and S (Figure 3.6c) have size <5 μm.

- **Type 4 – (V/L and V>L**) display from irregular to negative crystal shapes (size <20 μm) and $F \leq 0.20$. Inclusions are distributed in groups or in linear trends (Figure 3.6d);

- **Type 5 (rare) – (L/V**) show tabular o negative crystal shapes and size <5 μm. These inclusions occur in clusters.

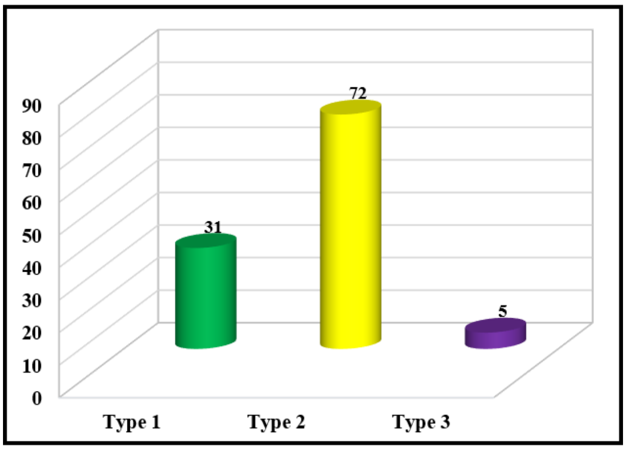

Figure 3.5. Distribution histogram showing FIs Types and their frequency in the sample *Zi 07-17*.

Widespread necking down and reequilibration (stretching and leakage) processes are observed in the core and along the crystal's corners. Stretching and leakage are mainly perpendicular to the crystal growth, in contrast, necking down is parallel. Sample shows medium degree of fracture.

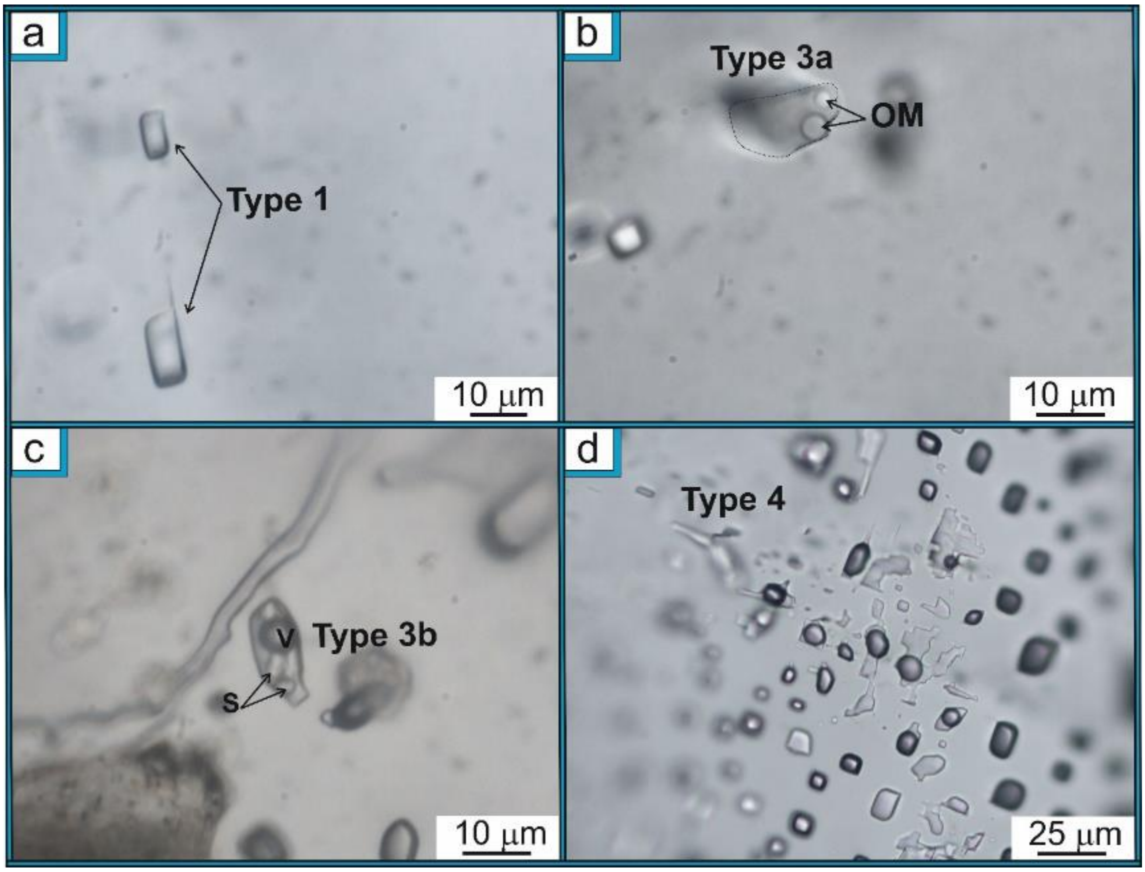

Figure 3.6. a) Type 1 inclusions showing tabular shape; b) individual Type 3a inclusion (black dotted line) showing irregular shape and rounded organic matters (OM) along the crystal rim; (c) individual Type 3a inclusion showing elongated solids trapped in inclusion; d) Type 4 inclusions are organized in groups and show necking-down phenomena.

In the sample *Zi 11-17*, three hundred ninety-five primary FIs (Figure 37) throughout the wafer (10 cm^2 of area investigated on 12.5 cm^2 off the total surface) are observed: sixteen Type 1, two hundred fifty-nine Type 2 and one hundred thirty-five Type 3b-c. Scattered secondary inclusion trails are observed. Pseudo-secondary FIs are rare. FIs Types observed are:

- **Type 1 – (L)** show negative crystal shapes (size <50 μm). Inclusions occur in parallel trails (Figure 3.8a).

- **Type 2 – (L+V)** show tabular or negative crystal shapes and range in size between 24 and 400 μm (av.~38 μm). They occur parallel to the crystal growth ($0.70 \geq F \geq 0.90$);

- **Type 3 (a-b-c) – (L±V±OM±S)** show tabular or negative crystal shapes, range in size between 10 and 200 μm (av.~67 μm) and are distributed in individual FI parallel to the crystal growth (Figure 3.8b). Type 3a and Type 3c inclusions show OMs with orange, brown or transparent appear (Figure 3.8c). These materials have rounded shape and very strong red (Figure 3.8d) or blue fluorescence (Figure 3.8f) under UV light. Type 3b and Type 3c inclusions include rounded, hexagonal or cubic solid crystals (Figure 3.8c-e). OM and S have size <30 μm.

- **Type 4 – (V/L and V>L**) display from irregular to negative crystal shapes (size <20 μm and $F \leq 0.20$). FIs are distributed in groups or in linear trends.

- **Type 5 (rare) – (L/V**) show tabular o negative crystal shapes and size <5 μm. FIs occur in clusters.

Type 1, Type 2 and Type 3 reflect growth zonation – chevron morphologies (Figure 3.8a), that sometimes end abruptly by clear halite free inclusions. 112 crystal growth zonation in 2.5 cm of halite crystal were counted.

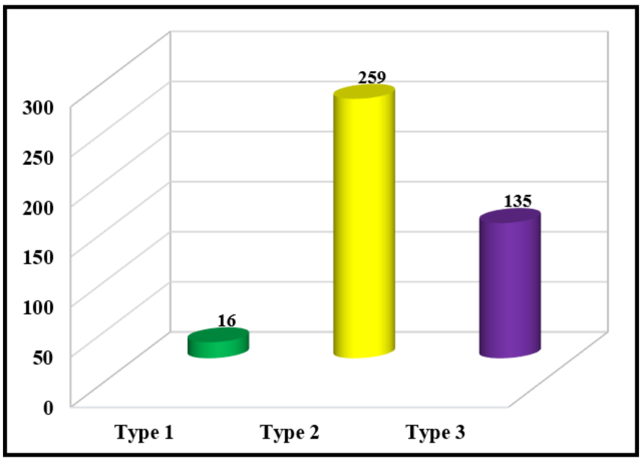

Figure 3.7. Distribution histogram showing FIs Types and their frequency in the sample *Zi 11-17*.

Faint necking down and reequilibration (stretching) process are observed in the core and along the crystal corners. Sample shows poor degree of fracture.

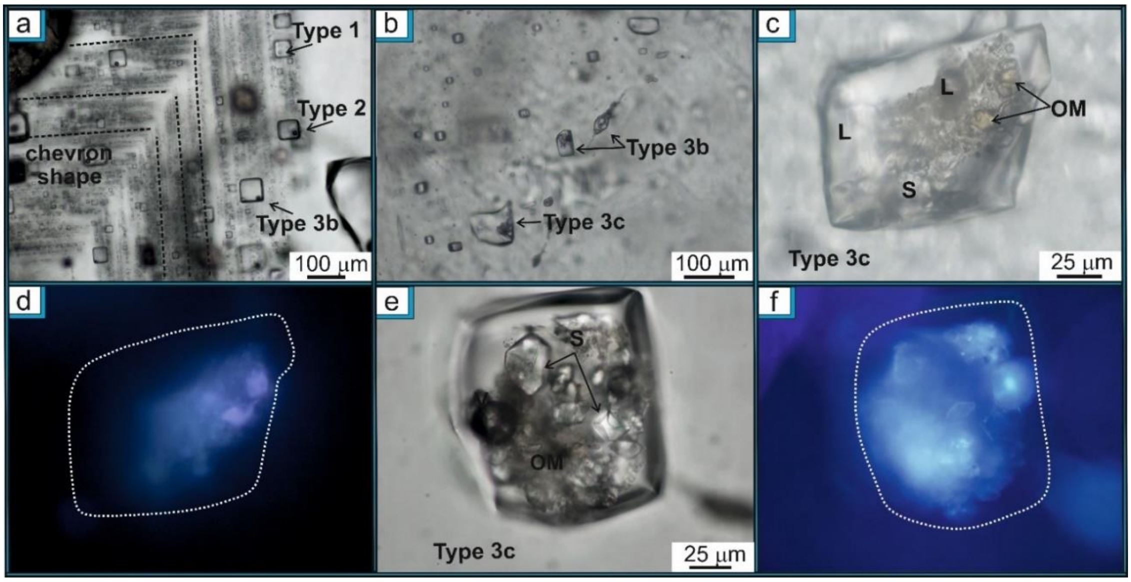

Figure 3.8. a) Primary FIs occurs in linear trails parallel to the crystals growth that define chevron shape (relict primary structures); b) Type 3 inclusions distributed in trail; (c) and (d) Type 3c with orange OM that shows strong red fluorescence under UV light (d) and rounded solid crystals; (e) and (f) Type 3c with dark OM that shows very strong blue fluorescence under UV light (f) and S with different shapes (hexagonal and cubic).

In the sample *Zi 12-17*, eighty-eight primary FIs (Figure 3.9) throughout the wafer (11 cm^2 of area investigated on 15 cm^2 off the total surface), are observed: sixty-three Type 1, eleven Type 2 and fourteen Type 3a-b. Secondary inclusion trails throughout the sample and rare pseudo-secondary FIs are observed. FIs Types observed are:

- **Type 1 – (L)** show elongated, tabular or negative crystal shapes and range in size from 14 to 145 μm (av.~24 μm). These inclusions occur within trails parallel (Figure 3.10a) to the crystal growth zones or in cluster;

- **Type 2 – (L+V)** show elongated, tabular or negative crystal shapes and range in size between 10 and 30 μm (av.~17 μm). They occur as individual inclusions or distributed in cluster ($0.50 \geq F \geq 0.90$);

- **Type 3 (a-b-c) – (L±V±OM±S)** show tabular or negative crystal shapes and range in size between 10 and 400 μm (av.~ 141 μm). They are distributed in individual FI or in clusters. Type 3a inclusions show light-yellow or brown organic matters (size <30 μm) (Figure 3.10b) with rounded and elongated shapes (Figure 3.10b) and medium blue/red or green fluorescence under UV light (Figure 3.10c). Type 3b inclusions show rounded and elongated/tabular solid crystals (Figure 3.10d-e); Type 3c inclusions (Figure 3.10f-i) show dark brown OMs and tabular solid crystals (size <60 μm) distributed throughout the inclusion. Solid crystals trapped in the inclusions show second order birefringence colours under XPL observation (Figure 3.10h).

- **Type 4 (V/L and V>L) and Type 5 (L/V)** are rare and display from irregular to negative crystal shapes (size <20 μm and $F \leq 0.20$). These inclusions are distributed in groups or in linear trends.

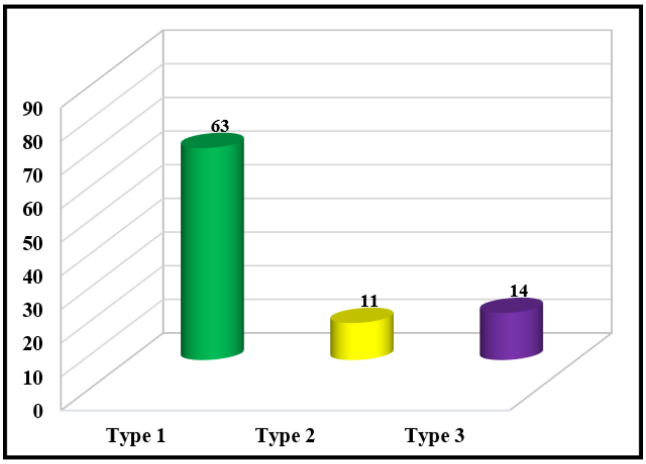

Figure 3.9. Distribution histogram showing FIs Types and their frequency in the sample *Zi 12-17*.

Faint necking down process in the core and along the crystal corners is observed. Sample shows poor degree of fracture.

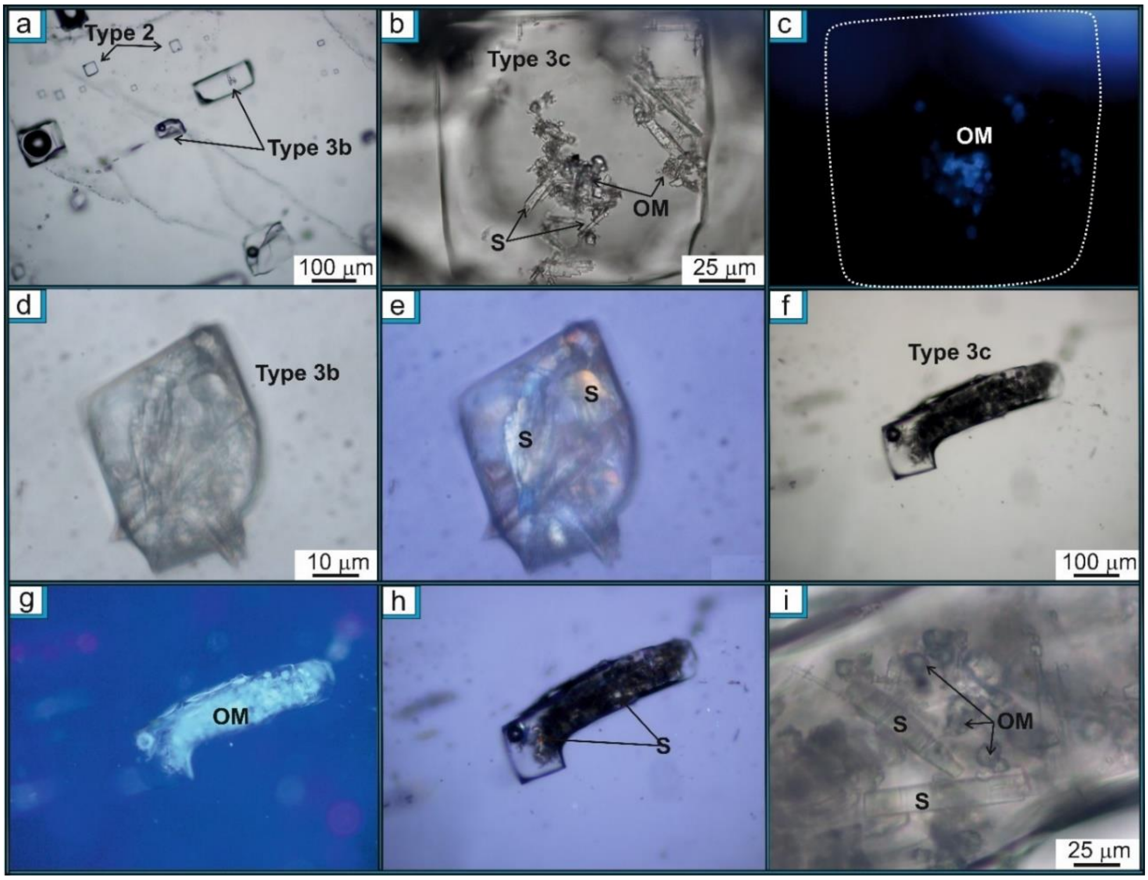

Figure 3.10. a) Types 2 and 3a inclusions in linear trails; b) and c) individual Type 3c inclusion with rounded yellow OMs (b) and tabular solids. In the (c) OMs shows medium blue fluorescence under UV light (white dotted line indicates FIs rim); d) and e) Type 3b inclusion showing elongated solids trapped in inclusion (XPL - e); f) Type 3c inclusion shows dark brown material with very strong blue fluorescence under UV light (g) and coloured solids under XPL; (i) magnification of (f) with tabular solids and rounded organic matters.

(c) Verzino:

In the sample *Ru 17-17*, fifty-six primary FIs (Figure 3.11) throughout the wafer are investigated (8 cm^2 of area investigated on 11 cm^2 off the total surface): three Type 1, thirty Type 2 and twenty-three Type 3a-b-c inclusions. A lot of secondary trails are observed. Pseudo-secondary FIs are less abundant than secondary. FIs Types observed are:

- **Type 1 – (L)** show irregular or negative crystal shapes (size <30 μm) and occur within trails parallel to the crystal growth zones;

- **Type 2 – (L+V)** show elongated, tabular or negative crystal shapes and range in size between 10 and 175 μm (av.~50 μm). They occur in parallel trails to the crystal growth ($0.70 \geq F \geq 0.90$);

- **Type 3 (a-b-c) – (L±V±OM±S)** show irregular or tabular shapes, range in size between 20 and 155 μm (av.~64 μm) and are distributed in individual FI, in linear trails or in cluster. Type 3a and Type 3c inclusions show rounded transparent or brown organic matters (Figure 3.12a-c) (size <10 μm) with faint blue fluorescence under UV light. Type 3b and Type 3c inclusions show transparent solid crystals with rounded or cubic shape (size <10 μm) (Figure 3.12b-c).

- **Type 4 – (V/L and V>L**) display from irregular to negative crystal shapes (size <20 μm and $F \leq 0.20$). These inclusions are distributed in groups or in linear trails.

- **Type 5 (rare) – (L/V**) show tabular or negative crystal shapes and size <5 μm. FIs occur in clusters.

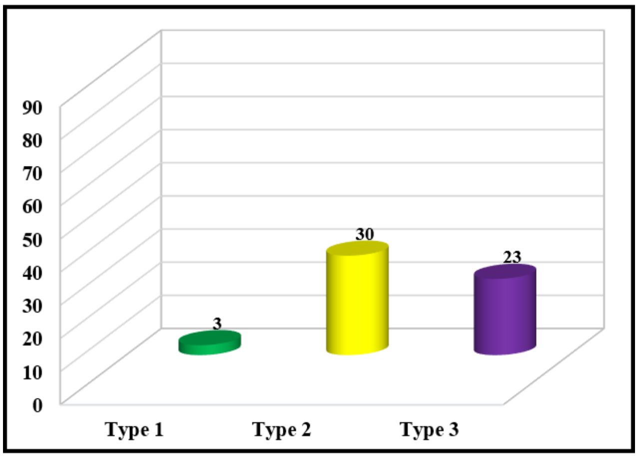

Figure 3.11. Distribution histogram showing FIs Types and their frequency in the sample *Ru 17-17*.

Moderate necking down and reequilibration (stretching) process in the core and along crystals corners are observed. These phenomena are distributed parallel to the crystal growth. Sample shows medium degree of fracture.

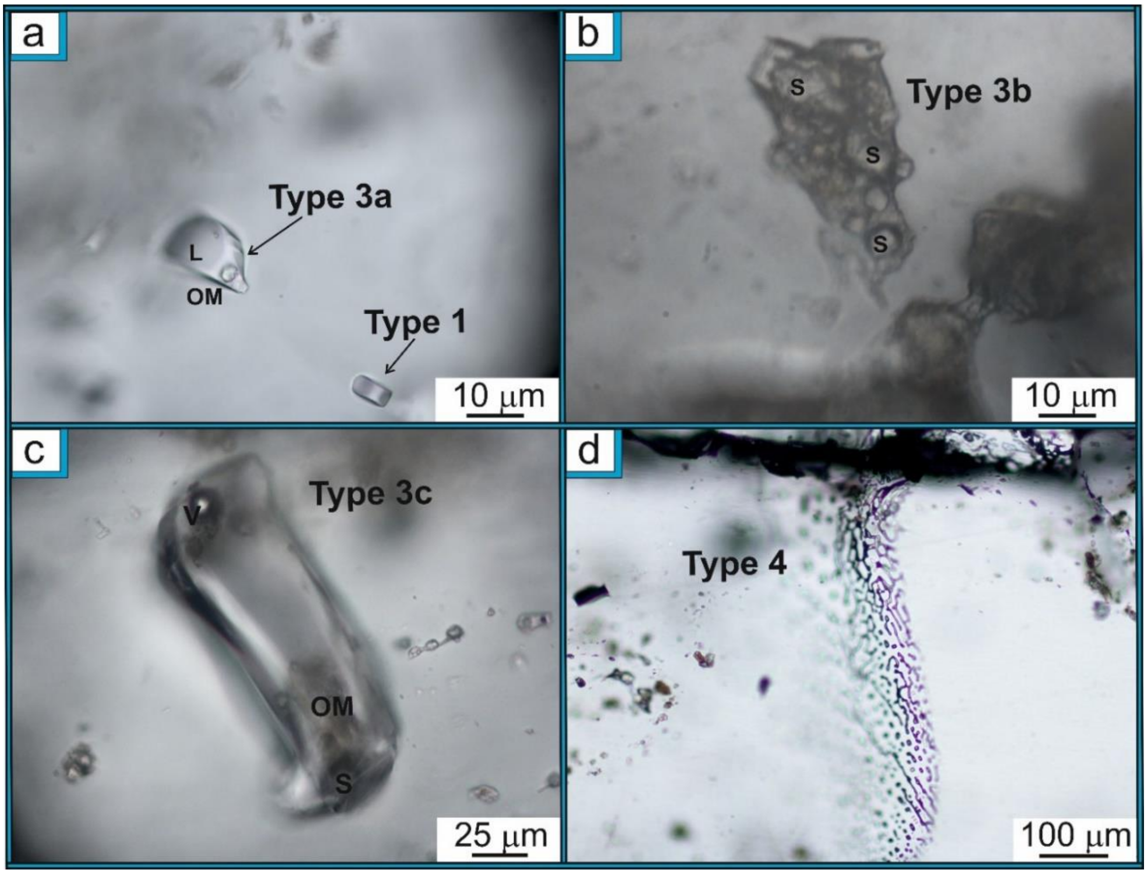

Figure 3.12. a) Type 1 and Type 3a inclusions showing tabular and irregular shapes; b) individual and irregular Type 3b inclusion containing rounded solids; (c) individual elongated Type 3c inclusion with S and brown OM trapped in inclusion; d) Type 4 inclusions occurs in groups and shows necking down phenomena perpendicular to the crystal growth.

In the sample *Ru 19-17*, fifty-six primary FIs (Figure 3.13) throughout the wafer (6 cm^2 of area investigated on 12 cm^2 off the total surface) are investigated: sixteen Type 1, thirty-nine Type 2 and one Type 3a inclusion. A lot of secondary trails and a minor amount of pseudo-secondary FIs are observed secondary. FIs Types observed are:

- **Type 1 – (L)** show tabular or negative crystal shapes (size <20 μm) and occur within trails parallel to the crystal growth zones (Figure 3.14a);
- **Type 2 – (L+V)** show tabular or negative crystal shapes (Figure 3.14a) and range in size between 5 and 90 μm (av.~15 μm). They occur in trails parallel to the crystal growth.
- **Type 3 (a) – (L±V+OM)** show irregular or negative crystal shapes (size < 20 μm) and are distributed in individual FI or in cluster. OMs (size <10 μm) trapped within inclusion shows rounded shape and transparent colour. (Figure 3.142b). Under UV light they show faint blue fluorescence.
- **Type 4 – (V/L and V>L**) display from irregular to negative crystal shapes (size <20 μm and F≤0.40). FIs are distributed in groups or in linear trends.
- **Type 5 (rare) – (L/V**) show tabular o negative crystal shapes and size <5 μm. FIs occur in clusters.

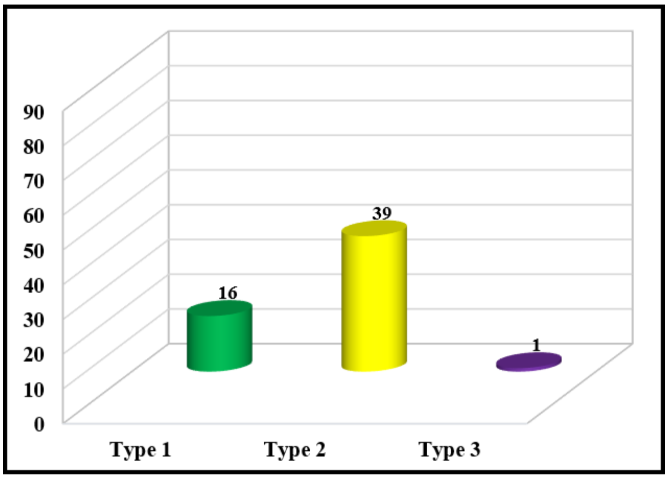

Figure 3.13. Distribution histogram showing FIs Types and their frequency in the sample *Ru 19-17*.

Widespread necking down and reequilibration (stretching and leakage) process (Figure 3.14c) are observed in the core and along the crystal's corners. These phenomena are distributed parallel to the crystal growth. Sample shows high degree of fracture.

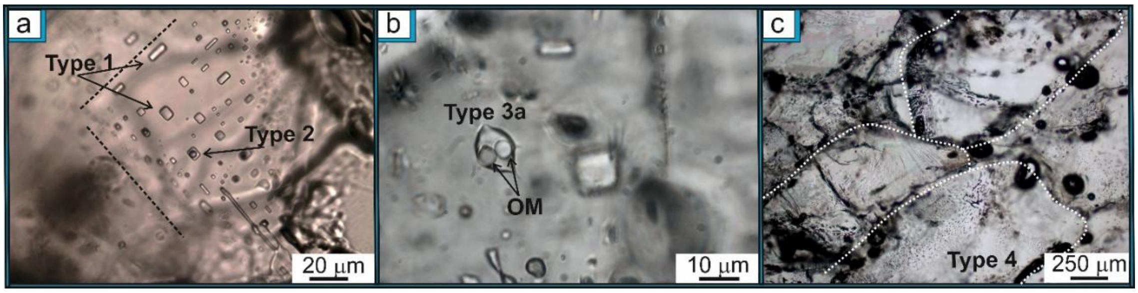

Figure3.14. a) Type 1 and Type 2 inclusions showing tabular and irregular shapes parallel to the crystal growth; b) individual Type 3a inclusion showing irregular shape and transparent rounded OMs trapped in the inclusion; c) diffuse and strong necking down throughout the crystal and along the crystal rims (white dotted lines).

In the following summary table (Table 1) reequilibration/ necking down processes and degree of fracture for the halite samples are reported.

SAMPLES	REEQUILIBRATION PROCESS		NECKING DOWN PROCESS (maturity)		DEGREE OF FRACTURE
	Stretching	**Leakage**	**Weak**	**Strong**	
Cs 04-17	Yes	No	Yes	No	medium
Zi 07-17	Yes	Yes	Yes	Yes	medium
Zi 11-17	Yes	No	Yes	No	poor
Zi 12-17	No	No	Yes	No	poor
Ru 17-17	Yes	No	Yes	No	medium
Ru 19-17	Yes	Yes	X	Yes	high

Table 1. Schematic classification diagram showing reequilibration, necking down processes and degree of fracture in all halite samples.

3.2.2 FIs in the selenite crystals (Marcellinara quarry)

Fluid inclusions in 13 selenite crystals belong to the banded and branching facies have been observed. In this paragraph, the primary FIs are identified by relationship to growth surface. They run parallel to the faster growth (100) and (010) faces. 1149 primary FIs have been observed, but also, secondary and pseudo-secondary FIs in minor amount. Clear and cloudy microfacies reveal primary FIs with different Type, size and distribution (Figure 3.15), in contrast secondary and pseudo-secondary FIs have the same characteristics in terms of distribution (linear trends and chaotical distribution), shape (tabular, cubic and irregular) and size (secondary FIs <20μm and pseudo-secondary <10 μm).

Reequilibration and Necking down phenomena are observed in all samples (in the core or in the crystal’s rims).

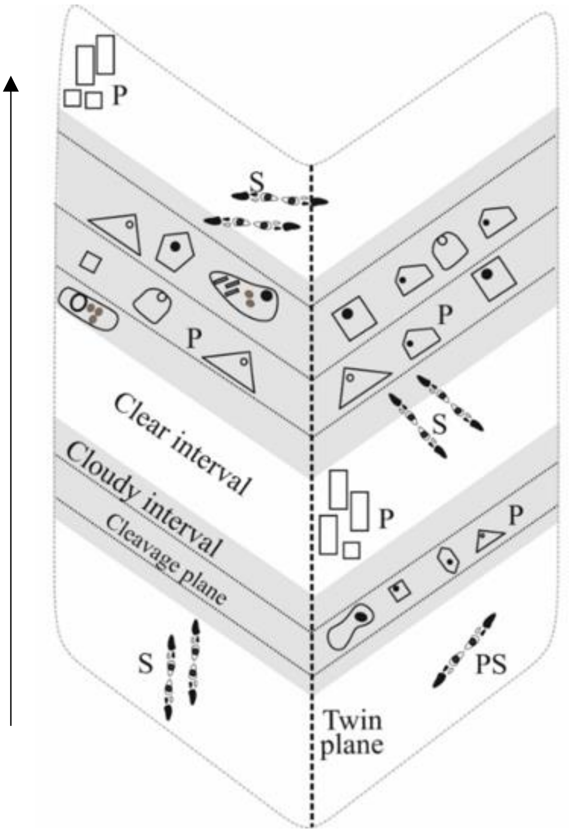

Figure 3.15. Single selenite crystal showing FIs with different types and distribution in cloudy and clear intervals. In cloudy intervals are visible cleavage planes (black dotted lines). Black arrow indicates crystal growth direction.

Detailed FIs observations in the selenite samples from the best deposits (in sector 4 and sector 5) and from branching facies (from the Riato conglomerate) are reported.

(a) Sector 4:

In the ***Ma 19-17*** **sample**, one hundred twenty-five primary FIs throughout the wafer have been observed: thirty-eight in clear intervals and eighty-seven in cloudy intervals. Abundant secondary FIs trails are scattered and distributed parallel to the twin plane. Pseudo-secondary FIs are less abundant than secondary. The sample shows faint necking down (strong maturity), stretching as reequilibration) process and high degree of fracture.

In the clear intervals FIs are parallel to the crystal growth. FIs Types observed are:

- **Type 1 – (L – n. 34 FIs)** show tabular and irregular shapes and range in size from 5 to 80 μm (av.~15 μm). These inclusions occur in cluster or within trails parallel to the crystal growth zones;

- **Type 2 – (L+V – n. 4 FIs)** show irregular shapes and range in size from 50 to 100 μm (av.~70 μm). They occur in trails, in cluster or as individual inclusions ($0.60 \geq F \geq 0.90$);

In the cloudy intervals FIs are parallel to the cleavage planes. FIs Types recognised are:

- **Type 1 – (L – n. 79 FIs)** show irregular and tabular shapes range in size from 5 to 40 μm (av. ~12.5 μm). These inclusions are distributed in groups or in linear trails**;**

- **Type 2 – (L+V – n. 8 FIs)** show irregular, tabular or elongated shapes and range in size from 5 to 40 μm (av.~ 25.5 μm). They occur as individual inclusions or distributed in linear trails ($0.60 \geq F \geq 0.98$);

Summary (Figure 3.16): Types 1 don't show individual arrangement and are more abundant than Type 2.

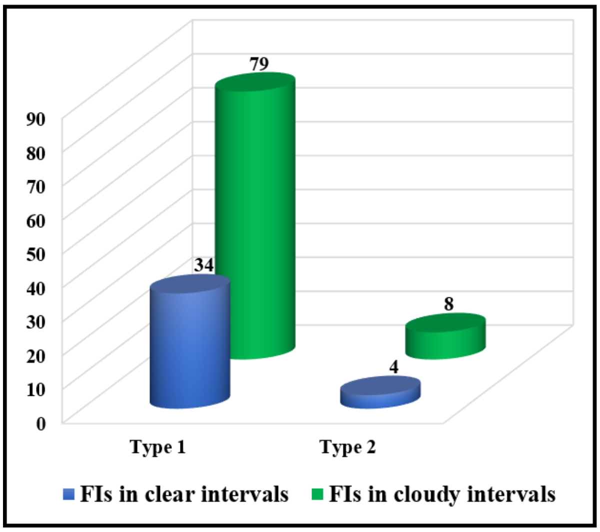

Figure 3.16. Frequency graph showing fluid inclusion types and their frequency in cloudy (green colour) and clear (blue colour) intervals. On the right side are reported the different shapes and arrangement observed in the two intervals. Sample *Ma 19-17*.

In the ***Ma 24-17* sample**, one hundred and fifty-one primary FIs throughout the wafer have been observed: ninety-two in the clear intervals and fifty-nine in the cloudy intervals. Secondary inclusion trails are scattered and parallel to the twin plane. Pseudo-secondary FIs are less abundant than secondary.

The sample shows faint necking down (strong maturity), stretching as reequilibration process and high degree of fracture.

In the clear intervals FIs are parallel to the crystal growth. FIs Types observed are:

- **Type 1 – (L – n. 90 FIs)** show elongated, tabular and trapezoidal shapes and range in size from 5 to 100 μm (av.~ 29 μm). These inclusions occur in cluster or within trails parallel to the crystal growth zones;
- **Type 2 – (L+V – n. 1 FIs)** shows irregular shape and size~40 μm. It's occurs as individual inclusion (F≥0.80);
- **Type 3(a) – (L±V+OM – n. 1 FIs)** has elongated shape and size~40 μm. It's individual inclusion within Type 1 group. Organic matter, organized in groups and, arranged along the inclusion 'rim, shows dark brown colour and faint blue fluorescence under UV light.

In the cloudy intervals FIs are parallel to the cleavage planes. FIs Types observed are:

- **Type 1 – (L – n. 40 FIs)** show tabular, pentagonal, hexagonal and trapezoidal shapes and range in size from 5 to 20 μm (av.~8.5 μm). These inclusions are distributed in groups or in linear trails**;**
- **Type 2 – (L+V n. 19 FIs)** show irregular, elongated, triangular, tabular, trapezoidal and hexagonal shapes and range in size between 5 and 60 μm (av.~ 23 μm). They occur in groups or in linear trails (0.60≥F≥0.98);

Summary (Figure 3.17): Types 1 are more abundant than Type 2 and Type 3. Only one Type 3(a) has been observed.

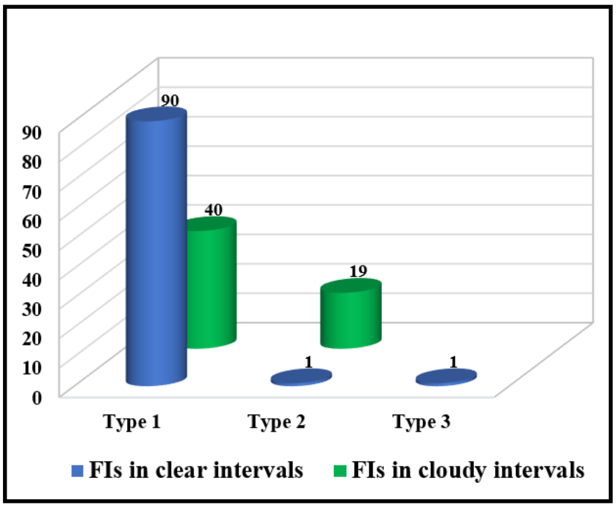

Figure 3.17 Frequency graph showing fluid inclusion Types and their frequency in cloudy (green colour) and clear (blue colour) intervals. On the right side are reported the different shapes and arrangement observed in the two intervals. Sample *Ma 24-17*.

In the ***Ma 27-17*** **sample**, thirty-two primary FIs throughout the wafer are observed: twenty-four in the clear intervals and six in the cloudy intervals. Secondary inclusion trails are scattered and parallel to the twin plane. Pseudo-secondary FIs are less abundant than secondary. The sample shows faint necking down (strong maturity), stretching and leakage as reequilibration process. Degree of fracture is poor.

<u>In the clear intervals</u> FIs are parallel to the crystal growth. FIs Types observed are:

• **Type 1 – (L – n. 21 FIs)** show elongated, tabular, trapezoidal and hexagonal shapes and range in size from 30 to 50 μm (av. ~43 μm). These inclusions occur within trails parallel to the crystal growth zones;

• **Type 2 – (L+V– n. 3 FIs)** show irregular, and trapezoidal shapes and range in size from 20 to 30 μm (av.~27 μm). They occur within trails parallel to the crystal growth zones (F≥0.80);

<u>In the cloudy intervals</u> FIs are parallel to the cleavage planes. FIs Types observed are:

• **Type 2 – (L+V – n. 4 FIs)** show irregular, elongated and trapezoidal shapes and range in size between 14 and 22 μm (av.~14 μm). They occur as individual inclusions or in linear trails (F≥0.80);

• **Type 3a – (L±V+OM – n. 4 FIs)** show irregular and elongated shapes and range in size between 20 and 60 μm (av.~40 μm). They occur as individual inclusion or within Type 1 group. Organic matter, organized in groups (in the core of FI) shows dark brown colour and strong blue fluorescence under UV light.

Summary (Figure 3.18): FIs in the clear intervals show more forms than the FIs in the cloudy.

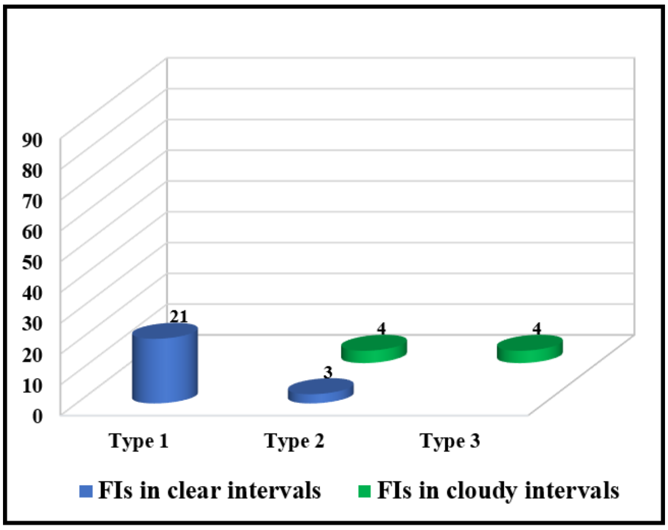

Figure 3.18. Frequency graph showing fluid inclusion Types and their frequency in cloudy (green colour) and clear (blue colour) intervals. On the right side are reported the different shapes and arrangement observed in the two intervals. Sample *Ma 27-17*.

(b) Sector 5

In the ***Ma 01-17* sample**, ninety-six primary FIs throughout the wafer are observed: twenty-three in the clear intervals and seventy-two in the cloudy intervals. Secondary inclusion trails are scattered and parallel to the twin plane. Pseudo-secondary FIs are less abundant than secondary. The sample shows faint necking down (strong maturity), stretching as reequilibration process and high degree of fracture.

In the clear intervals FIs are parallel to the crystal growth. FIs Types observed are:

- **Type 1 – (L – n. 6 FIs)** show elongated shapes and range in size from 10 to 25 μm (av.~ 21 μm). These inclusions occur within trails parallel to the crystal growth zones;
- **Type 2 – (L+V – n. 16 FIs)** show triangular, elongated, trapezoidal and tabular shapes and range in size between 5 and 24 μm (av.~13 μm). They occur in groups or within trails parallel to the crystal growth zones ($0.60 \geq F \geq 0.90$);
- **Type 3b – (L±V+S – n. 2 FIs)** show tabular shapes and range in size between 20 and 60 μm (av.~45 μm). They occur as individual inclusions within Type 2 groups. Rounded transparent solids are located along inclusion's rim.

In the cloudy intervals FIs are parallel to the cleavage planes. FIs Types observed are:

- **Type 1 – (L – n. 20 FIs)** show irregular, elongated, tabular, trapezoidal, triangular and pentagonal and range in size between 10 and 60 μm (av.~35 μm). These inclusions are distributed in linear trails**;**
- **Type 2 – (L+V – n. 50 FIs)** show several shapes (elongated, trapezoidal, pentagonal, triangular, hexagonal and irregular, tabular) and range in size between 7 and 100 μm (av.~ 24 μm). These inclusions are distributed in linear trails ($0.60 \geq F \geq 0.98$);
- **Type 3b – (L±V+S – n. 2 FI)** show tabular and irregular shape and size~9 μm. They occur as individual inclusion within Type 2 group. Rounded transparent solids are located along inclusion's rim.

Summary (Figure 3.19): FIs in the clear intervals show only tabular, elongated and trapezoidal shape and occur in trail or in group, in contrast, FIs in the cloudy intervals show a greater number of shapes and prefer the trail arrangement. Moreover, in cloudy intervals a lot of small primary FIs (<15 µm in size) are observed.

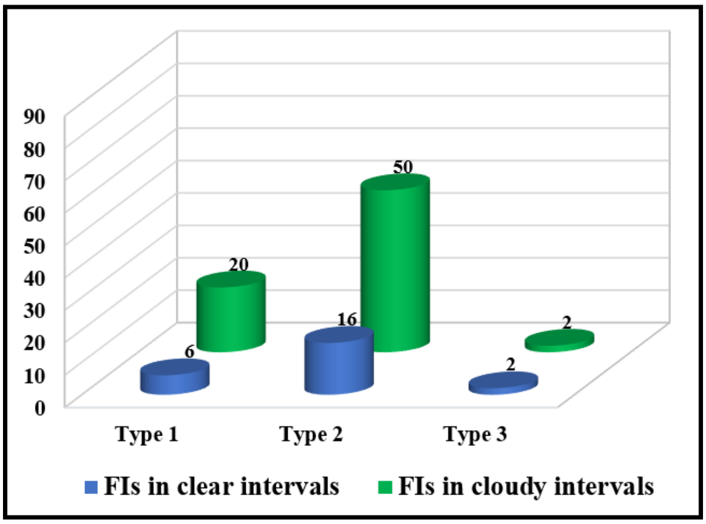

Figure 3.19. Frequency graph showing fluid inclusion Types and their frequency in the cloudy (green colour) and clear (blue colour) intervals. On the right side are reported the different shapes and arrangement observed in the two intervals. *Ma 01-17* sample.

In the ***Ma 02-17*** **sample**, one hundred-two primary FIs throughout the wafer are observed: twenty-five in the clear intervals and one hundred two in the cloudy intervals. FIs are mainly concentrated at the bottom and top of the crystal, the central part is disturbed/fractured. Secondary inclusion trails are parallel or perpendicular to the twin plane. They are more abundant at the top of the crystal. Pseudo-secondary FIs are less abundant than secondary. The sample shows moderate necking down (strong maturity), stretching as reequilibration process and high degree of fracture.

<u>In the clear intervals</u> FIs are parallel to the crystal growth. FIs Types observed are:

- **Type 1 – (L – n. 13 FIs)** show triangular tabular, irregular and trapezoidal shapes and range in size from 10 to 40 μm (av.~24 μm). These inclusions occur in cluster, within trails parallel to the crystal growth zones or as individual inclusions;

- **Type 2 – (L+V – n. 13 FIs)** show elongated, tabular and triangular shapes and range in size between 10 and 40 μm (av.~17 μm). They occur in trails or in cluster (0.70≥F≥0.99);

<u>In the cloudy intervals</u> FIs are parallel to the cleavage planes. FIs Types observed are:

- **Type 1 – (L – n. 33 FIs)** show several shapes (elongated, trapezoidal, pentagonal, hexagonal and irregular) and size between 10 and 50 μm (av.~24 μm). These inclusions are distributed in cluster or in trail**;**

- **Type 2 – (L+V– n. 67 FIs)** show several shapes (tabular, elongated, trapezoidal, pentagonal, triangular, hexagonal, dome and irregular) and range in size between 10 and 136 μm (av.~36 μm). These inclusions are distributed in cluster, in trails or in individual FI (0.60≥F≥0.96);

- **Type 3a – (L±V+OM – n. 2 FIs)** show irregular and tabular shapes and range in size between 10 and 40 μm (av.~16 μm). They occur as individual inclusion or within Type 2 group. Organic matters are dispersed throughout the inclusion, show brown and yellow colour and rounded shape. Under UV light don’t show fluorescence.

Summary (Figure 3.20): FIs in cloudy intervals show individual arrangement and smaller size (<15 μm in size).

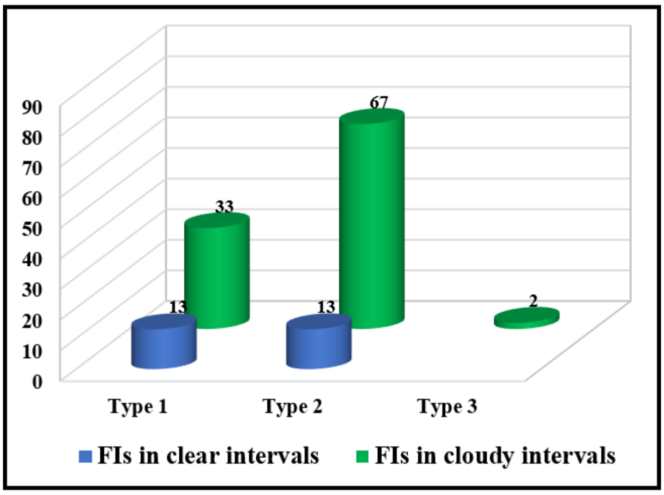

Figure 3.20. Frequency graph showing fluid inclusion Types and their frequency in the cloudy (green colour) and clear (blue colour) intervals. On the right side are reported the different shapes and arrangement observed in the two intervals. *Ma 02-17* sample.

In the ***Ma 03-17* sample**, forty-eight primary FIs throughout the wafer are observed: one in the clear intervals and forty-seventh in the cloudy intervals. Secondary inclusion trails are parallel or perpendicular to the twin plane. Pseudo-secondary FIs are less abundant than secondary. The sample shows moderate necking down (strong maturity), stretching and leakage as reequilibration process and poor degree of fracture.

<u>In the clear intervals</u> FIs are parallel to the crystal growth. FIs Types observed are:

- **Type 2 – (L – n. 1 FIs)** shows tabular shape and 19 μm in size (F=0.96).

<u>In the cloudy intervals</u> FIs are parallel to the cleavage planes. FIs Types observed are:

- **Type 1 – (L – n. 6 FIs)** show elongated, tabular, trapezoidal and pentagonal shapes and range in size from 10 to 36 μm (av.~16 μm). These inclusions are distributed in linear trails or individuals**;**

- **Type 2 – (L+V – n. 39 FIs)** show several shapes (elongated, dome, trapezoidal, pentagonal, triangular and irregular) and range in size between 6 and 136 μm (av.~28 μm). They occur as individual inclusions or in linear trails ($0.60 \geq F \geq 0.96$);

- **Type 3b – (L±V+S – n. 2 FIs)** show tabular shapes and size ~ 22 μm. They occur within linear trail. Transparent solid trapped shows rounded shape and are located along the inclusion's rim.

Summary (Figure 3.21): the clear intervals are very thin and don't show appreciable fluid inclusions. Linear trails predominate over other arrangements.

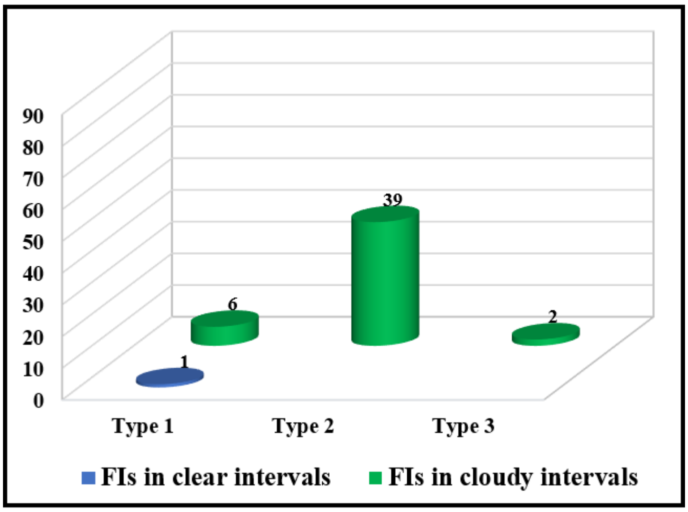

Figure 3.21. Frequency graph showing fluid inclusion Types and their frequency in the cloudy (green colour) and clear (blue colour) intervals. On the right side are reported the different shapes and arrangement observed in the two intervals. *Ma 03-17* sample.

In the ***Ma 04-17*** **sample**, forty-eight primary FIs throughout the wafer are observed: twenty-seven in the clear intervals and twenty-one in the cloudy intervals. Secondary inclusion trails are perpendicular or parallel to the twin plane. Pseudo-secondary FIs are less abundant than secondary. The sample shows widespread necking down (weak maturity), stretching and leakage as reequilibration process and high degree of fracture. In the clear intervals FIs are parallel to the crystal growth. FIs Types observed are:

- **Type 1 – (L – n. 25 FIs)** show irregular, elongated, tabular, pentagonal shapes and range in size between 6 and 40 μm (av.~21.5 μm). They occur in groups or in linear trails;
- **Type 2 – (L+V– n. 2 FIs)** show elongated and tabular shapes and range in size between 5 and 45 μm (av.~25 μm). They are in groups or in trails (F≥0.80);

In the cloudy intervals FIs are parallel to the cleavage planes. FIs Types observed are:

- **Type 1 – (L – n. 1 FI)** shows elongated shape and 6.6 μm in size. It occurs as individual inclusion within Type 1 and Type 2 trail;
- **Type 2 – (L+V – n. 19 FIs)** show several shapes (elongated, trapezoidal, pentagonal, and triangular, tabular) and range in size between 5 and 40 μm (av.~12 μm). They occur in linear trails (0.60≥F≥0.96);
- **Type 3b – (L±V+S– n. 1 FI)** shows tabular shape and size~ 10 μm. It occurs as individual inclusion within Type 1 and Type 2 trail. Transparent solid trapped shows rounded shape and is located along inclusion’s rim.

Summary (Figure 3.22): FIs in clear intervals prefer trails arrangement rather than groups.

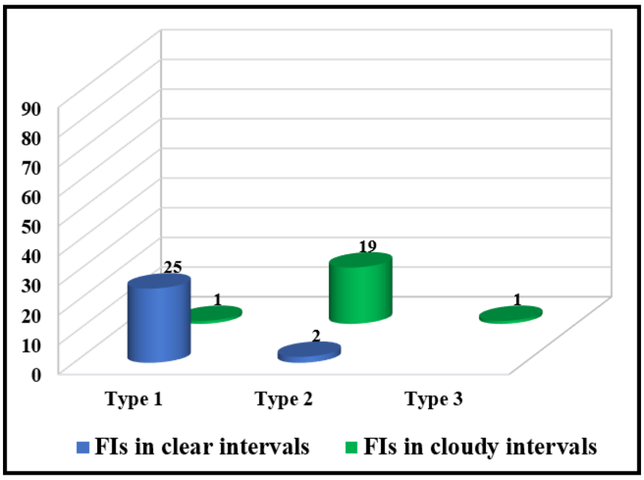

Figure 3.22. Frequency graph showing fluid inclusion Types and their frequency in the cloudy (green colour) and clear (blue colour) intervals. On the right side are reported the different shapes and arrangement observed in the two intervals. *Ma 04-17* sample.

In the ***Ma 05-17* sample**, only fourteen primary FIs in cloudy intervals (Figure 3.23) are recognised due to disturbances in the crystal. Secondary FIs (trail) are parallel or perpendicular to the twin plane. Pseudo-secondary FIs are less abundant than secondary. The sample shows medium necking down (weak maturity), stretching and leakage as reequilibration process and high degree of fracture.

In the cloudy intervals FIs occur in linear trails parallel to the cleavage plane. FIs Types observed are:

- **Type 1 – (L – n. 1 FIs)** shows triangular shape and size ~30 µm.
- **Type 2 – (L+V– n. 13 FIs)** show several shapes (elongated, trapezoidal, pentagonal, triangular and irregular) and range in size between 7 and 60 µm (av.~ 25 µm), (0.70≥F≥0.96);

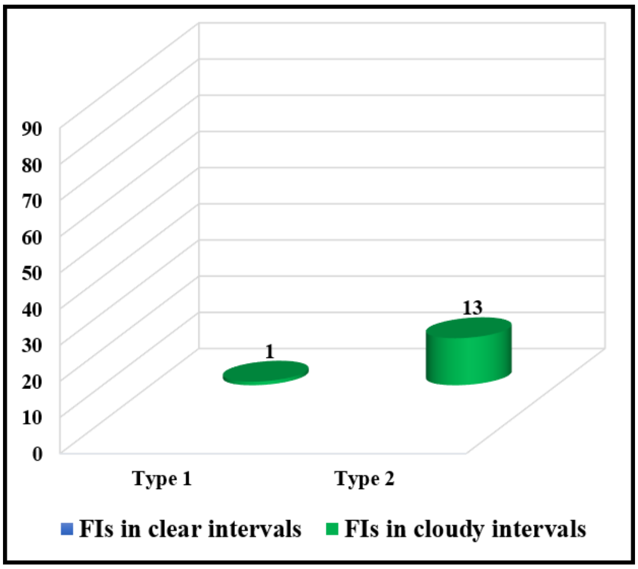

Figure 3.23. Frequency graph showing fluid inclusion Types and their frequency in the cloudy (green colour) interval. On the right side are reported the different shapes and arrangement observed. Clear intervals are FIs free. *Ma 05-17* sample.

In the ***Ma 06-17* sample**, one hundred thirty-four primary FIs throughout the wafer are observed: sixty-nine in the clear intervals and sixty-five in the cloudy intervals. Secondary inclusion trails are perpendicular or parallel to the twin plane. Pseudo-secondary FIs are less abundant than secondary. The sample shows medium necking down (weak maturity), stretching and leakage as reequilibration process and medium degree of fracture.

<u>In the clear intervals</u> FIs are parallel to the crystal growth. FIs Types observed are:

- **Type 1 – (L – n. 54 FIs)** show tabular and pentagonal shapes and range in size between 5 and 100 μm (av.~26 μm). They occur in groups or within linear trails;

- **Type 2 – (L+V– n. 9 FIs)** show elongated, tabular and hexagonal shapes and range in size from 8.5 to 37 μm (av.~ 19 μm). They occur in groups or within linear trails (0.50≥F≥0.96);

- **Type 3a – (L±V+OM – n. 6 FIs)** shows tabular shapes and range in size from 40 to 80 μm (av.~ 50 μm). They occur as individual inclusion within Type 1 and Type 2 trail. Organic matters, distributed in the core and along inclusion rims, trapped show light yellow colour (faint fluorescence under UV light) and rounded shape.

<u>In the cloudy intervals</u> FIs are parallel to the cleavage planes. FIs Types observed are:

- **Type 1 – (L – n. 26 FIs)** shows tabular, elongated, trapezoidal, hexagonal and pentagonal shapes and range in size from 10 to 50 μm (av.~23 μm). They occur in groups or within linear trails**;**

- **Type 2 – (L+V – n. 38 FIs)** show several shapes (tabular, elongated, dome, trapezoidal, pentagonal, triangular, hexagonal and irregular) and range in size between 5 and 100 μm (av.~25 μm). They occur in groups or within linear trails (0.50≥F≥0.97);

- **Type 3b – (L±V+S – n. 1 FIs)** shows pentagonal shape and ~12.5 μm in size. It occurs as individual inclusion within Type 1 and Type 2 group. Solid trapped shows rounded shape and transparent colour.

Summary (Figure 3.24): in the clear intervals FIs prefer group arrangement, while in the cloudy prefer trails arrangement.

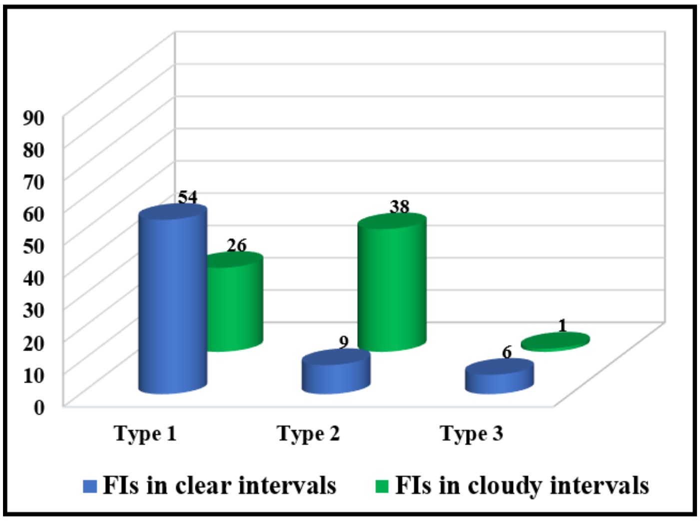

Figure 3.24. Frequency graph showing fluid inclusion Types and their frequency in the cloudy (green colour) and clear (blue colour) intervals. On the right side are reported the different shapes and arrangement observed in the two intervals. *Ma 06-17* sample.

In the ***Ma 07-17* sample**, sixty-nine primary FIs throughout the wafer have been observed: eighteen in the clear intervals and fifty-one in the cloudy intervals. Secondary inclusion trails are perpendicular or parallel to the twin plane. Pseudo-secondary FIs are less abundant than secondary.

The sample shows medium necking down (weak maturity), stretching and leakage as reequilibration process and medium degree of fracture.

In the clear intervals FIs are parallel to the crystal growth. FIs Types observed are:

- **Type 1 – (L – n. 12 FIs)** show elongated, tabular and trapezoidal shapes and range in size from 5 to 80 μm (av.~22 μm). Inclusions occur in linear trails or in group;
- **Type 2 – (L+V – n. 6 FIs)** show trapezoidal and tabular shapes and range in size from 20 to 56 μm (av.~38 μm). They occur in linear trails or in group (F=0.90);

In the cloudy intervals FIs are parallel to the cleavage planes. FIs Types observed are:

- **Type 1 – (L – n. 31 FIs)** show elongated, tabular, trapezoidal hexagonal and pentagonal shapes and range in size from 5 to 50 μm (av.~16 μm). Inclusions occur in linear trails or in group;
- **Type 2 – (L+V – n. 20 FIs)** show elongated, trapezoidal, pentagonal, tabular, triangular and irregular shape and range in size between 6 and 50 μm (av.~20 μm). They occur in linear trails ($0.85 \geq F \geq 0.93$);

Summary (Figure 3.25): FIs in cloudy and clear intervals don’t show individual arrangements.

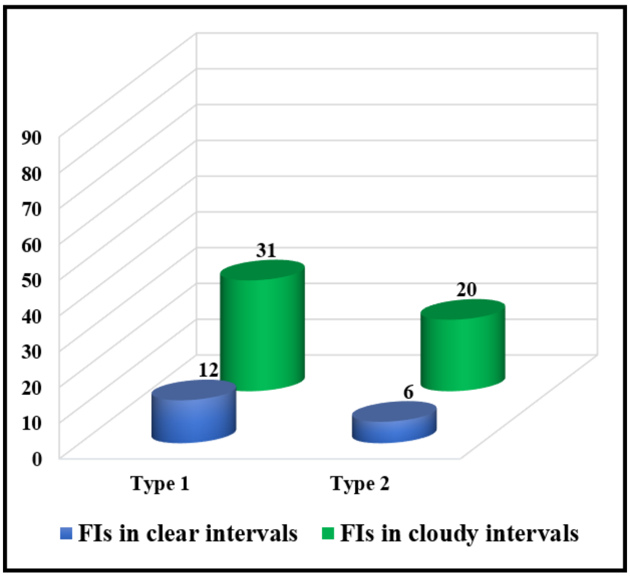

Figure 3.25. Frequency graph showing fluid inclusion Types and their frequency in the cloudy (green colour) and clear (blue colour) intervals. On the right side are reported the different shapes and arrangement observed in the intervals. *Ma 07-17* sample.

In the ***Ma 08-17* sample**, one hundred ninety-six primary FIs throughout the wafer are observed: ninety-six in the clear intervals and one hundred in the cloudy intervals. FIs are mainly concentrated at the crystal bottom. Secondary inclusion trails are perpendicular or parallel to the twin plane. Pseudo-secondary FIs are less abundant than secondary.

The sample shows widespread necking down (weak maturity), stretching and leakage as reequilibration process and high degree of fracture.

<u>In the clear intervals</u> FIs are parallel to the crystal growth. FIs Types observed are:

• **Type 1 – (L – n. 64 FIs)** show elongated, tabular, pentagonal and hexagonal shapes and range in size between 5 and 120 μm (av.~36 μm). They occur in linear trails or in group;

• **Type 2 – (L+V – n. 31 FIs)** show elongated, tabular, trapezoidal, pentagonal, irregular, triangular and hexagonal shapes and range in size from 6 to 74 μm (av.~22 μm). They occur in linear trails, in groups or as individual inclusions ($0.50 \geq F \geq 0.96$);

• **Type 3b – (L±V+S – n. 1 FI)** shows elongated shape and size~42 μm. It occurs as individual inclusion within Type 1 and Type 2 group. Solid trapped shows rounded shape and transparent colour.

<u>In the cloudy intervals</u> FIs are parallel to the cleavage planes. FIs Types observed are:

• **Type 1 – (L – n. 53 FIs)** show irregular, elongated, pentagonal, trapezoidal, hexagonal and tabular shapes and range in size from 5 to 60 μm (av.~20 μm). They occur in groups or in linear trails**;**

• **Type 2 – (L+V – n. 45 FIs)** show several shapes (elongated, trapezoidal, pentagonal, triangular, dome, hexagonal and irregular) and range in size between 5 and 92 μm (av.~ 32 μm). They occur in cluster or in linear trails ($0.50 \geq F \geq 0.97$);

• **Type 3a and 3b – (L±V+S+OM – n. 2 FIs)** show tabular and pentagonal shape and size between 11 and 30 μm (av.~20 μm). They occur as individual inclusion within Type 1 and Type 2 trails. In Type 3a organic matters show brown colour (medium blue fluorescence under UV light), rounded shapes and are concentrated throughout the FI. In Type 3b solids trapped show rounded shape and transparent colour. It occurs as individual inclusion within Type 1 and Type 2 group.

Summary (Figure 3.26): only Type 2 and Type 3 inclusions (observed in the cloudy intervals) show individual arrangement.

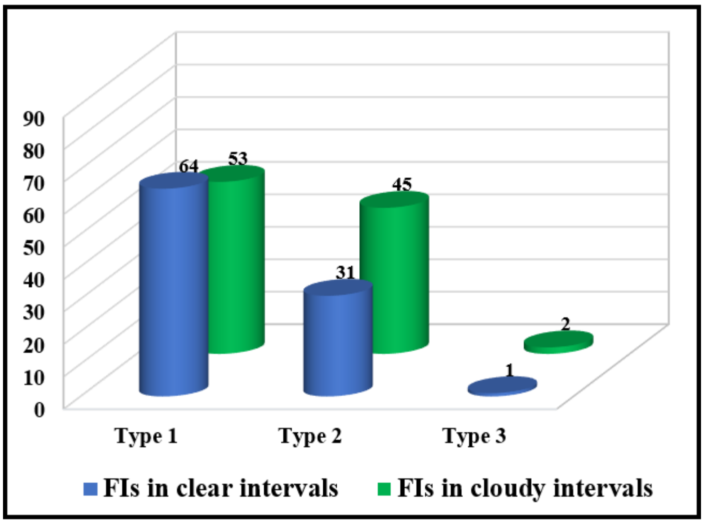

Figure 3.26. Frequency graphs showing fluid inclusions types and their frequency in the cloudy (green colour) and clear (blue colour) intervals. On the right side are reported the different shapes and arrangement observed in the two intervals. *Ma 08-17* sample.

In the ***Ma 09-17* sample**, ninety-eight primary FIs throughout the wafer are observed: seventy-five in the clear intervals and twenty-three in the cloudy intervals. Secondary inclusion trails are perpendicular or parallel to the twin plane. Pseudo-secondary FIs are less abundant than secondary.

The sample shows faint necking down (weak maturity), stretching and leakage as reequilibration process and poor degree of fracture.

<u>In the clear intervals</u> FIs are parallel to the crystal growth. FIs Types observed are:

- **Type 1 – (L – n. 71 FIs)** show tabular shapes and range in size between 5 and 70 μm (av.~26 μm). They occur in groups;
- **Type 2 – (L+V– n. 4 FIs)** show tabular and pentagonal shapes and range in size from 12 to 30 μm (av.~17 μm). They occur in groups or as individual inclusions (0.65≥F≥0.90);

<u>In the cloudy intervals</u> FIs are parallel to the cleavage planes. FIs Types observed are:

- **Type 1 – (L – n. 7 FIs)** shows elongated, tabular, trapezoidal, hexagonal and pentagonal shape and range in size from 10 to 53 μm (av.~30 μm). They occur in trails or as individual inclusions;
- **Type 2 – (L+V – n. 16 FIs)** show several shapes (elongated, trapezoidal, hexagonal, tabular, pentagonal, triangular and irregular) and range in size between17 and 60 μm (av.~ 32 μm). They occur in trails or as individual inclusions (0.60≥F≥0.93);

Summary (Figure 3.27): FIs in the clear intervals show individual or group arrangement, in contrast, FIs in the cloudy intervals show individual or linear trail arrangement.

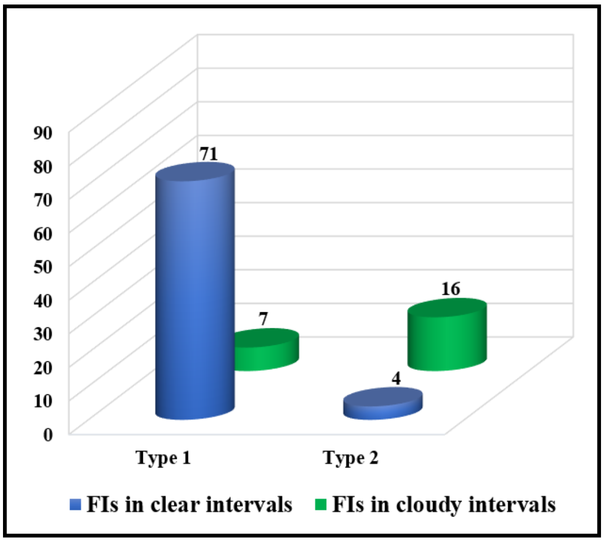

Figure 3.27. Frequency graph showing fluid inclusion Types and their frequency in the cloudy (green colour) and clear (blue colour) intervals. On the right side are reported the different shapes and arrangement observed in the two intervals. *Ma 09-17* sample.

A summary of the main FI Types observed in selenite crystals (Figure 3.28).

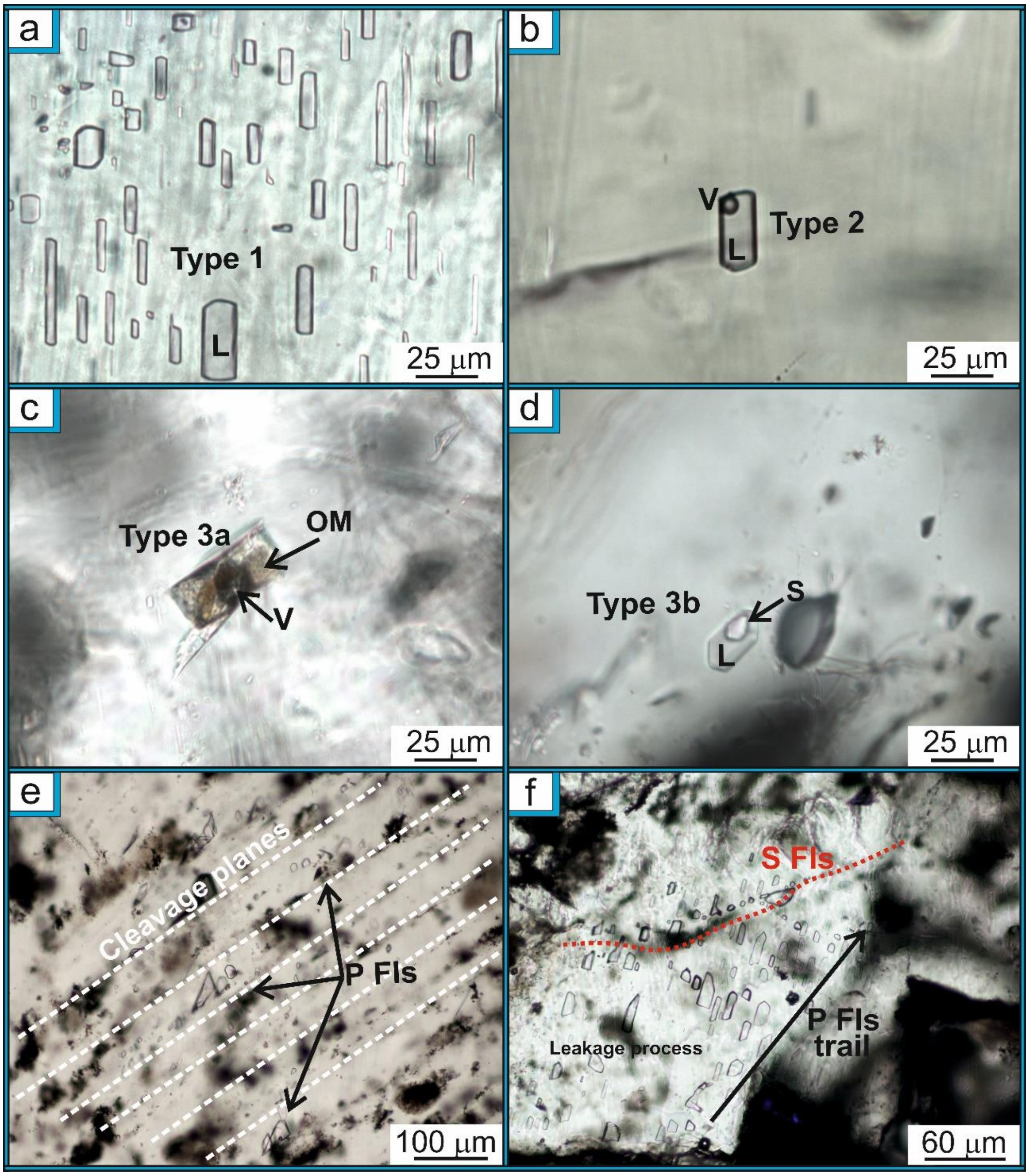

Figure 3.28. a) Trail of Type 1 FIs with tabular shape in the clear interval; b) individual Type 2 FI with tabular shape in the cloudy interval; c) Type 3 FIs with brown OM trapped in inclusion in the cloudy interval; d) individual Type 3b FI that shows transparent solid crystal in the cloudy interval; e) Cleavage plane (white dotted lines) rich in P FIs in the cloudy intervals; f) P FIs distribute in trail subject to leakage process and S FIs that cut the P FIs.

Table (Table 2) of reequilibration, necking down processes and degree of fracture recognised in the selenite samples.

SAMPLES	RE-EQUILIBRATION PROCESS		NECKING DOWN PROCESS (maturity)		DEGREE OF FRACTURE
	Stretching	**Leakage**	**Weak**	**Strong**	
Ma 19-17	Yes	X	No	Yes	high
Ma 24-17	Yes	X	No	Yes	high
Ma 27-17	Yes	Yes	No	Yes	poor
Ma 01-17	Yes	No	No	Yes	high
Ma 02-17	Yes	No	Yes	No	high
Ma 03-17	Yes	Yes	Yes	No	poor
Ma 04-17	Yes	Yes	Yes	No	high
Ma 05-17	Yes	Yes	Yes	No	high
Ma 06-17	Yes	Yes	Yes	No	medium
Ma 07-17	Yes	Yes	Yes	No	medium
Ma 08-17	Yes	Yes	Yes	No	high
Ma 09-17	Yes	Yes	Yes	No	poor

Table 2. Schematic classification diagram showing reequilibration and necking down processes and degree of fracture observed in the selenite samples.

(c) Riato conglomerate

In the Ma Br sample, primary FIs are not distinguishable from the secondary. Only one FIs Type 3a has been observed, while necking down (strong maturity) and reequilibration (stretching and leakage) process has diffused throughout the sample.

3.2.3 FIs in the selenite crystals (Benestare quarry)

Selenite samples observed contain very few P inclusions (Figure 3.29a) Type 1 and Type 2 (<50 mm in size) that show tabular, trapezoidal and irregular shapes. These inclusions occur in parallel trails to the growth zone or as isolated inclusion. Abundant S inclusions (Type 4) are observed throughout the crystals. Leakage is the main reequilibration process (Figure 3.29b).

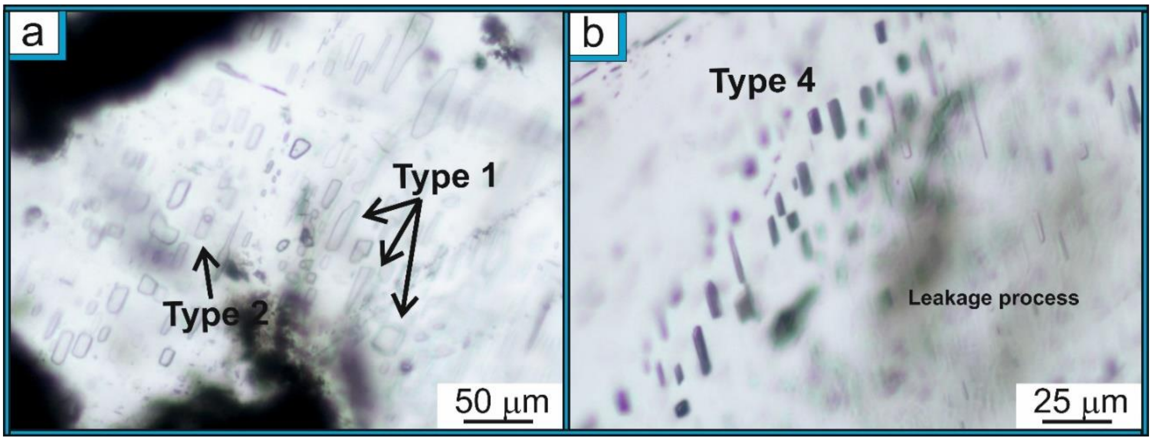

Figure 3.29. Primary and secondary FIs observed in samples from the Benestare quarry. a) Trail of Type 1 and Type 2 FIs showing tabular shape; b) Trail of Type 4 inclusions show leakage process.

3.3 Summary and discussion

Detailed FIs petrography observation have been conducted on six halite samples from the Crotone Basin, twelve selenite samples from the Catanzaro Trough and three selenite samples from the Benestare area. The FIs frequency and their distributions are very important to understand the origin (primary or secondary), the formation environment and the crystals evolution during burial and exhumation.

3.3.1 FIs in halite crystals from the Coste del Sale, Zinga and Verzino

a) The banded facies show primary and secondary FIs contrary to what was indicated in previously works (see Lugli *et al.*, 2007). Primary FIs are trapped during crystals formation at brine-atmosphere surface (see chapter 2 for more details on the banded facies formation) along the crystal surface imperfections (rapid growth) and sometimes can trap small air bubble (Robert & Spencer, 1995); If dissolution processes during their growth and deposition are not marked, crystals can show growth zonation (relicts primary structures) highlighted by FIs distribution. In the samples from the **Coste del Sale** (*Cs 04-17*) and **Zinga** (*Zi 07-17*), the relict structures are more visible than samples from **Verzino** (*Ru 17-17 and Ru 19-17*). Indeed, these last are further fractured and deformed and show more reequilibration phenomena associated at a plastic (stretching) and ductile (leakage) strain during burial and/or exhumation (Vityk *et al.*, 2000) that partially removes the primary structures. The presence of Type 3 inclusions with organic matters trapped inside them, testify a not total recrystallization.

b) The white facies shows primary and rare secondary FIs. Primary fluid inclusions (already been observed by Lugli *et al.*, 2007) define chevron structures (Goldstein & Reynolds, 1994) that indicate growth pulses. Each pulse is characterised either by thin layers of less saline salts or by inclusions of brine that were poikilitically enclosed during crystal precipitation. This crystal layering reflects high-frequency of change of the precipitation rate in crystals induced by short-term changes (see chapter 2 for more details on the white facies formation). FIs Type 2 are abundant and there is some doubt on bubble origin. Some authors consider these inclusions as metastable due to reequilibration phenomena and necking down process (Benison & Goldstein, 1999; Speranza *et al.*, 2013), other ones as trapped atmosphere (Benison, 2013); we suppose that the bubble forms or due to slight change of temperature/pressure (nucleation after crystals deposition) or as trapped atmosphere because the crystals show (i) abundant FIs Type 3a (several organic matters trapped) and (ii) faint reequilibration and necking down process that testify a very slight deformation. Microthermometric analysis could clarify this uncertainty (see chapter 4).

c) The transparent facies shows trails of primary FIs and rare secondary inclusions. The trails define chevron morphologies with a low-frequency of pycnocline oscillation than white facies. Abundant FIs Type 3a (several organic matters trapped) indicate a primary origin of this facies, confirmed by faint reequilibration and necking down process.

Banded, White and Transparent facies trap a lot of solids and organic matters that determinate the inclusions shape (from irregular to negative crystal shape). Organic matters could be Dunaliella cells (Sankaranarayanan *et al.*, 2011) and green/yellow microalgae. Solid are investigated using Raman Spectroscopy (see chapter 4)

3.3.2 FIs in the selenite crystals from the Marcellinara quarry

In selenite samples belonging to the banded facies, 1149 FIs (Type 1, n=674; Type 2, n=449; Type 3, n=26) have been observed. The greatest amount of inclusions is trapped in the cloudy intervals because during their formation, the crystals was disturbed by fresh water inflow that generates crystallographic irregularities favouring the entrapment of the inclusions, in contrast, during the clear interval’s formation, the crystals grew a stable environment, trapping occasional FIs. The several FIs shapes observed reflect the crystallographic disorders. For these reasons, FIs frequency, shape and distribution in clear and cloudy intervals are correlated to the crystal growth environment.

All crystals preserve primary features. Necking down process, reequilibration phenomena and fractures have only partially obliterated these structures.

In *Ma Br* sample belonging to the branching facies from the Riato conglomerate, primary structures have been almost completely deleted.

3.3.3 FIs in the selenite crystals from the Benestare quarry

In all selenite samples, FIs study has allowed us to affirm that the crystals have undergone many deformations after their deposition because the few inclusions present are not easily ascribable to primary or secondary origin. Primary structures have been cancelled. These observations make us suppose that this is a secondary and not a primary deposit.

CHAPTER 4. Microthermometric studies

4.1 Introduction

The determination of temperature of phase changes in fluid inclusions during heating and cooling is called microthermometry. The technique is invaluable for discovering the temperature at which minerals form, the thermal history a rock has experienced, and the compositions of the fluids that traversed a rock in its history (Goldstein & Reynolds, 1994), assuming that no modification took place since trapping *e.g.* reequilibration or necking-down processes. Temperature at which minerals form is called Temperature of homogenization (T_H) and can be taken to be a minimum trapping temperature. It can be used in conjunction with the density of the fluid to give the true trapping temperature (T_T). Two hypothetical cases of fluid entrapment, termed "homogeneous entrapment" and "heterogeneous entrapment" can be observed in nature (Diamond, 2003):

- Homogeneous entrapment implies inclusion formation from a one-phase fluid. Other phases, either solid or fluid, may be present locally in the rock during inclusion formation, but only one fluid phase is trapped in the inclusions.
- Heterogeneous entrapment implies that more than one phase is trapped during inclusion formation. The possible trapped phases are two fluids, a fluid and a solid, two fluids and one solid, and so on.

During freezing, a fluid inclusion is cooled below room temperature until the liquid phase becomes solid. The melting point of each solid phase is measured during the subsequent reheating of the solid formed. The temperature at which appears the first liquid (after reheating of the frozen solid) is called Temperature of first melting (T_{FM}). It represents the Eutectic temperature (Te) which provides information on the fluid composition.

The freezing point depression of an aqueous fluid corresponds to the last ice melting temperature (T_{LM}, Shepherd *et al.*, 1985). This is directly proportional to the amount of salt present. The salinity recorded is referred to as “equivalent weight %NaCl” (eq. wt.%NaCl) as it equates to an experimentally determined amount of NaCl in a solution (Shepherd *et al.*, 1985). The data collected at the last ice melting refer to the density of the fluid.

Analytical methods and examples of the full procedure followed during heating and freezing runs for FIs in halite (*images C_1a* and *C_1b*) and selenite (*image C_1c*) crystals are shown in *Appendix C*.

Temperature of first melting allow us to hypnotize the crystals environment formation, in fact, in according to Warren (1999, 2006) and Eugster & Hardie (1978), evaporite origin may be (a) marine, (b) nonmarine or (c) mixed marine-nonmarine brine (hybrid):

(a) Evaporation of seawater produces two types of brine: Na-Cl and Mg-Cl-SO_4. In the salinity range 35-330‰ Na-Cl dominate, while at higher salinities the brine become progressively dominated by Mg-Cl-SO_4, as a result of the preferential removal of Na by halite precipitation. While Mg becomes the dominant cation at higher salinities, follow by K, chloride remains the dominant anion throughout the evaporation sequence.

(b) Evaporation of nonmarine brine produces five major water types in continental evaporite basins:

1. Ca-Mg-Na (K)-Cl
2. Na-(Ca)-SO_4-Cl
3. Mg-Na-(Ca)-SO_4-Cl
4. Na-CO_3
5. Na-CO_3-SO_4-Cl

as any one of these waters concentrates within a particular evaporites basin.

(c) Mixed marine-nonmarine brine are a typical combination of seawater seepage, continental inflow, and hydrothermal spring outflows. These basins could have a composition of Ca-Mg-Na (K)-Cl if it occurs dissolution of older exhumed evaporites.

4.2 Microthermometric investigation

To obtain environmental and chemical information, microthermometric analyses have been carried out on 166 FIs in halite samples and 222 FIs in selenite samples (>15 μm in size).

According to the overall distribution, in primary FIs six different salt system have been recognised as indicated by Shepherd *et al*., (1985).

1) T_{FM} between -60° and -50°C is close to the eutectic temperature of the H_2O-NaCl-$CaCl_2$ system (-55°C);

2) T_{FM} between -54.5° and 44.5°C close to the eutectic temperature of H_2O-$CaCl_2$ system (-49.5°C);

3) T_{FM} between -40° and -30°C is close to the eutectic temperature of H_2O-$FeCl_2$ or H_2O-NaCl-$MgCl_2$ systems (35°C); -35°C is the transition T_{FM} between the iron-rich system and the magnesium-rich one;

4) T_{FM} between -38.6° and -28.6°C is close to the eutectic temperature of H_2O-$MgCl_2$ system (-33.6°C);

5) T_{FM} between -28.5° and -18.5°C is close to the eutectic temperature of the H_2O-NaCl-KCl system (-23.5°C);

6) T_{FM} between -21° and -19°C is close to the eutectic temperatures of systems: H_2O-NaCl-SO_4 (T_{FM}=21.7°C), H_2O-NaCl-$NaHCO_3$ (T_{FM}=21.8°C), H_2O-NaCl-Na_2CO_3 (T_{FM}=21.4°C) and H_2O-NaCl (T_{FM} between -21.2° and -20.8°C).

Using AqSo software, salinity values has been obtained through several formulas based on the phases observed during the heating. In details have been used:

- *Sterner, 1988* for the H_2O-NaCl-KCl system and positive T_{LM} values –oversaturated system in hydrohalite (T_{FM}=between 0° and +0.1°C) or halite (T_{FM} over +0.1°C);
- *Hall, 1987* for the H_2O-NaCl-KCl system and negative T_{LM} values;
- *Oakes, 1990* for H_2O-$CaCl_2$ the system;
- *Dubois & Marignac, 1997* for H_2O-$MgCl_2$ the system;
- *Bodnar, 1993* for all other systems.

4.2.1 The halite samples

In 166 primary FIs observed, the temperature of first ice melting shows a range between -45° and -27°C while the temperature of last ice melting has a range between -1.1° and + 2.8°C corresponding to salinity values from 26 to 26.5 eq. wt% NaCl. Temperature of homogenization displays a range between +20° and +32°C.

In detail are analysed:

(a) **111** FIs in microcrystalline halite samples belonging to the **banded facies** (*Cs 04-17*, *Zi 07-17*, *Ru 17-17* and *Ru 19-17*);

(b) **31** FIs in macrocrystalline halite samples belonging to the **white facies** (*Zi 11-17*);

(c) **26** FIs in macrocrystalline halite samples belonging to the **transparent facies** (*Zi 12-17*).

1) Sample *Cs 04-17* (n= 17 FIs):

T_{FM}= between -37° and -34°C (Type 1, Type 2 and Type 3)

T_{LM}= -1.1°C corresponding to salinity value of 26.1 eq. wt% NaCl (Type 1 and Type 2) and +1.3°C equal to salinity value of 26.5 eq. wt% NaCl (Type 3).

Salt system= H_2O-NaCl-$MgCl_2$ - with variable amount of $FeCl_2$, Na_2CO_3 and K_2CO_3

T_H= +32°C

2) sample *Zi 07-17* (n= 30 FIs):

T_{FM}= between -45° and -34°C (Type 1, Type 2 and Type 3)

T_{LM}= from -0.5° to +1.8°C corresponding to salinity value between 26 and 26.2 eq. wt% NaCl (Type 1, Type 2 and Type 3)

Salt system= H_2O-$MgCl_2$ and H_2O-$FeCl_2$ with variable amount of NaCl, Na_2CO_3 and K_2CO_3

T_H= +20°C

3) sample *Ru 17-17* (n= 18 FIs):

T_{FM}= between -37° and -25°C (Type 1, Type 2 and Type 3)

T_{LM}= from -0.9° to +2.8°C corresponding to salinity value between 26 and 26.2 eq. wt% NaCl (Type 1, Type 2 and Type 3)

Salt system= H_2O-$MgCl_2$ with variable amount of $FeCl_2$, NaCl, Na_2CO_3 and K_2CO_3

T_H= between +33° and +44°C (av. +37°C)

4) sample *Ru 19-17* (n= 46 FIs):

T_{FM}= between -45° and -30°C (Type 1, Type 2 and Type 3)

T_{LM}= from -1.1° to -0.2°C corresponding to salinity value between 26 and 26.2 eq. wt% NaCl (Type 1, Type 2 and Type 3)

Salt system= H_2O-$MgCl_2$ with variable amount of $FeCl_2$, NaCl, Na_2CO_3 and K_2CO_3

T_H= +40°C.

5) sample *Zi 11-17* (n= 31 FIs):

T_{FM}= between -36° and -33°C (Type 1 and Type 2)

T_{LM}= from -1.8° to -1.5°C corresponding to salinity value of 26 eq. wt% NaCl (Type 1, and Type 2)

Salt system= H_2O-$MgCl_2$ with variable amount of NaCl, Na_2CO_3 and K_2CO_3

T_H= between +30° and +33°C.

6) sample *Zi 12-17* (n= 24 FIs):

T_{FM}= between -40° and -32°C (Type 1 and Type 2)

T_{LM}= from -2° to -0.4°C corresponding to salinity value between 26 and 26.2 eq. wt% NaCl (Type 1, and Type 2)

Salt system= H_2O-$MgCl_2$ with variable amount of NaCl, $FeCl_2$, Na_2CO_3 and K_2CO_3

T_H= between +20° and +22°C.

Based on data collected, the distribution of inclusions (Type 1, Type 2 and Type 3), in relation to salinity and T_{FM}, was reported in a scattered graph (Figure 4.1).

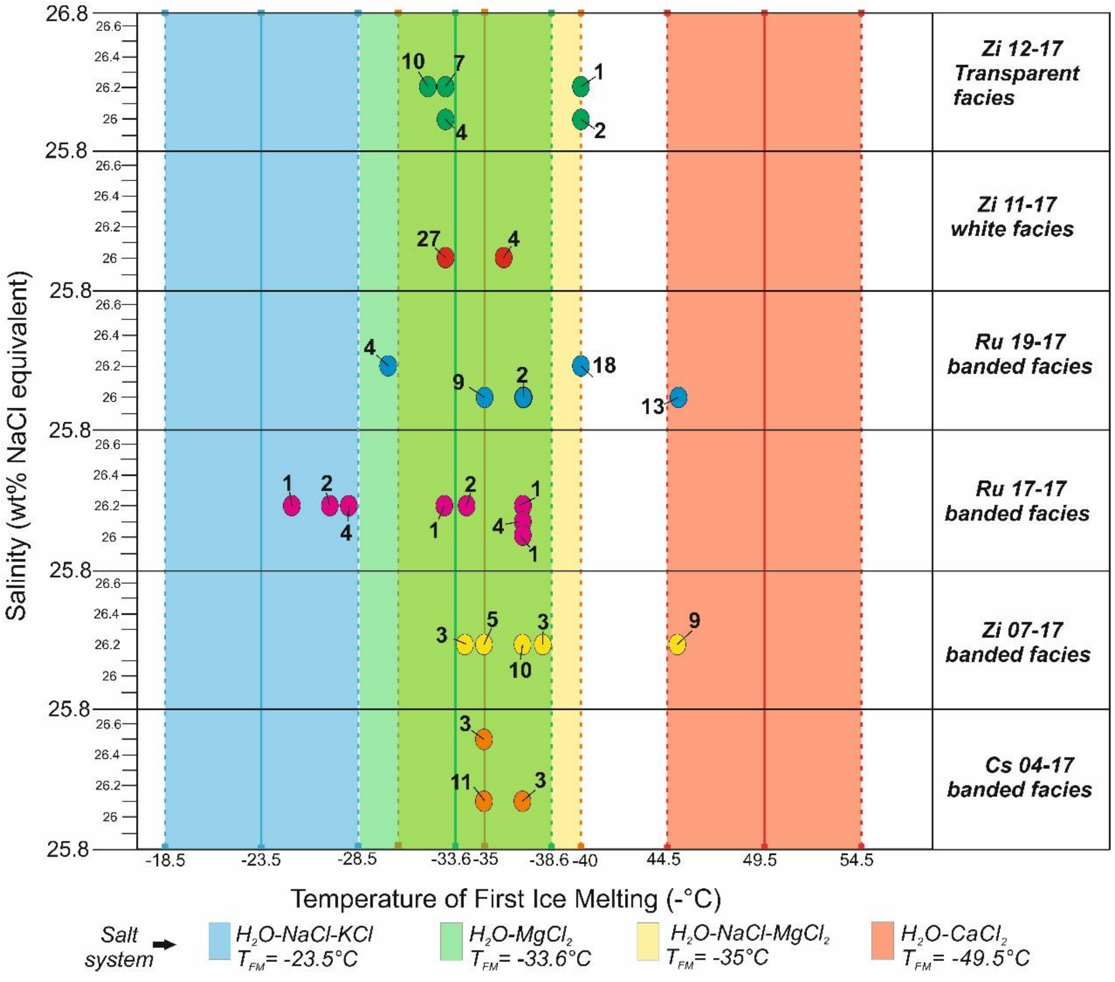

Figure 4.1. Scattered graph of Temperature of First Ice Melting versus Salinity (eq. wt% NaCl) showing the different chemistry of FIs Type 1, 2 and 3 in banded, white and transparent facies. The numbers in the graph indicate the FIs number analysed. Temperature of salt systems are from Shepherd *et al.*, 1985.

Follows a summary Table 1 with T_{FM}, salt system, T_{LM} and salinity obtained in macrocrystalline and microcrystalline halite samples.

T_{FM} °C (range)	N: number of analyses	Salt Systems	T_{LM} °C (range)	Salinity (eq. wt% NaCl)
-45	22	H_2O-$CaCl_2$	-1.1 +0.2	26 – 26.2
-40 - 30	137	H_2O-$MgCl_2$ ±NaCl	-1.3 +1.3	26 – 26.2
-28 -27	7	H_2O-NaCl-KCl	-0.6 +1.1	26.2

Table 1. Summary table showing Temperature of First Melting (T_{FM}), Salt Systems, Temperature of Last Melting (T_{LM}) and Salinity obtained in microcrystalline halite.

Primary Type 3b inclusions containing precipitated daughter phases and trapped solid phases are abundant in halite samples. When multiphase inclusions are heated, daughter minerals begin to dissolve. During analyses, solids trapped have highlighted two behaviours: a group dissolves between +33° and +35°C during heating while a second one does not dissolve below temperature of homogenization (<60°C).

Petrographic observations and Raman spectroscopy analysis carried out on these phases showed the presence of both phases: halite, gypsum, sylvite like as daughter crystals and rare calcite like as trapped solid. Figure 4.2 shows a big inclusion (>50 µm in size) with daughter crystals (mainly gypsum and halite), solid crystal (calcite) and organic matters (strong blue fluorescence under UV light) trapped at the same time. Liquid is composed of H_2O enriched in potassium (K).

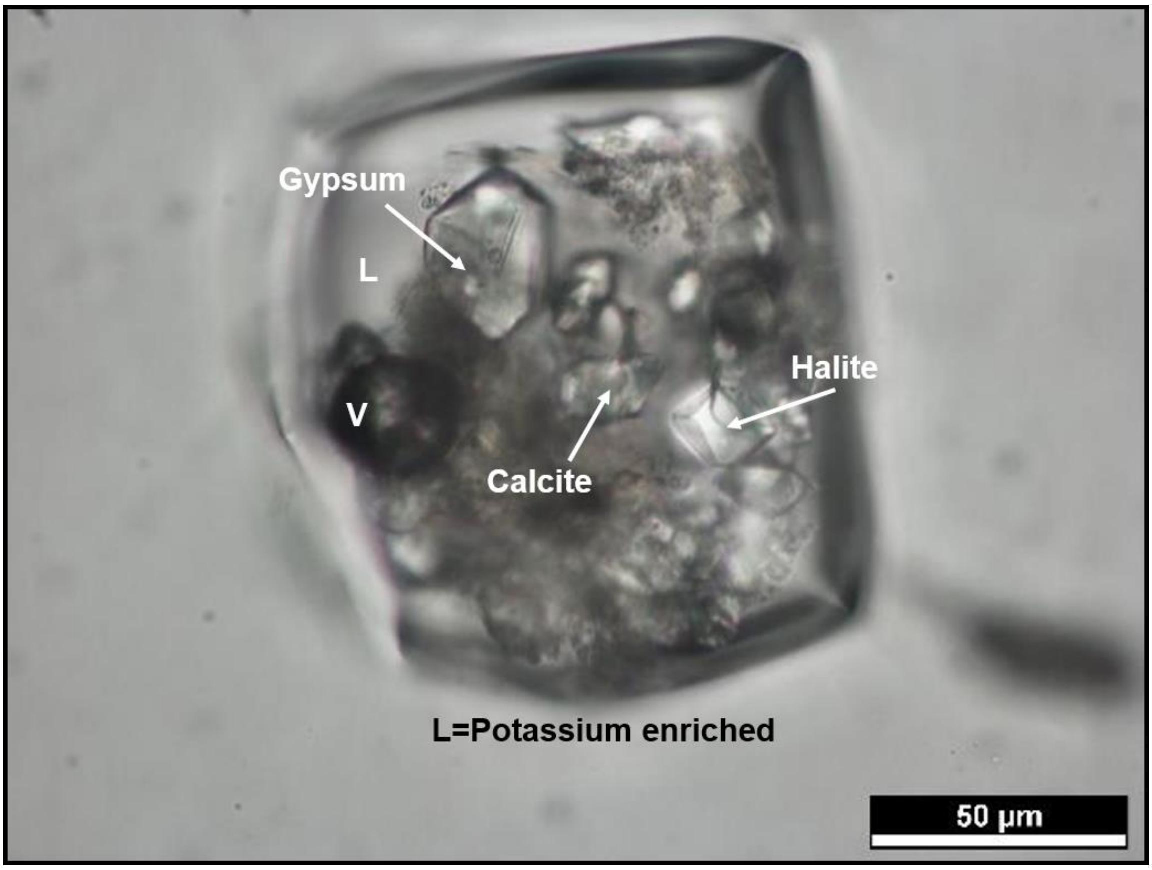

Figure 4.2. Type 3 inclusion with daughter mineral (gypsum and halite) and solid trapped (calcite), immersed in scattered brown materials (organic matters).

Further information on fluid inclusions has been obtained by carrying out semiquantitative analysis conducted with a SEM on fresh rock piece (Figure 4.3). It revealed:

(a) solid made up of Cl (49%), O (22%), K (16%), Mg (10%) and Na (3%) (Figure 4.4a - analysis done in the blue point);

(b) inclusions made up of Cl (63%) and Na (36%) elements (analysis done in the green point) and Cl (57%), Na (12%), Mg (5%) and O (12) as dominant element (Figure 4.4b - analysis in the pink point).

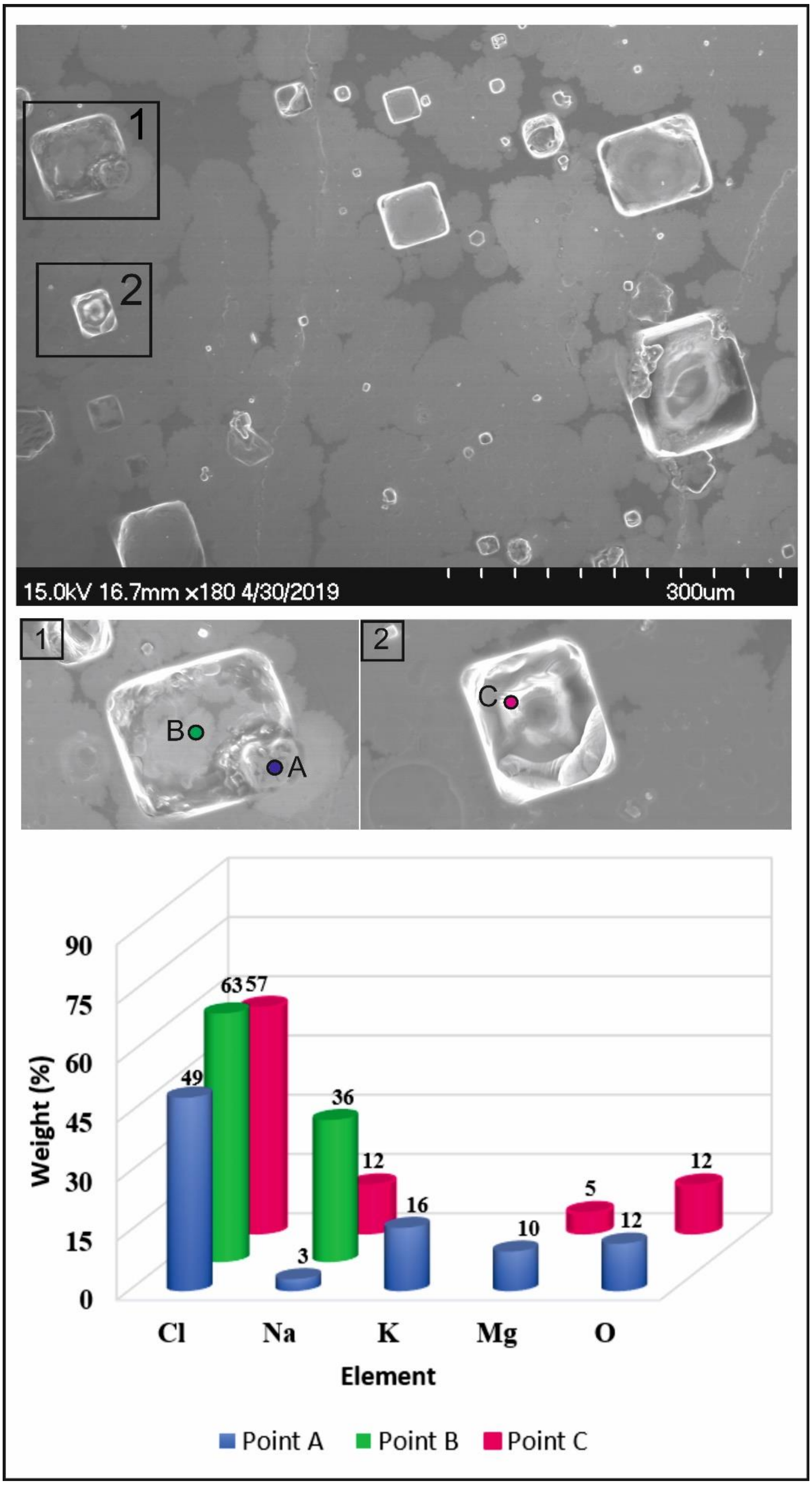

Figure 4.3. Different weight % of elements in FIs Types 2 (A, B and C points) and solid daughter crystal (A point).

4.2.2 The selenite samples (Marcellinara quarry)

222 primary FIs in cloudy and clear intervals from the selenite samples belong to the banded facies located in the sector 5 of the quarry (*Ma 01-17*, *Ma 02-17*, *Ma 03-17*, *Ma 04-17*, *Ma 05-17*, *Ma 06-17*, *Ma 07-17*, *Ma 08-17* and *Ma 09-17*) have been analysed.

Temperature of first ice melting shows range between -58° and -18.5°C, while temperature of last ice melting displays ranges from -9° to + 4°C. Salinity range is between 0.2 and 22.3 eq. wt% NaCl.

Follow a detailed description for each crystal (from the bottom to the crystal's top).

1) In the ***Ma 01-17* sample** (Figure 4.4), microthermometric analysis has been carried out on 26 FIs Type 1 and Type 2 recognised in two clear intervals and in three cloudy intervals. Average salinity value is ~13.2 eq. wt% NaCl in clear intervals and ~3.4 eq. wt % NaCl in cloudy intervals. Total salinity crystal is ~5.1 eq. wt% NaCl.

Interval	**T_{FM} (°C)**	**Salt System**	**T_{LM} (°C)**	**Salinity (eq. wt% NaCl)**
1st Clear (n. 2 FIs)	-33	H_2O-$MgCl_2$	-1.3	~4.55
1st Cloudy (n. 5 FIs)	-25 -23	H_2O-NaCl-KCl	-1.2 -0.4	min: 1 max: 2 (av.~1.5)
	-40	H_2O-NaCl-$MgCl_2$	-2.8 -1.7	min: 3.6 max: 5.6 (av.~4.3)
2nd Clear (n. 2 FIs)	-28 -25	H_2O-NaCl-KCl	-2.7 -0.6	min: 21.6 max: 21.9 (av.~21.8)
2nd Cloudy (n. 4 FIs)	-27	H_2O-NaCl-KCl	-4.4	~7
	-50 -45	H_2O-$CaCl_2$	-1.9 -0.2	min: 0.4 max: 4 (av.~1.7)
3rd Cloudy (n. 13 FIs)	-37.8	H_2O-NaCl-$MgCl_2$	-2.7 -2°	min: 3.4 max: 4.5 (av.~4.1)
	-50 -46	H_2O-$CaCl_2$	-3.8 -0.2	min: 2.2 max: 7.2 (av.~3.5)

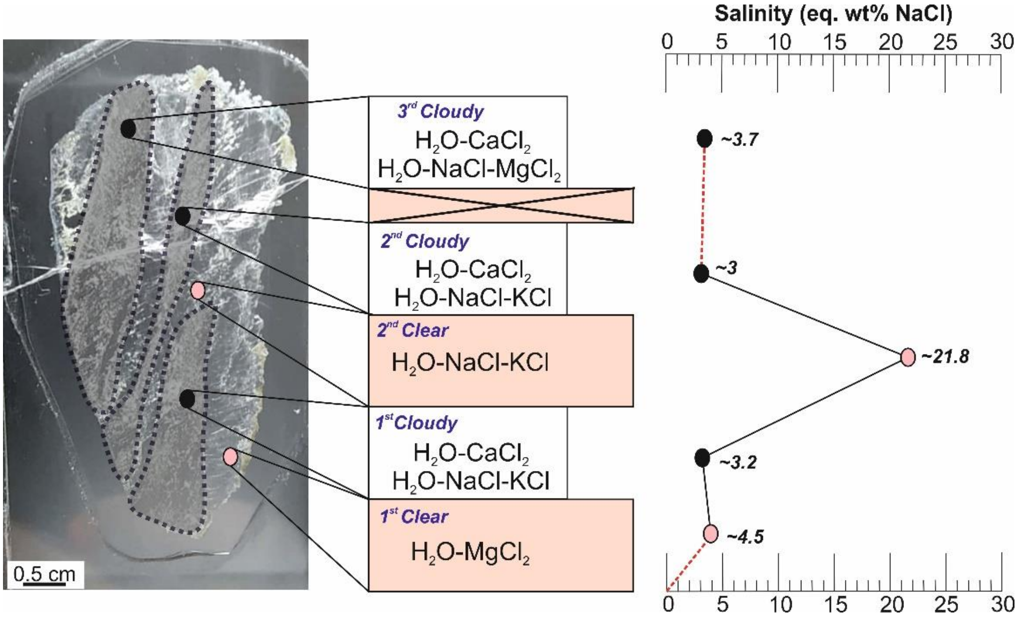

Figure 4.4. *Ma 01-17* sample with salt system composition in three cloudy intervals (white box) and two clear intervals (pink box). On the right salinity average values for each interval. Red dotted lines indicate absence of data.

2) In the ***Ma 02-17* sample** (Figure 4.5), microthermometric analysis has been carried out on 35 FIs Type 1, Type 2 and Type 3 recognised in three clear intervals and in eight cloudy intervals. Average salinity value is ~3.7 eq. wt% NaCl in clear intervals and ~3 eq. wt% NaCl in cloudy intervals. Total salinity crystal is ~3.2 eq. wt% NaCl.

Interval	**T_{FM} (°C)**	**Salt System**	**T_{LM} (°C)**	**Salinity (eq. wt% NaCl)**
1st Cloudy (n. 2 FIs)	-40	H_2O-NaCl-$MgCl_2$	-3	~6
2nd Clear (n. 5 FIs)	-45	H_2O-$CaCl_2$	-1.8 -0.3	min: 0.2 max: 6 (av.~3.3)
	-25	H_2O-NaCl-KCl	-0.1	~0.2
2nd Cloudy (n. 1 FIs)	-33	H_2O-$MgCl_2$	-1.7	~3.7
4th Clear (n. 2 FIs)	-25 -23	H_2O-NaCl-KCl	-0.2 +0.2	~21.9
5th Clear (n. 2 FIs)	-50 -45	H_2O-$CaCl_2$	-0.1 -0.2	min: 0.2 max: 0.5 (av.~0.3)
5th Cloudy (n. 1 FI)	-24	H_2O-NaCl-KCl	-1.7	~2.4
6th Cloudy (n. 1 FI)	-33	H_2O-$MgCl_2$	-2.2	~4.4
9th Cloudy (n. 3 FIs)	-35 -38	H_2O-NaCl-$FeCl_2$	-0.9 -0.3	min: 0.5 max: 1.6 (av. ~1.2)
10th Cloudy (n. 6 FIs)	-47 -45	H_2O-$CaCl_2$	-1.3 -1	min: 2.2 max: 2.8 (av. ~2.3)
11th Cloudy (n. 6 FIs)	-45	H_2O-$CaCl_2$	-2 +2	~4.2
12th Cloudy (n. 6 FIs)	-37	H_2O- NaCl -$MgCl_2$	-2	~3.4
	-49	H_2O-$CaCl_2$	-1.5 -0.8	min: 1.8 max: 3.2 (av. ~2.6)

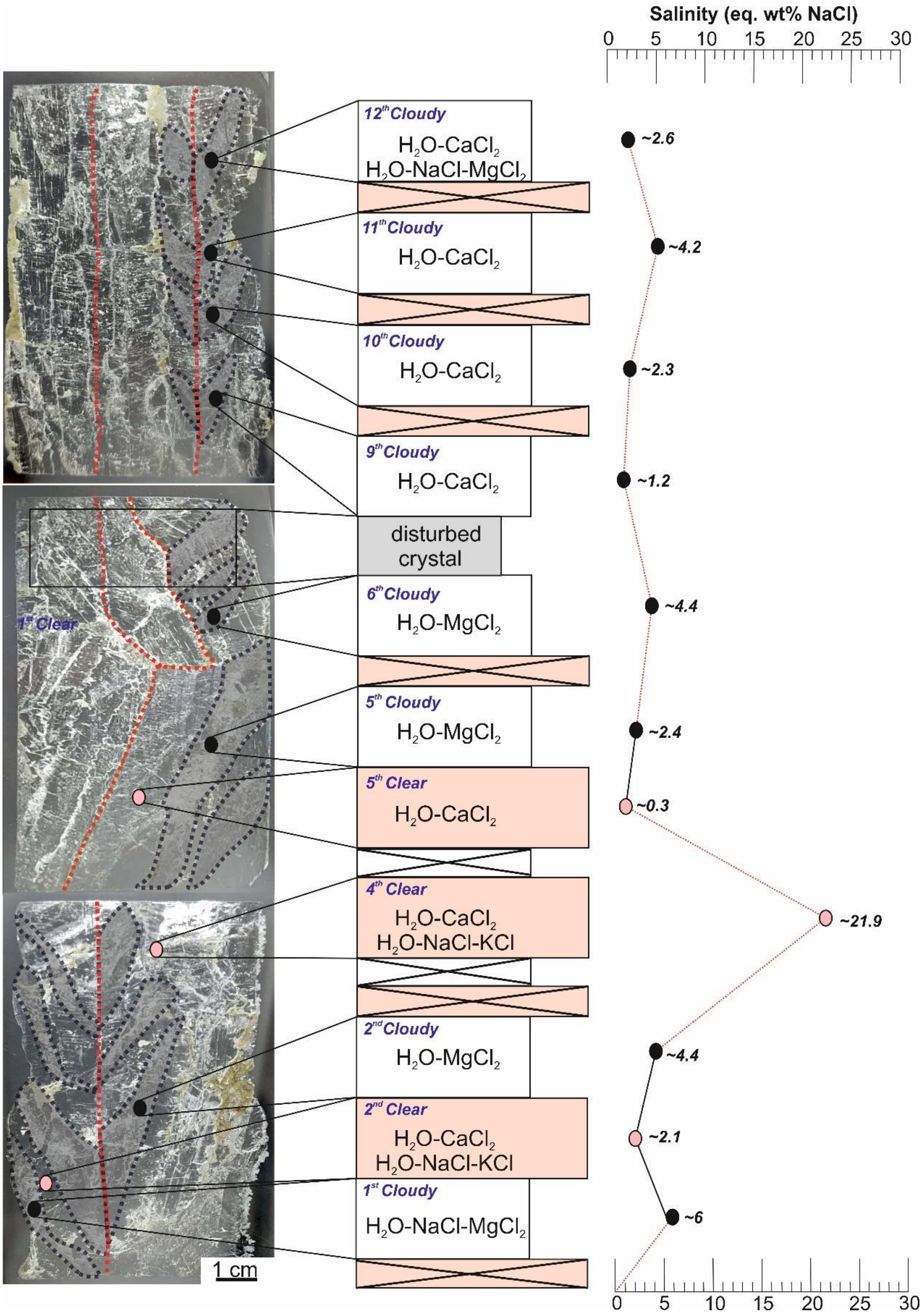

Figure 4.5. *Ma 02-17* sample with salt system composition in eight cloudy intervals (white box) and three clear intervals (pink box). On the right salinity average values for each interval. Red dotted lines indicate absence of data.

3) In the ***Ma 03-17* sample** (Figure 4.6), microthermometric analysis has been carried out on 18 FIs Type 1 and Type 2 recognised in one clear interval and in three cloudy intervals. Average salinity value is ~21 eq. wt% NaCl in clear intervals and ~3.7 eq. wt% NaCl in cloudy intervals. Total salinity crystal is ~4.8 eq. wt% NaCl.

Interval	**T_{FM} (°C)**	**Salt System**	**T_{LM} (°C)**	**Salinity (eq. wt% NaCl)**
1st Clear (n. 3 FIs)	-28	H_2O-NaCl-KCl	+0.4	~21
1st Cloudy (n. 2 FIs)	-33	$H_2O-MgCl_2$	-1.4 -0.4	min: 1.8 max: 3.2 (av. ~2.5)
2nd Cloudy (n. 8 FIs)	-25	H_2O-NaCl-KCl	-4.3	~6.8
	-30	$H_2O-MgCl_2$	-0.5	~1.4
	-51 -45	$H_2O-CaCl_2$	-3 -2.6	min: 3.6 max: 5 (av. ~3.8)
3rd Cloudy (n. 5 FIs)	-23 -19	H_2O-NaCl-KCl (prevalent) ±Na_2SO_4; ±$NaHCO_3$- ±Na_2CO_3	-3 -1.7	min: 2.7 max: 4.8 (av. ~3.7)
	-52	$H_2O-CaCl_2$	-2.32	~4.7
	-38	H_2O- NaCl-$MgCl_2$	-2.7 -1.8	min: 3 max: 4.5 (av. ~3.7)

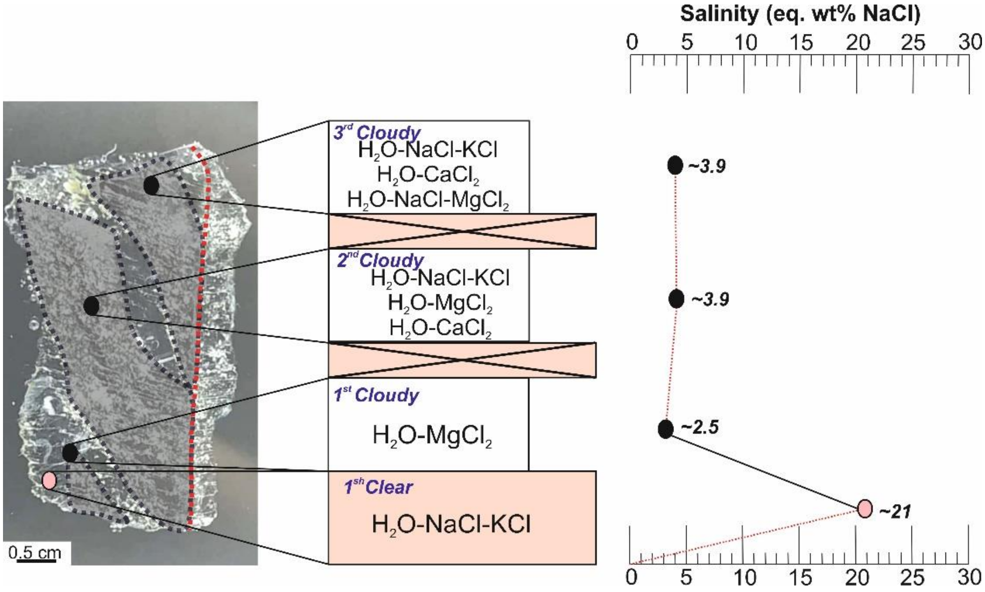

Figure 4.6. *Ma 03-17* sample with salt system composition in three cloudy intervals (white box) and one clear interval (pink box). On the right salinity average values for each interval. Red dotted lines indicate absence of data.

4) In the ***Ma 04-17* sample** (Figure 4.7), microthermometric analysis has been carried out on 10 FIs Type 1 and Type 2 recognised in one clear interval and in four cloudy intervals. Average salinity value is ~21.8 eq. wt% NaCl in clear intervals and ~3.7 eq. wt% NaCl in cloudy intervals. Total salinity crystal is ~7.3 eq. wt% NaCl.

Interval	**T_{FM} (°C)**	**Salt System**	**T_{LM} (°C)**	**Salinity (eq. wt% NaCl)**
3rt Clear (n. 2 FIs)	-28	H_2O-NaCl-KCl	-1.1	~21.8
1st Cloudy (n. 1 FI)	-33	H_2O-$MgCl_2$	-1.8	~0.4
2nd Cloudy (n. 1 FI)	-27	H_2O-NaCl-KCl	-0.8	~1.3
3rd Cloudy (n. 3 FIs)	-30	H_2O-$MgCl_2$	-2	~4.2
4th Cloudy (n. 3 FIs)	-35 - 31	H_2O-$MgCl_2$	-3 -2.5	min: 5 max: 5.5 (av. ~5.1)

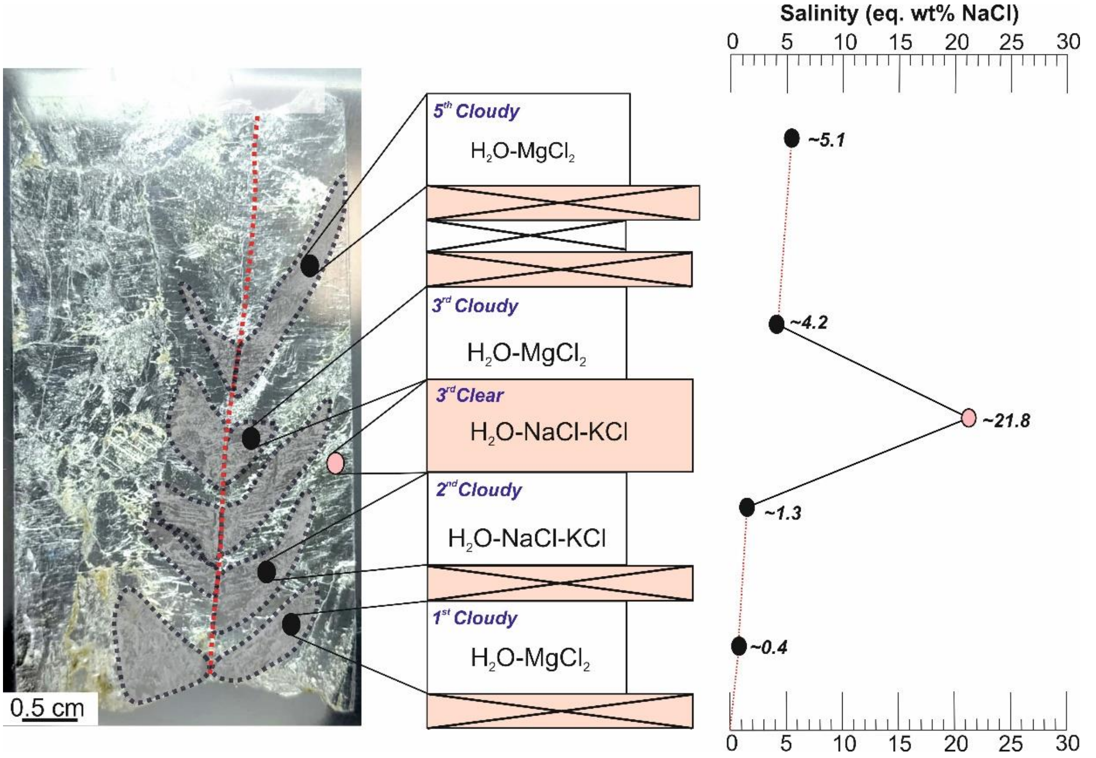

Figure 4.7. *Ma 04-17* sample with salt system composition in four cloudy intervals (white box) and one clear interval (pink box). On the right salinity average values for each interval. Red dotted lines indicate absence of data.

5) In the ***Ma 05-17* sample** (Figure 4.8), microthermometric analysis has been carried out on 10 FIs Type 1 and Type 2 recognised in only four cloudy intervals. Average salinity value is ~2.8 eq. wt% NaCl.

Interval	**T_{FM} (°C)**	**Salt System**	**T_{LM} (°C)**	**Salinity (eq. wt% NaCl)**
1st Cloudy (n. 3 FIs)	-37	H_2O- $NaCl$-$MgCl_2$	-1.3	~2.2
	-32	H_2O-$MgCl_2$	-0.8	~2
2nd Cloudy (n. 2 FIs)	-37	H_2O- $NaCl$-$MgCl_2$	-2.3	~3.9
	-34	H_2O-$MgCl_2$	-1.5	~3.4
3rd Cloudy (n. 3 FIs)	-34	H_2O-$MgCl_2$	-2.5	~4.8
4th Cloudy (n. 2 FIs)	-44	H_2O-$CaCl_2$	-0.2	~0.5

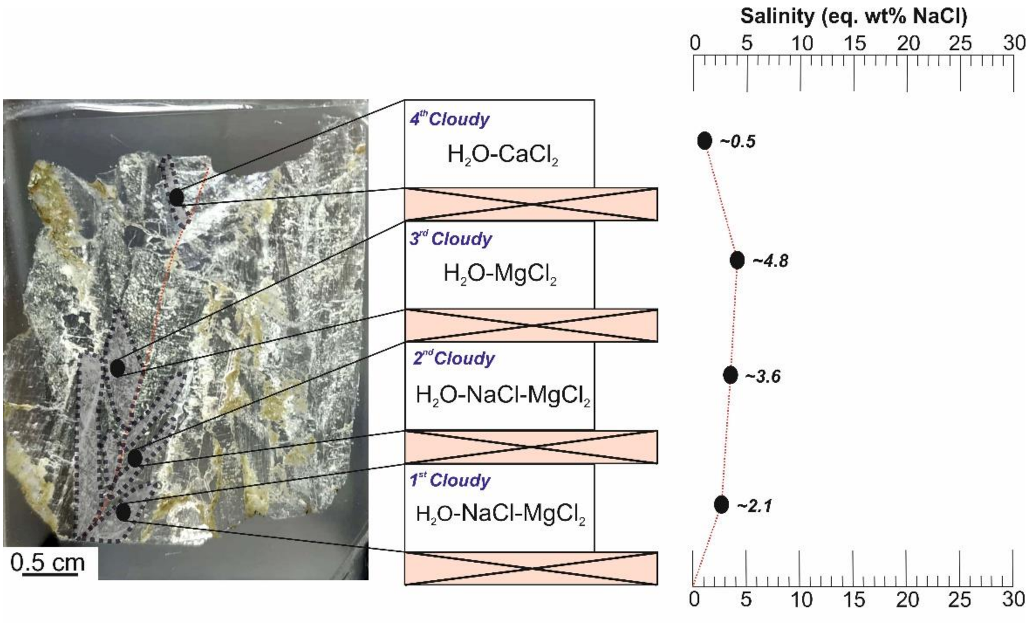

±

Figure 4.8. *Ma 05-17* sample with salt system composition in four cloudy intervals (white box) and respective salinity average values on the right. Red dotted lines indicate absence of data in clear intervals.

6) In the ***Ma 06-17* sample** (Figure 4.9) microthermometric analysis has been carried out on 27 FIs Type 1 and Type 2 recognised in two clear intervals and in five cloudy intervals. Average salinity value is ~21.8 eq. wt% NaCl in clear intervals and ~2.4 eq. wt% NaCl in cloudy intervals. Total salinity crystal is ~14 eq. wt% NaCl.

Interval	**T_{FM} (°C)**	**Salt System**	**T_{LM} (°C)**	**Salinity (eq. wt% NaCl)**
1st Clear (n. 8 FIs)	-23	H_2O-NaCl-KCl	+0.8 4	~22
1st Cloudy (n. 2 FIs)	-52	H_2O-KCl-$CaCl_2$ or H_2O-$CaCl_2$	-3 -0.9	min: 2 max: 6 (av. ~4)
2nd Clear (n. 4 FIs)	-23 -20	H_2O-NaCl-KCl ±Na_2SO_4; ±$NaHCO_3$; ±Na_2CO_3	-0.9 +0.8	min: 21.3 max: 21.8 (av. ~21.4)
2nd Cloudy (n. 7 FIs)	-45	H_2O-$CaCl_2$	-4	~7.5
3rd Cloudy (n. 3 FIs)	-52 -46	H_2O-$CaCl_2$	-3.1 -0.3	min: 0.7 max: 6.1 (av. ~2.5)
4th Cloudy (n. 2 FIs)	-40	H_2O-NaCl-$MgCl_2$	-4	~0.7
5th Cloudy (n. 1 FI)	-48	H_2O-$CaCl_2$	-2.9	~2

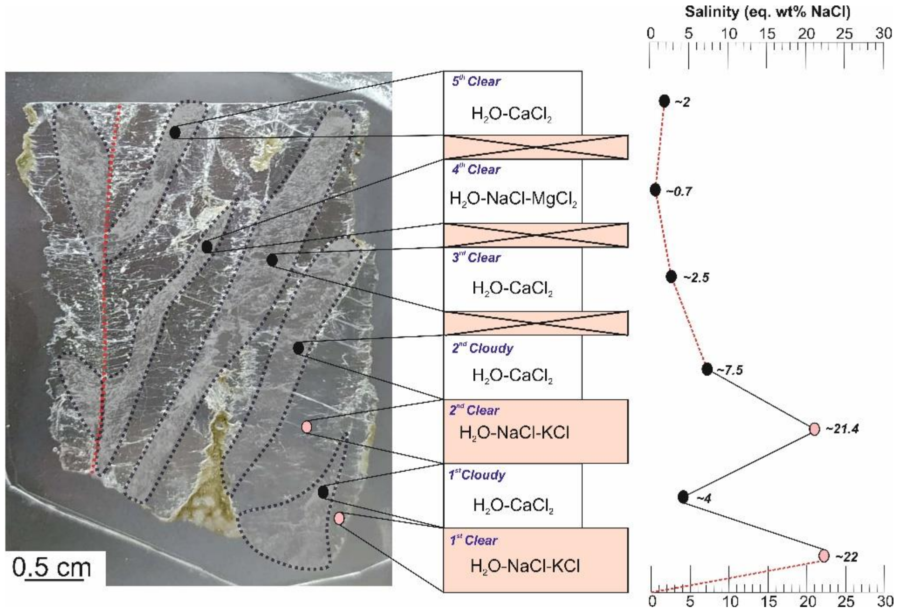

Figure 4.9. *Ma 06-17* sample with salt system composition in five cloudy intervals (white box) and two clear intervals (pink box). On the right salinity average values for each interval. Red dotted lines indicate absence of data.

7) In the ***Ma 07-17* sample** (Figure 4.10), microthermometric analysis has been carried out on 13 FIs Type 1 and Type 2 recognised in two clear intervals and in two cloudy intervals. Average salinity value is ~4 eq. wt% NaCl in clear intervals and ~3.9 eq. wt% NaCl in cloudy intervals. Total salinity crystal is ~4 eq. wt% NaCl.

Interval	**T_{FM} (°C)**	**Salt System**	**T_{LM} (°C)**	**Salinity (eq. wt% NaCl)**
2^{nd} Clear (n. 2 FIs)	-51	H_2O-$CaCl_2$	-1.8	~3.8
	-33	H_2O-$MgCl_2$	-3.5	~6.1
2^{nd} Cloudy (n. 3 FIs)	-49 -46	H_2O-$CaCl_2$	-1.3	min: 2.8 max: 5.6 (av. ~3.7)
3^{rd} Clear (n. 3 FIs)	-52 -45	H_2O-$CaCl_2$	-2.3 -0.5	min: 1.1 max: 4.7 (av. ~3.3)
3^{rd} Cloudy (n. 5 FIs)	-35	H_2O-$MgCl_2$	-3 -1.5	min: 3.4 max: 5.5 (av. ~4)

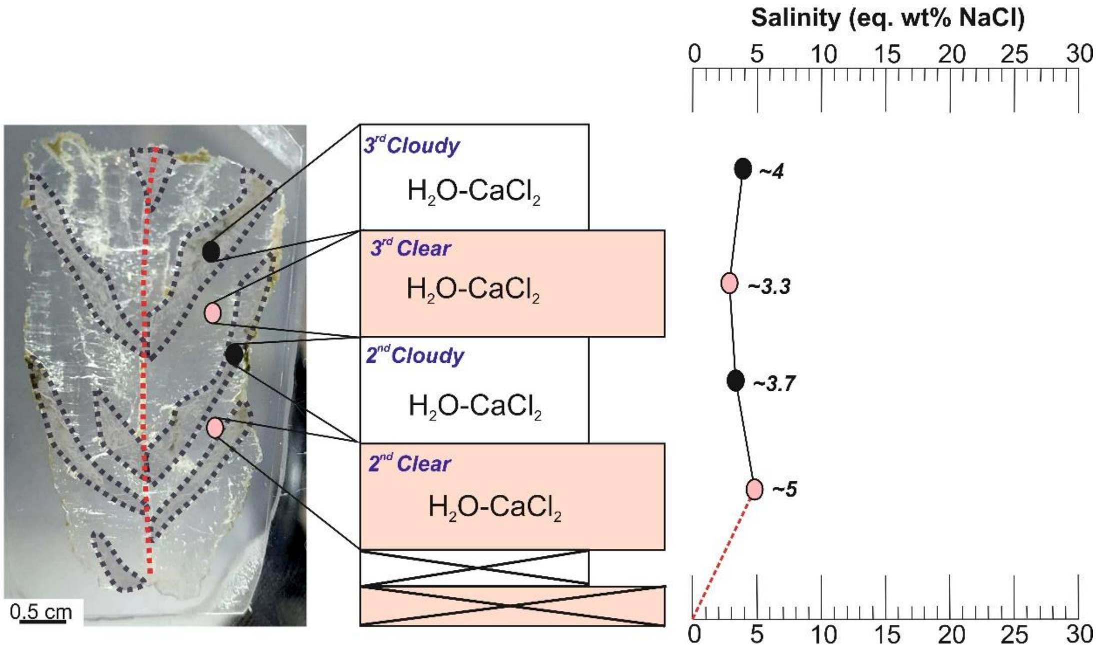

Figure 4.10. *Ma 07-17* sample with salt system composition in two cloudy intervals (white box) and two clear intervals (pink box). On the right salinity average values for each interval. Red dotted lines indicate absence of data.

8) In the ***Ma 08-17* sample** (Figure 4.11), microthermometric analysis has been carried out on 63 FIs Type 1 and Type 2 recognised in three clear intervals and in seven cloudy intervals. Average salinity value is ~4 eq. wt% NaCl in clear intervals and ~3.9 eq. wt% NaCl in cloudy intervals. Total salinity crystal is ~8.8 eq. wt% NaCl.

Interval	**T_{FM} (°C)**	**Salt System**	**T_{LM} (°C)**	**Salinity (eq. wt% NaCl)**
1st Clear (n. 3 FIs)	-23	H_2O-NaCl-KCl	-2.7	~22.1
1st Cloudy (n. 4 FIs)	-40 -37	H_2O-NaCl-$MgCl_2$	-0.8 -0.2	min: 0.4 max: 1.4 (av. ~0.8)
2nd Cloudy (n. 1 FIs)	-26	H_2O-NaCl-KCl	-4	~6.3
3rd Cloudy (n. 11 FIs)	-45	H_2O-$CaCl_2$	-1.3 -0.4	min: 1 max: 2.8 (av. ~2)
5th Clear (n. 2 FIs)	-23	H_2O-NaCl-KCl	-1 -0.2	~21.9
6th Cloudy (n. 6 FIs)	-33	H_2O-$MgCl_2$	-2	~4.2
	-37	H_2O-NaCl-$MgCl_2$	-1	~1.7
7th Cloudy (n. 8 FIs)	-34 -33	H_2O-$MgCl_2$	-2.8 -1	~2.5
	-40 -38	H_2O-NaCl-$MgCl_2$	-2 -0.7	min: 1.2 max: 3.4 (av. ~1.9)
8th Cloudy (n. 10 FIs)	-27	H_2O-NaCl-KCl	-1.5	~2.4
	-30	H_2O-$MgCl_2$	-2	~4.2
	-36	H_2O-NaCl-$MgCl_2$	-1	~1.7
9th Clear (n. 15 FIs)	-28	H_2O-NaCl-KCl	+2 +4.4	22.1
9th Cloudy (n. 3 FIs)	-40 -37	H_2O-NaCl-$MgCl_2$	-2.5 -1.6	min: 2.7 max: 4.2 (av. ~3.4)

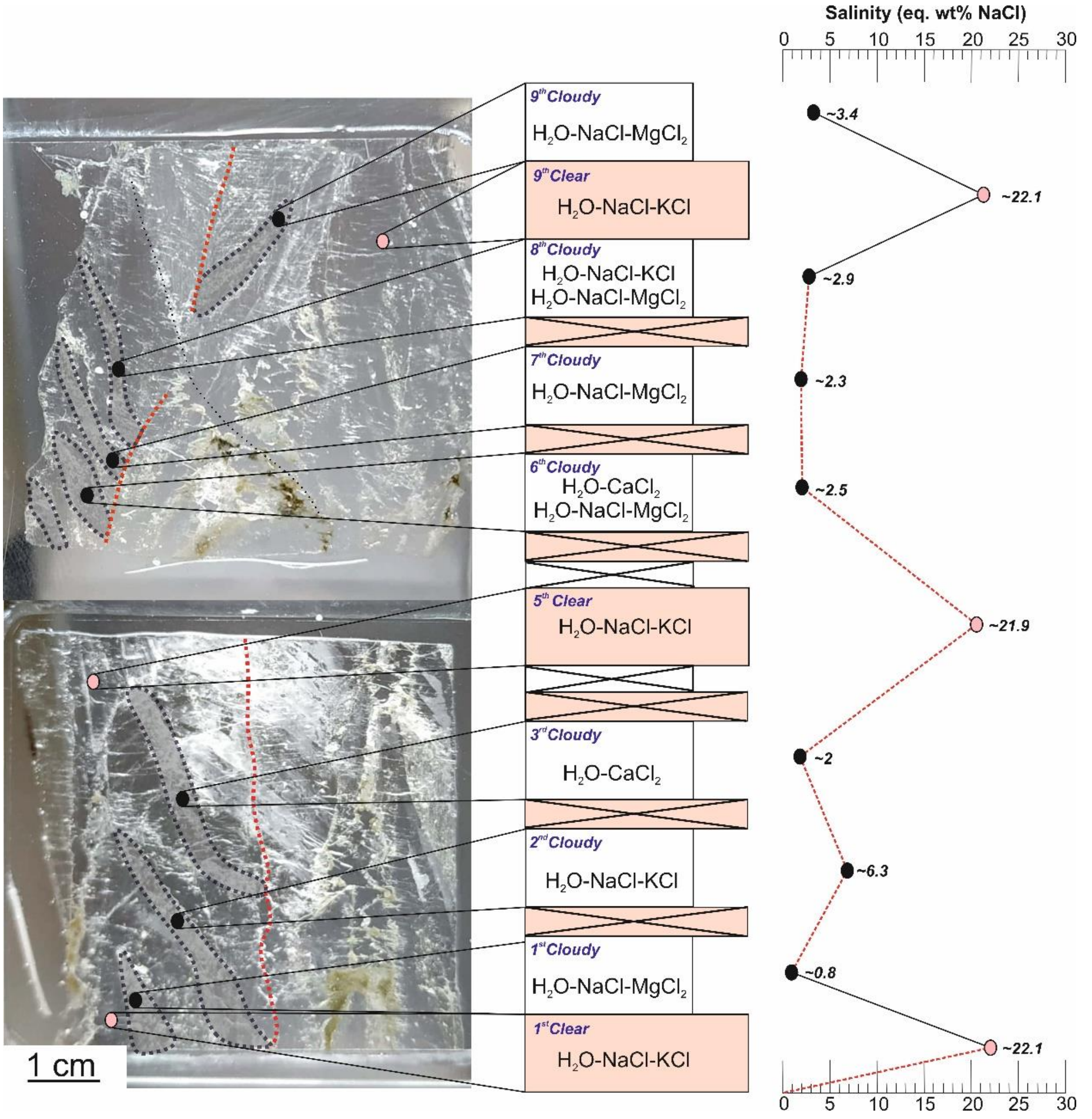

Figure 4.11. *Ma 08-17* sample with salt system composition in seven cloudy intervals (white box) and three clear intervals (pink box). On the right salinity average values for each interval. Red dotted lines indicate absence of data.

9) In the ***Ma 09-17* sample** (Figure 4.12), microthermometric analysis has been carried out on 21 FIs Type 1 and Type 2 recognised in three clear intervals and in five cloudy intervals. Average salinity value is ~21.9 eq. wt% NaCl in clear intervals and ~5.2 eq. wt% NaCl in cloudy intervals. Total salinity crystal is ~8 eq. wt% NaCl.

Interval	**T_{FM} (°C)**	**Salt System**	**T_{LM} (°C)**	**Salinity (eq. wt% NaCl)**
1st Clear (n. 2 FIs)	-24	H_2O-NaCl-KCl	-2.4	~21.7
1st Cloudy (n. 3 FIs)	-50	H_2O-$CaCl_2$	-2.4 -0.8	min: 2 max: 5 (av. ~3)
2nd Cloudy (n. 3 FIs)	-47	H_2O-$CaCl_2$	-2.8 -2.3	min: 4.7 max: 5.6 (av. ~5)
3rd Clear (n. 1 FI)	-37	H_2O- NaCl-$MgCl_2$	-4.2	~6.7
3rd Cloudy (n. 1 FI)	-58	H_2O-NaCl-$CaCl_2$	-1.3	~2.2
4th Cloudy (n. 3 FIs)	-47	H_2O-$CaCl_2$	-3.4 –1.5	min: 3.4 max: 6.6 (av. ~4.6)
5rd Clear (n. 2 FIs)	-26	H_2O-NaCl-KCl	+3.4	~22.3
5h Cloudy (n. 5 FIs)	-50 -47	H_2O-$CaCl_2$	-4.5 -3.5	min: 6.7 max: 8.2 (av. ~6.6)
6th Clear (n. 1 FI)	-28	H_2O-NaCl-KCl	-1.6	~21.8

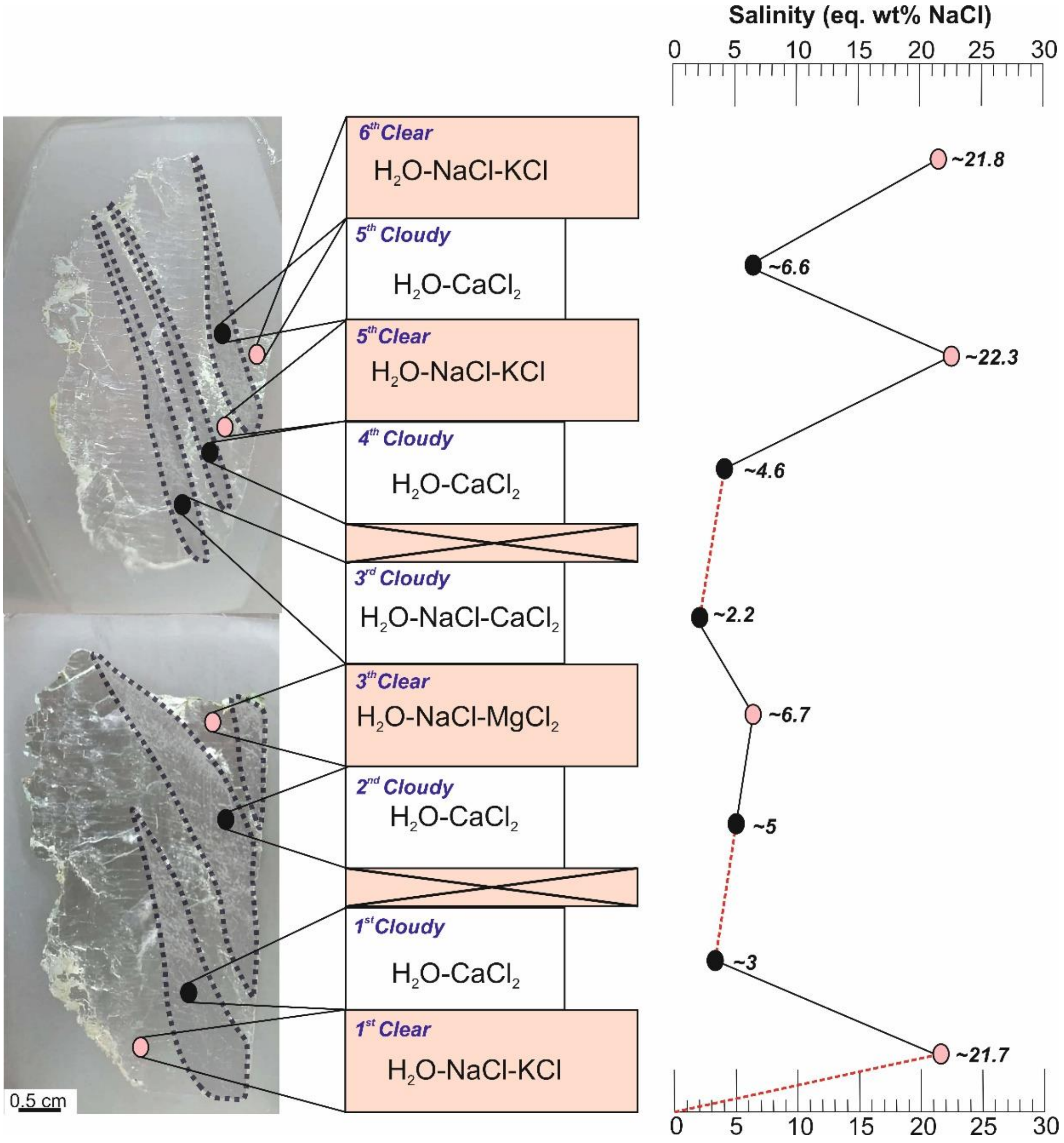

Figure 4.12. *Ma 09-17* sample with salt system composition in five cloudy intervals (white box) and three clear intervals (pink box). On the right salinity average values for each interval. Red dotted lines indicate absence of data.

Moreover, salinity values from all selenite crystals (clear and cloudy intervals – Figure 4.13) are compared with those of Natalicchio *et al.*, (2014), for Messinian gypsum from the North Italy (Lower Gypsum – without discriminating between two microfacies). Salinity values from cloudy intervals are very similar because they fit into carbonate precipitation field and show low salinity values, in the contrast, salinity values recorded in clear intervals show high values and fit into gypsum precipitation field. Few inclusions observed in clear intervals showing low salinity values could be pseudo-secondary or secondary in origin or testify a different brine condition due to climate changes.

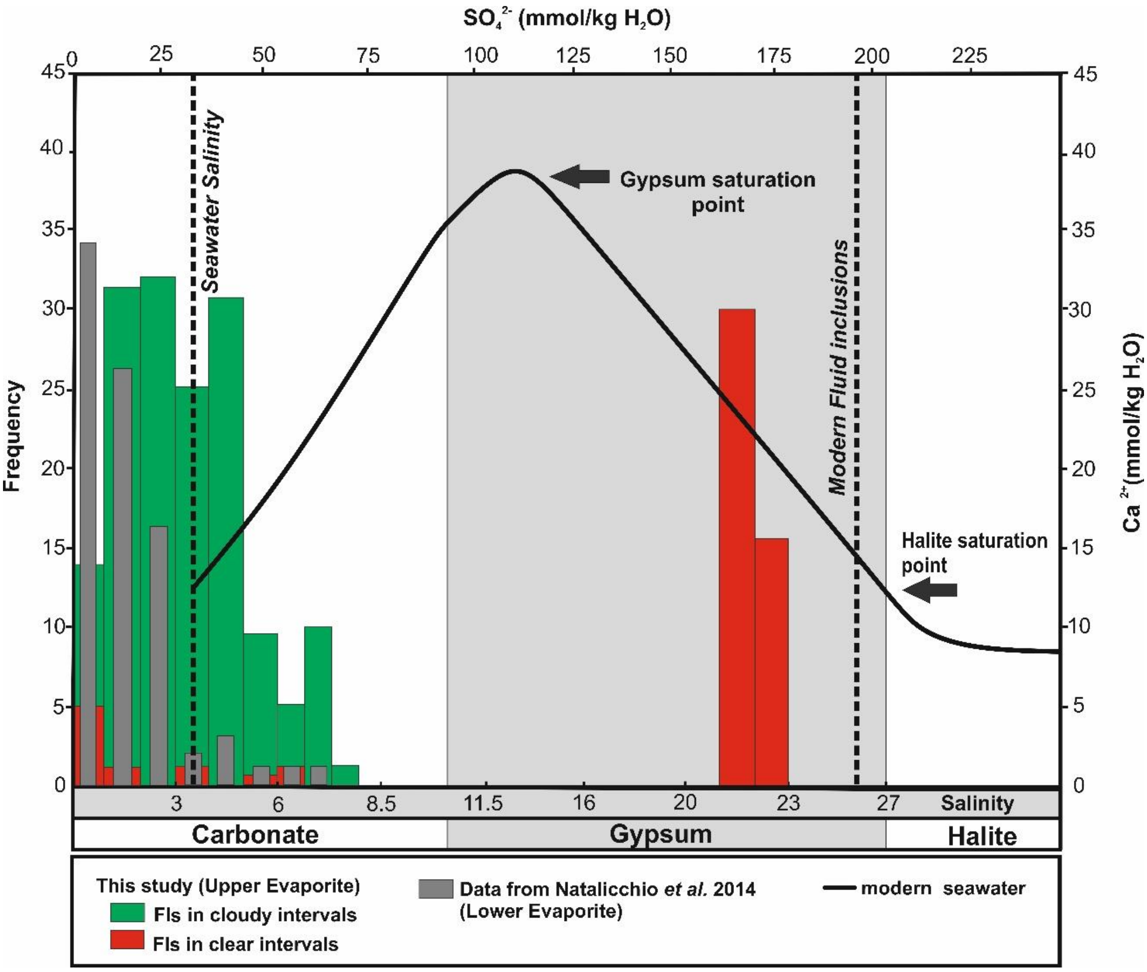

Figure 4.13. Salinity values obtained in cloudy (in green colour) and clear (in red colour) intervals compared with those of Natalicchio *et al.*, (2014) in grey colour (modified from Natalicchio *et al.*, 2014).

4.3 Discussions

The microthermometric results have highlighted four key achievements:

a) the possibility to obtain the microthermometric parameters from different FIs Types:

- microthermometric analyses carry out on FIs Type 1 and Type 2 observed in the same assemblage, provide identical results. This testify that the bubble trapped is not the result of strong metastability. In microcrystalline halite (banded facies) could be air trapped, while for the macrocrystalline halite and the selenite samples could be **(i)** air trapped (Benison, 2013), **(ii)** an artefact product of inclusion stretching for small variations in temperature and pressure (Ayllón-Quevedo *et al.*, 2007) or even, **(iii)** the bubble could derive from the presence of small impurities in heterogenous entrapment condition (Tecce *et al.*, 2016). This would explain the presence of abundant FIs Type 2 in those parts of the crystal rich in organic matters and/or clay minerals (e.g. cloudy intervals in the selenite samples). Instead, values not always comparable were obtained from FIs Type 3, perhaps due to the presence of minerals (daughter and solids trapped) which melting increase the salinity of the system;

b) in these evaporite samples the analysis is reproducible but not replicable:

- halite and selenite are minerals subject to easy alteration and subjected to multiple cycles of cooling and heating have shown distortions on the inclusions rim and an increased in~3-5°C of the T_{FM} and T_{LM} values for each repetition cycle;

c) an accurate observation of phases that formed and dissolved during cooling/heating permit to use several formulas typical of the salt system observed:

- the identification of hydrohalite during heating (through the birefringence colour, the shape and T_{LM} value), is important to estimate the salinity values (especially in the selenite crystals). In fact, the presence of Hydrohalite involves a shift towards the phase constituted by Hydrohalite+Liquid (HH+Liq) in the H_2O-NaCl phase diagram (hypnotized a pure system). In this filed you cannot use the formulas for low salinity systems (Ice+Liquid field in the phase diagram) used by Hall (1987), Oakes, (1990), Dubois & Marignac (1997) and Bodnar (1993) but it is more appropriate to use the formula of Sterner, (1988) for high salinity system. The formulas used by Hall (1987) for H_2O-NaCl-KCl system at low salinity, Oakes, (1990) for H_2O-$CaCl_2$ system and Dubois & Marignac (1997) for H_2O-$MgCl_2$ system, return analogous salinity values compared with the values obtained by Bodnar (1993) for all low salinity systems (*see Appendix C_2:* Binary system H_2O-NaCl – salinity in the cloudy and clear intervals (selenite crystals)).

d) brine composition obtained allow us to hypnotize the environment formation of the crystals

4.3.1 Brine composition and depositional environment

In the halite samples, the distribution of the data points shows that Na, Cl, Mg, K and Ca are the dominant elements in the inclusions, while Fe and CO_3 are present but in minor amount. The brine could have a nonmarine or hybrid origin. However, salinity recognised in all FIs (from different facies) shows a range between 26 and 26.5 eq. wt% NaCl which can be associated with salinity of the "*Penesaline brine stage"* (25 to 35 eq. wt% NaCl) that is formed in marine setting (Warren, 1999, 2006). In light of the acquired data, it is believed that:

(a) the chemical composition and salinity of the brine could have a hybrid origin;

(b) hybrid brine could have originated where the water varies from fresh (river/rain) to marine, and consequently, the halite deposits could have formed in a coastal-marine environment.

(c) facies types are not affected by variation of salinity. In fact, the salinity value is similar for all three facies. This allows to think that the different formation of banded, white and transparent facies could be attributed at the different depth to which the crystal grew, associated with the pycnocline oscillations and evaporation rate (function of air temperature, relative humidity and wind velocity);

(d) pycnocline oscillations and evaporation rate could explains the different T_H values found in the three facies, in fact in according with facies origin (see chapter 2):

-the banded facies shows temperature of homogenization between +20° and +32°C (average value ~ 26°C). The high temperature could be associated with strong evaporation on the air-brine interface.

-the white facies shows temperature of homogenization from +30° to +33°C (average value ~ 31.5°C), associated with fast pycnocline oscillations (pulse growth - daily or seasonal) and high temperature.

-the transparent facies shows temperature of homogenization between +20° and +22°C (average value ~ 21°C). This facies grows on the top of the white facies and show a minor number of pycnocline oscillation.

Temperature of homogenization values of the white facies (average T_H ~ 31.5°C) disagree with those recognised of Speranza *et al*., (2013) (average T_H ~ 21°C). We believe that this is due to the pulsing crystals growth (see chapter 3) associated at different seasonal intervals (winter/summer oscillation).

Moreover, in this discussion, are not considered the high T_H values found in *Ru 17-17* and *Ru 19-17* samples, most likely due to active tectonic phenomena (Speranza *et al.*, 2013).

Solid trapped in inclusions showed two behaviours: a group dissolve between +33° and +35°C during heating while a second group did not undergo dissolution below the maximum temperature reached (maximum T_H 60°C). Petrographic observations and Raman and SEM analyses in according with Wang & Lowenstein (2017), leads us to believe that the first group is made of sylvite crystals as daughter phase (dissolution temperature between 20-83°C), while the second group is probably made up of carnallite ($MgCl_2 \cdot KCl \cdot 6H_2O$) and/or carnallite+sylvite crystals as daughter phases (dissolution temperature >60°C). These crystals are in according with Ca-Mg-Na (K)-Cl brine composition.

<u>In the selenite samples</u> the distribution of the data points shows that NaCl, KCl, $MgCl_2$, $FeCl_2$ and $CaCl_2$ are the dominant phases in the inclusions while Na_2SO_4, $NaHCO_3$ and Na_2CO_3 are also present but in minor amount. As in the halite samples, this composition testifies an hybrids origin brine, but unlike the latter, in selenite crystals the different water input is more evident due to the presence of cloudy and clear interval. In fact, the data obtained show that:

-clear intervals are enriched in NaCl and KCl and allow to suppose an input of marine water (high salinity values – av.~ 16 eq. wt% NaCl) or a moment without continental inflow;

-cloudy intervals are enriched in Mg and Ca and testify a nonmarine setting (low salinity values – av.~3 eq. wt% NaCl);

58 salinity variations have been documented throughout the outcrop, which makes us to suppose that proportion of fresh water, that fed the system, was recurring over time. The salinity oscillations are well shown in Figure 4.14, where the black, green and red lines are respectively the average salinity values of the nine selenite cycles, of the cloudy intervals (linear trail) and of the clear intervals (irregular trend). Dotted lines indicate absence of data. When salinity values are different in the clear intervals belonging to the same crystals, it can be assumed that, the FIs with low salinity are pseudo-secondary or secondary in origin.

The seasonal effect is also evident in those crystals that have been folded by the brine current. In these crystals the salinity values dropping testifying a more brine dilution because of abundant continental water inflow, with the exception of the sample *Ma 08-17* which, although folded, has many fluid inclusions and conserves a higher salinity than the others. Probably the brine current that flowed into the basin bent the crystal, but being low flow did not significantly lower the salinity.

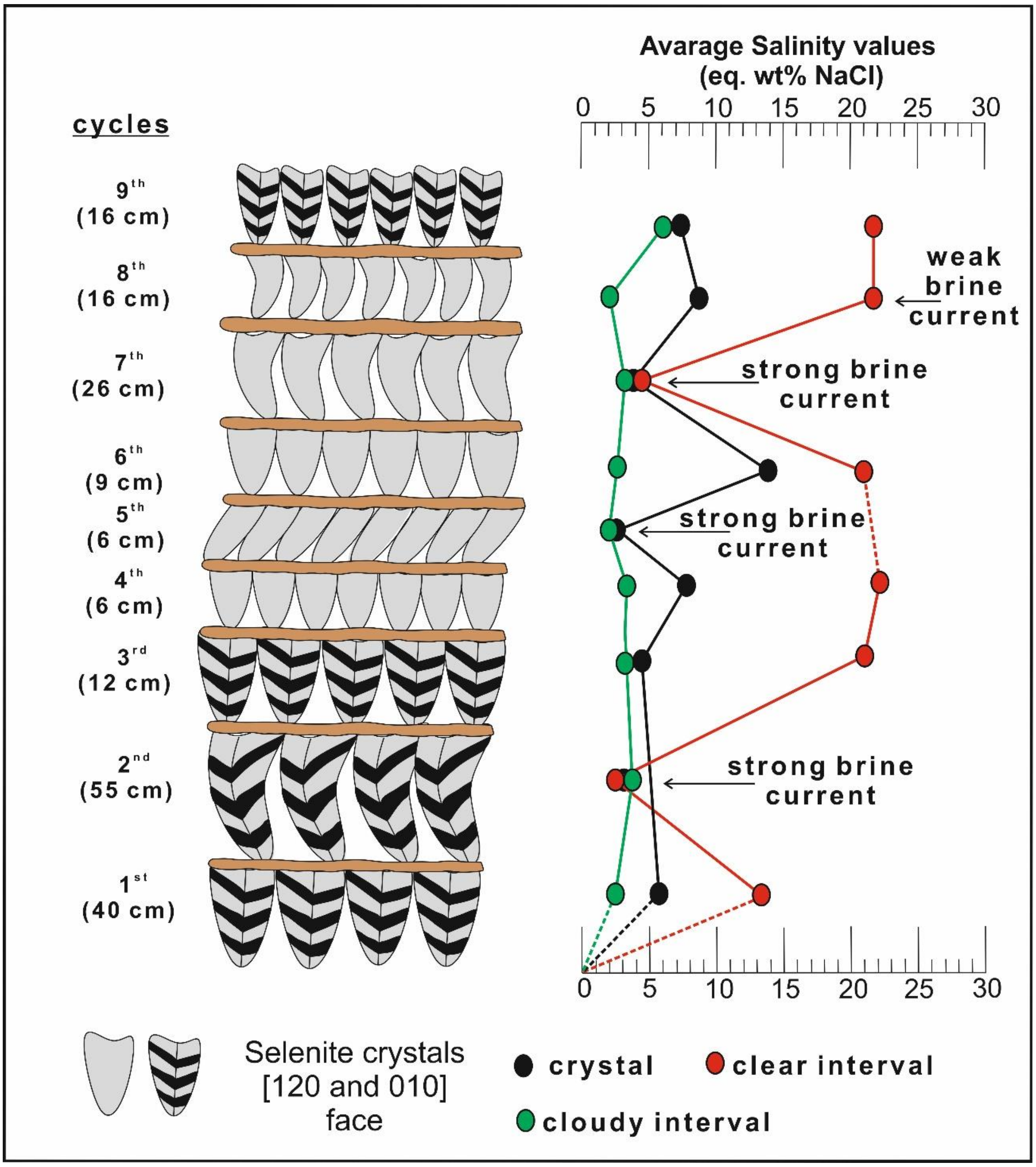

Figure 4.14. Stratigraphic column of the selenite deposit correlating with the average salinity values from the 1st cycle to the 9th cycle (black trend); green regular trend is the average salinity in cloudy intervals; red irregular trend lines is the average salinity in clear intervals. Fifth cycle doesn't show appreciable FIs in clear intervals (red dotted line). Low salinity values testify brine currents.

CHAPTER 5. $^{87}Sr/^{86}Sr$ isotopic study

5.1 Introduction

The $^{87}Sr/^{86}Sr$ ratio of the ocean at a certain moment in the Earth life is the same throughout the water column due to the very long residence time of strontium with respect to the mixing time of ocean waters (Flecker & Ellam, 2006). The ratio variation through time has been used for building a curve, which can be used as a chronostratigraphic tool (McArthur *et al*., 2001; McArthur *et al*., 2012); its accuracy is relatively good especially in those time intervals characterized by rapid change of the isotope ratio (Roveri *et al*., 2014).

The Sr isotope ratio of water in a semi-enclosed basin connected to the global ocean is controlled by simple mixing between ocean water and other Sr-bearing water sources feeding the basin e.g. river run-off and rain (Ingram & Sloan, 1992; Reinhardt *et al*., 1998). If available, hydrothermal fluids may also contribute to the Sr isotope signature of the marginal marine basin (Brass, 1976). Sr concentration differs from one water source to another. Ocean water has a Sr concentration ~ 40 times higher than average global river water (Palmer & Edmond, 1992). The degree of domination depends on the Sr concentration of river water and the isotopic contrast (i.e. $^{87}Sr/^{86}S$ difference) between oceanic and river $^{87}Sr/^{86}Sr$.

Taking into account the analytical uncertainties on both individual Sr isotope measurements and the ocean water Sr isotope curve, the proportion of river water needs to exceed ~50% of the total inflow in order to generate a distinct non-oceanic Sr isotope signal in the Mediterranean (Flecker *et al*., 2002). Only when ocean water inflow drops below this threshold can the marginal marine basin $^{87}Sr/^{86}Sr$ evolve towards non-oceanic ratios. Progressive increase in the proportion of fresh water feeding the system results in a progressive increase in the deflection to-wards fresh water Sr isotope ratios. Where fresh water inflow has a strongly contrasting $^{87}Sr/^{86}Sr$, the resulting deflection will be greater than the precision of the measurement.

The Mediterranean is unusual in being surrounded by atypical continental crust including large amounts of carbonates and mantle derived volcanic. Different rivers flowing into the Mediterranean have different Sr isotope ratios. Almost all of them have Sr isotope ratios lower than present-day sea water (Brass, 1976; Palmer & Edmond, 1992). In contrast with most marginal marine systems, the mixing of substantial quantities of river water with oceanic inflow entering the Mediterranean, commonly results in a depression of the $^{87}Sr/^{86}Sr$ with respect to the coeval ocean water ratio. The Mediterranean Evaporite incorporate the $^{87}Sr/^{86}Sr$ of the water in which they precipitated without fractionation and therefore can provide important information on the origin of brine in the basin (continental or marine).

5.2 Messinian Evaporite signature

In semi-enclosed basins, as the Mediterranean presumably was during the Messinian, the Sr isotope ratio is a function of the balance between ocean and riverine input, which are characterized by strong variations in the Sr concentration and $^{87}Sr/^{86}Sr$ signature, thus providing a valuable proxy of its hydrological structure. Since the first geochemical characterization of the deep Messinian evaporites of the Tyrrhenian (Müller *et al.*, 1990) and Balearic basins (Müller & Mueller, 1991), the existence of two distinct populations of $^{87}Sr/^{86}Sr$ values has been recognized. The considerable number of values obtained through time from Messinian deposits has led to the reconstruction of a curve of variation of the Mediterranean $^{87}Sr/^{86}Sr$ ratio during the MSC (Flecker *et al.*, 2002; Flecker & Ellam, 2006; Topper *et al.*, 2011). The curve has a typical pattern of progressive and rapid detachment from the ocean curve starting around the Messinian salinity crisis (MSC) onset toward considerably lowered values (i.e. from 0.709000 down to 0.708500). This has been interpreted as related to the gradual decrease of ocean input for the closure of the gateways and/or to the increase of freshwater input from rivers (Nile and Rhone) or from the Paratethys (Flecker *et al.*, 2002; Flecker & Ellam, 2006; Gladstone *et al.*, 2007; Topper *et al.*, 2011; Topper & Meijer, 2013).

The advancements achieved in the comprehension of the MSC issues, summarized in the CIESM Consensus Report (CIESM, 2008), in the chronological and paleoenvironment for the Upper Gypsum of Sicily from Manzi *et al.*, (2009) and the new isotopic data from Roveri *et al.*, (2014), resulted in progressive refinement of evaporite facies models. The deep evaporite suite has been classically subdivided into three units (the Messinian trilogy), namely, from the bottom, Lower Evaporites (LE) , Messinian Salt (5.60-5.55

Ma) and Upper Evaporites (UE) and is correlating with the Sicilian onshore record (Decima & Wezel, 1971), which shows a similar threefold subdivision in Lower Gypsum, Halite and Upper Gypsum (see chapter 1 for more details).

Each of the three Messinian units seems to bear a characteristic $^{87}Sr/^{86}Sr$ signature, which records the changes in the hydrological balance of the Mediterranean and may thus have a good chronostratigraphic value (Manzi *et al*., 2009; Roveri *et al*., 2014).

The $^{87}Sr/^{86}Sr$ values recognized in the different stages by previous authors (Roveri *et al*., 2014 and references therein) are:

<u>Lower Gypsum (stage 1→ 5.97-5.60 Ma)</u>: show values between 0.709024 and 0.708890 that are in the range or slightly detached from the global Ocean field.

<u>Resedimented Lower Gypsum and Halite (stage 2→ 5.60-5.55 Ma)</u>: show respectively values between 0.708960 and 0.708820, and between 0.709034 and 0.708801. These values suggest the presence of an even more diluted water mass with respect to the previous one, but still connected with the global Ocean

<u>Upper Gypsum (stage 3→ 5.55-5.53 Ma)</u>: show the lowest and most depleted values compared with the coeval Ocean, mainly below 0.708800 (as low as 0.708600);

5.3 Samples selected

As has been seen in the previously chapters, the Calabria region shows several halite and selenite facies never investigated from a paleo-hydrological point of view. However, the possibility to identify the hydrological variation allows to obtain important information regarding paleoclimatic and paleogeographic aspects, mainly to clarify the deposits of dubious origin (e.g. giant facies). In this regard, have been analysed:

1) from the Crotone Basin have been analysed five halite crystals belonging to different facies: *Cs 04-17, Zi 07-17 and Ru 17-17* from the banded facies, *Zi 11-17* from the white facies) *and Zi 12-17* from the transparent facies. (banded facies), *Zi 11-17* (white facies), (banded facies)

2) From the Catanzaro Trough have been analysed:

(i) Three selenite crystals belonging to the banded facies taken from the sector 5 that shows the nine selenite cycles. The crystals have been sampled in the bottom, the middle and the in top of the outcrop. Moreover, for each sample have been analysed the cloudy and the clear intervals, to verify possibly changes in water supplies (continental or marine):

- *Ma 02-17a* (cloudy interval)

  Ma 02-17b (clear interval)
- *Ma 05-17a* (cloudy interval)

  Ma 05-17b (clear interval)
- *Ma 07-17a* (cloudy interval)

  Ma 07-17b (clear interval);

(ii) one sample belonging to the branching facies from the Riato conglomerate: *Ma Br;*

(iii) one sample belonging to giant facies to understand its origin (Lower Gypsum? Resedimented? Upper Gypsum?): *Gi 01*.

3) From the Ionian Basin have been analysed one selenite crystals belonging to the branching facies: *Be 05-17*.

See *Appendix D_1* for sample preparation: Sr extraction and $^{87}Sr/^{86}Sr$ ratio.

5.4 Isotopic analysis result

Halite samples show $^{87}Sr/^{86}Sr$ between 0.708918 and 0.709050, while in selenite crystals (banded facies) revels values between 0.708786 and 0.708805, in the sample *Gi 01* (giant facies) shows values of 0.708797, and in the samples *Ma Br* and *Be 05-17* (branching facies) show values of 0.709045 and 0.709082.

In the table isotopic results of each sample are reported (Table 1).

Rock type	**Sample**	**$^{87}Sr/^{86}Sr$**	**2σ**
Halite	Cs 04-17	0.708950	±0.000008
	Zi 07-17	0.708918	±0.000006
	Zi 11-17	0.708934	±0.000007
	Zi 12-17	0.709050	±0.000007
	Ru 17-17	0.708925	±0.000007
Selenite	Ma 02-17a (cloudy)	0.708786	±0.000008
	Ma 02-17b (clear)	0.708794	±0.000007
	Ma 05-17a (cloudy)	0.708800	±0.000007
	Ma 05-17b (clear)	0.708789	±0.000007
	Ma 07-17a (cloudy)	0.708800	±0.000007
	Ma 07-17b (clear)	0.708805	±0.000007
	Gi 01	0.708797	±0.000006
	Ma Br	0.709045	±0.000007
Gypsum	Be 05-17	0.709082	±0.000007

Table 1. Table showing $^{87}Sr/^{86}Sr$ ratio and error (2σ) of each halite crystal sampled.

5.5 Discussions

The $^{87}Sr/^{86}Sr$ data from this study are plotted on the Sr isotope curve (Figure 5.1) during the Messinian in the Mediterranean Sea and Global Ocean in accordance with the CIESM (2008).

The $^{87}Sr/^{86}Sr$ ratio of the halite samples falls between the global Ocean field and Mediterranean Sea curve. These values suggest the presence of a diluted water mass but connected with the Ocean, in fact the value of *Zi 12-17* sample falls slightly below the range of global Ocean. According to Manzi *et al.*, (2009), halite crystals would have been deposited over very short time, comprising glacial isotope stages TG14 (5.589 Ma) and TG12 (5.550 Ma).

In selenite crystals, cloudy and clear intervals don’t show significant difference of the $^{87}Sr/^{86}Sr$ ratio which makes us believe that proportion of fresh water, that fed the system, during cloudy formation, was not significantly important to change the isotopic trace in the basin. The $^{87}Sr/^{86}Sr$ ratio arranges these crystals in the Upper Gypsum of Sicily formation period (0.708760-0.708680). In detail, Upper Gypsum Unit of Sicily was controlled by precession-driven arid (gypsum-free cycles - eccentricity minimum at around 5.38 Ma) and wet (thickest gypsum bodies - eccentricity maximum at around 5.43 Ma) climate oscillations records. Stratigraphic and petrographic observations of selenite crystal in this study make us assume that these crystals formed during the Lago Mare event (eccentricity maximum - insolation minima) around 5.43 Ma (Figure 5.1).

Surprising results emerge from the isotopic analysis conducted on the sample belonging to the giant facies. Its value isotopes insert it in the Upper Gypsum and it is the first time that this facies, typical of the Lower Gypsum, appears in the Upper Gypsum confirming its contemporary origin with the banded facies recognised in the Marcellinara quarry.

Samples belonging to branching facies show value falling on the global Ocean field. This makes us assume that both samples were formed between 5.9 and 5.6 Ma, during the deposition of the Lower Gypsum Unit and that subsequently they have been eroded and resedimented.

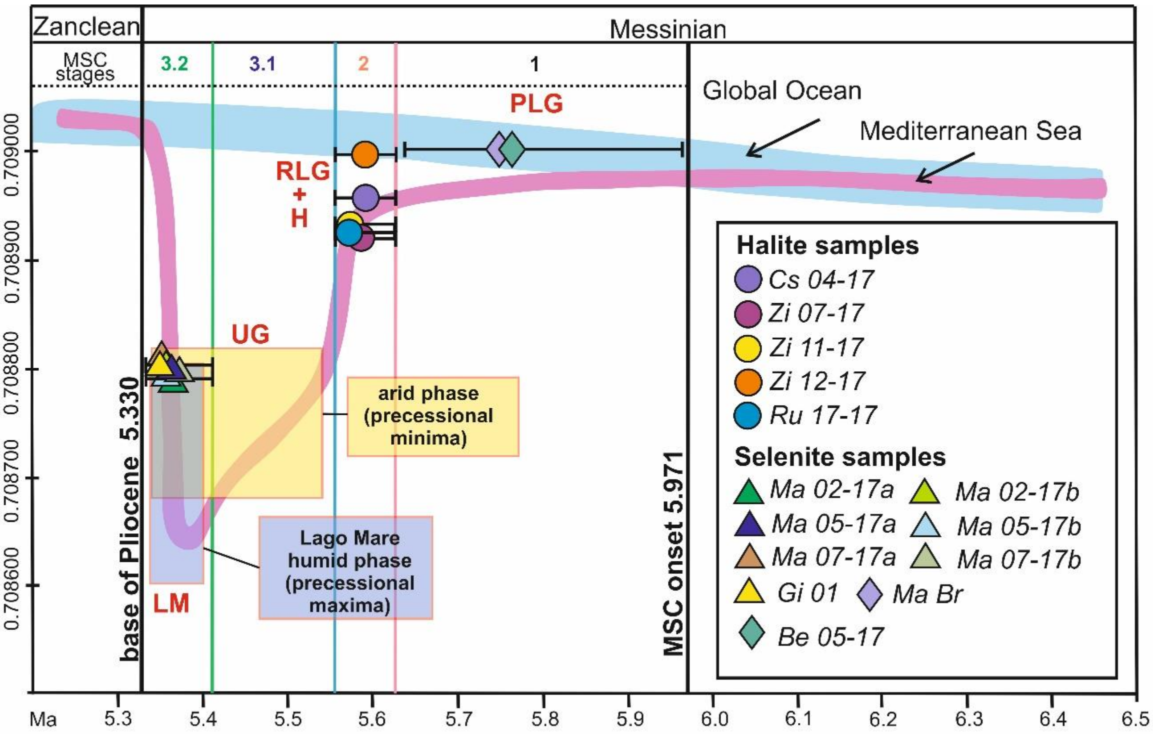

Figure 5.1. Sr isotope curve in the Mediterranean Sea and Global Ocean during the Messinian age. The distribution documents the progressive change in the isotopic composition of Mediterranean waters during the Messinian salinity crisis. PLG: Primary Lower Gypsum; H: Halite; RLG: Resedimented Lower Gypsum; UG: Upper Gypsum; LM: Lago Mare. Figure modified after Roveri *et al.*, (2014).

CHAPTER 6. Summary, conclusions and depositional models

This research uses petrographic, fluid inclusion and geochemical studies to increase the knowledges on the Calabrian Messinian evaporites, poorly studied previously. The Calabrian evaporites, inserted into the interpretive framework of the MSC, can contribute improving the interpretation of the several uncertainties relating to one of the most complex and important geological events of the Cenozoic.

The main aims of this PhD project have been: **(i)** the identification and description of the (a) different halite and selenite facies (primary or secondary), (b) biological content and (c) deformation degree (plastic/ductile strain), **(ii)** interpreting of the evolution of paleoenvironment and paleoclimatic conditions (salinity, temperature of homogenization, chemical composition), **(iii)** dating the crystals, **(iv)** interpretation of the sedimentological facies and their relationships with the hydrological and geochemical factors characterizing the original depositional environments **(v)** creation of new depositional models for the halite and selenite outcrops.

6.1 The halite facies from the Crotone Basin

In the Crotone Basin, salt domes outcrop in Coste del sale, Zinga and Verzino areas (active tectonic zones) and show three facies made of macro and microcrystalline halite. The first two called *banded* and *white* facies were investigated in previously study in contrast, the *transparent* is first described.

In this work, we have:

- revisited and increased the information on the *banded* and *white* facies;
- characterized the new *transparent* facies;
- created a new complete depositional model based on the data obtained.

6.1.1 The banded facies

6.1.1.1 New evidences

From the banded facies, composed of microcrystalline halite (~ 5 mm in length), four samples have been sampled and analysed: *Cs 04-17*, *Zi 07-17*, *Ru 17-17* and *Ru 19-17*.

All crystals show **(i)** primary structures, **(ii)** syn-depositional and **(iii)** post depositional diagenetic features, **(iv)** comparable characteristics of the brine and **(v)** biota. In detail:

(i) Relict primary structures are highlighted by corners crystals and growth zonation defined by distribution of Fluid inclusions (FIs) that run parallel to the faster active growth faces (100). FIs Types are mainly monophase liquid (Type 1) and two-phase liquid rich (Type 2); FIs multiphase (Type 3), which trap organic matters (mainly green microalga) and/or solid, are recognised in minor amount. **The relict primary structures are a new evidence that testify a not complete recrystallization of the samples.**

(ii) Syn-depositional diagenetic growth features are represented by rounded crystals shape, syntaxial overgrowth, halite cement, dissolution boundary (sometimes sharp) and clay matters that separates the halite cement from the halite crystal indicating a dissolution processes during earlier depositional phase. **These characteristics testify a deposition non-constant (in the basin) influenced by fluid circulation and clay matters, which favoured small sizes than large ones** (see macrocrystalline halite).

(iii) Post depositional diagenetic features are testified by the presence of (a) equigranular mosaics crystals with boundaries that meet at triple junctions (~120° angles), (b) secondary FIs (mainly two-phase vapour rich), (c) necking-down (from weak to strong), (d) reequilibration processes (stretching and leakage) and (e) different degree of fracture (from medium to high). **These features attest ductile and plastic deformation phenomena due to temperatures and pressures increase** (tectonic activity, burial and/or exhumation processes) whereby grains ‘optimize’ their size, shape and orientation in order to minimize energy.

Cs 04-17 is the sample showing the smallest degree of deformation and greater relict primary structures, in contrast *Ru 19-17* is the most deformed sample. *Zi 07-17* is very similar to *Cs 04-17*, while *Ru 17-17* is closer to *Ru 19-17*.

(iv) Geochemical brine characteristics were detected by using of Microthermometric Raman and SEM analyses that revel Na, Cl, Mg, K and Ca as dominant elements in the inclusions, that, associated with $^{87}Sr/^{86}Sr$ ratio (values from 0.708950 to 0.708918) **confirm a precipitation in a dilute marine water** (sea water ± continental water). The basin had temperature of homogenization from +20° to +32°C and salinity values between 26 and 26.5 eq. wt% NaCl.

Hight temperature of homogenization recognised in *Ru 17-17* and *Ru 19-17* are attributable to active tectonic phenomena (>38°C).

(v) Biota observed and investigated through UV light and SEM, subsequently compared with the literature data, have highlighted the presence of different organic matter inside the crystals and FIs. Organic matters recognised are blue (Oscillatoriales), green (Chlorophytas, Dunaliella cells and Nannochloropsis/ Chroococcidiopsis) and red microalgae (Rhodophyta). **The combination of these organisms is indicative of saline environment subject to continental inflow phenomena and mixing of the water column.**

In general, microalgae live in basin with temperature until +35°C, while the presence of carotenoids and phycoerythrin pigments produced by photosynthesis processes **testify a depositional environment with depth not greater than 150 m.**

6.1.1.2 Formation, deposition and evolution

The data obtained provide important new and information on the crystals formation and their evolution. In light of historical and new acquired data, the crystals, belonging to the banded facies, grow via solar concentration (called *rafts*) at the air-brine interface when surface water salinities are suitable. During their formation, the *rafts* trap liquid and air bubbles in primary inclusions (FIs Type 1 and 2). When become heavy fall down to the bottom of the basin and continue to grow competitively undisturbed. Here, they trap fluid inclusion organic matters and clay minerals.

The banded halite formation (in deep or shallow basin) and its accumulation depend on the combination of these factors: (a) high temperatures (seasonal effect) and low intensity of wind and waves for its formation; (b) pycnocline, halocline and chemocline stables and no stratification of the water for its accumulation.

Banded facies prefers microcrystalline size due to continuous influx of fresh water (rain/river) testified by clay materials that separate and cover the crystals. Fresh water amount (related to wet periods) however, is must be assumed that was small due the presence of continuous supersaturated brine (stable deposition).

After deposition, banded facies was affected by ductile and plastic deformation phenomena for increasing of temperature and pressure due to tectonic activity, burial and/or exhumation processes (post depositional diagenetic feature). A greater understanding of these deformations may provide important information for reconstructing the thermal history of these deposits.

6.1.2 The white facies: old and new information

The white facies is made of macrocrystalline halite (> 5cm in size) and shows grey (enriched of FIs) and white (impoverished of FIs) bands visible to naked eyes. One sample have been collected and analysed (*Zi 11-17*).

In detail, this facies grows on the bottom of the basin and reflects changes in crystal precipitation rate induced by short-term (daily) or seasonal changes in salinity. This is possible if the column water is affected by pycnocline fluctuations. During pycnocline oscillations, when the water is more dense (high salinity), crystal grows quickly and traps FIs Type 1, 2 and 3 (grey bands), instead, if the water is less dense (minor salinity but always supersaturated) crystal grows slowly without trapping the FIs (white bands). This growth pulses create primary textures called as “chevron fabric”.

During their growth, the crystals register syn-depositional diagenetic features like dissolution on the boundary with formation of halite cement.

Crystals record also post depositional diagenetic feature like: **(i)** secondary FIs, **(ii)** stretching process (fragile deformation), **(iii)** weak necking-down, **(iv)** poor degree of fracture and **(v)** halite cement. These evidences indicate little burial and/or exhumation with local recrystallization.

Microthermometric, Raman and SEM analyses revel Na, Cl, Mg, K and Ca as dominant elements in the inclusions that associated with ^{87}Sr/^{86}Sr ratio (0.708934) confirm a precipitation from hybrid brine. Brine geochemical characteristics and organic matters observed in the crystal and inside the FIs are the same as those observed in the banded facies.

The white facies formed in a shallow basin suffering from pycnocline oscillation, because the brines in deep water are too dense and too stable to change with the rapidity required to form the mm-cm scale discontinuities that characterise the internal structures of this growth.

Moreover, the microthermometric analysis shows a salinity values, estimated for the first time in these samples, about 26 eq. wt% NaCl and temperature of homogenization around +33°C. The temperature of homogenization is disagreed with Speranza *et al.*, (2013) that obtained temperature of homogenization with average ~21°C. This is possible due to the pulsing crystals growth associated at different seasonal intervals (winter/summer oscillation).

6.1.3 The transparent halite: new primary facies

The transparent facies, not discussed in previous literature data, is recognised in continuity of deposition with the white facies and it is made of macrocrystalline halite (>5cm in size). One sample have been collected and analysed (*Zi 12-17*).

Initially, these facies showed macroscopically features typical of recrystallized facies, but, the presence of individual trails of FIs mainly Type 3c testify certainly a primary origin. FIs trails register growth pulse less frequent than those seen in the white facies. Perhaps, this depends on the brine density (less dense) that causes less pycnocline oscillations and a slower growth (no FIs). Faster growth is observed only in correspondence of the FIs trails. Most likely, this facies is formed during a longer wet periods characterized by seasonal environment variations less important than those recognised in the white facies. These hypotheses are confirmed by temperature of homogenization around 21°C, lower than white facies.

Microthermometric, Raman and Sem analyses associated with isotopic studies (0.709050 ^{87}Sr/^{86}Sr ratio) attest a precipitation from hybrid brine (connected with the Ocean?).

Moreover, geochemical brine characteristics and organic matters observed in the crystal and inside the FIs are the same as those observed the banded and white facies.

6.1.4 Halite growth rate

The data obtained show that the banded, white and transparent facies record same brine composition and salinity but different growth rate due to pycnocline oscillations.

According to Manzi *et al*., (2009), halite crystals would have been deposited over a very short time, comprising glacial isotope stages TG14 (5.589 Ma) and TG12 (5.550 Ma). Instead, growth rate is established from Schreiber & Hsü (1980), which estimate a rate of approximately 10 m per 1000 years (~1 cm per 1 year). This could be valid for the banded and the transparent facies that form in a brine with a stable pycnocline. In contrast, the white facies, registering daily (day-night) or seasonal pycnocline oscillations, can forms with a faster growth rate.

Using data from Schreiber & Hsü (1980) and assuming a continuity of deposition not interrupted by dissolution events or not deposition, 2.5 cm of crystal belonging to the banded facies forms in~2.5 years, while for the transparent facies it is slightly lower as it shows moments of faster growth. For the white facies is more complicate because it shows growth pulses. In fact, in the white facies 56 pulses in 2.5 cm of crystal are counted.

Considering daily oscillations, 56 pulses are formed in~ 28 days, while, supposing seasonal oscillations, they are formed in~ 28 seasonal, testifying a fast (daily) or slow (seasonal) deposition rate in relation to the oscillations of temperature and pycnocline.

6.1.5 Halite depositional model

Halite depositional model is based on Zinga deposits because this is the only area where all three facies outcrop (Figure 6.1).

In light of the new evidences and in according with “the Salin Pan Cycle” of Lowenstein (1985), the banded, white and transparent facies recognised in the Crotone Basin formed during “*Evaporite concentration*”, in coastal-marine environment (no deeper than 50 m – hybrid brine) characterised by a seasonal fill. In detail:

a) **<u>the banded facies</u>** marks the *initial phase* characterised by **(i)** stable evaporation rate, **(ii)** stables pycnocline, halocline and chemocline, **(iii)** low intensity of wind and waves, **(iv)** same deposition rate and, **(v)** low or no stratification of the water column;

b) **<u>the white facies</u>** indicates the *intermediate phase* characterised by **(i)** unstable evaporation rate, **(ii)** high pycnocline oscillation, **(iii)** not subject to the action of wind and waves, **(iv)** different deposition rate and, **(v)** low stratification of the water column;

c) the transparent facies marks the *final phase* characterised by **(i)** slight instability of evaporation rate, **(ii)** low pycnocline oscillation, **(iii)** not subject to the action of wind and waves, **(iv)** different deposition rate and, **(v)** low stratification of the water column.

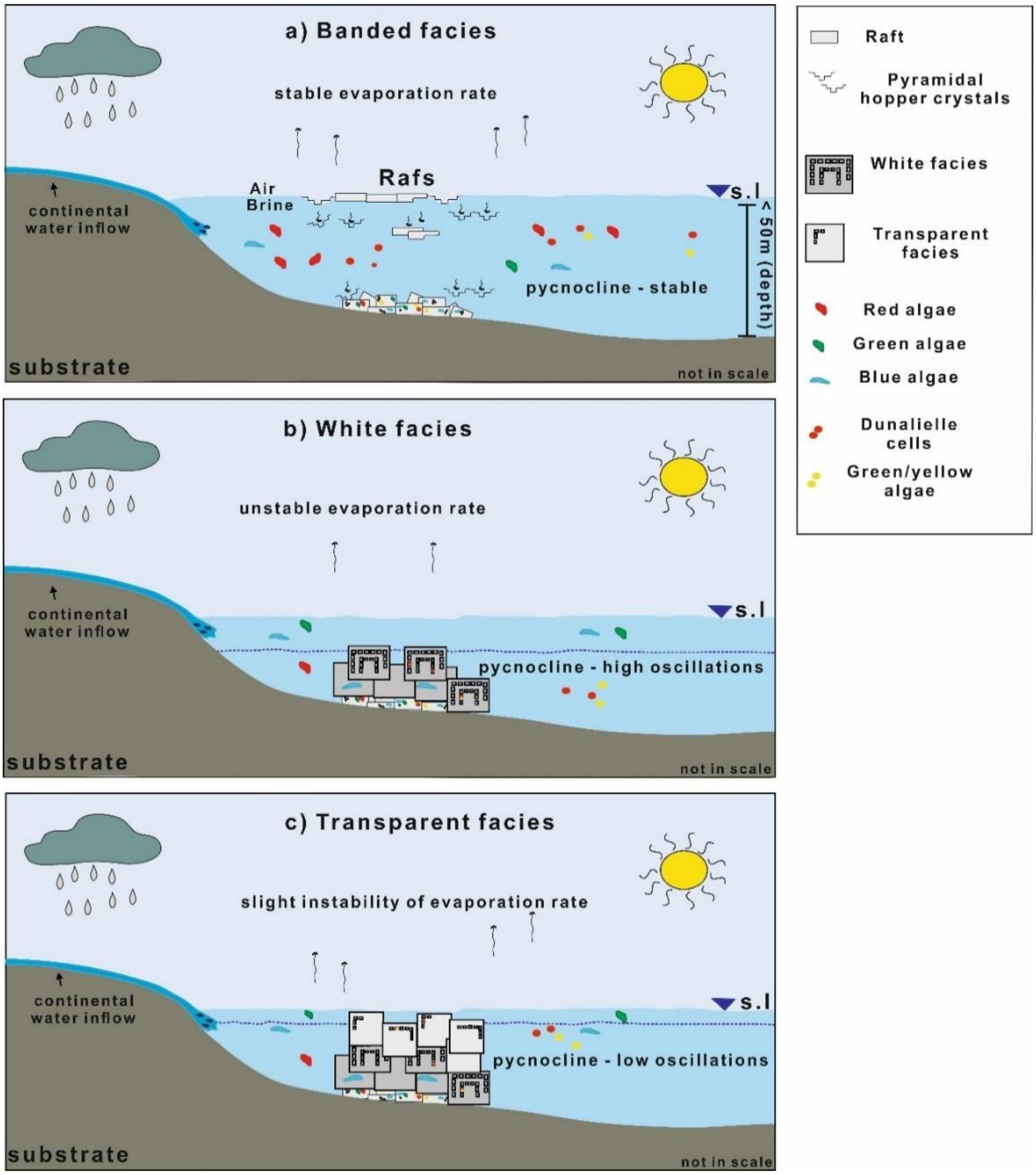

Figure 6.1. Schematic model of the three halite facies (a) banded, (b) white and (c) transparent, recognised in the Crotone Basin and formed during Evaporite concentration. The facies are associated with different pycnocline variations (not in scale). Banded facies formed during initial phase, white facies formed during intermediate phase and the transparent facies formed during final stage of Evaporite concentration of the "Salin Pan Cycle" of Lowenstein (1985).

Data obtained from the multidisciplinary study and the model reconstruction of the three facies associating with different depositional stage have been an important step for understanding the halite formation mechanisms. Identification of three different facies outcropping in the same basin, is a unique case in Italy and shows us how important the intrinsic characteristics of each basin (chemical/physical conditions, depth, biological content) for the development of the different facies.

6.2 Selenite facies from the Catanzaro Trough

Selenite deposit is located in the Marcellinara quarry. The quarry shows: **(i)** giant selenite blocks, **(ii)** domes structures, **(iii)** reworked selenite with massive selenite crystals and, **(iv)** banded crystal layers.

Stratigraphic observations and preliminary studies (Costanzo *et al*., 2019; Cianflone *et al*., 2011, 2012) suggest that the quarry is made of selenite crystals belonging to the Upper Gypsum and reworked deposits related to the Resedimented facies. Reworked deposits derive from dismantling product of the Lower Gypsum due to the rapid lowering of the sea level which produced an instability of the margins and their subsequent re-deposition. The presence of ancient and dismantled Lower Gypsum is confirmed by the finding of facies belonging to the Lower Gypsum: **(i)** the branching facies found as blocks within the Riato conglomerate (located near the quarry), **(ii)** the giant facies like as blocks and **(iii)** reworked selenite recognised in several points of the quarry.

6.2.1 Banded facies

The sector 4 and 5 of the quarry (see chapter 2) show **(i)** selenite layers belonging to the banded facies separated by **(ii)** dissolution surfaces, **(iii)** breccia layer or **(iv)** thin argillaceous/calcareous laminae. Data collected show that each of these phases is associated with a particular depositional moment in the basin. In detail:

(i) The banded layers indicate supersaturation condition (i.e. the gypsum-saturation interface) and minimum brine level; the crystals show competitive growth (fast growth rate) and vertical or oblique twin plane. Oblique growth testifies a brine currents that folded and fracture the crystals;

(ii) the dissolution surfaces (or no selenite precipitation) testify pycnocline variations associated with unsaturated condition caused by a number of factors such as brine dilution (inflow of freshwater – winter dilution) or deposition of sediment on the crystal apices (Ortì, 2011);

(iii) the breccia layers probably derived from sub-aerial exposure (lowering of the brine level) and subsequent erosion of other selenite crystals which, due to gravitational flows, were deposited (like as chaotical deposit) on top of the selenite layers; the breccia layers could testify marine storm (mechanical erosion); the low corrosion rounding of the clastic breccia suggests a minimum transport;

(iv) the thin argillaceous/calcareous laminae (1-2 mm in size) indicate unsaturated condition and become poikilitically enclose within the selenite during the subsequent growth episode.

These alternation of layers and laminae could be associated with *middle-frequency climatic oscillation*, where the banded layers formed during arid periods while, the argillaceous/calcareous laminae and breccia layers are deposited during wet periods.

However, also a *high-frequency cyclicity* has been observed within the selenite crystals (microscale) highlighted by two microfacies - cloudy and clear - testifying different environment of formation:

(a) the cloudy intervals are rich in organic matters, fluid inclusions and clay minerals; their growth is disturbed by clay minerals and organic substance that generate crystallographic irregularities. These imperfections favour the entrapment of inclusions and materials (organic and inorganic) present in the water column. These intervals record seasonal episode of *ecological bloom* because trap abundant and diversified organic matters that tolerate different salinity (see chapter 2) within the crystals and inside the FIs;

Furthermore, the microthermometric analysis reveals low salinity values (av.~3 eq. wt% NaCl) and an enrichment in Mg and Ca that testify a closed hydrological system where the brine composition depends mainly on the rivers and groundwaters. Clay matters, from continental and substrate, contribute to the increase ions concentrations in the brine. These results are in agreement with those of Natalicchio *et al.*, (2014), that provided low salinity values, fitting the carbonate precipitation filed, for the Messinian gypsum located in North Italy (Lower Gypsum – without discriminating between two microfacies);

(b) the clear intervals are impoverished in organic matters, FIs and clay minerals but evidence high salinity values (av. ~21.5 eq. wt% NaCl) and an enrichment in NaCl and KCl that allow to suppose marine water input or a step without continental inflow. Sometimes, in these intervals, the salinity values do not fit into gypsum precipitation field (high salinity) but fit into carbonate precipitation field (low salinity) and show same values obtained in FIs trapped in the cloudy intervals. It could testify a pseudo-secondary or secondary FIs origin or a different brine condition due to climate changes.

Moreover, the entrapment of blue (Oscillatoriales) and green microalgae (Chlorophytas) that occurred only in the crystal and not within the inclusions suggests that these microalgae died during high salinity stages.

The seasonal growth could be demonstrated using the growth rate proposed by Schreiber & Hsü, (1980) or by Komarov *et al*., (2000). The first estimate a rate of approximately 1-2 m per 1000 year (~1 cm per 10 year) while the seconds studied the gypsum growth into a thermostated at 18°C and 30°C, estimating a growth rate respectively of ~51 cm/y or ~154 cm/y.

Using data from Schreiber & Hsü (1980) and assuming a continuity of deposition, 6 cm of crystal formed in ~60 years, cloudy interval (average 3 mm in size) formed in ~3 years. Using data from Komarov *et al*., (2000) and considering a basin with a temperature of about +18°C, 6 cm of crystal formed in ~1.4 months (42 days), cloudy interval (average 3 mm in size) formed in ~ 2 days. Instead, considering a basin with a temperature of about +30°C, 6 cm of crystal formed in ~14 days while cloudy interval in ~17 hours.

In both models, is difficult establish if the clear intervals formed slower or faster than cloudy intervals, because the presence of few inclusions suggest a slower growth, in contrast the high salinity suggests a faster growth than the cloudy intervals.

Moreover, according to Manzi *et al*., (2009), selenite crystals formed during the Lago Mare event (eccentricity maximum - insolation minima) around 5.43 Ma. A general wet climate would favour the cloudy intervals formation.

Overall, all the data obtained allow us to hypothesize two climatic variations:

- arid and wet periods associated with pycnocline oscillation at the outcrop scale (dm scale - middle-frequency) that produced changes between selenite layers, dissolution surface and argillaceous/calcareous laminae;
- arid and wet phase associated with inflow of continental water at the crystal scale (mm scale - high-frequency) that produced alternation of the cloudy and clear intervals.

Isotopic analysis conducted on the cloudy and clear intervals don’t show significant difference of the ^{87}Sr/^{86}Sr ratio. This means that the inflow of fresh water during cloudy formation was not significantly important to change the isotopic trace in the basin. The ^{87}Sr/^{86}Sr ratio attributes these crystals to the Upper Gypsum (0.708760-0.708680).

6.2.2 Giant facies

The sector 1 of the quarry (see chapter 2) shows giant selenite like as blocks (sample *Gi 01*). These facies, in other Mediterranean basin, was recorded only in the Lower Gypsum (Manzi *et al.*, 2009; Lugli *et al.*, 2010). They formed during the maximum brine level (stable pycnocline) permanent covered of Ca sulphate-saturated brine (Babel, 2004) and vertical space and time for undisturbed syntaxial crystal growth. The high salinity is highlighted by the presence of *Chroococcidiopsis* (live in high salinity environment) observed in the crystals.

Surprising results emerge from the isotopic analysis that shows $^{87}Sr/^{86}Sr$ ratio value of 0.708797. This result attributes certainly this facies to the Upper Gypsum. It is the first time that the giant facies, typical of the Lower Gypsum, appears in the Upper Gypsum confirming its contemporary origin with the banded facies.

Therefore, considering that this facies is:
(i) stratigraphically inferior to the other deposits,
(ii) associated with dome structures known as “cavoli”,
(iii) accompanying at reworked deposits (unstable environment),
(iv) made of large size crystals that suggest formation during the maximum brine level (they need to be permanently covered by saturated brines - Babel, 2004),
it can be assuming that the giant facies formed before the banded facies, about 5.55 and 5.43 in the arid phase.

6.2.3 Branching facies

Sample *Ma Br* collected from the Riato conglomerate, is made up of fractured gypsum crystals immersed in a brown yellow matrix enriched in small gypsum crystals, clay minerals and red organic matters (biofilm structures of cyanobacteria) that emit blue fluorescence under UV light. Primary structures have been almost completely deleted. The $^{87}Sr/^{86}Sr$ ratio shows value of 0.709045 falling on the global Ocean field. This data confirms its belonging to the Lower Gypsum Unit (5.9 and 5.6 Ma), subsequently eroded and resedimented. Macroscopically, this sample shows characteristics like those observed by Lugli *et al.*, (2001) in the branching facies (formed due to brine current) from Lower

Gypsum in Sicily, but microscopically it shows features of a resedimented facies and not primary.

6.2.4 Selenite depositional model

Stratigraphic and petrographic observations of selenite crystals make us assume that these crystals formed during the Lago Mare event (eccentricity maximum - insolation minima) around 5.43 Ma.

Starting from the bottom (deep basin) to the top (shallow basin) and considering the temporal and spatial evolution of the Marcellinara quarry, the evolution of the selenite deposits in the basin can thus be schematized (Figure 6.2):

1) the branching facies forms during the Lower Gypsum deposition stage (5.9 - 5.6 Ma) and Resedimented Lower Gypsum (around 5.6 -5.5 Ma); subsequently eroded and incorporated in the Riato conglomerate;

2) the giant and massive facies (sector 1) belonging to the Upper Gypsum (5.43 Ma) testify the maximum brine level (Figure 6.2A - B);

3) dome structures and reworked deposits (sector 2 and 6), which involves the previous massive facies, attest flooding events (Figure 6.2C-D);

4) the banded facies (sector 5) forms during aridity acme (Figure 6.2E). Selenite cycles testify different environments of formation, in detail:

- the first, third, fourth, sixth and ninth selenite cycle form in a quiet environment (vertical twin plane); the cloudy and clear intervals reflect season change;
- the second, fifth and seventh selenite cycle form in an unstable environment (folded and fractured crystal with oblique twin plane); the cloudy and clear intervals reflect season change but the clear interval show a decrease of salinity values associated with abundant continental water inflow (brine current at high flow) that diluted the brine;
- the eighth selenite cycle although shows folded crystals, has many fluid inclusions and records a higher salinity than the others. Probably the brine current was more saline compared to the brine in the basin;

5) the banded facies and breccia layers (sector 4) mark the final stage (Figure 6.2F).

The brine current observed in selenite crystals arrived in the Catanzaro Trough (paleochannel) from east (Ionian Sea or eastern Mediterranean) and west (Tyrrhenian Sea or western Mediterranean) direction. Consequently, the crystals formed in nearshore environment (wave action – not exceeding 50 m of depth). This environment is confirmed by abundant and several organic matters observed in the crystals that tolerate different salinity (e.g. Oscillatoriales, Chlorophyta, Rhodophyta). In general, microalgae live in basin with temperature until +35°C, while the presence of carotenoids and phycoerythrin pigments produced by photosynthesis algae processes designate a shallow depositional environment.

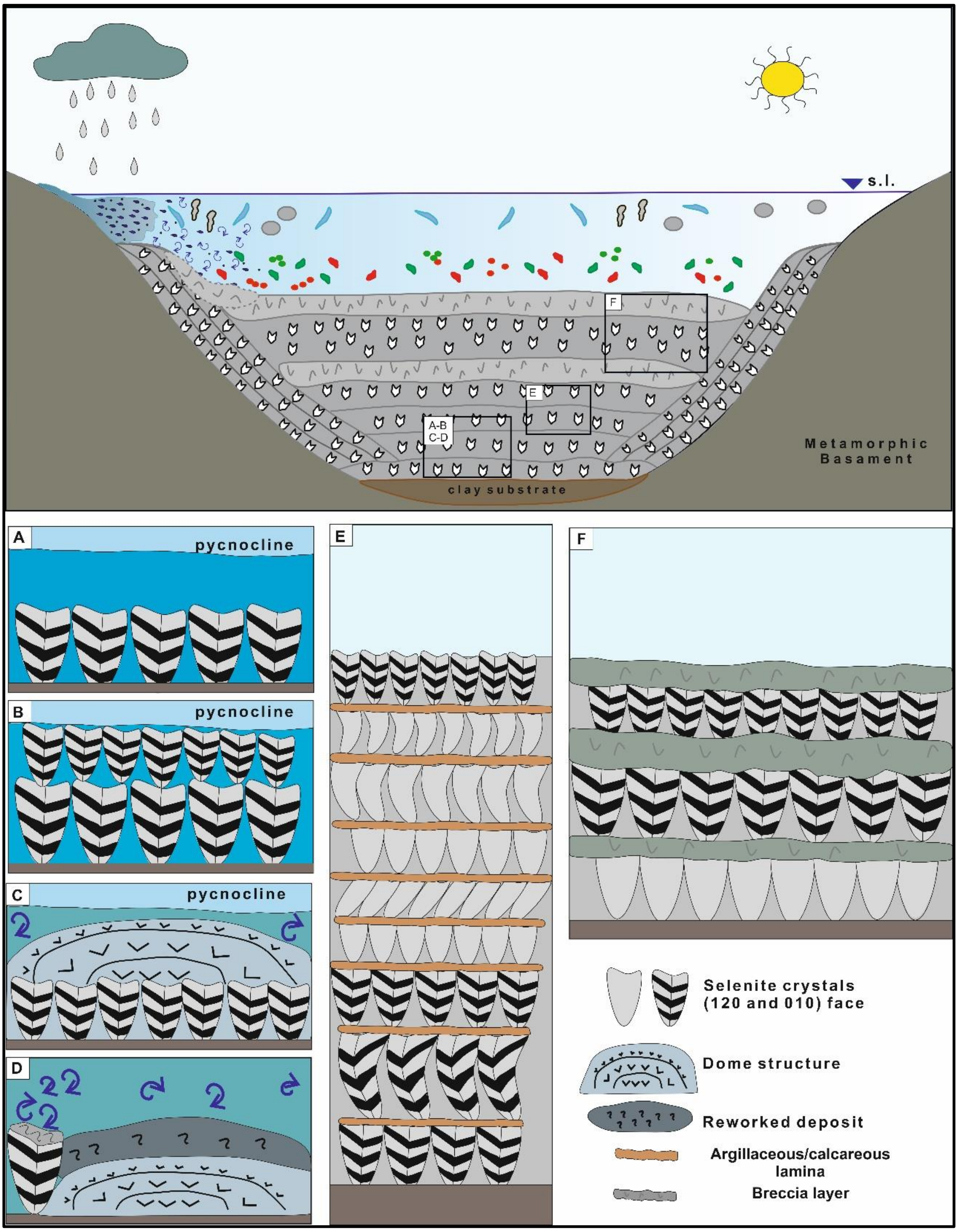

Figure 6.2. Schematic model of the main facies belonging to the Upper Gypsum recognised in the Marcellinara quarry (see text for description). A) Giant facies; B) massive facies growing on the top of the giant facies; C) dome structure on the massive facies; D) reworked deposits associating with dome structure; E) best deposit made up of nine selenite cycles interbedded by argillaceous lamina; F) deposit made up of selenite and breccia layers. Not in scale.

Data obtained allow us to affirm that the Marcellinara quarry, even if it's small area, shows a processes variability at macro and micro scale correlating with different depositional step. The presence of giant facies associating with the Upper Gypsum rather than to the Lower Gypsum, as it instead occurs for other Mediterranean basins, is a unique case in Italy and testify how selenite formation is triggered and influenced by multiple factors (chemical/physical conditions, depth, biological content) characteristic of that specific deposition basin.

6.3 Selenite facies from the Ionian Basin

The Benestare quarry, located in the Ionian Basin, is made up of selenite and carbonate deposits. Macroscopic observations on the selenite deposit suggested that crystals belong to the banded and branching facies. Nevertheless, all samples collected from two facies were shown to be fractured, folded and with chaotic orientation. Samples show crystals with rare primary FIs immersed in a yellow-brown matrix. Crystals fractured show twin plane which leads us to suppose they were originally selenite crystals and subsequently eroded and immersed in the matrix enriched in clay minerals and organic matters (red and blue algae and biofilm structures of cyanobacteria). These observations are confirmed by $^{87}Sr/^{86}Sr$ ratio that shows a value of 0.709082. Therefore, this selenite deposit is an olistostrome that can be related to the Resedimented Lower Gypsum.

6.4 New insight on the microthermometric analysis

In this work, new evidences have emerged from microthermometric analysis, improving the scientific debate about the correct or incorrect use of FIs Type 1 or Type 2.

A) Microthermometric analyses carry out on FIs Type 1 and Type 2 observed in the same assemblage, provide identical results. This testify that the bubble trapped could be **(i)** air trapped, **(ii)** an artefact product of inclusion stretching for small variations in temperature and pressure or, **(iii)** could derive from the presence of small impurities in heterogenous entrapment condition. Regardless of bubble origin, can be used both FIs in condition of low crystal deformation.

B) The analysis is reproducible but not replicable in these materials easily deformed. FIs subjected to multiple cycles of cooling and heating have shown distortions on the inclusions rim and an increased in~3-5°C of the T_{FM} and T_{LM} values for each repetition cycle

C) The identification of hydrohalite during heating is important to estimate the salinity values using the binary system H_2O-NaCl. The presence of Hydrohalite involves a shift towards the phase constituted by Hydrohalite+Liquid in the diagram, necessitating usage of Sterner’s formula (1988) for high salinity system. Through this observation it was possible to discriminate, for the first time, the different salinities in the cloudy and clear intervals.

6.5 Final considerations

The overall objective of this research has been to increase the knowledge on the Messinian Salinity Crisis, studying with multidisciplinary approaches the Calabrian evaporite deposits for the first time.

Data obtained, prove how the Calabria is the only region in the Mediterranean area to have a surprising variety and diversity of evaporite rocks. Their study allowed to understand the main formation mechanisms of the deposits, date and insert them in the three stages of Messinian age and to reconstruction the formation paleoenvironment associated at high and middle-frequency climatic oscillations. Moreover, the characterization of the Calabrian Messinian deposits is the first step for the revision of the stratigraphic schemes especially for the Catanzaro Trough and the Ionian Basin, uncertain to date.

This approach is based on strong bases and can be applied in similar areas.

Appendices

Appendix A - Chapter 2

A_1. Sampling procedure and wafer preparation

Sampling is the first of the most *delicate* and *important* steps of the work: *delicate* because the halite and selenite are highly alterable materials, *important* because for paleoenvironment reconstructions is necessary to sample the crystals with the right crystal orientation.

Each deposit has been photographed in the stratigraphic setting and sampled using latex gloves. Each sample has been individually packed in a plastic bag and labelled (locality name - number of sample - year). The sampling has been carried out follow the criterions to prevent external contaminations used in other works (see Panieri *et al.*, 2010).

All samples were transported to the University of Calabria (DiBEST) laboratory, where they were cleaned with an air compressor and artists brush. After cleaning, each sample was studied to determine the best orientation for the cutting phase, necessary for the subsequent wafer preparation. This is the second of the most important steps from which will depend the accuracy of the subsequent analysis. Samples were cut parallel to crystal growth direction to preserve trapped fluid inclusions and the microfacies visible to the naked eye.

Samples were studied in the Geofluids Research Laboratory at NUI Galway. Petrographic study of the crystals consists of use transmitted light microscopy on a Nikon Eclipse E200 polarizing microscope (with plane polarized light - PPL - and crossed polarized light - XPL), at various magnification (x4, x10, x40).

A_2. Organic matters investigation

Organic matters have been observed using *Ultra Violet microspectroscopy*. This technique has been conducted using a UV microscopy *Nikon Diaphot* microscope with a camera attachment and image analysis software. This microscopy is equipped with an epifluorescence attachment that determine the presence of organic materials.

A_3. The Laser Raman Spectroscopy (LRS)

The Laser Raman Spectroscopy (LRS) is a sensitive, non-destructive analytical technique requiring no sample preparation. It can be used to determine molecular species in fluids and used for the identification of a wide range of substances – solids, liquids and gases. Laser light focused with a microscope objective illuminates a diffraction-limited spot, providing microprobe analysis of areas that are 1 to 2 mm diameter. Raman spectrometer involves illuminating a sample with monochromatic light and using a spectrometer to examine light scatted by the sample. The Raman effect probes the vibrational energy levels of molecules and can provide immediate and useful information on the structure and identify of substances in solid, liquid and gaseous phases. This investigation was carried out at the National University of Ireland Galway using Horiba Scientific LabRam HR. The Technical Specifications are:
confocal system
600 slit grating ~1 cm-1 spectral resolution
spectral range= 100 – 400 cm-1
dual Laser excitation= -532 nm (green; inorganics)
-785 nm (NIR; organics)
spatial resolution ~2 mm.

A_4. The Scanning Electron Microscope (SEM)

A scanning electron microscope (SEM) is a type of electron microscope that produces images of a sample by scanning the surface with a focused beam of electrons. The electrons interact with atoms in the sample, producing various signals that contain information about the surface topography and composition of the sample. The electron beam is scanned in a raster scan pattern, and the position of the beam is combined with the intensity of the detected signal to produce an image. In the most common SEM mode, secondary electrons emitted by atoms excited by the electron beam are detected using a secondary electron detector. This investigation was carried out at the National University of Ireland Galway using Hitachi S-4700 and at University of Calabria (Italy) using FEI/Philips ESEM FEG QUANTA 200 Philips equipped with an X-ray microanalysis system (EDS: Energy Dispersive X-ray Spectroscopy) with EDAX model Si / Li crystal detector.

A_5. Spectrum of Carotene pigment

Spectrum of Carotene pigment found in Dunaliella cell (using Raman spectroscopy). The bands of carotenoids commonly appear between 1000-1020 cm^{-1}, 1150-1570 cm^{-1} and 1500-1550 cm^{-1} (Vitek *et al.*, 2009; Jehlička & Oren, 2013).

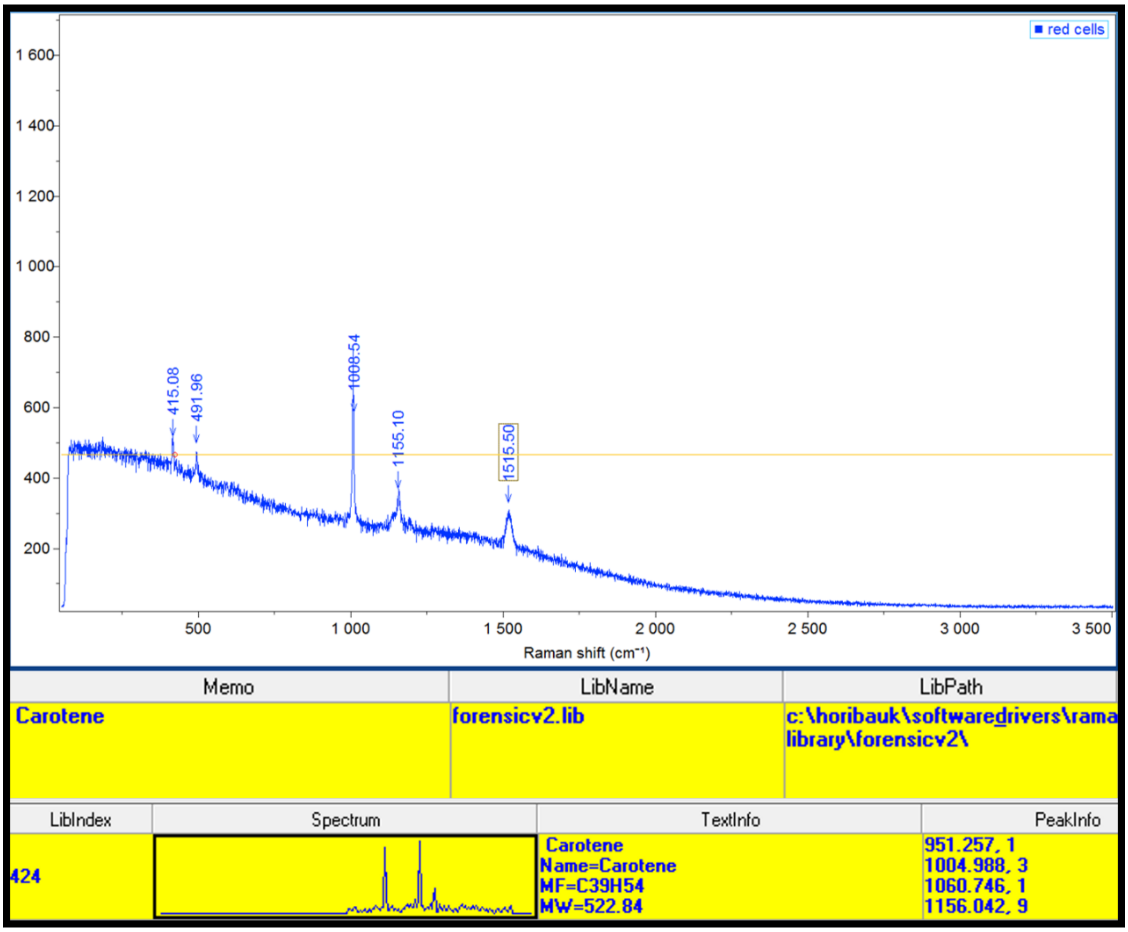

Memo	LibName	LibPath
Carotene	forensicv2.lib	c:\horibauk\softwaredrivers\rama library\forensicv2\

LibIndex	Spectrum	TextInfo	PeakInfo
424		Carotene Name=Carotene MF=C39H54 MW=522.84	951.257, 1 1004.988, 3 1060.746, 1 1156.042, 9

Appendix B - Chapter 3

B_1: Analytical methods for FIs classification and measurements

Fluid inclusion analysis was conducted on halite and selenite wafers (~500 μm in thickness for halite and ~200 μm for selenite). Classification and measurements of the inclusion were carried out using *Lucia Archive Software*, a system for image processing and analysis. Fluid Inclusions were described and classified using a number of parameters such as phases present, size, morphology and degree of fill. Estimate of degree of fill was calculated using the following equation $F=V_L(V_L+V_V)$ where V_L is the volume of the liquid phase and V_V the volume of the vapour phase.

Appendix C - Chapter 4

C_1: Analytical methods for FIs microthermometric studies

Fluid inclusion microthermometric studies were performed on doubly polished wafers (500-200 μm in thickness) using Linkam THM&-600 heating-freezing stage mounted on a Nikon Labophot transmitted light microscope equipped with a range of objective lenses including a 100x lens. The phase behaviour of fluid inclusions was analysed over the temperature interval -80° to +60°C in halite samples and -80°C to +50°C in gypsum samples. The estimated accuracy of measurements is ± 0.2°C during freezing runs and ±1.0°C during heating runs. The rate of heating and freezing experiments was varied as a function of the velocity of phase transitions in the inclusions and ranged from 0.1 to 10°C/min. The error in estimating salinity using the depression of freezing point methods of NaCl equivalent is ± 0.05 wt% all temperatures (Shepherd *et al.*, 1985).

Usually, for microthermometric analyses, all-liquid aqueous inclusions are preferred because they indicate very stable entrapment conditions, so the vapour bubble must be generated artificially during the freezing of the inclusions, in order to apply the phase diagrams (Goldstein & Reynolds, 1994). In this study, the microthermometric analyses have been tested on all Types, comparing the results. Moreover, to estimate the standard error, more analyses were conducted on the same inclusions that showing an increase in ~ 5°C in the T_{FM} and T_{LM} values. This resulted in a drastic decrease on the FIs number usable, since for each little piece of crystal only one groups of FIs could be analysed.

It was not possible to use microthermometry on secondary FIs because metastable and small (<10 μm in size).

Image C_1a: example of the full procedure followed during heating and freezing runs for a Type 2 fluid inclusion in microcrystalline halite sample from the banded facies.

At room temperature (A) the inclusion with a degree of fill of 0.9 contained two phases (L+V). At -65°C inclusion becomes dark-brown in colour (B). (C) First melting was recorded at -34°C, the inclusion very granular and contains a mass of ice, hydrohalite crystals and a little liquid. (D) and (E) Ice gradually dissolve (-14°C), leaving a small hydrohalite single crystal at -1°C, which completely dissolves at +1.3+°C (T_{LM}). Salinity at this temperature corresponds to 26.2 eq. wt% NaCl. The vapour bubble reforms when the temperature reaches +10°C, and with further heating the bubble gradually decreases until it totally disappears at + 20°C. At this temperature the partial homogenisation (to the liquid phase) has been reached.

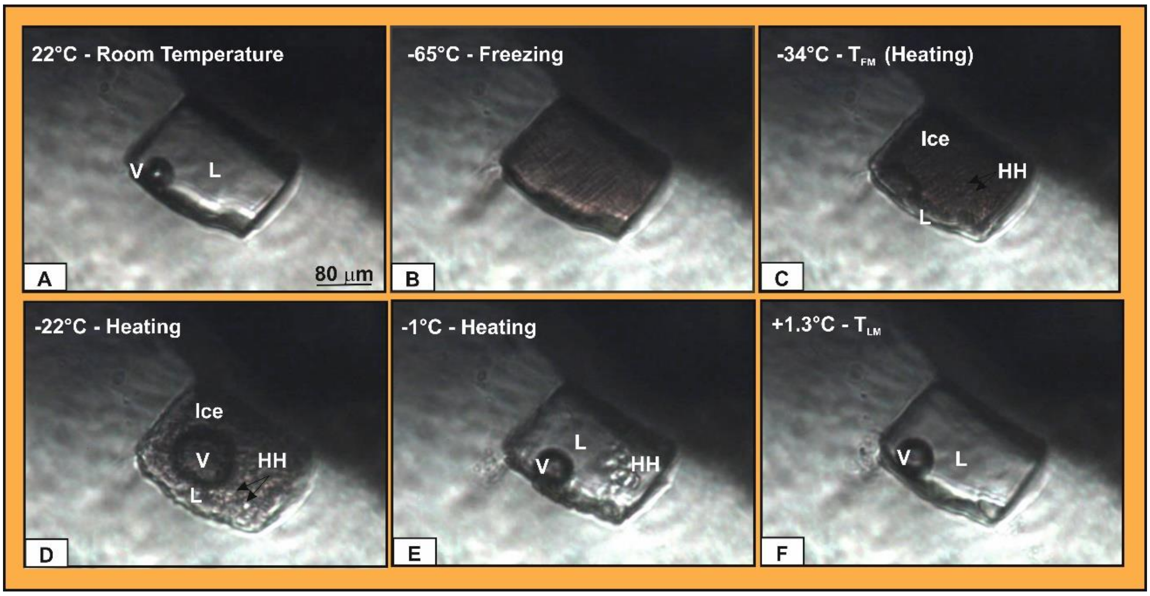

Image C_1a. Phase behaviour of Type 2 fluid inclusion (sample *Zi 07-17*) with a salinity of ~26.2 eq. wt% NaCl. During heating from high temperature. T_{FM}: Temperature of First Melting; T_{LM}: Temperature of Last Melting; V: vapour; HH: hydrohalite; L: liquid. Note the hydrohalite crystals indicated by the arrows.

Image C_1b: example of the full procedure followed during heating and freezing runs for a Type 2 fluid inclusion in macrocrystalline halite sample from the white facies. At room temperature (A) the inclusion with a degree of fill of 0.9 contained two phases (L+V). At -75°C inclusion becomes dark-brown in colour (B). (C) First melting was recorded at -33°C, the inclusion very granular and contains a mass of ice, hydrohalite crystals and a little liquid. (D) Bubble vapour deforms and increase liquid phase. (E) At -22°C small ice and hydrohalite crystals immersed in liquid. Hydrohalite gradually dissolve (-21°C), leaving a small ice single crystal between-6° and -3°C (F-G), which completely dissolves at -1.5+°C (H - T_{LM}). Salinity at this temperature corresponds to 26 eq. wt% NaCl. The vapour bubble reforms when the temperature reaches +15°C, and with further heating the bubble gradually decreases until it totally disappears at +30°C. At this temperature the partial homogenisation (to the liquid phase) has been reached.

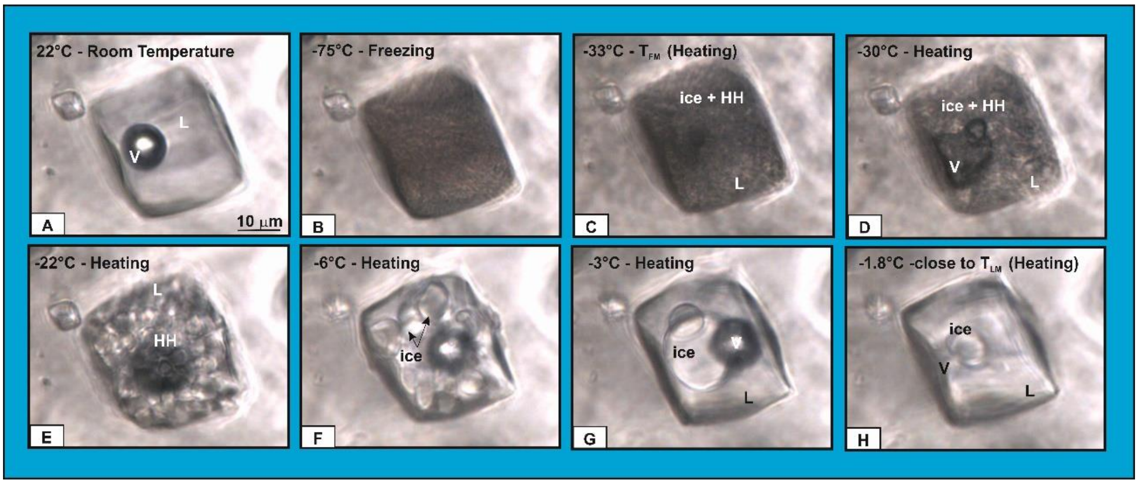

Image C_1b: Phase behaviour of Type 2 fluid inclusion (sample *Zi 11-17*) with a salinity of circa 26 eq. wt% NaCl. During heating from high temperature. TFM: Temperature of First Melting; TLM: Temperature of Last Melting; V: vapour; HH: hydrohalite; L: liquid. Note the ice crystals indicated by the arrows. Full description is given in the text.

Images C_1c: example of the full procedure followed during heating and freezing runs for a Type 2 fluid inclusion in selenite sample (*Ma 01-17* - cloudy interval). At room temperature (A) the inclusion with a degree of fill of 0.9 contained two phases (L+V). At -40°C inclusion freezing and becomes translucent in colour (ice+ hydrohalite-HH) (B). (C) First melting was recorded at -33°C, the inclusion shows irregular ice crystals and a little liquid. (D) Ice crystals become bigger and more regular and increase liquid phase. (E) At -6°C one small ice crystal is immersed in liquid, which completely dissolves at -1.3+°C (H - T_{LM}). Salinity at this temperature corresponds to 4.5 eq. wt% NaCl.

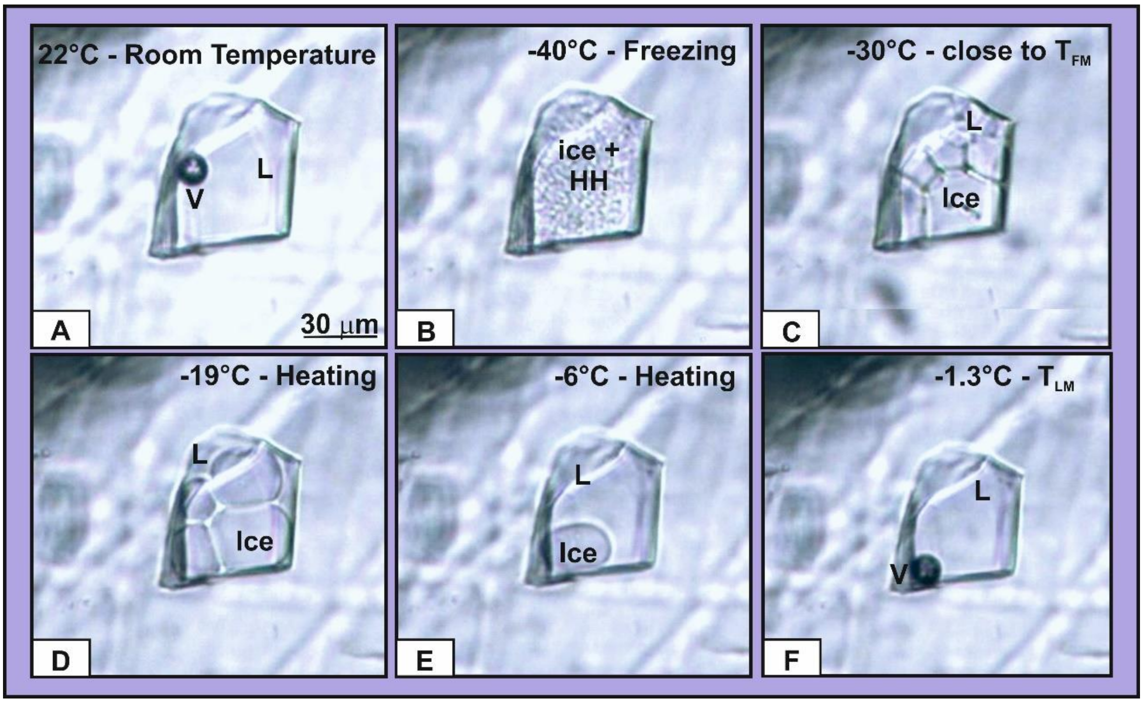

Image C_1c. Phase behaviour of FI Type 2 (sample *Ma 01-17*) with a salinity of circa 4.5 eq. wt% NaCl. T_{FM}: Temperature of First Melting; T_{LM}: Temperature of Last Melting; V: vapour; L: liquid. Full description is given in the text.

C_2: Binary system H_20-NaCl – salinity in the cloudy and clear intervals (selenite crystals)

Each group of FIs, starting from at room temperature (about 20°C – Figure 5 A and B), has been cooled and frozen (between -36° and -48°C) and subsequently heated. During heating, FIs showed Ice+hydrohalite (HH – Figure 5 A1 and B1). In the clear microfacies the ice dissolve between -15°C and 0°C leaving HH (through the birefringence colour, the shape and TLM value - Figure 5 B1), while in the cloudy HH dissolve around -21.4°C preserving only ice (Figure 5 A1). This difference is well visible using binary system H_2O-NaCl (Shepherd *et al.*, 1985), where the FIs observed in cloudy intervals fall in the left side of the diagrams, while the FIs recognised in clear interval fall in the right side. In this filed you cannot use the formulas for low salinity systems (Ice+Liquid field in the phase diagram) used by Hall (1987), Oakes, (1990), Dubois & Marignac (1997) and Bodnar (1993) but it is more appropriate to use the formula of Sterner, (1988) for high salinity system.

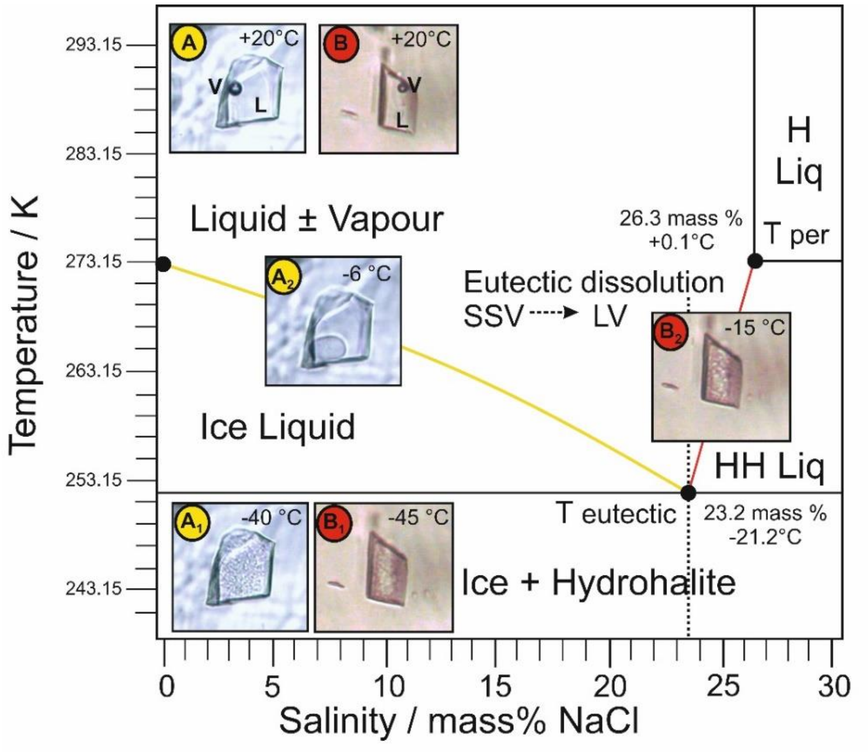

Image C_2c. Binary system H_2O-NaCl. (A) and (B) in red are FIs in cloudy and clear intervals respectively at room Temperature +20°C. During cooling, around -40° and -45°C (A_1 and B_1), FIs freeze showing lumpy appearance (ice +HH). During heating, FI in the cloudy interval shows well visible ice crystals as last phase (A_2) and follows the left curve (in yellow colour) at low salinity, while FI in the clear interval shows small and rounded crystals of HH as last phase (B_2) following the right curve (in red colour) at high salinity.

Appendix D - Chapter 5

D_1: Sample preparation: Sr extraction and ^{87}Sr/^{86}Sr ratio

The following procedure has been carried out in an ISO 6 class clean room and the mass spectrometry laboratory at Department of Earth, Environment and Resources - University of Naples Federico II.

The powdered sample has been weighted in a clean PFA SavillexTM vial (hereafter PFA vial) - ca. 100 mg for halite; ca. 20 mg for gypsum. 4 ml of 18.2 MΩ resistivity Milli-Q® de-ionized water (hereafter Milli-Q water) have been added to the sample, then the vial has been left closed on a hot plate at 160°C for 1 hour.

The vial has been put in an ultrasonic bath for 8 minutes. Then, the sample has been transferred to a clean centrifuge tube and centrifuged at 4500 rpm for 10 minutes.

Ca. 3.5 ml of the supernatant solution has been picked up through a pipette with a sterilized tip carefully avoiding the solid residue, and transferred to a clean PFA vial, left open on hot plate at 90°C until complete dryness has been achieved. Evaporation has been carried out under a plexiglas laminar flow hood equipped with HEPA filters (hereafter laminar flow hood).

The dried sample has been re-dissolved in 1 ml 2.5 N HCl of Suprapur® grade in the same PFA vial and left in ultrasonic bath for 8 minutes. After ca. 1-hour rest, the solution appears clean, with no visible solid residue. Then, the solution has been transferred to a clean centrifuge tube and centrifuged at 4500 rpm for 10 minutes.

0.5 ml of the supernatant solution has been picked up through a pipette with a sterilized tip and loaded on a pre-conditioned quartz column packed with 3.5 ml of AG® 50W X-8 (200-400 mesh BioRadTM) cation exchange resin to separate the strontium from the sample matrix, using 2.5 N HCl of Suprapur® grade as liquid phase. After a discard of ca. 19 ml, the Sr has been collected in 4.5 ml of 2.5 N HCl in a clean PFA vial, then left open on hot plate at 160°C until complete dryness has been achieved, under a laminar flow hood. Then, the dried Sr chloride has been converted to Sr nitrate by adding two droplets of 14 N HNO3 of Suprapur® grade in the PFA vial and left open on hot plate at 160°C until complete dryness has been achieved, under a laminar flow hood.

Subsequently, the sample has been re-dissolved in 1 µl of 1 N HNO_3 of Suprapur® grade through a micropipette with a sterilized tip and loaded on a previously degassed 99.98% pure rhenium filament held at 1 A current, under a laminar flow hood. 1 µl of $TaCl_5$ solution (as activator) and 1 µl of 1% H_3PO_4 solution have been added to the sample to achieve complete adhesion on the filament. Then, the current to the filament has been increased until a few seconds-long mild burnings have been achieved (at ca. 2.5 A).

The Sr isotopes measurement has been carried out through thermal ionization mass spectrometry techniques (TIMS), using a Thermo Scientific^{TM} Triton Plus® solid-source multicollector mass spectrometer. The instrument is equipped with 9 (1 fixed and 8 adjustable) Faraday caps and 1 Retarding Potential Quadrupole (RPQplus®) filter installed on the central Secondary Electron Multiplier (SEM) ion counting channel.

The Sr isotope measurements have been carried out with a signal intensity of ca. 4 V on the ^{88}Sr. 150 single runs (15 blocks of 10 cycles each) with an integration time of 16.777 seconds have been acquired for each sample. Possible mass interference on ^{87}Sr by ^{87}Rb has been checked and corrected throughout all measurements. Sr isotope ratios (^{87}Sr/^{86}Sr) have been normalized for within-run isotopic fractionation to ^{88}Sr/^{86}Sr = 8.375209 using an exponential low for correction. The final ^{87}Sr/^{86}Sr value is reported as the mean of the 150 single runs at 2σ confidence level according to Goldstein *et al.*, (2003).

The running conditions for sample analysis have been tested by measuring the ^{87}Sr/^{86}Sr ratio of National Institute of Standards and Technology (NIST) SRM 987 ($SrCO_3$) standard solution (recommended value: 0.710248 ± 0.000011; Thirlwall, 1991). Replicate measurements of the NIST SRM 987 standard in the period of evaporite samples analysis have provided an average value of ^{87}Sr/^{86}Sr = 0.710243 ± 0.000006 (2σ, N = 29; external reproducibility according to Goldstein *et al.*, 2003). A correction of + 0.000005 has been applied to the measured ^{87}Sr/^{86}Sr values to normalize them to the recommended value.

The Sr blank has been on the order of 200 pg during the period of chemical processing of the samples, thus negligible.

List of figures

List of tables

Chapter 2

Chapter 3

Chapter 4

Chapter 5

References

Alfred, R., Loeblich, Jr., Helen, T. (1978). I: *The Coccolithophorid Genus Calcidiscus Kamptner and its synonyms*. Journal Article, **52**, 1390-1392.

Amodio-Morelli, L., Bonardi, G., Colonna, V., Dietrich, D., Giunta, G., Ippolito, F., Liguori, V., Lorenzoni, S., Paglionico, A., Perrone, V., Piccarreta, G., Russo, M., Scandone, P., Zanettin-Lorenzoni, E., Zuppetta, A. (1976). I: *L'arco Calabro-Peloritano nell'orogene appenninico Maghrebide (The Calabrian-Peloritan Arc in the Apennine-Maghrebide orogen)*. Memorie della Società Geologica Italiana, **17**, 1-60.

Angì, G., Cirrincione, R., Fazio, E., Ortolano, P., Pezzino, A. (2010). I: *Metamorphic evolution of preserved hercynian crustal section in the Serre massif (Calabria-Peloritani orogen, southern Italy)*. Lithos, **115** (1-4), 237-262.

Ayllón-Quevedo, F., Souza-Egipsy, V., Sanz-Montero, M.E., Rodríguez-Aranda, J.P. (2007). I: *Fluid inclusion analysis of twinned selenite gypsum beds from the Miocene of the Madrid basin (Spain). Implication on dolomite bioformation*. Sedimentary Geology, **201**, 212-230.

Babel, M. (2004). I: *Models for evaporite, selenite and gypsum microbialite deposition in ancient saline basin*. Acta Geological Polonica, **54**, 219-249.

Upper, M., Dominici, R., Muto, F., Critelli., S. (2008). I: *Detrital models in a late Miocene wedge-top basin, Northeastern Calabria, Italy: compositional record of wedge-top partitioning*. Journal of Sedimentary research, **79**, 693-711.

Benison, K.C., Goldstein, R.H. (1999). I: *Permian paleoclimate data from fluid inclusions in halite*. Chemical Geology, **154**, 113-132.

Benison, K.C. (2013). I: *Acid saline fluid inclusions: examples from modern and Permian extreme lake systems*. Geofluids, **13**, 579-593.

Benson, R.H. (1991). I: *Biodynamics, saline giants and late miocene catastrophism*. Carbonates and Evaporite, **6**, 127-168.

Birgel, D., Guido, A., Liu, X.L., Hinrichs, K.U., Gier, S., Peckmann, J. (2104). I: *Hypersaline conditions during deposition of the Calcare di Base revealed from archaeal di- and tetraether inventories*. Organic Geochemistry,77.

Bodnar, R.J., Reynolds, T.J., Kuehn, C.A. (1985). I: *Fluid-inclusion systematics in epithermal systems*. In Berger, B.R., Bethke, P.M. (eds). Geology and Geochemistry of Epithermal Systems: Society of economic Geologists, Reviews in Economic Geology, **2**, 73-97.

Bodnar, R.J. (2003). I: *Re.equilibration of fluid inclusions*. In: Samson, I., Anderson, A., Marshal, D., (eds). Fluid inclusions: Analysis and interpretation. Mineralogical Association of Canada, Short Course Ser. **32**, 213-230.

Bonardi, G., Cavazza, W., Perrone, V., Rossi, S. (2001). I: *Calabria-Peloritani terrane and northern Ionian Sea*. In: Vai, G.B., Martini, I.P. (eds.), Anatomy of an Orogen: The Apennines and Adjacent Mediterranean Basins. Kluwer Academic Publishers, Bodmin, 287-306.

Bonardi, G., Giunta, G., Perrone, V., Russo, M., Zuppetta, A., Ciampo, G. (1980). I: *Osservazione sull'evoluzione dell'Arco Calabro-Peloritano nel Miocene inferiore: la Formazione di Stilo-Capo d'Orlando.* Bollettino Società Geologica Italiana, **99**, 365-393.

Bouillin, J.P., Majeste-Menjoulas, C., Ollivier-Pierre, M.F., Tambareau, Y., Villatte, J. (1985). I: *Transgression de l'Oligocene inferieur (formation de Palizzi) sur un karst a remplissage bauxitique dans les zones internes calabro-peloritaines (Italie)*. Académie des Sciences (Paris), Compte-rendu, **301**, 415-420.

Brass, G. (1976). I: *The variation of the marine* $^{87}Sr/^{86}Sr$ *ratio during Phanerozoic time: Interpretation using a flux model.* Geochimica et Cosmochimica Acta. **40**, 721-730.

Brutto, F., Muto, F., Loreto, M.F., De Paola, N., Tripodi, V., Critelli, S., Facchin, L. (2016). I: *The Neogene-Quaternary geodynamic evolution of the central Calabrian Arc: A case study from the western Catanzaro Trough basin*. Journal of Geodynamics. DOI: 10.1016/jog.2016.09.002.

Butler, R.W.H., Lickorish, W.H., Grasso, M., Pedley, H.M., Ramberti, L. (1995). I: *Tectonics and sequence stratigraphy in Messinian basins, Sicily: constrains on the initiation and termination of the Mediterranean "salinity crisis"*. Geological Society of America, **107**, 425-439.

Carta Ispra: Moretti A., Vincenzi S. Note illustrative della Carta Geologica D'Italia alla scala 1:50.000 foglio 561 San Giovanni in Fiore. ISPRA (Istituto Superiore per la Protezione e la Ricerca Ambientale), Servizio Geologico d'Italia. Progetto CARG.

Caruso, C., Cianflone, G., Dominici, R., Sonnino., Vetri, M. (2013). I: *Continental to marine deposits of the Stilo-Capo d'Orlando Formation (Oligo-Miocene) in the area of Agnana Calabra (southern Ionian Calabria, Italy); Inferred from sedimentological and ichnological data*. Journal of Mediterranean Earth Sciences, **5**, 27-29.

CASMEZ (1967). "Carta geologica della Calabria 1:25.000", Poligrafica e Carte valori, Ercolano – Napoli.

Catalano, S., De Guidi, G., Monaco, C., Tortorici, G., Tortorici, L. (2008). I: *Active faulting and seismicity along the Siculo-calabrian Rift zone (southern Italy)*. Tectonophysics, **453**, 177-192.

Cavazza, W., Barone, M. (2010). I: *Large-scale sedimentary recycling of tectonic mélange in a forearc setting: the Ionian basin (Oligocene – Quaternary, southern Italy)*. Geology Society American Bullet, **122**, 11-12.

Cavazza, W., DeCelles, P.G. (1993). I *Miocene submarine canyons and associated sedimentary facies in southeastern Calabria, southern Italy*. Geology Society American Bullet, **105**, 1297-1309.

Chiarella, D., Moretti, M., Longhitano, S.G., Muto, F. (2016). I: *Deformed cross-stratified deposits in the Early Pleistocene tidally-dominated Catanzaro strait-fill succession, Calabrian Arc (Southern Italy): triggering mechanisms and environment significance*. Sedimentary Geology, **344**, 277-289.

Cianflone, G., Dominici, R. (2011). I: *Stratigrafia fisica della successione sedimentaria miocenica del settore Nord-orientale della Stretta di Catanzaro (Calabria centro-orientale)*. Rendiconti Online della Società Geologica Italiana, **17**, 63-69.

Cianflone, G., Dominici, R., Sonnino, M. (2012). I: *Studio preliminare delle facies evaporitiche e carbonatiche del Messiniano della Stretta di Catanzaro (Calabria Centrale)*. Rendiconto Online della Società Geologica Italiana, **21**, 71-73.

CIESM (2008). *The Messinian salinity crisis from mega-deposits to microbiology*. A consensus report. In: Briand, F., Monaco (eds.), 33ème CIESM Workshop Monographs, **33**, 91-96.

Cirrincione, R., Ortolano, G., Pezzino, A., Punturo, R. (2008). I: *Poly-orogenic multi-stage metamorphic evolution inferred via P-T pseudosections: an example from Aspromonte Massif basement rocks (Southern Calabria, Italy)*. Lithos, **103**, 466-502.

Cita, M.B. (2001). I: *The messinian salinity crisis in the Mediterranean*. In: Briegel, U., Xiao, W. (eds.), Paradoxes in Geology. Elsevier Science, **16**, 353-359.

Clauzon, G. (1973). I: *The eustatic hypothesis and the pre-Pliocene cutting of the Rhône valley*. In: Ryan, W.B.F., Hsü, K.J. (eds.), Initial reports of the Deep Sea Drilling Project, 13. U.S. Government Printing Office, Washington D.C., 1251-1256.

Clauzon, G., Suc, J.-P., Gautier, F., Berger, A., Loutre, M.F. (1996). I: *Alternate interpretation of the Messinian salinity crisis, controversy resolved?* Geology, **24**, 363-366.

Colalongo, M.L., di Grande, A., d'Onofio, S. (1979). I: *Stratigraphy of Late Miocene Italian sections straddling the Tortonion-Messinian boundary*. Bollettino della Società Paleontologica Italiana, **18**, 258-302.

Colonna, V., Lorenzoni, S., Zanettin-Lorenzoni, E. (1973). *I: Sull'esistenza lungo il bordo sudorientale del Massiccio Granitico delle Serre (Calabria).* Bollettino della Società Geologica Italiana, **92**, 801-830.

Costa E., Dominici R., Lugli S. (2010). I: *Tectonic Evolution of the Salt-Bearing Crotone Basin (Southern Italy)*. Search and Discovery Article, AAPG International Conference and Exhibition, Rio de Janeiro, Brazil, November 15-18.

Costanzo, A., Cipriani, M., Feely, M., Cianflone, G., Dominici, R. (2019). I: *Messinian twinned selenite from the Catanzaro Trough, Calabria, Southern Italy: filed, petrographic and fluid inclusion perspectives*. Carbonates and Evaporites. DOI:10.1007/s13146-019-00516-0.

Critelli, S., Muto, F., Tripodi, V. (2016). I: *Note illustrative della Carta Geologica D'Italia alla scala 1:50.000 foglio 603 Bovalino*. ISPRA, Servizio Geologico d'Italia. Progetto CARG.

Cumbers, J., Rothschild, L.J. (2014). I: *Salt tolerance and polyphyly in the cyanobacterium Chroococcidiopsis (Pleurocapsales)*. Journal of Phycology.

David, R., Kurt, I., Olivier, B., Dirk, R., Andres, W., Michel, A. (2005). I: *Bacteria associated with spores of the arbuscular mycorrhizal fungi Glomus geosporum and Glomus constrictum*. Applied and environment microbiology. DOI:10.1128/AEM.71.11.6673-6679.2005.

Decima, A., Wezel, F.C. (1971). I: *Osservazioni sulle evaporiti Messiniane della Sicilia centro meridionale*. Rivista Mineraria Siciliana, **130-134**, 172-187.

Diamond, L.W. (2003). I: *Systematics of H_2O inclusions*. In: Samson, I., Anderson, A., Marshall, D. (eds.), Fluid Inclusions: Analysis and Interpretation. Mineralogical Association of Canada Short Course, chapter 3, **32**.

Dubois, M., Marignac, C. (1997). I: *The H_2O-NaCl-$MgCl_2$ ternary phase diagram with special application to fluid inclusion studies*. Economic Geology, **92,** 114-119

Dominici, R., Sonnino, M. (1999). I: *Interpretazione della successione basale della Formazione di stilo Capo d'Orlando nella zona di Agnana Calabra e canolo (Oligocene, Calabria jonica)*. Giornale di Geologia, Rivista di geologia sedimentaria e geologia marina, **61**, serie 3.

Eugster, H.P., Hardie. L. A. (1978). I: *Saline lakes*. In: Lerman, A. (eds), Chemistry, geology, physics, New York. NY. Springer-Verlag, 237-293.

Ferrini, G., Moretti, A., Di Sabatino, D., Frattaroli, A. (2003). I: *I piani carsici del massiccio del Gran Sasso: morfologia ed insediamento antropico*. In: Convocazione Nazionale CAI "L'Ambiente Carsico e l'Uomo" - preprint. Frabosa Soprana (CN), 5- 8 settembre 2003, 17.

Flecker, R., de Villiers, S., Ellam, R.M. (2002). I: *Modelling the effect of evaporation on the salinity – $^{87}Sr/^{86}Sr$ relationship in modern and ancient marginal-marine systems: the Mediterranean Messinian*. Earth and Planetary Science Letters, **203**, 221-233.

Flecker, R., Ellam, R.M. (2006). I: *Identifying Late Miocene episodes of connection and isolation in the Mediterranean-Paratethyan realm using Sr isotopes*. Sedimentary Geology, **188-189**, 189-203.

Fortuin, A.R. and Krijgsman, W. (2003). I: *The Messinian of the Nijar Basin (SE Spain): sedimentation, depositional environments and paleogeographic evolution*. Sedimentary Geology, **341**,1-30.

Gautier, F., Clauzon, G., Suc, J.-P., Cravatte, J. And Violanti, D. (1994). I: *Age et durée de la crise de salinitè messinienne*. Académie des Sciences, **318**, 1103-1109.

Gladstone, R., Flecker, R., Valdes, P., Lunt, D., Markwick, P. (2007). I: *The Mediterranean hydrologic budget from a Late Miocene global climate simulation*. Palaeogeography, Palaeoclimatology, Palaeoecology, **251**, 254-267.

Goldstein, R.H. (2003). I: *Petrographic analysis of fluid inclusions*. In Samson, I., Anderson, A., Marshall, D. (eds), Fluid Inclusions: Analysis and Interpretation, Short Course 32: Mineralogical Association of Canada, Quebec, Canada, 9-53.

Goldstein, R.H., Reynolds, T.J. (1994). I: *Systematics of fluid inclusions in diagenetic minerals*. SEPM Short Course, **31**.

Goldstein, S.L., Deines, P., Oelkers, E.H., Rudnick, R.L., Walter, L.M. (2003). I: *Standards for publication of isotopic ratio and chemical data in Chemical Geology*. Chemical Geology. **202**, 1-4.

Graessner, T., Schenk, V. (1999). I: *Low – pressure metamorphism of Palaeozoic pelites in the Aspromonte, southern Calabria: constraints for the thermal evolution in the Calabrian crustal cross-section during the hercynian orogeny*. Journal Metamorphic Geology, **17**, 157-172.

Guiry, M., D. (1987). I: *The evolution of life history types in the Rhodophyta: an appraisal*. Cryptogamie, Algologie, **8**, 1-12.

Gullà, G., Antronico, L., Sorriso-Valvo, M., Tansi, C. (2005). I: *Proposta metodologica per la valutazione di indicatori di pericolo e rischio da frana a scala intermedia: l'area della stretta di Catanzaro (Calabria, Italia)*. Geologica Romana, **38**, 97-121.

Hall, D.L., Sterner, S.M., Bodnar, R.J. (1988). I: *Freezing point depression of NaCI-K&H20 solutions*. Economic Geology **83**, 197-202.

Handford, C.R. (1991). I: *Marginal marine halite; sabhas and Salinas*, in J.L. Melvin, (eds), Evaporites, petroleum and mineral resources, Elsevier Developments in Sedimentology, **50**, 1-66.

Hilgen, F.J., Krijgsman, W. (1999). I: *Cyclostratigraphy and astrochronology of the Tripoli diatomite formation (pre-evaporite Messinian, Sicily, Italy)*. Terra Nova, **11**, 16-22.

Hsü, K.J., Ryan, W.B.F.b, Cita, M.B.C. (1973). I: *Late miocene desiccation of the Mediterranean*. Nature, **242**, 240-244.

Iovine, G., Tansi, C. (1998). I: *Gravity-accommodated 'structural wedges' along thrust ramps: A kinematic scheme of gravitational evolution*. Natural Hazards, **17**, 195-224.

Ingram, B.L., Sloan, D. (1992). I: *Strontium isotopic composition of estuarine sediments as paleosalinity–paleoclimate indicator*. Science, **255**, 68-72.

Jehlička, J., Oren, A. (2013). I: *Raman spectroscopy in halophile research*. Frontiers in Microbiology, **4**, 380.

Komarov, V.F., Severin, A.V., Melikhov, I.V. (2000). I: *Fluctuations in growth rate of gypsum crystals*. Crystallography Reports, **45**, 364-370.

Krijgsman, W., Fortuin, A.R., Hilgen, F.J., Sierro, F.J. (2001). I: *Astrochronology for the Messinian Sorbas basin (SE Spain) and orbital (precessional) forcing for evaporite cyclicity*. Sedimentary Geology, 43-60.

Krijgsman, W., Hilgen, F.J., Raffi, I., Sierro, F.J., Wilsonk, D.S. (1999). I: *Chronology, causes and progression of the Messinian salinity crisis*. Nature, **400**, 652-655.

Lo Cicero, G, Catalano, R. (1976). I: *Facies and petrography of some Messinian evaporites of the Ciminna Basin (Sicily)*. Memorie della Società Geologica Italiana, **16**, 63-81.

Longhitano, S.G., Chiarella, D., Di Stefano, A., Messina, C., Sabato, L., Tropeano, M. (2012). I: *Tidal signatures in Neogene to Quaternary mixed deposits of southern Italy straits and bays*. Sedimentary Geology, **279**, 74-96.

Longhitano, S.G., Chiarella, D., Muto, F. (2014). I: *Three-dimensional to two-dimensional cross-strata transition in the lower Pleistocene Catanzaro tidal strait transgressive succession (southern Italy)*. Sedimentology, **61**, 2136-2171.

Lowenstein, T.K., Hardie, L. (1985). I: *Criteria for the recognition of salt-pan evaporites*. Sedimentology, **32**, 627-644.

Lowenstein, T.K., Li, J., Brown, C.B. (1998). I: *Paleotemperatures from fluid inclusions in halite: method verification and 100,000 year paleotemperature record, Death Valley, CA*. Chemical Geology, **150**, 223-245.

Lowenstein, T.K. (2012). I: *Advances in Understanding the Biology of Halophilic Microorganisms*. R.H. Vreeland (eds), 117-139.

Lugli, S., Charlotte Schreiber, B., Triberti, B. (1999). I: *Giant polygons in the realmonte mine (agrigento, sicily): Evidence for the desiccation of a messinian halite basin*. Journal of Sedimentary Research, **69**, 764-771.

Lugli, S., Dominici, R., Barone, M., Costa, E., Cavozzi, C. (2007). I: *Messinian halite and residual facies in the Crotone basin (Calabria, Italy)*. From Schreiber, B.C., Lugli, S. & Babel, M. (eds), Evaporites Through Space and Time. The Geological Society of London, **285**, 169-178.

Lugli, S., Manzi, V., Roveri, M., Schreiber, B.C. (2010). I: *The Primary Lower Gypsum in the Mediterranean: A new facies interpretation for the first stage of the Messinian salinity crisis*. Palaeogeography, Palaeoclimatology, Palaeoecology, **297**, 83-99.

Manzi, V., Gennari, R., Lugli, S., Roveri, M., Scafetta, N., Schreiber, B.C. (2012). I: *High-frequency cyclicity in the Mediterranean messinian evaporites: evidence for Solar-Lunar climate forcing*. Journal of Sedimentary Research, **82**, 991-1005.

Manzi, V., Lugli, S., Ricci Lucchi, F., Roveri, M. (2005). I: *Deep-water clastic evaporites deposition in the Messinian Adriatic foredeep (northern Appennines, Italy): did the Mediterranean ever dry out?* Sedimentology, **52**, 875-902.

Manzi, V., Lugli, S., Roveri, M., Charlotte Schreiber, B. (2009). I: *A new facies model for the Upper Gypsum of Sicily (Italy): Chronological and palaeoenvironment constraints for the Messinian salinity crisis in the Mediterranean*. Sedimentology, **56**, 1937-1960.

McArthur, J.M., Howarth, R.J., Bailey, T.R. (2001). I: *Strontium isotope stratigraphy: LOWESS version 3: best fit to the marine Sr-isotope curve for 0–509 Ma and accompanying look-up table for deriving numerical age*. Journal of Geology, **109**, 155-170.

McArthur, J.M., Howarth, R.J., Shields, G.A. (2012). I: *Strontium isotope stratigraphy*. In: Gradstein, F.M. (Ed.), The Geologic Time Scale 2012. Elsevier Science Limited. 127-144.

Müller, D.W., Mueller, P.A. (1991). I: *Origin and age of the Mediterranean Messinian evaporites: implications from Sr isotopes*. Earth and Planetary Science Letters, **107**, 1-12.

Müller, D.W., Mueller, P.A., McKenzie, J.A., (1990). I: *Strontium isotopic ratios as fluid tracers in Messinian evaporites of the Tyrrhenian Sea (western, Mediterranean Sea)*. Proceeding of the Ocean Drilling Program, Scientific Results, **107**, 603-614.

Natalicchio, M., Dela Pierre, F., Lugli, S., Lowenstein, T.K., Feiner, S.J., Ferrando, S., Manzi, V., Roveri, M., Clari, P. (2014). I: *Did Late Miocene (Messinian) gypsum precipitate from evaporated marine brines? Insights from the Piedmont Basin (Italy).* Geology, **42**, 179-182.

Nesteroff, W.D. (1973). I: *Mineralogy, petrography, distribution and origin of the Messinian Mediterranean evaporites*. In RYAN, WJ. HSÜ et al., (eds.). Initial reports on the deep sea drilling, **13**, 673-694.

Oakes, C.S., Bodnar, R.J., Simonson, J.M. (1990). I: The system NaCl-CaCl-$_2$H$_2$O: I. *The ice liquidus at 1 atm total pressure*. Geochimica et Cosmochimica Acta. https://doi.org/10.1016/0016-7037(90)90356-P.

Ogniben, L. (1955). I: *Le argille scagliose del Crotonese*. Istituto di Geologia Applicata Napoli, Memorie e Note, **6**, 1-72.

Ohneiser, C., Florindo, F., Stocchi, P., Roberts, A.P., DeConto, R.M., Pollard, D. (2015). I: *Antarctic glacio-eustatic contributions to late Miocene Mediterranean desiccation and reflooding*. Nature Communications. DOI: 10.1038/ncomms9765.

Orszag-Sperber, F. (2006). I: *Changing perspectives in the concept of "Lago-Mare" in Mediterranean Late Miocene evolution*. Sedimentary Geology, **188-189**, 259-277.

Ortì, F. (2011). I: *Selenite facies in marine evaporites: a review*. international association of sedimentologists special publications, **43**, 431-464.

Palmer, M.R., Edmond, J.M. (1992). I: *Controls over the strontium isotope composition of river water*. Geochimica et Cosmochimica Acta. **56**, 2099-2111.

Panieri, G., Lugli, S., Manzi, V., Roveri, M., Schreiber, B.C., Palinska, K.A. (2010). I: *Ribosomal RNA gene fragments from fossilized cyanobacteria identified in primary gypsum from the late Miocene, Italy*. Geobiology, **8**, 101-111.

Reinhardt, E.G., Stanley, D.J., Patterson, R.T. (1998). I: *Strontium paleontological method as a high-resolution paleosalinity tool for lagoonal environments*. Geology. 26, 1003-1006. Report. In: Briand, F., Monaco (eds.), 33ème CIESM Workshop Monographs. **33**, 91-96.

Reynolds, C.S., Huszar, V., Kruk, C., Naselli-Flores, L., Melo, S. (2002). I: *Towards a functional classification of the freshwater phytoplankton*. Journal of Plankton Research, **24**, 417-428.

Riding, R., Braga, J.C., Martín, J.M., Sánchez-Almazo, I.M. (1998). I: *Mediterranean Messinian salinity crisis: Constraints from a coeval marginal basin, Sorbas, southeastern Spain*. Marine Geology, **146**, 1-20.

Robert, S.M., Spencer, R.J. (1995). I: *Paleotemperatures preserved in fluid inclusions in halite*. Geochimica et Cosmochimica Acta, **59**, 3929-3942.

Roda C. (1965). I: *Geologia della Tavoletta Belvedere di Spinello* (Prov. Catanzaro, F. 237, I-SE). Bollettino della Società Geologica Italiana, **84**, 159-285.

Roda, C. (1964). I: *Distribuzione e facies dei sedimenti Neogenici nel Bacino Crotonese*. Geology Roman, **3**, 319-366.

Roedder, E. (1984). I: *Fluid inclusion*. Mineralogic Society of America, **12**, 11-45.

Rossi, V.M., Longhitano, S.G., Mellere, D., Dalrymple, R.W., Steel, R.j., Chiarella, D., Olariu, C. (2017). I: *Interplay of tidal and fluvial processes in an early Pleistocene, delta-fed, strait margin (Calabria, Southern Italy)*. Marine and Petroleum Geology, **87**, 14-30.

Rouchy, J.M. (1982). I: *La genèse des évaporites messiniennes de Méditerranée*. Museum National d'Histoire Naturelle, Paris, Mémoires, Nouvelle Série, Série C, Sciences de la Terre, **50**, 1-267.

Rouchy, J.M., Caruso, A. (2006). I: *The Messinian salinity crisis in the Mediterranean basin: A reassessment of the data and an integrated scenario*. Sedimentary Geology, **188-189**, 35-67.

Rouchy, J.M., Saint Martin, J.P. (1992). I. *Late Miocene events in the Mediterranean as recorded by carbonate–evaporite relations*. Geology, **20**, 629-632.

Roveri, M., Bassetti, M.A., Ricci Lucchi, F. (2001). I: *The mediterranean Messinian salinity crisis: An Apennine foredeep perspective*. Sedimentary Geology, **140**, 201-214.

Roveri, M., Lugli, S., Manzi, V., Schreiber B.C. (2008). I: *The Messinian Sicilian stratigraphy revisited: new insights for the Messinian salinity crisis*. Terra Nova, **00**, 1-6.

Roveri, M., Lugli, S., Manzi, V., Gennari, R., Schreiber, B.C. (2014). I: *High-resolution strontium isotope stratigraphy of the Messinian deep Mediterranean basins: Implications for marginal to central basins correlation.* Marine Geology, **359**, 113-125.

Sankaranarayanan, K., Lowenstein, T.K., Timofeeff, M.N., Schubert, B.A., Lum, J.K. (2014). I: *Characterization of ancient DNA supports long-term survival of haloarchaea*. Astrobiology, **14**.

Schreiber, B.C., Hsü, K.J. (1980). I: *Evaporites*. In: Hobson, G., D., (eds.), Developments in Petroleum Geology, 2. Applied Science Ltd., London, 87-138.

Schreiber, B.C. (1997). I: *Field trip to Eraclea Minoa: Upper Messinian*. “Neogene Mediterranean Paleoceanography”, Exursion Guide Book Palermo-Caltanisetta-Agrigento-Erice (Sicily), 72.80.

Schreiber, B.C., Bąbel, M., Lugli, S. (2007). I: *Introduction and overview*, in Evaporites Through Space and Time, Geological Society, London, Special Publications, **285**, 1-13.

Selli, R. (1960). I: *Il Messiniano Mayer-Eymar 1867*. Proposta di un neostratotipo. Giornale di Geologia, 28, 1-33.

Shepherd, T., Rankin, A.H., Alderton, D.H.M. (1985). I: *A practical guide to fluid inclusions studies*. *Blackie & Son Limited*, Glasgow, 239.

Sierro, F.J., Hilgen, F.J., Krijgsman, W., Flores, J.A. (2001). I: *The Abad composite (SESpain): a Messinian reference section for the Mediterranean and the APTS*. Palaeogeography, Palaeoclimatology, Palaeoecology, **168 (1-2)**, 141-169.

Speranza, G., Cosentino, D., Tecce, F., Faccenna, C. (2013). I: *Paleoclimate reconstruction during the Messinian evaporite drawdown of the Mediterranean Basin: Insights from microthermometry on halite fluid inclusions*. Geochemistry, Geophysics, Geosystems, **14**.

Stanton, R.L., Gorman, H. (1968). I: *A phenomenological study of grain boundary migration in some common sulphides*. Economic Geology, **63**, 907-923.

Sterner, S.M., Hall, D.L., Bodnar, R.J. (1988). I: *Synthetic fluid inclusions. V. Solubility relations in the system NaCl-KCl-H2O under vapor-saturated conditions*. Geochimica Cosmochimica Acta **52**, 989-1005.

Suc J.-P. & Bessais E. (1990). I: *Pérennité d'un climat thermo-xérique en Sicile avant, pendant, après la crise de salinité messinienne.*C. R. Acad. Sci. Paris, sér. **2**, 310:1701-1707.

Suc, J.P., Violanti, D., Londeix, L., Londeix, L., Poumot, C., Robert, C., Clauzon, G., Gautier, F., Jean Louis, T., Ferrier, J., Chikhi, H., Cambom, G. (1995). I: Evolution of the Messinian Mediterranean environmens; the Tripoli Formation at Capodarso (Sicily, Italy). Review of Palaeobotany and Palynology, **87**, 51-79.

Tecce, F., Cannatelli, C., De Vivo, B. (2016). I: *Le inclusioni fluide e silicatiche nei minerali*. Conoscenza geochimica del territorio, **12**.

Thirlwall, M.F. (1991). I*: Long-term reproducibility of multicollector Sr and Nd isotope ratio analysis*. Chemical Geology, **94**, 85-104.

Topper, R.P.M., Flecker, R., Meijer, P. Th., Wortel, M.J.R. (2011). I: *A box model of the Late Miocene Mediterranean Sea: implications from combined* $^{87}Sr/^{86}Sr$ *and salinity data*. Paleoceanography, **26**, 3223.

Topper, R.P.M., Meijer, P. Th. (2013). I: *A modelling perspective on spatial and temporal variations in Messinian evaporite deposits*. Marine Geology, **336**, 44-60.

Tripodi, V., Muto, F., Brutto, F., Perri, F., Critelli, S. (2018). I: Neogene-Quaternary evolution of the forearc and backarc regions between the Serre and Aspromonte Massifs, Calabria (southern Italy). Marine and Petroleum Geology, **95**, 328-343.

Tripodi, V., Muto, F., Critelli, S. (2013). I: Structural style and tectono-stratigraphic evolution of the Neogene – quaternary Siderno Basin, southern Calabrian arc, Italy. International Geology Review, **55**, 468-481.

Vai, G.B., Ricci Lucchi, F. (1977). I: Algal crusts, autochtonous and clastic gypsum in a cannibalistic evaporite basin; a case history from the Messinian of Northern Appennine. Sedimentology, **24**, 211-244.

Van Dijk J.P. (1991). I: Basin dynamics and sequence stratigraphy in the Calabrian Arc (Central Mediterranean); records and pathways of the Crotone Basin. Geologie en Mijnbouw, **70**, 187-201.

Van Dijk, J.P., Bello M., Brancaleoni, G.P., Cantarella, G., Costa, V., Frixa, A., Golfetto, F., Merlini, S., Riva, M., Torricelli, S., Toscano, C., Zerilli, A. (2000). I: A regional structural model for the northern sector of the Calabrian Arc (southern Italy.) Tectonophysics, **324**, 267-320.

VIDEPI Project 2009-2019. "Visibility of petroleum exploration data in Italy" - web site (www.videpi.com).

Vítek, P., Jehlička, J., Edwards, H.G.M., Osterrothová, K. (2009). I: *Identification of β-carotene in an evaporitic matrix—evaluation of Raman spectroscopic analysis for astrobiological research on Mars*. Analytical and Bioanalytical Chemistry, **393**, 1967-1975.

Vityk, M.O., Bodnar, R.J., Doukhan, J.C. (2000). I: *Synthetic fluid inclusions. XV. TEM investigation of plastic flow associated with re-equilibration of fluid inclusions in natural quartz*. Contributions to Mineralogy and Petrology, **139**, 285-297.

Waggoner, B.M. (1995). I: *Ediacaran Lichens: A Critique*. Paleobiology, **21**, **3**, 393-397.

Wang, J., Lowenstein, T.K. (2017). I: *Anomalously high Cretaceous paleobrine temperatures: Houthouse, hydrothermal or solar heating?* Minerals. DOI:10.3390/min7120245.

Warren, J., K. (1982). I: *Hydrologic setting, occurrence, and significance of gypsum in late Quaternary salt lakes, South Australia*. Sedimentology, **29**, 609-637.

Warren, J.K. (1999). I: *Evaporites their evolution and Economics.* Blackwell Science Ltd.

Warren, J.K. (2006). I: *Evaporites: sediments, resources and hydrocarbons*. Springer.

Weltje, G. (1988). I: De Stilo – Capo D'Orlando Formation in Het Zuidoostelijk Deel Van Het Aspromonte Massief (Zuid – Calabrië, i Calabrië Italië). Internal report. Institute of Earth Science, University of Utrecht, 80-113.

Zecchin, M., Massari, F., Mellere, D., Prosser, G. (2004). I: *Anatomy and evolution of a Mediterranean-type fault bounded basin: the Lower Pliocene of the northern Crotone Basin (Southern Italy).* Basin Research **16**, 117-143.

Zecchin M., Mellere D., Roda C. (2006). I: *Sequence stratigraphy and architectural variability in growth fault-bounded basin fills: a review of Plio-Pleistocene strata units of the Crotone Basin, southern Italy*. Journal of the Geological Society, London, **163**, 471-486.

Zecchin M., Civile D., Caffau M., Muto F., Di Stefano A., Maniscalco R Critelli S. (2012a). I: *The Messinian succession of the Crotone Basin (southern Italy)* I: Stratigraphic architecture reconstructed by seismic and well data. Marine and Petroleum Geology, 1-19.

Zecchin M., Caffau M., Civile D., Critelli S., Di Stefano A., Maniscalco R., Muto F., Sturiale G., Roda C. (2012b). I: *The Plio-Pleistocene evolution of the Crotone Basin (southern Italy): an interplay between sedimentation, tectonics and eustasy in the frame of Calabrian Arc migration*. Earth Science Reviews, **115**, 273-303.

Zecchin, M., Civile, D., Caffau, M., Muto, F., Di Stefano, A., Maniscalco, R., Critelli, S. (2013). I: *The Messinian succession of the Crotone Basin (southern Italy) II: facies architecture and stratal surface across the Miocene-Pliocene boundary*. Marine and Petroleum Geology, **48**, 455-473.

Ringraziamenti

La realizzazione di questo progetto di ricerca è frutto dell'aiuto sia materiale che emotivo di molte persone, senza le quali tutto ciò non sarebbe stato possibile.

Ringrazio in particolar modo i miei supervisori, il Dr. Rocco Dominici e la Dr. Alessandra Costanzo, i quali hanno sempre creduto in me, trasmettendomi passione e molte delle loro conoscenze.

Il Prof.re Martin Feely per avermi donato dolcezza e amorevolezza durante tutto il mio soggiorno in Irlanda.

Il Prof.re Luca Caracciolo e la Prof.re Elissavet Dotsika per aver letto la tesi e avermi fornito importanti spunti di riflessione.

Tutti i tecnici e i professori, principalmente il Prof.re Lowenstein, per il supporto ed i suggerimenti costruttivi.

Il Prof. Massimo D'Antonio per la sua collaborazione nelle analisi isotopiche, la sua celerità ha consentito di ampliare i dati di questa tesi.

Tutti gli amici che hanno sempre cercato di spronarmi con affetto e determinazione; Francesca e Fabiola, colleghe con le quali ho intrapreso questo percorso, Federica e Gloria, colleghe ed amiche che, con la loro curiosità e voglia di vivere, mi hanno insegnato che tutto è possibile se lo si affronta con il sorriso.

Le mie amiche, in particolare Alice sempre pronta ad aiutare e ad ascoltare ogni mio malumore, Alessia, Mabel, Adele, Anna, Antonella, Noemi, Rosy, Annarita e Chiara per essermi state sempre vicine, seppur lontane.

Un grazie di vero cuore alle mie due ancore, mia madre e mio fratello Francesco, senza il loro sorriso, amore e supporto sarebbe stato tutto più difficile. Vi voglio un mondo di bene!!!

A te papà, che tre anni fa mi spronasti ad intraprendere questo percorso. Sono sicura che oggi, dall'alto, sei orgoglioso di come la tua bambina abbia portato a termine tutto ciò, nonostante il grande vuoto che hai lasciato.

Ringrazio la mia seconda famiglia, Maria Luisa, Emilio, Alba, Stefy, nonna Evelina, zia Patrizia e zia Pina, per avermi dimostrato, giorno dopo giorno, il sacro valore della famiglia.

Aldo e Pina, zii acquisiti, sempre pronti ad aiutare e portarmi in giro per il mondo.

Dulcis in fundo, ringrazio te Giovanni, per essermi stato sempre vicino con la forza e la dolcezza di chi ama incondizionatamente e con tutto il cuore, non esistono parole per dirti quanto io sia grata alla vita per avermi donato te. La Geologia ci ha fatto incontrare, il destino innamorare.

A tutti voi, io dedico questo importante traguardo, con la speranza di essere sempre all'altezza delle vostre e delle mie aspettative.

Con amore,
Mara Cipriani